



**LINCOLN
UNIVERSITY**
TE WHARE WĀNAKA O AORAKI



Universität für Bodenkultur Wien
University of Natural Resources
and Life Sciences, Vienna

Master Thesis

Evaluation of multi-level methodical soil moisture measurements: Agricultural application for spatial variability detection

Submitted by

David MARIN, BSc

in the framework of the international Master programme

Natural Resources Management and Ecological Engineering (NARMEE)

in partial fulfilment of the requirements for the academic degree

Master of Science

Vienna, October 2021

Co-Supervisor:

Senior Lecturer Dr. Henry Chau
Faculty of Agriculture and Life Sciences
Dept. Soil- and Physical Sciences
Lincoln University
New Zealand

Main Supervisor:

Univ. Prof. DI. Dr. nat. techn. Josef Eitzinger
Institute of Meteorology and Climatology
Dept. Water, Atmosphere and Environment
Univ. of Natural Resources and Life Sciences
Vienna

Declaration

I hereby declare that I have written this thesis by myself without any help or assistance from a third party. All external literature is cited thoroughly. The references are listed in the corresponding section.

All mentioned information is in accordance with fact or truth up to my knowledge.

Vienna, October 25th, 2021

.....

Abstract

Keywords: soil moisture estimation, spatial variability detection, crop-modeling, microwave satellite soil moisture product, Marchfeld

Climate change-related extreme weather events emerge more frequently in several parts of Europe including, the Marchfeld in Lower Austria. Such drought and heavy rainfall events require sound knowledge about soil moisture regimes on an agricultural field scale to strengthen future crop production.

This study investigates different soil moisture measurement methods for agricultural application. Tools and management strategies are evaluated to assess spatial variability and to identify impacts on soil moisture.

In-situ measurements on an experimental field in 2019 and 2020 were used to analyze statistical, satellite remote sensing, and crop-water-balance simulation methods (ARIS, AquaCrop) for soil moisture estimation.

The analysis shows that spatial variability at the sub-field cannot be detected with the investigated satellite sensor products and crop-water-balance simulation methods. Nevertheless, the analysis shows a good correlation of soil moisture estimation on field-scale between the in-situ sensors and the S1ASCAT satellite remote sensing product as well as the ARIS-, and AquaCrop crop-simulation results. The SMAP sensor product underestimates soil moisture in winter and correlates inadequately with the in-situ reference sensors. On larger scale applications is the SMAP product likewise a viable estimation tool for soil moisture.

The research shows that complementary methods can estimate soil moisture on the field scale reasonably well, which comprise a crucial tool to identify soil moisture limitations for crop production. To conclude, the findings provide insight into the spatio-temporal soil moisture estimation methodologies of satellite and simulation estimations at field scale without the necessity of available in-situ measurements on-site for the conditions in our study.

Limitations in the scientific field of soil moisture estimation are low to non-existing measuring networks of high spatial resolution. Further, to validate satellite or simulation methods with in-situ sensors, difficulties of comparability of volumetric and relative soil moisture occur.

To better understand the implications of these results, further research should address the spatial variability detection of high spatial resolution data based on drones or sophisticated satellite sensors.

Zusammenfassung

Schlagwörter: Bodenfeuchtemessung, Bestimmung räumlicher Variabilität, Nutzpflanzensimulation, Mikrowellenbasierte Satelliten-Bodenfeuchte, Marchfeld

Klimabedingte Extremwetterereignisse treten vermehrt in Teilen Europas auf, auch im niederösterreichischen Marchfeld. Dürre- und Starkregenereignisse erfordern genaue Kenntnis über Bodenfeuchtereime auf landwirtschaftlichen Feldern, um zukünftige Pflanzenproduktionen zu optimieren.

Diese Studie untersucht Bodenfeuchtemessmethoden zur Anwendung in der Landwirtschaft. Hierbei werden Instrumente und Messstrategien evaluiert, um räumliche Variabilität auf Feldebene zu bewerten und negative Auswirkungen von Bodenfeuchtigkeit besser zu erkennen.

In-situ Messungen wurden auf einem Versuchsfeld 2019/20 durchgeführt. Diese wurden mit satellitengestützten Fernerkundungsdaten und Simulationen (ARIS, AquaCrop) für eine Bodenfeuchteschätzung verglichen und analysiert.

Die untersuchten Satellitenprodukte und Simulationen zeigen keine räumliche Variabilität auf Subfeldebene, da auch die Eingangsdaten auf einem räumlichen Mittelwert basieren. Dennoch zeigt die Analyse eine gute Korrelation der räumlich höher aufgelösten, aus einem Gitter gemittelten, in-situ-Sensoren zum Satellitenprodukt S1ASCAT, sowie den ARIS- und AquaCrop-Simulationen. Das SMAP-Satellitenprodukt unterschätzt die Bodenfeuchte im Winter und korreliert unzureichend mit den in-situ-Referenzsensoren. Für großflächige Anwendungen ist SMAP dennoch hilfreich zur Bodenfeuchtemessung. Weiters wird gezeigt, dass die Darstellung der Bodenfeuchte auf Versuchsfeldebene ein entscheidendes Instrument ist, um negative Auswirkungen auf die Pflanzenproduktion zu erkennen.

Die Ergebnisse geben Einblick in die räumlich-zeitlichen Verläufe und Unsicherheiten von Satelliten- sowie Simulationsmesswerten auf Versuchsfeldebene. Mithilfe derer kann Bodenfeuchte auch ohne verfügbare in-situ Messungen ermittelt werden.

Einschränkungen in der Bodenfeuchtemessung sind kaum bis nicht vorhandene in-situ Messnetze. Die Validierung von Satelliten- oder Simulationsdaten mit in-situ Sensoren werden auch durch unterschiedliche Maßeinheiten von Bodenfeuchte, wie volumetrischer oder relativer Bodenfeuchtigkeit, erschwert.

Weiterführende Forschung zur hochauflösenden räumlichen Variabilitätserkennung von Bodenfeuchte sollte Drohnen oder hochauflösende Satellitensensoren beinhalten.

Acknowledgments

The present Master Thesis was accomplished at the Institute of Meteorology and Climatology of the University of Agriculture and Life Sciences, BOKU Vienna. I want to thank my primary supervisor, Professor Josef Eitzinger, who always had an open ear for any questions I had. He allowed me to work in a professional environment, offered me great insight into his enriching expertise, and had valuable advice. With this Thesis topic, he offered me the opportunity to expand my experience in remote sensing and agrometeorology.

In addition, I want to thank Gerhard Kubu, who had an open ear and helped me with any professional questions regarding my Master Thesis.

Many thanks go to my brother Marco, my friends Daniel, Peter, René, and Sebastian, whose suggestions, discussions, technical assistance, and encouragement were beneficial, offering me new skills and perspectives.

I also would like to thank Katrin for supporting me during my Masters, especially throughout my Thesis.

Indeed, I want to take this opportunity to thank my parents for their continuous encouragement and support during my education, especially for the patience and the ongoing motivation to pursue an academic degree, and for the financial support during my education.

In addition, I would like to thank my study colleagues, who accompanied and encouraged me during my studies. Many thanks to my friends I met during my studies at BOKU, especially team NVUM and team NARMEE, with whom I could spend inexpressible time abroad in the US and New Zealand. Likewise, many thanks to my childhood friends Clemens, Julian, Marius, and Martina, who supported me along my way. The same applies to all who supported me, whom I could not name in person.

I would also like to thank my friends Clarissa and Chris for their hard work proofreading my Master Thesis.

Contents

1. Introduction	8
1.1 Soil moisture and climate change	8
1.2 Why is there the need to research spatial variability of crop soil water relations?	9
1.3 Limiting factors in our case study region - Marchfeld	9
1.4 Foundation and difficulties of the research	10
1.5 Research Questions	11
1.6 Objectives	11
1.7 Hypothesis	11
2. Fundamentals	12
2.1 How is SM estimated?	12
2.1.1 In-situ measurements	12
2.1.2 Remote Sensing	13
2.1.3 Modelling	14
2.2 Crop Types	14
2.2.1 Summer Barley - <i>Hordeum vulgare</i>	14
2.2.2 Winter Wheat – <i>Triticum aestivum</i>	15
2.2.3 Winter Rye – <i>Secale cereale</i>	15
3. Material and Methods	17
3.1 Research location	17
3.1.1 Study area	17
3.1.2 Climate	18
3.1.3 Soil Conditions	19
3.1.4 Management Strategy	21
3.2 In-situ sensors for data acquisition	21
3.2.1 Time Domain Reflectometry (TDR)	21
3.2.2 Concept behind TDR and FDR sensors	22
3.2.3 Data Generation	25
3.2.4 Parrot Flower Power (Parrot)	26
3.2.5 METEO weather station	27

3.3 Remote sensing applications.....	29
3.3.1 Optical and thermal wavebands (Passive Remote Sensing) ...	29
3.3.2 NDVI and LAI to determine Canopy Cover	30
3.3.3 ASCAT for SM detection (Active Remote Sensing).....	32
3.3.4 SMAP for SM detection (Active Remote Sensing)	33
3.4 Simulation Programs and SM.....	34
3.4.1 ARIS	34
3.4.2 AquaCrop	36
3.5 Statistical Analysis.....	43
3.6 Scaling of the datasets	44
3.6.1 Preparation of in-situ, satellite, and simulation data for comparison.....	44
3.6.2 Definition of FC and PWP for the experimental field	45
3.6.3 Calibration of in-situ sensors.....	45
3.6.4 Transformation of satellite and simulation data based on soil porosity.....	45
3.7 Overview of the analysis scheme	47
4. Results.....	48
4.1 AquaCrop simulation analysis based on LAI-MODIS observations	48
4.2 Spatial Variability of soil moisture (SM)	50
4.3 Validation of in-situ Parrot sensors	57
4.3.1 Analysis of Parrot and TDR in-situ measurements in 2019	57
4.3.2 Analysis of Parrot and FDR met-station in-situ measurements in 2019	58
4.3.3 Overview of R ² and RMSE.....	59
4.4 Temporal correlation analysis 2019 with satellite products and models	59
4.4.1 Comparison with simulation models (ARIS and AquaCrop)	62
4.4.2 Summary of the year 2019 analysis.....	64
4.4.3 Overview of R ² and RMSE.....	66
4.5 Temporal correlation analysis 2020 with satellite products and models	67

4.5.1 Comparison of simulation models (ARIS and AquaCrop).....	68
4.5.2 Summary of year 2020 analysis.....	70
4.5.3 Overview of R ² and RMSE.....	72
4.6 Temporal correlation analysis 2018 with satellite products and models	73
4.6.1 Summary of year 2018 analysis.....	77
4.6.2 Overview of R ² and RMSE.....	79
5. Discussion.....	80
5.1 Tools for detecting SM at high spatial resolution by satellite remote sensing and model simulations	80
5.1.1 Results achieved in the context of state-of-the-art	82
5.2 Estimation of SM to combat increasing droughts.....	83
5.3 The combination of methods for SM estimation.....	87
5.4 Limitations of simulation and remote sensing techniques	88
6. Conclusion and prospects for future.....	90
Appendix.....	91
Complimentary Baseline Analysis	91
Vegetation Period 2019.....	92
Vegetation Period 2020.....	100
Vegetation Period 2018.....	110
List of Acronyms	118
Table of Contents.....	120
Equations	120
Figures.....	120
Tables	122
Annex.....	123
References.....	125

1. Introduction

1.1 Soil moisture and climate change

In the foreseeable future, an increase in water deficiencies will force global action to tackle rising resource emergencies (Lalic, Firanj Sremac, *et al.*, 2018). With climate change occurring, extreme weather events emerge, green and blue water shortages surge (WWAP (United Nations World Water Assessment Programme), 2015). Consequently, data and tools for the assessment and management of water resources need to be developed (WWAP (United Nations World Water Assessment Programme), 2015).

10 Overall, global agrarian production will be subject to climate change-related alterations by the end of 2050, with spatial differences and impacts (Hoekstra *et al.*, 2011). High spatial variabilities affect the global climate system with varying consequences (e.g., ice shield melting, water body evaporation) (Lalic, Eitzinger, *et al.*, 2018). In addition, increasing population coupled with climate change-driven water shortages require optimization in crop water use (Ezenne *et al.*, 2019).

For instance, certain regions in central Europe may experience summer drought events, enhanced by low soil water storage capacity (Eitzinger *et al.*, 2008). Such water shortages are expected in agrarian production regions.

20 Ongoing changes of climatic constraints, like deviations in the meteorological weather mean and its variability, will have an increasing impact on agricultural cropping systems (Trnka *et al.*, 2010; Thaler *et al.*, 2012). Observed changes like this are based on reliable projections related to anthropogenic climate change impacts (Lalic, Eitzinger, *et al.*, 2018).

Eventually, soil water availability is therefore paramount for crop production. Such soil water availability is determined by weather patterns and the ability of the soil to retain the water (Saue and Kadaja, 2014). Therefore, crop production depends heavily on the soil-climate relationship, with water being the interface for vegetation (Saue and Kadaja, 2014). Indeed, different spatio-temporal scales with fluctuations of uncertain ecosystem responses like precipitation events control the recharge of soil water (Saue and Kadaja, 2014). The available water for plants within the root zone is dependent on rainfall, irrigation, or the capillary rise of groundwater (Thaler *et al.*, 2018).

30 Thus, soil water availability is ultimately determined by the prevalent soil physical characteristics of a site, such as particle size, organic matter, and bulk density. These soil characteristics control the soil water budget with inflow and outflow processes and the water-holding capacity determining evaporation, transpiration, and runoff (Saue and Kadaja, 2014). Concerning a more in-depth observation, the spatial variability of soil moisture (SM) becomes more critical.

Such spatial variability in SM results from a site's topography, including different soil textures, vegetation cover, and soil hydraulic properties. Moreover, underlying management practices and meteorological patterns with impacts on precipitation influence its variability (METER, 40 2020).

Some key factors influencing spatial variability of soil water content is the time constant, which changes with seasonal weather impacts of droughts, precipitation, and evapotranspiration.

For instance, as a climatic phenomenon, a drought damages agricultural systems and other sectors, with a high potential of wreaking havoc eventually (Mozny *et al.*, 2012).

Mozny *et al.* (2012) demonstrated that models and information on humidity regimes of soils could act as a warning system for current and future global climate change scenarios. Regardless of that possibility, the basic idea behind sound knowledge of SM is assessing the water needs of the plant directly (Lalic, Eitzinger, *et al.*, 2018).

50 The plant's available water is understood as the difference between permanent wilting point (PWP) and field capacity (FC). This available water determines the amount of plant-available water stored in the soil pores ready to be extracted by respected flora. Therefore, to increase crop yield or achieve a steady yield, soil water content typically requires values well above the PWP (METER, 2020).

Therefore, an applied irrigation management application can be designed based on SM regimes (METER, 2020), resulting from models and available SM data or estimations as a combined approach of methods.

1.2 Why is there the need to research spatial variability of crop soil water relations?

60 In the lowland regions of East- and Southern Austria, the occurrence of drought- and heatwaves are increasing, eventually negatively impacting crop yields (APCC, 2014; Thaler *et al.*, 2012).

The Marchfeld region is considered one of Austria's major field crop production areas (Thaler *et al.*, 2012). However, it is also one of the driest. With climate change altering weather patterns, the region's ability to continue crop production may be in question.

It is predicted that the Marchfeld region will experience seasonal water shortage from April to June, which are known to be critical stages in crop production (Eitzinger *et al.*, 2003; Trnka *et al.*, 2010).

70 As Dubrovsky *et al.* (2009) indicated, dry agricultural areas will experience droughts and heat stresses, limiting crop production at sensitive stages of plant development. According to Thaler *et al.* (2012), the crop-growing period in the 'Marchfeld' region will be shortened by up to 20 days with a respective temperature increase of 2°C, leading to reduced yield potential of winter Wheat. Such a scenario is featured in Lalic *et al.* (2018), related to the climate normal and its spatial scale, indicating global temperature increase regardless of the location.

80 With inter-annual variability in crop production, these aggravated conditions foster a growing necessity for an efficient technique for seasonal forecasting and adapted crop management (Lalic, Firanj Sremac, *et al.*, 2018). Digital techniques such as remote sensing with satellite images have good applicability to detect crop water stress before irreparable losses occur (Ezenne *et al.*, 2019). Such measurements have a high potential to supplement in-situ methods like Time Domain Reflectometry (TDR) testing to optimize agricultural production (Ezenne *et al.*, 2019). Nevertheless, spatio-temporal variability is unaccounted for with in-situ measurements.

Another advantage can be the application of agronomic growth models, interfaced with remote sensing data, which accounts for the incorporation of geographic heterogeneity (Todoroff, De Robillard, and Laurent, 2010). Precision agriculture's aim is hereby less input (e.g., water) while increasing the quality and quantity of the agricultural output (Ezenne *et al.*, 2019).

Todoroff, De Robillard, and Laurent (2010) showed that remote sensing data interfaced with agronomic models are robust and cheap to estimating the total available water capacity of the soil, especially on large-scale applications.

90 1.3 Limiting factors in our case study region - Marchfeld

Regions without limited water access will presumably boost production potential with rising temperatures and subsequently have more extended vegetation periods (Lalic, Eitzinger, *et al.*, 2018).

However, semi-arid conditions, prevalent within the 'Marchfeld' region, combined with scarce SM during sensitive growth stages, significantly impact crop yield or even crop failure (Thaler *et al.*, 2018). This regional limiting factor strongly influences yield potential (Lalic, Eitzinger, *et*

al., 2018). Lalic *et al.* (2018) showed in simulations that this low soil water storage capacity causes significant yield response with cultivars like winter Wheat.

100 One of the most determining factors for crop growth is its soil's total available water capacity affecting physical characteristics and soil depth (Todoroff, De Robillard, and Laurent, 2010). As Saseendran *et al.* (2015) mentioned, the failure to supply the root zone with adequate water supply is directly connected to plant water stress, which leads to a reduction in crop quality and yield (Saseendran *et al.*, 2015).

According to Hall (2001), frequent heat stress leads to intense water stress, causing the plant's stomata to close, resulting in lower yields. Such rising leaf temperatures and reduction of transpiration cooling effects occur thus at the same time.

110 The resistance to drought depends on the plant or crop and the stage of reproductive development concerning flowering and fruit development stages (Hall, 2001). For example, dry grain production of crops has relatively higher drought resistance than fleshy fruit production (Hall, 2001).

Another essential factor is the rise in CO₂ atmospheric concentrations, which may boost photosynthetic activity and biomass accumulation (e.g., higher water use efficiency) of specific plants (e.g., C3 crops) (Lalic, Eitzinger, *et al.*, 2018). Nevertheless, it is crucial to keep in mind that lower CO₂ concentrations may limit the factor for photosynthesis of plants (Lalic, Eitzinger, *et al.*, 2018).

1.4 Foundation and difficulties of the research

120 The research's core foundations are the in-situ measurements of TDR, Frequency Domain Reflectometry (FDR), and Parrot sensors. Unfortunately, these point measurements reflect the spatio-temporal resolution inadequately. In addition, long-term in-situ measurements are costly and time-consuming. Thus, remote sensing data and simulation models such as S1ASCAT, ARIS, SMAP and, AquaCrop are implemented to increase spatio-temporal resolution to measure and subsequently estimate SM on site.

A combined approach to estimate and measure SM is one of the underlying drivers of this research. A sound understanding of coherences between the in-situ sensors and remote sensing and simulation data on a small-scale farm paddock is particularly investigated. For example, Todoroff, De Robillard, and Laurent (2010) found that field data with probes help perform spatial visualization as maps in a geographic information system. Nevertheless, high soil heterogeneity complicates such projections (Todoroff, De Robillard, and Laurent, 2010).
130 Hence, understanding the spatial variability over time is an additional important aspect considered in the present study. A combination of remote sensing and simulation methods is analyzed to achieve better estimation results.

The especially coarse spatial resolution of remote sensing images for farm-scale usage might require additional input parameters or leverage simulation models to increase SM's spatial variability detection and estimation.

Therefore, combining simulation models with remote sensing is a promising opportunity to achieve higher spatio-temporal SM estimation for farm-scale usage.

140 1.5 Research Questions

1. How can satellite-based remote sensing contribute to high spatial resolution crop-soil-water relation analysis at arable land (using a case study at an experimental field of BOKU in Rutzendorf)?
2. In what way are current microwave and modeling remote sensing techniques like S1ASCAT and modeling tools, such as ARIS or AquaCrop, applicable in estimating spatial variability of SM to contributing towards improved irrigation scheduling and further management practices to combat increasing droughts?
- 150 3. What are the limitations of various SM estimation methods and the potentials for a combination of strategies?

1.6 Objectives

The main objective of the thesis is to evaluate modeling and remote sensing methods vs. in-situ methods for spatio-temporal SM assessments in agricultural fields. The idea is to help improve land management strategies for crop production and promote easier and reliable measurement methods for crop soil-water relations in the spatial context.

- 160 1. Examination and comparison of the applied methods of the on-site field measurements and the available modeling and remotely sensed data, including delineation of the spatial variability of the soil-water relations.
2. Analysis of the spatio-temporal relationship (of the grid layer at the test-site Rutzendorf) between the soil, soil water content, and crop condition, using the spatial variability of results from different approaches (measurements and models) to delineate possible enhancement practices for crop production.
3. Identification of potentials, using synergy effects of combined SM estimation methods, determines factors and dynamic processes of spatio-temporal variability of soil-water relations for crop production enhancement (using crop simulation software).

170 1.7 Hypothesis

1. Calibrated S1ASCAT and ARIS data and AquaCrop simulated soil water content are beneficial tools to achieve crop-soil-water relations and delineate SM's spatial (and temporal) variability compared with in-situ measuring devices.
2. The estimation of SM with S1ASCAT, SMAP, ARIS, or AquaCrop channels further developments in management practices or even in irrigation scheduling.
3. A combination of methods such as remote sensing with modeling can improve or increase calibration significantly for delineation of spatio-temporal SM.

180

2. Fundamentals

2.1 How is SM estimated?

Modern SM estimation is provided by three different approaches at the current stage, comprised of in-situ observations like TDR or FDR, remote sensing techniques with thermal infrared (TIR) or microwave sampling, or modeling approaches (Brocca, Ciabatta, *et al.*, 2017). These techniques are researched among the scientific society to achieve SM estimation methods (Brocca *et al.*, 2017).

190 According to Thaler *et al.* (2018) pose satellite-based SM products an innovative source of SM information concerning spatio-temporal scales. Satellite data prepared with geographic information systems (GIS), in combination with crop modeling is thus, an essential asset in analyzing interactions between spatial and temporal phenomena (Todoroff, De Robillard, and Laurent, 2010). Hence, the combination of approaches like these is promising for SM estimations.

2.1.1 In-situ measurements

The overall reference method for SM measurements is the gravimetric technique. However, it is time-consuming and invasive, with soil samples being extracted from the site (Brocca, Ciabatta, *et al.*, 2017).

Equation 1 shows how gravimetric water content (w) is calculated. The mass of water is divided by the mass of soil.

200

Equation 1: Gravimetric water content (θ_g or w)

$$w \text{ or } \theta_g = \frac{M_{moist} - M_{dry}}{M_{dry}}$$

In comparison, Equation 2 highlights how volumetric water content is defined. It is like Equation 1, however, on a volume basis.

Equation 2: Definition of volumetric water content (θ_v)

$$\theta_v = \frac{V_{water}}{V_{soil}}$$

210 As a result of this, the volume of water is divided by the volume of soil $\left[\frac{m^3}{m^3}\right]$.

As featured in Figure 1, the soil comprises soil minerals, fauna, and organic matter. Its pores are filled with water and air, depending on the porosity and the soil texture.

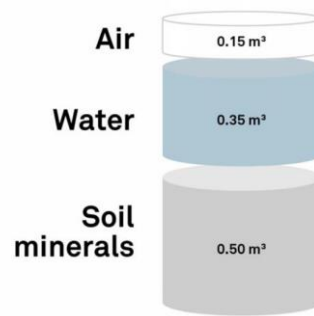


Figure 1: Components of a known volume of soil (Source: METER, 2020)

In Equation 3, the volumetric water content equals the gravimetric water content times the bulk density of the soil.

220

Equation 3: Calculation of volumetric water content (θ_v)

$$\theta_v = w \times \rho_b$$

Nevertheless, new methods are calibrated and tested according to the above reference methods.

A common standard approach for SM measurements was found in TDR sensors, providing accurate measurements for a wide range of soils, replacing the initial reference method, the gravimetric technique (Brocca, Ciabatta, *et al.*, 2017). The benefits of TDR are its less time consumption and little to no disturbance during measurements (Brocca, Ciabatta, *et al.*, 2017).

230

As Brocca *et al.* (2017) show, the FDR technique is currently the most used approach for applied in-situ SM measurements due to its lower costs than TDR sensors.

However, in-situ measurements, such as TDR and FDR measurements, provide only low spatial representativeness, which comes with the point in-situ measurements of SM (Brocca, Ciabatta, *et al.*, 2017). Regular point measurements of SM, for instance, require high maintenance of the measurement networks with elevated economic costs and human resource inputs (Brocca, Ciabatta, *et al.*, 2017).

2.1.2 Remote Sensing

Innovations in satellite remote sensing offer modern and new research fields for SM measurements, with limitations in-depth and dense vegetation (Rahimzadeh-Bajgiran and Berg, 2016). According to Brocca *et al.* (2017), these large-scale SM measurements are best to obtain soil water information remotely. Different methods were developed for SM measurements, such as microwave, optical, and thermal sensors (Rahimzadeh-Bajgiran and Berg, 2016).

240

Microwave instruments are the most common methods, designed either as passive or active sensors (Brocca, Ciabatta, *et al.*, 2017).

The advantage of microwave remote sensing applications for SM estimation is the relatively high Spatio-temporal coverage regarding costs (Brocca, Ciabatta, *et al.*, 2017). However, the accuracy is lower than for in-situ measurements as remote sensing applications for SM are limited by the topsoil layer penetration of radar sensors (2-7 cm), its coarse spatial resolution (>10 km), and quality issues with mountainous terrain or highly vegetated surfaces (Brocca *et*

250

al., (2017). Such high spatio-temporal coverage provides valuable insight into large-scale soil water fluxes.

Besides microwave sensors, TIR remote sensing methods are available to determine SM. Their high spatio-temporal resolution and long-term acquisition are advantageous, yet, the TIR surface penetration is minimal with 1 mm and limited due to vegetation density (Rahimzadeh-Bajgiran and Berg, 2016).

260 2.1.3 Modelling

According to Lalic *et al.* (2018), process-oriented simulation models can assess complex soil-crop-atmosphere systems. AquaCrop or other simulation programs such as the Agricultural Risk Information System (ARIS) help to model and estimate vital parameters of cropping systems (Lalic, Eitzinger, *et al.*, 2018). Several other simulation programs provide modeling approaches featuring different scenarios.

Nevertheless, such agroclimatic models can be used to investigate crop yield or SM content under specific boundary conditions and to find adequate strategies for adaptation to mitigate adverse climate change effects on crops (Lalic, Eitzinger, *et al.*, 2018).

270 Thaler *et al.* (2018) show in their research how crop model simulations provide an attractive tool to monitor drought and water status, which eventually leads to more efficient use of soil water and improved irrigation practices. It aligns with the research of Aydin (2008), stating that strategies for soil water conservation are directly linked to knowledge about soil water balance and thus, constitute an effective management strategy.

Particularly knowledge about characteristics of cropping systems establish the foundation of understanding crop available water in the root zone (Aydin, 2008).

Input parameters of such models are vital to accurately simulate complex models (Thaler *et al.*, 2018). Despite that, models still represent simplifications of fairly complex interactive systems (Thaler *et al.*, 2012; Lalic, Eitzinger, *et al.*, 2018).

280 Abundant modeling concepts have been invented in the past and researched to simulate predictions. Nevertheless, assumptions need field data and field experiments for background information as well as calibration.

2.2 Crop Types

2.2.1 Summer Barley - *Hordeum vulgare*

During the vegetation period of April to July 2018, Buckwheat and Grain Pea were cultivated. However, due to similarities in cultivation, Barley is used for the AquaCrop simulation and ARIS data extraction. Thus, Barley is featured within this descriptive section.

290 Barley has the broadest range of production areas worldwide, from high altitudes to deserts and towards the arctic circle. Its adaption to climate conditions is intensely competitive. Hence, this safe and annual cool-season crop is ranked fourth in the world production behind Maize, Rice, and Wheat, concerning yield. Barley is traditionally used for livestock feed and forage as well as human food and malt beverages. The different uses require quality traits and cultivar acceptance to meet demands (Anderson *et al.*, 2009).

Higher protein levels of winter Barley and its higher yield are subsequently used to boost animal fodder production. However, lower protein levels (<11.5%) of summer Barley, on the contrary, are thus primarily used for malting and brewing (BMLRT, 2020).

Moreover, the yields and planting dates differ between winter and summer Barley. Indeed, winter Barley is sown at the beginning of October and demanding less quality to soil, utilizing humidity more beneficial over the winter. Additionally, composition nutrients of winter Barley benefit from an uptake over a more extended period. In contrast, summer Barley is planted in

300 early spring, requires specific soil conditions, and develops less sophisticated or stress-resistant root systems (BMLRT, 2020).

In Austria, the production of summer Barley declines due to the emerging production of winter Barley (BMLRT, 2020). However, especially rising biofuel production efforts with crops like Maize, Rapeseed or, Wheat increase the overall expenses of Barley, respectively (Anderson *et al.*, 2009).

Typically, the growth time of summer cereal is only a couple of months, starting with the sowing date in spring and harvest in the summer months, depending on the climate (BMLRT, 2018).

2.2.2 Winter Wheat – *Triticum aestivum*

310 *Triticum aestivum* (Wheat) has three growth habits. It can be categorized as winter-, facultative- and spring Wheat. In contrast, these growth habits need to be seen as a continuum, starting with winter Wheat in winter over facultative in between and finishing with summer Wheat (Anderson *et al.*, 2009).

According to the crop rotation scheme in Rutzendorf, winter Wheat was cultivated on the experimental plot during the period of 2018 to 2019 (Freyer *et al.*, 2013). Its sowing date was during the winter months in November of 2018.

With its ability to withstand prolonged cold temperatures below freezing point, winter Wheat also benefits from its drought tolerance. With the worldwide expanded cultivation of Wheat for human consumption, it is by far the most planted crop worldwide. Primarily it is used for human consumption (Anderson *et al.*, 2009).

320 Annual summer crops are complementarily grown in a crop rotation scheme with winter Wheat. Growth parameters like season and moisture availability determine the crop rotation scheme. However, in a broader sense, winter Wheat can be separated into gene pools or groups based on end-use properties or agroecological adaptations (Anderson *et al.*, 2009).

The main crop in Austria is Wheat due to its favorable conditions with an average yield of 5.5 tons per hectare. In 2019, the yield from the test site was 4.6 tons per hectare.

Typical regions for Wheat cultivation are central and eastern Lower Austria and the northern and central Burgenland with its Pannonian climate zone.

330 These regions with deep, humus-rich soils foster high-quality Wheat. Nevertheless, western Lower Austria and Upper Austrian Wheat production benefit from higher water availability resulting in elevated annual yields (BMLRT, 2020).

In general, winter cereals are planted around September, depending on crop type and weather conditions, with final harvests around June to July in the following year (BMLRT, 2020).

2.2.3 Winter Rye – *Secale cereale*

Rye is a minor but traditional cereal originating and mainly grown in Europe (Poutanen, Katina, and Heiniö, 2014). Indeed, the countries of Russia, Belarus, Poland, and Germany contribute about 75% to the total global production (Anderson *et al.*, 2009).

The primary benefit of Rye is the overwintering capability and high tolerance towards salt, aluminum, and drought stresses (Anderson *et al.*, 2009).

340 Its productivity is relatively high on low fertile, sandy, or acidic soils. Thus, Rye can be cultivated in regions where low to no suitability for other cereal crops predominates (Poutanen, Katina and Heiniö, 2014). Its composition is comparable to Wheat, including more dietary fiber (Poutanen, Katina, and Heiniö, 2014).

The main cultivation area in Austria is the Waldviertel region of Lower Austria. Its requirements regarding climate are relatively low (BMLRT, 2020). Austrian Rye is mainly cultivated as winter cereal, with most of its production used for bread and human food, because of its good source of micronutrients, vitamins, and minerals (Poutanen, Katina and Heiniö, 2014; BMLRT, 2020).

Regardless, the production of fodder, biofuel, and alcohol are also connected to Rye cultivation (Anderson *et al.*, 2009). Winter Rye is planted around September and grows throughout the winter months towards maturity in June to July (BMLRT, 2020).

3. Material and Methods

3.1 Research location

3.1.1 Study area

The experimental field for this research is located close to the village Rutzendorf, in the north-eastern part of Austria (Lat. 48.2075° N, Lon. 16.625° (Figure 2). It comprises one paddock, managed by the organic farm of the 'Landwirtschaftlichen Bundesversuchswirtschaften (BVW) GmbH'. Rutzendorf is part of the municipality of Groß-Enzersdorf, situated about 8 km to the east of the borders of Vienna in the district 'Weinviertel'.

The region is commonly called 'Marchfeld' (Figure 2), covering 90'000 ha, known as Austria's largest plain and granary (Thaler *et al.*, 2012).

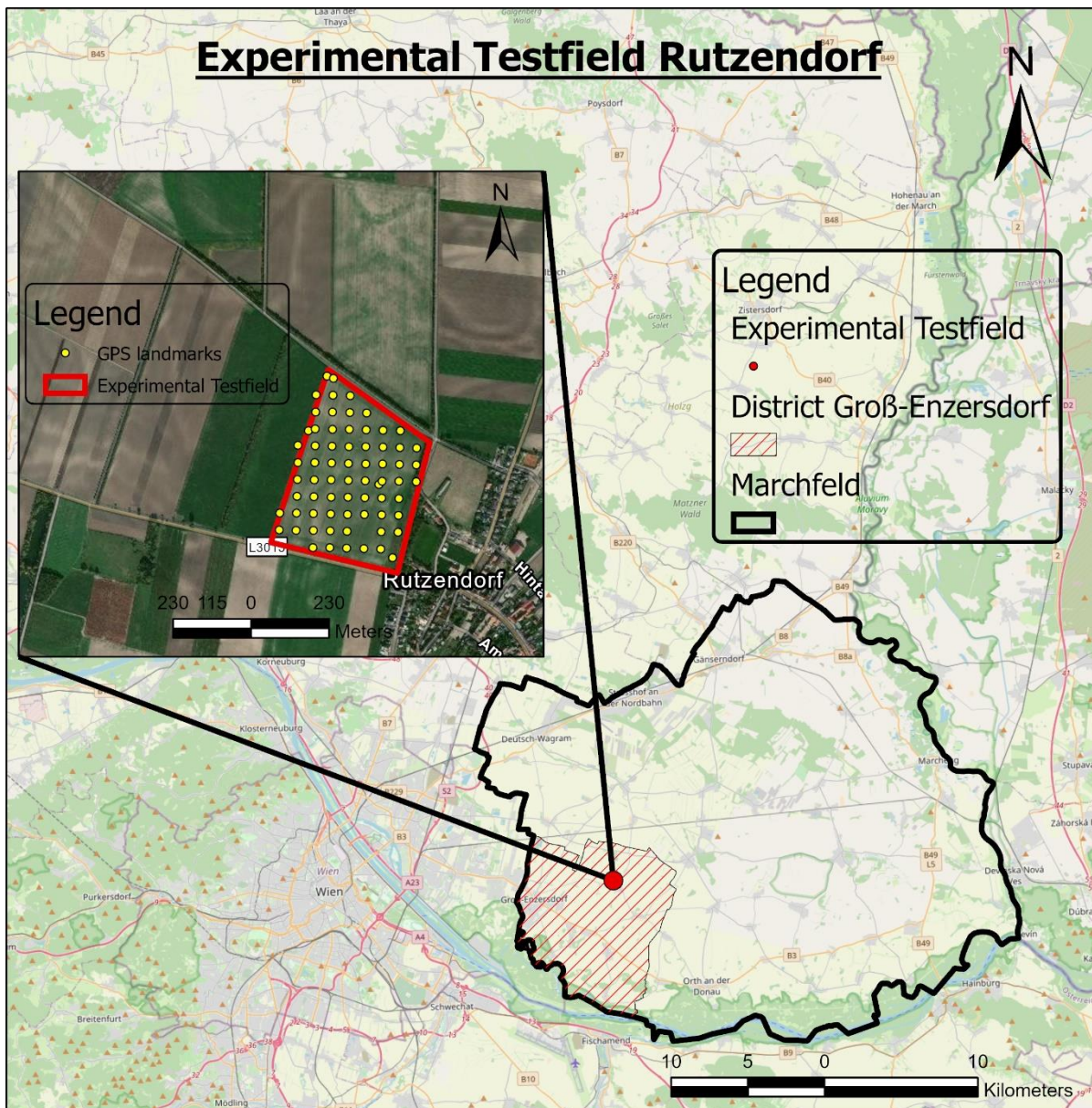


Figure 2: Map of the study area located in the district of Groß-Enzersdorf, Marchfeld, including an orthophoto of the study site with GPS landmarks in yellow

Typical rain-fed crop types in the Marchfeld are winter Wheat or cereals. In contrast, other essential crop types are often subject to irrigation throughout the year with respect to vegetables, potatoes, maize, and sugar beets (Thaler *et al.*, 2012; Novelli *et al.*, 2019).

The terrain is flat, and the geomorphology is shaped by the river Danube running along the west and south. Variations in elevation range between 143 to 178 m above sea level (Thaler *et al.*, 2012). Especially the former floodplains and terraces of the river Danube were subject to sedimentation and deposits from meandering (Stadt Wien, 2020). Over time, Loeß depositions from the ice age in the region Weinviertel, one-quarter of the state Lower Austria, provide an abundance of soil types and thus foster a great arable plain for crop production such as the Marchfeld offers (Brandtner, 1954).

The test side in Rutzendorf is divided into eight individual sections with different crop types, rotating on an annual basis. However, the experimental field researched is section one, with its 17 ha and 150 m above sea level (MUBIL project report, 2012).

3.1.2 Climate

The climate in the Marchfeld region is warm-temperate and fully humid with warm summers. It lies in the transition zone of a semi-humid Western-European and continental East-European climate (Thaler *et al.*, 2012).

During summer, the climate is hot and periodically dry. In winter, the conditions are cold with frosts and little snow cover. Especially in summer and early fall, stable high-pressure systems occur with a tendency to lower wind speeds. Conversely, in winter and especially in spring, low-pressure systems convey higher wind speeds to the Marchfeld (Mueller, 1993).

High levels of sunshine and temperature with low precipitation during the growing period result from the phytogeographical and climatological aspects of the Marchfeld, or the so-called 'Pannonicum' (Thaler *et al.*, 2012). A mean temperature of $>5^{\circ}\text{C}$ throughout the growing period from the middle of March until the middle of November provides the region with approximately 240 days of growing period (Cepuder and Schlederer, 2002).

Between 1989 to 2020, the total annual precipitation lies at 469 mm, and its mean temperature is 11.2°C per year, characterizing the semi-arid region of Marchfeld (Figure 3).

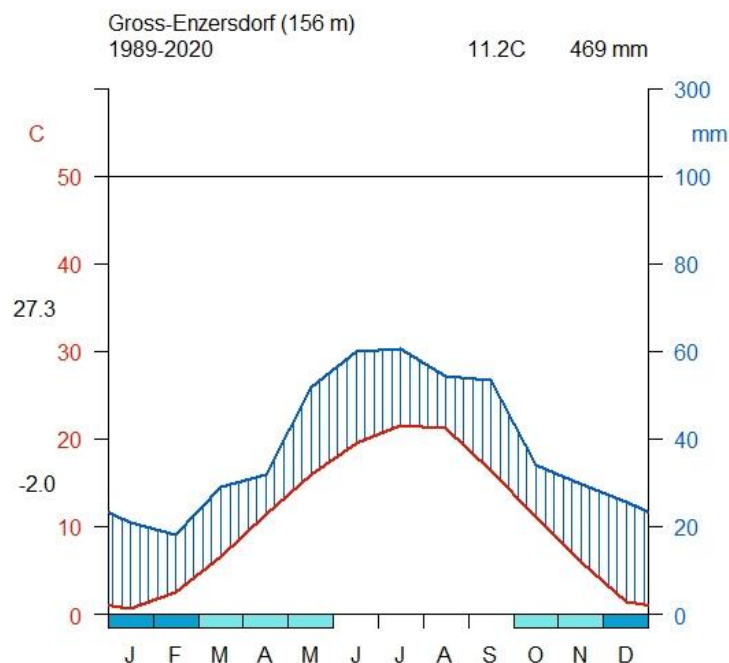


Figure 3: Climate diagram of the town Groß-Enzersdorf

3.1.3 Soil Conditions

Several soil parameters were determined during the 'MUBIL' project started in 2002. With the help of a soil survey, these parameters were assessed. Still, a shift from conventional farming practices to organic farming practices changed soil parameters throughout the project phase. This thesis's current state of the soil parameters is based on 'eBod' and the MUBIL project reports.

400

From a geological perspective, the Marchfeld is part of the Viennese basin, with the area around Rutzendorf shaped by the 'Prater Terraces' with young river depositions of Loeß, consisting of loamy silt increasing with depth (Sperl, 2013; Stadt Wien, 2020). The soil's parent material in Rutzendorf consists of fine sediments, with Chernozem being the prevalent soil type (BFW, 2020). Chernozems are typically rich in organic matter, located predominantly in regions with cold winters and hot, dry summers, driven by a continental climate (Micheli, Schad and Spaargaren, 2006).

According to the digital soil map eBod, roughly three different soil types are located within the study area, as depicted in Figure 4. The soil depths are primarily deep and medium-heavy to heavy. Predominantly the upper soil horizon (A₁, A₂, AC) of the south- (soil type B1) and (horizons A, AC) of the western (soil type B2) part of the experimental field is composed of loamy sand. However, loamy silt and sandy clay are located in the north-eastern test site (soil type B3) (horizons A, AC). Within the C horizons in the south-western parts exists loamy sand to sand with gravel starting at a depth of 60 cm. The eastern part (B3) of the study site has a C1 and C2 horizon consisting of sandy silt and sand to sandy silt (BFW, 2020)

410

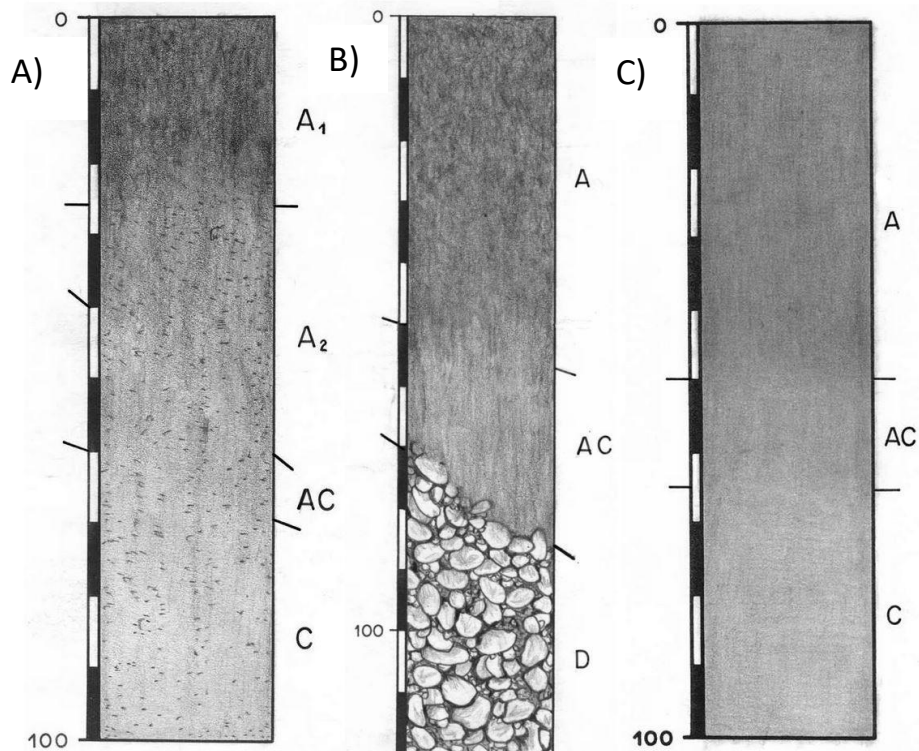


Figure 4: Visualization of soil type A) one (B1), B) two (B2), and C) three (B3) (Source: BFW, 2020)

The topsoil has a composition of humus and clay. Its soil type is Chernozem, with the mineral soil surface layer being loamy sand and sandy silt loam (Eitzinger *et al.*, 2003; Freyer *et al.*, 2003). Figure 5 features the different soil types spread out over the experimental field.

420

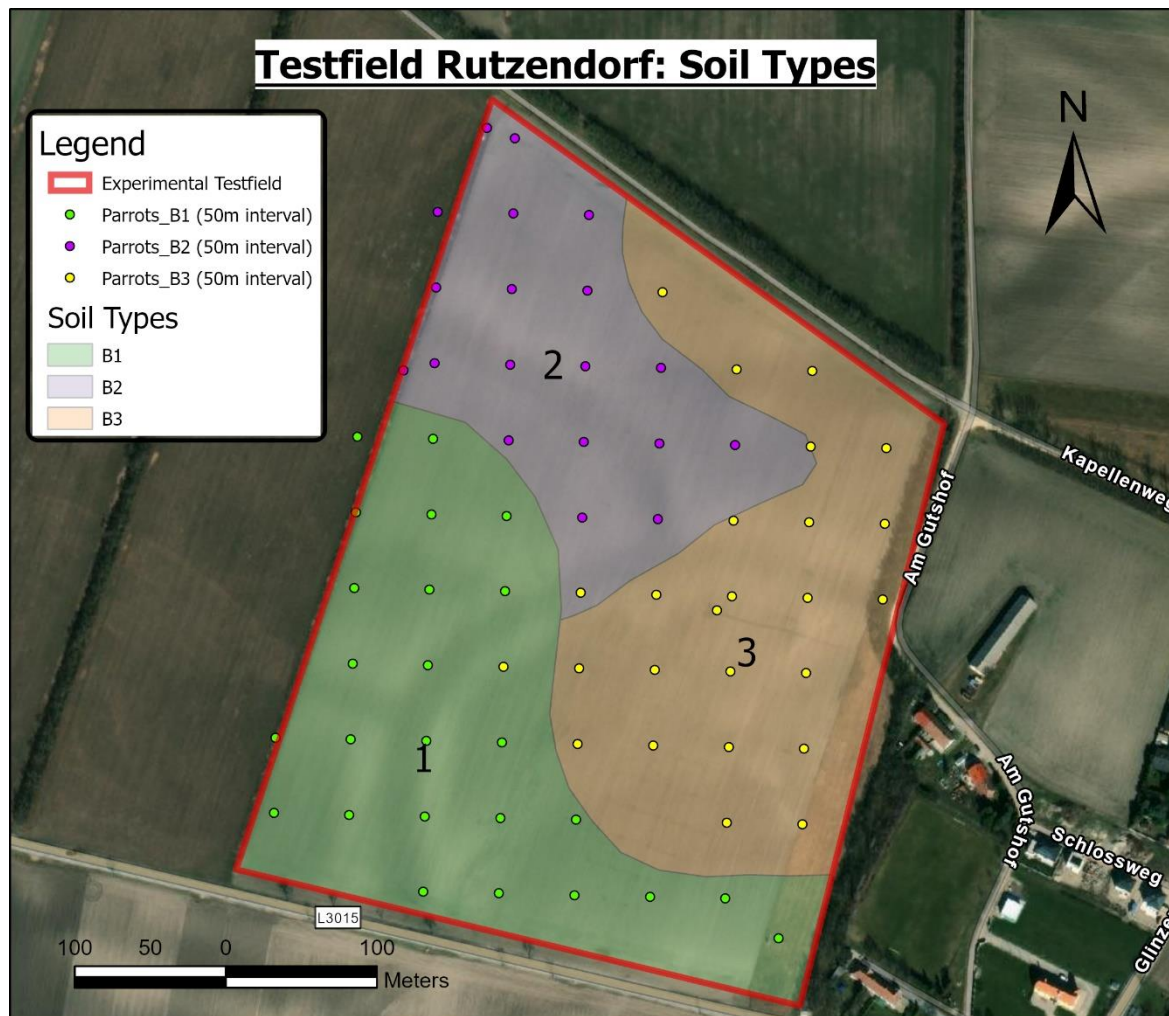


Figure 5: Orthophoto of the experimental field in Rutzendorf, depicting the three prevalent soil types (B1, B2, B3) on-site with colored dots indicating the in-situ sensors (Source: modified after BFW, 2020)

The soil in Rutzendorf has a high heterogeneity with different soil types (Figure 5). However, the prevalent soil type is silt loam, which has a field capacity of around 27 % vol. The wilting point lies at 13-14 % vol. in the topsoil layers (METER, 2020).

430 The Parrot sensors are ordered according to the prevalent soil types, respectively.

The groundwater table in the Marchfeld region is typically below 6 m depth; nevertheless, it fosters high spatial variations of water storage capacity (Eitzinger *et al.*, 2003). The influence of groundwater on the rooting zone of crops depends on the crop type, respectively.

440 The available water content (AWC) varies throughout section one from low over moderate to low and moderate to high. Field capacity (FC) ranges between 60 – 300 mm. Although, soil drainage on-site can be categorized into moderately well-drained to well-drained (BFW, 2020). The carbon content and the pH of the chernozem soil in Rutzendorf increases with depth; the content is typical for this kind of soil. Overall, its carbon content lies at >5.0% carbonate (Freyer *et al.*, 2003). The soil of the experimental test site is alkaline per definition and according to its respective pH range between 7.3 and 8.0 units (BFW, 2020).

Generally, the arable land of the experimental test site is classified and fluctuates between moderate to high ratings (BFW, 2020). Concerning cation exchange capacity, the rating of the soils decreases as the CEC decreases with depth (Freyer *et al.*, 2003). Nitrate retention capacity on-site provides moderate (260 – 340 mm) to high (340 – 420 mm) values, according to the web-based digital soil map eBod (BFW, 2020).

3.1.4 Management Strategy

450 The BVW GmbH operates the experimental test fields rain-fed organically since 2002. The final goal is a crop rotation scheme featuring six different crop types, alternating during eight years. Nevertheless, eight different test sections foster the crop rotation scheme accordingly. Crops featured in the rotation scheme are summer Barley, winter Barley, Alfalfa, winter Wheat, winter Rye, Grain Pea, and Grain Maize. The rearrangement towards organic management consists of a fertilizer application scheme comprising mineral fertilizer, liquid biogas manure, stable manure, compost, and green manure (Freyer *et al.*, 2003, 2013).

After the project started in 2002, wildflower strips were applied in accordance with existing shrub and forest strips along the edges of the sections throughout the experimental field. The total area of wildflower strips counts 5.10 ha. Hedges along the border of sections provide wind speed reduction and foster ecological variety for flora and fauna (Freyer *et al.*, 2003, 2013).

460 As a previous step to cash crop sowing, basic tillage in the form of plowing is part of the management strategy. In the case of Lucerne planting, a cultivator is used before seeding. The annual harvest is executed mechanically in accordance with organic farming practices (Freyer *et al.*, 2013).

3.2 In-situ sensors for data acquisition

3.2.1 Time Domain Reflectometry (TDR)

The TDR sensor was used for data acquisition of reference samples. Throughout the summer of 2019 and summer 2020, data samples were acquired on the experimental test field to evaluate the accuracy of volumetric water content measurements.

470 The TDR device in use is portable in a backpack (Figure 6), powered with a 12 V car battery, and requires roughly 20 seconds to acquire the value of volumetric water content in percent. The setup features a voltmeter that gives the final output of volumetric water content.

Amongst the advantages of TDR measurements is the missing requirement of soil-specific calibration (METER, 2020). Moreover, the TDR sensor's accuracy is superior to other SM measurements, with its simple procedure to obtain volumetric soil water content values (Jones, Wraith and Or, 2002).

Another important aspect and benefit of a TDR measurement is the low susceptibility to error compared to capacitance sensors. Nevertheless, it is important to stress that the visual interpretation of TDR sensor output can be likewise subject to errors (METER, 2020).

480

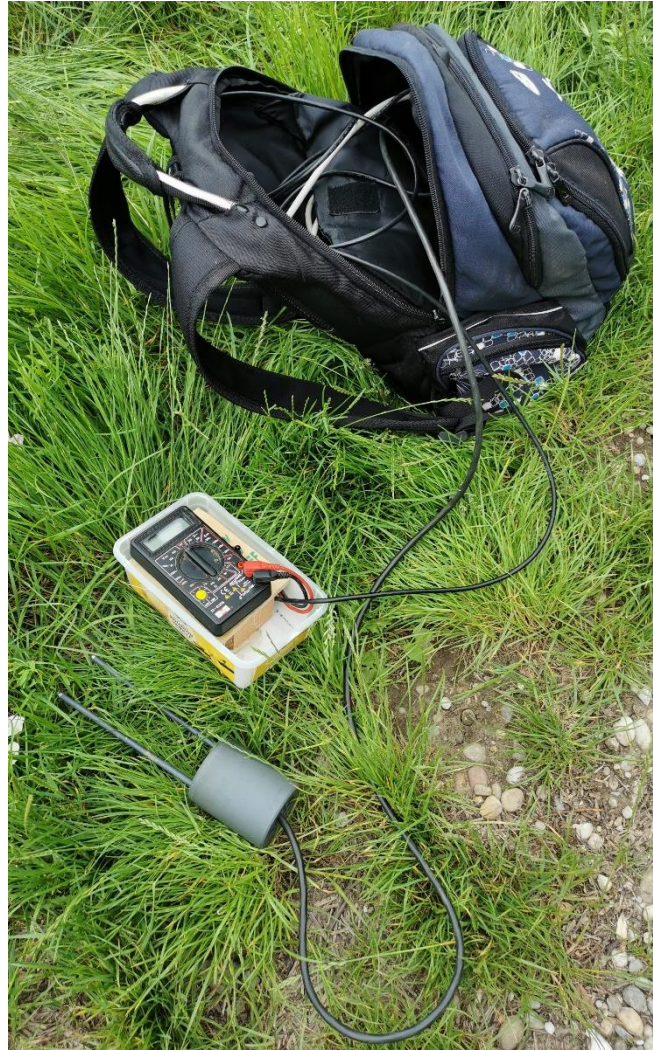


Figure 6: Setup of the TDR measuring instrument, comprising of a voltmeter, a car battery, the sensor, and a portable backpack

3.2.2 Concept behind TDR and FDR sensors

The main principle of TDR measurements is the embedment of the sensor's probe in the soil (Jones, Wraith, and Or, 2002). The TDR in-situ measurement with its probe generates an electromagnetic pulse traveling through the soil between the sensor's electrodes (Jones, Wraith and Or, 2002; Krzic *et al.*, 2010). Along this transmission line L, the electromagnetic wave propagates through surrounding matter with respect to time (Krzic *et al.*, 2010). This transit time t is related to the dielectric permittivity of the medium k (k is not featured in Equation 4). Hence, the dielectric permittivity in soils (k) is strongly related to the water content and the unique properties of water molecules, respectively (Krzic *et al.*, 2010).

Equation 4: Transit time through matter

$$t = \frac{2L\sqrt{x}}{c}$$

In Equation 4, the letter t is the transit time of an electromagnetic pulse to return, with relation to the dielectric permittivity of the medium k (the letter k is not featured in Equation 4), where

500 L is the length of the transmission line and c is the speed of light ($3 \times 10^8 \left[\frac{m}{s} \right]$ in a vacuum) (METER, 2020).

As TDR or capacitance probes (FDR sensors) measure reflection or charge in the soil medium, an oscillating voltage must be applied. Capacitance probes cover frequencies between 50 and 100 MHz, whereas TDR probes have much higher frequencies (Jones, Wraith, and Or, 2002). Research suggests that frequencies lower <10 MHz are more likely subject to errors related to salinity or temperature fluctuations. Thus, oscillation frequencies are essential for the respective SM measurements (METER, 2020).

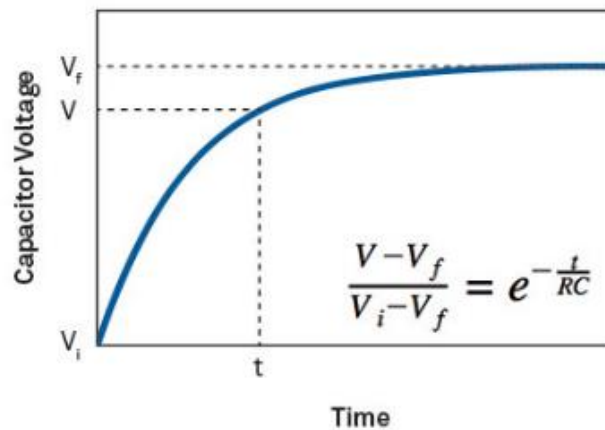
510 TDR and capacitance sensor systems are analogical SM measurements assessing the dielectric permittivity of the soil. Compared to TDR measurements determining the travel time, the capacitance technique determines the charge time of the dielectric permittivity of the medium. However, these two techniques frequently get confused because both measurements define the volumetric soil water content (METER, 2020).

In comparison, the capacitance technique is featured in Equation 5 and defines the relationship between time t to charge a capacitor with a starting voltage V_i towards a voltage V_f . In Equation 5, the letter C is the capacitance, R is the resistance in series, and the letter t represents the charge time (METER, 2020).

Equation 5: Capacitance calculation

$$e^{\frac{-t}{RC}} = \frac{V - V_f}{V_i - V_f}$$

To get an idea how the charging looks like, Figure 7 provides an illustration of the process.



520 Figure 7: Charging process of a capacitor with respect to time (Source: METER, 2020)

The charge time t of the capacitor is reached if the voltage and resistance ratios are constant. After constant resistance and voltage ratio, Equation 6 gives us the charge time of the capacitor (METER, 2020).

Equation 6: Calculation of charge time t of the capacitor

$$t = -RC \times \ln \left[\frac{V - V_f}{V_i - V_f} \right]$$

According to Equation 7, featuring a parallel plate capacitor, capacitance is a function of the dielectric permittivity of the medium (k) between the plates (METER, 2020).

530

Equation 7: Parallel plate capacitor and its capacitance

$$C = \frac{\chi A}{S}$$

This principle applies to parallel plate capacitors. In Equation 7, A defines the area of the plates, whereas S is the separation between the plates or sensor's plates. Nevertheless, both are fixed values. Thus, the charge time of the capacitor is a linear function of the dielectric permittivity of the medium (k) and can be calculated with Equation 8 (METER, 2020).

Equation 8: Linear function of the dielectric permittivity

$$\frac{1}{\chi} = \frac{1}{t} \left[\frac{RA}{S} \ln \left(\frac{V - V_f}{V_i - V_f} \right) \right]$$

540

Due to the relationship of parallel plate capacitors in Equation 7, different sensor rods are usable for soil probes. For example, TDR determines the dielectric permittivity (k) based on measurements of time t traveling as an electromagnetic wave along the transmission line L (METER, 2020).

Hence, a TDR measurement processes the transit time t of the electromagnetic pulse along the transmission line L , with respect to the dielectric permittivity (k) (Equation 9).

Equation 9: TDR determines k based on t along the transmission line

$$t = \frac{2L\sqrt{\chi}}{c}$$

550

Equation 9 features the length of transmission line L and c as the speed of light ($3 \times 10^8 \left[\frac{m}{s} \right]$ in a vacuum). However, the propagation time of the electromagnetic wave is a function of fixed values (c and $2L$). Theoretically, TDR measurements are less susceptible to alternating soil and environmental conditions (METER, 2020).

Concerning the dielectric constant, the air has a value of one, whereas water has a constant of 80. Hence, water strongly influences the transit time t of electromagnetic waves in a medium (Roth, Malicki, and Plagge, 1992).

In contrast, several solid soil components have dielectric constants between two and seven (Topp, Davis, and Annan, 1980). Therefore, the dielectric constant is a strong function of water content yet a helpful predictor of volumetric SM content (METER, 2020).

560 The absolute soil saturation for the TDR device used is expressed in volumetric terms $\left(\frac{m^3_{water}}{m^3_{soil}}\right)$. Relative SM in comparison is determined by a percent of saturation and dimensionless.

3.2.3 Data Generation

The reference data acquisition with the TDR sensor took place on April 4th, 2019. 35 GPS coordinates spread out on the experimental test field were subject to data acquisition. Seven more TDR measurements were taken on June 1st, 2019. On July 5th, 2019, 59 GPS coordinates were subject to measurements and data acquisition for additional reference data.

570 Another set of data acquisition took place on May 18th, 2020, with the TDR sensor and a total of 17 GPS coordinates were subject to SM measurements. On June 17th, 2020, 70 SM measurements were acquired for the respective GPS coordinates.

In summer 2020, a new approach featuring a zoom effect required additional data points and was acquired on July 24th, 2020. The new method consists of 36 data points within a 250x250 meter grid. A smaller grid comprising 125x125 m was introduced within the respective grid with an additional 36 data points. The last and considerably smallest grid with 50x50 m and another 36 data points is missing 27 observations due to the malfunctioning of the TDR sensor. However, nine observations could be acquired within the smallest (50x50 m) grid. The different grids featuring a zoom effect are depicted in Figure 8.

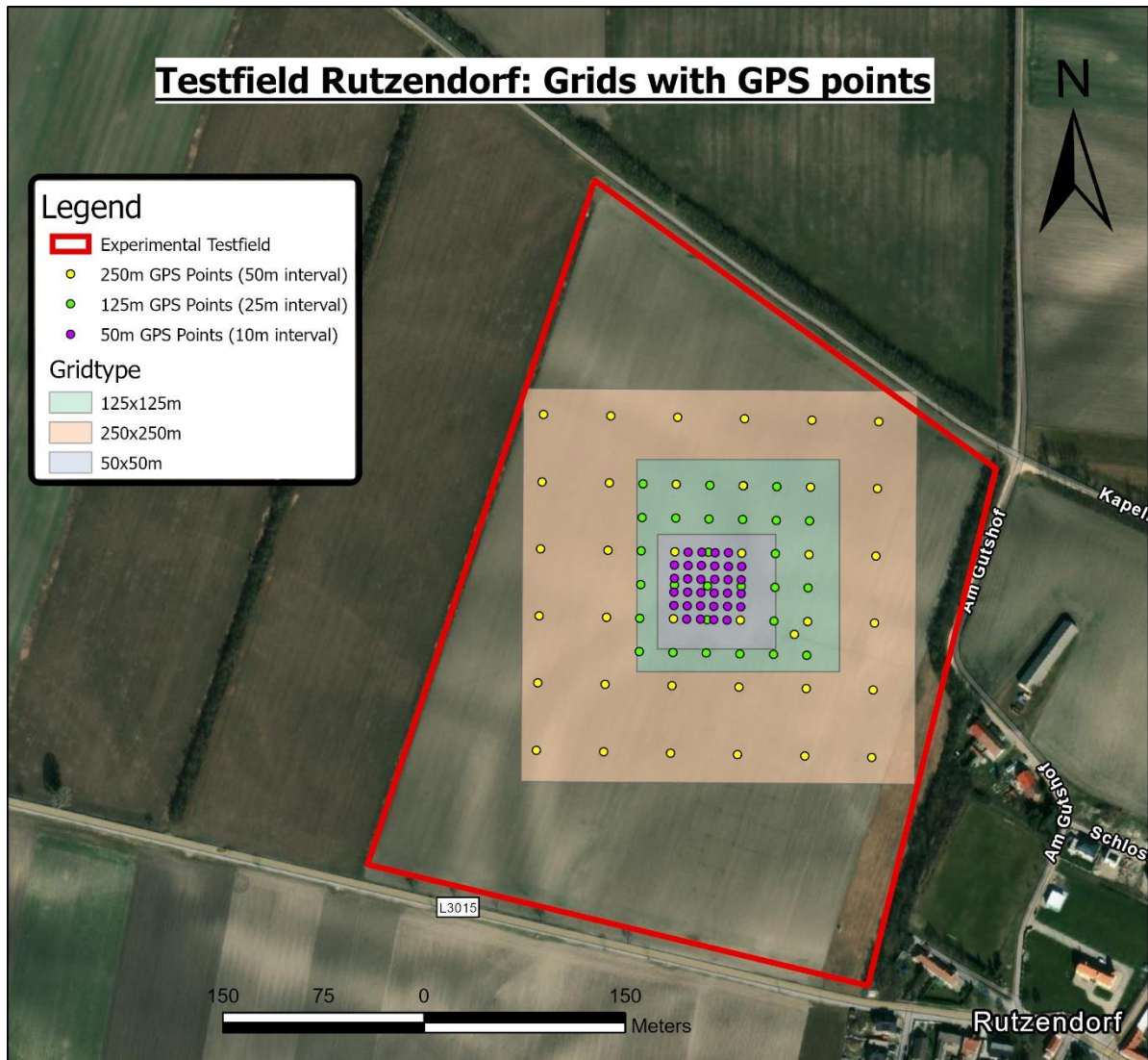


Figure 8: Orthophoto of the experimental field in Rutzendorf with different grids and different GPS points on July 24th, 2020

580

3.2.4 Parrot Flower Power (Parrot)

The sensor used in the study for the daily data generation from April to July 2019 was the Parrot sensor. It is developed by the French company Parrot SA and designed for private indoor usage to provide information about potted plants (Parrot, 2016). The sensor generates soil data, comprising air temperature, light intensity, soil humidity, and fertilizer content of the respective soil conditions (Parrot, 2016). According to Xaver *et al.* (2019), the Flower Power sensor measures the soil water content with a capacitance probe.

590

The capacitance method is widely researched, with an electromagnetic field being generated and transmitted into the soil via the sensor's electrodes (Kizito *et al.*, 2008). The respective charge time is related to the capacitance of the soil and thus related to the dielectric permittivity of the medium between the sensor's electrodes (Kizito *et al.*, 2008). As a result of the higher dielectric permittivity, the probe is sensitive to soil's water with a dielectric constant of 80, while respective soil constituents have constants between two and seven (Topp, Davis, and Annan, 1980; Roth, Malicki and Plagge, 1992; Kizito *et al.*, 2008).

The Parrot sensor's electrodes have a length of ten centimeters constantly in contact with the soil (Parrot, 2016). According to Xaver *et al.* (2019), the Parrot sensor assesses the soil water content with two flat rods. The fertilizer level assessment is based on the electric conductivity

and is featured in item 3 of Figure 9. Electric conductivity is described as the ability of ions in an electrolyte solution to conduct electricity (Otterson, 2015).

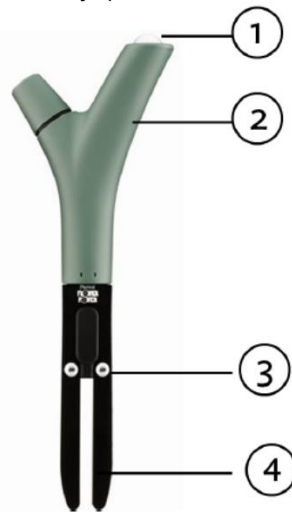


Figure 9: Composition of the Parrot Flower Power sensor (Source: Parrot, 2016)

Thus, the concentration of ions is proportional to an increasing electric conductivity. The higher the level of fertilizer, the higher the sensor unit's response.

In contrast, the temperature and light intensity is measured with the above-ground sensors of the Parrot unit. In Figure 9, the four different items of the Parrot sensor are visualized. The sensor's upper construction is shaped like a fork and fosters the thermometer and the light sensor, measuring a wavelength range between 400 and 700 nm to capture visible light (Xaver *et al.*, 2019).

According to Parrot (2016), its sensor is powered with one AAA battery, 1.5V. It can operate on one battery life between six to twelve months (Xaver *et al.*, 2019). However, weather conditions shape the time frame of the battery charge. Every 15 minutes, four observations can get unloaded and stored on the device. Data storage lasts up to 80 days before overwriting occurs (Parrot, 2016; Xaver *et al.*, 2019).

The manufacturer Parrot SA provides a specialized 'Flower Power app' to access the collected data from the sensor. It is available for both Android as well as iOS operating smartphones. The connection is executed via the Bluetooth interface of any given phone, provided the respective application is installed. As soon as the connection is set up, the observed data is transferred into the app. While connected to the internet, the observations are uploaded into the Parrot SA Cloud. The data periodicity can be displayed in a corresponding graph featuring long-term trends regarding the four parameters (Parrot, 2016).

The Flower Power sensors were set up in a 50 x 50 m interval to acquire relevant data for the experiments. Overall, 66 Flower Power sensors received temperature, light intensity, soil humidity, and fertilizer content from April 4th, 2019, until June 5th, 2019. The Flower Power sensors were set up in pairs to ensure optimal data acquisition and comparison of results for operational safety and error reduction.

3.2.5 METEO weather station

As part of the experimental field setup, various meteorological stations and instruments are installed to investigate and measure continuously (Figure 10). One of the weather stations is located to the western edge of the experimental field and connected to a data logger, powered by a solar panel with live transmission into a 'Zentra' cloud.

It is fully equipped, accommodating an air temperature probe, a rain gauge, and a four-component radiometer probe.

Diagonally across the field, a Scintillometer expands, consisting of a transmitter and receiver unit. These measurements detect small fluctuations of the refractive index of air parcels caused by temperature, humidity, and air pressure. A supplemental weather station is set up in the center of the experimental field to acquire data for former MUBIL project partners.

640 The relevant data of the METEO weather station in Rutzendorf was generated for the time frame of February 2019 to September 2020, including the daily minimum and maximum temperatures in °C, the overall daily precipitation [mm], wind speed $\left[\frac{m}{s}\right]$, the solar radiation $\left[\frac{MJ}{m^2}\right]$, relative humidity [%], vapor pressure [kPa], and complimentary water content measurements based on the capacitance technique with an FDR probe in ten and 20 cm soil depth [vol. %].

Complementary meteorological data were acquired from the ZAMG meteorological station in Groß-Enzersdorf from January 2018 to February 2019.

The meteorological data from the Z-station were used as input parameters for the AquaCrop simulation. The FDR SM measurements in 20 cm were used for comparison as reference data for the vegetation period of 2020.

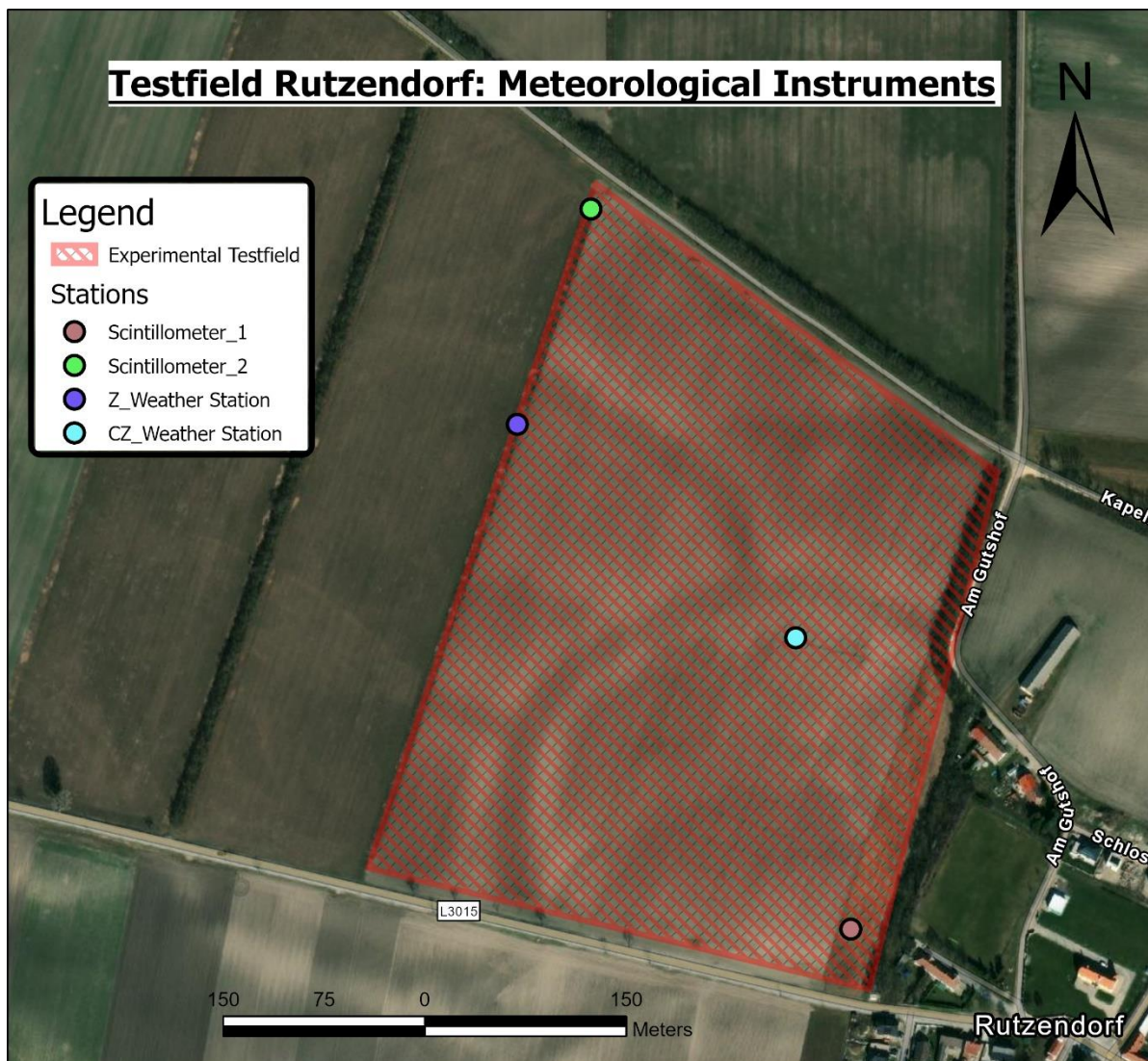


Figure 10: Orthophoto of the experimental field with locations of the meteorologic measuring instruments

650

3.3 Remote sensing applications

Remote sensing applications for SM measurements comprise active- and passive microwave sensors and passive optical/thermal infrared remote sensing methods (Rahimzadeh-Bajgiran and Berg, 2016).

However, the most common remote sensing instruments to obtain SM products are active microwave sensors (e.g., Synthetic Aperture Radars (SARs) and, for example, scatterometers from the Metop-A/B satellite sensor (ASCAT)). Scatterometers have a rather coarse spatial resolution (25 km), yet an almost daily and, thus, high temporal resolution (Brocca, Ciabatta, *et al.*, 2017; Lalic, Eitzinger, *et al.*, 2018).

660 Compared to the scatterometers, the SAR sensors have a low temporal resolution of several days up to a fortnight. However, its spatial resolution is rather high, with <1 km (Brocca, Ciabatta, *et al.*, 2017).

Passive sensors, on the other hand, with their spatio-temporal resolution, are characterized similarly to active microwave scatterometers such as the ASCAT sensor (Brocca, Ciabatta, *et al.*, 2017).

670 There are currently four different coarse resolution-satellite-surface soil-moisture products available, either with passive or active sensors (Brocca *et al.*, 2017). The SM Active and Passive (SMAP) mission (36 km and three-day spatio-temporal resolution) (Entekhabi *et al.*, 2010). The Advanced Microwave Scanning Radiometer 2 (AMSR2) mission (25 km and one-day spatio-temporal resolution) (Kim *et al.*, 2015). Onboard, the Metop-A/B satellites are the Advanced SCATerometer (ASCAT) sensor (25 km and one-day spatio-temporal resolution) (Wagner *et al.*, 2013; Thaler *et al.*, 2018), and lastly, the SM and Ocean Salinity (SMOS) mission product (50 km and two-day spatio-temporal resolution) (George, 2013).

Other subjective remote sensing applications are featured in Rahimzadeh-Bajgiran and Berg (2016), indicating advances in the field of passive TIR remote sensing methods for SM measurements.

680 Especially the high spatio-temporal resolution and long-term acquisition of these sensors like LANDSAT, MODIS, or Sentinel 2 are advantages for SM estimation (Rahimzadeh-Bajgiran and Berg, 2016).

However, amongst limitations of optical and thermal measurements are, according to Moran *et al.* (2004), impenetrable cloud cover, minimal surface penetration of 1 mm, vegetation density, but mostly, that after wetting incidents of the soil surface, rapid drying complicates relations of SM estimation (Rahimzadeh-Bajgiran and Berg, 2016).

3.3.1 Optical and thermal wavebands (Passive Remote Sensing)

Since the 80s, optical and thermal remote sensing has been subject to soil moisture estimation. The normalized digital vegetation index (NDVI) derivation is the most common vegetation index generated (Rahimzadeh-Bajgiran and Berg, 2016; Lalic, Eitzinger, *et al.*, 2018).

690 However, surface temperature (Ts) is amongst the products produced with optical and or thermal wavebands. The soil moisture estimation based on such sensors uses available information from NIR, TIR, and visible wavebands to determine the state of vegetation and phenological dynamics (Rahimzadeh-Bajgiran and Berg, 2016; Lalic, Eitzinger, *et al.*, 2018) With the help of combined optical/thermal bands (surface temperature Ts, vegetation index VI), an estimation of SM is a promising method, as Ts and vegetation have a dependence on SM (Rahimzadeh-Bajgiran and Berg, 2016).

Thus, according to Rahimzadeh-Bajgiran and Berg (2016), Ts is a good indicator for surface energy, which can be used as a surrogate for SM within the first 1-5 mm and estimation of

water stress of biomass. In the event of low SM, leaf temperature and surface temperature increase (Rahimzadeh-Bajgiran and Berg, 2016).

700 The vegetation index and surface temperature relationship are linked to the ET surface rate, which can be used for small-scale monitoring purposes of soil water or vegetation status to reduce topographic variation. The theory is that rising Ts lowers the NDVI and comes with reduced ET and vice versa (Rahimzadeh-Bajgiran and Berg, 2016).

Optical and thermal wavebands or passive remote sensing were not subject to direct SM estimation within this research. It comprises complementary information about current applications.

3.3.2 NDVI and LAI to determine Canopy Cover

710 In remote sensing, vegetation makes a significant difference, especially the interpretation of vegetated areas in general. The normalized digital vegetation index (NDVI) is used in several ecological and agronomic studies (Lalic, Eitzinger, *et al.*, 2018).

Earth-observing satellites equipped with multiband radiometers, like the SRS-NDVI, measure reflectance effortlessly in the NIR wavebands and provide the necessary information to calculate vegetation indices like the NDVI (Campbell, 2020). Based on calculations and approximations of NDVI, the LAI can be estimated (Campbell, 2020).

Hereby LAI allows the tracking of vegetation over time and provides valuable information about surface albedo (Lalic, Eitzinger, *et al.*, 2018).

The definition of LAI is the leaves per unit area of the ground surface of a canopy (Lalic, Eitzinger, *et al.*, 2018; Campbell, 2020).

720 LAI is highly variable with season and vegetation. However, it is often used in ecological or hydrological models to measure crop or forest growth and its productivity for spatial and temporal patterns (Campbell, 2020).

Direct and destructive measurements of LAI comprise of stripping the biomass off plants to assess LAI. An indirect and non-destructive measurement of LAI is related to variables, such as the amount of light transmitted or reflected from a canopy. Commercially available instruments for outdoor field usage utilize the amount of light energy transmitted by a plant canopy to estimate LAI (Campbell, 2020).

730 In comparison, remote sensing LAI is estimated with the help of reflected light of biomass. Only very low reflectance is achieved within the electromagnetic spectrum's visible range (400 – 700 nm). Nevertheless, wavelengths of the NIR (>700 nm) spectrum provide an elevated measurable reflection of biomass in correlation to its chlorophyll content (Campbell, 2020).

Reflections in the NIR wavelength are elevated for an individual leaf under normal illumination (Figure 11).

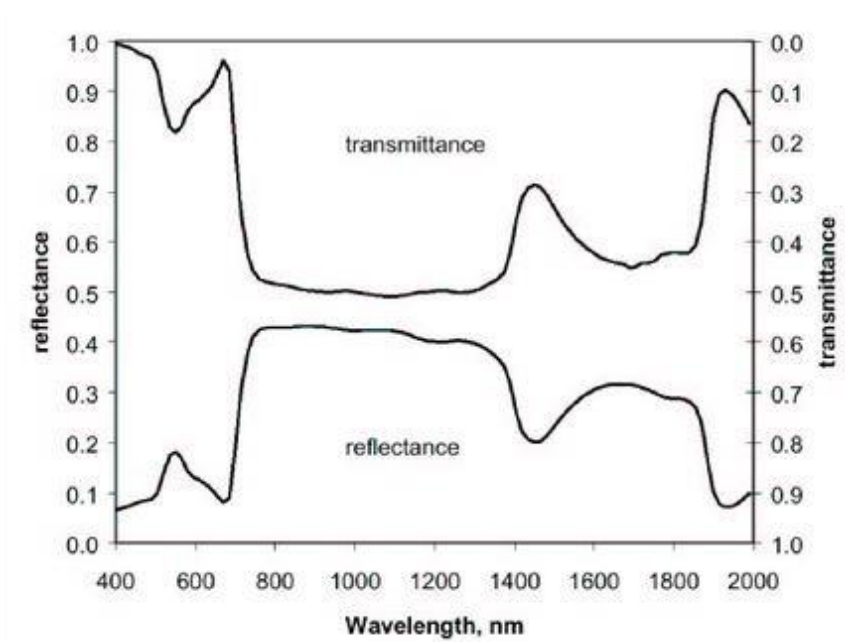


Figure 11: Transmittance and reflectance of an individual leaf from 400 to 2000 nm (Source: Knyazikhin, Marshak and Myneni, 2005)

A strong correlation exists between NDVI and LAI (Figure 12). Under field conditions, NDVI values range from zero to one, representing low and high LAI, respectively (Campbell, 2020).

740

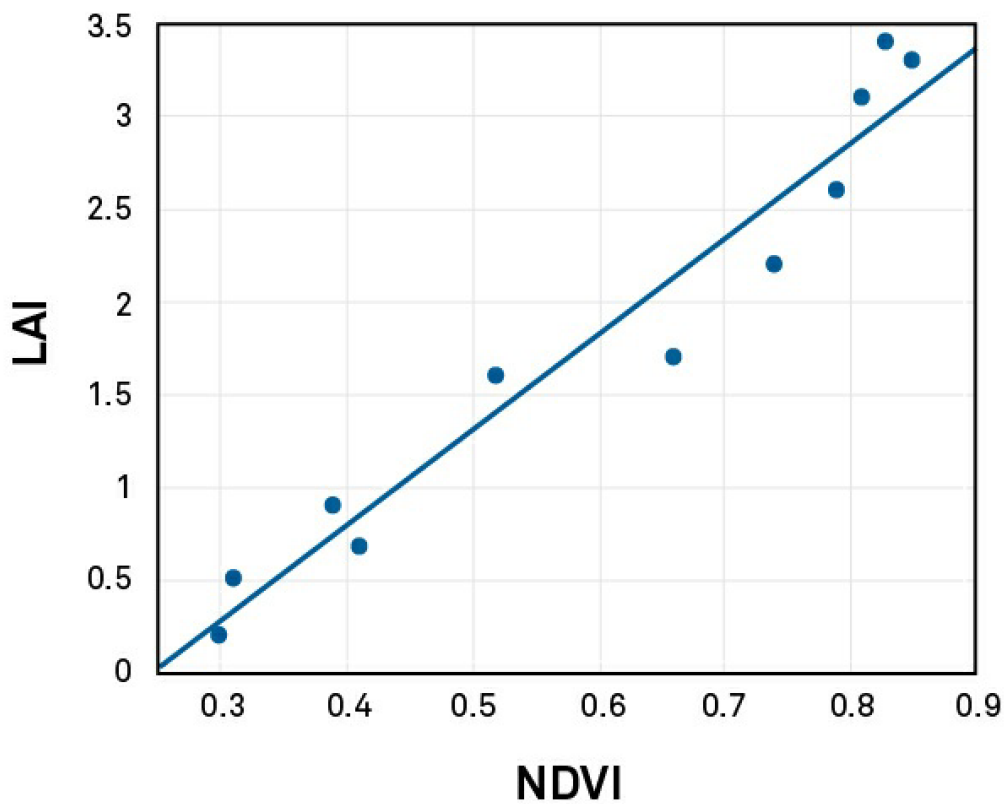


Figure 12: Relationship between NDVI and LAI (Source: Campbell, 2020)

Theoretically, to directly estimate LAI, a crop-specific correlative relationship using NDVI values is necessary. This robust empirical model saves effort and time in the long run. For

example, a fitted linear regression model predicts LAI from NDVI measurements (Campbell, 2020).

750 However, only LAI values are processed in this study based on Ramirez-Garcia, Almendros, and Quemada's (2012) research. According to Ramirez-Garcia, Almendros, and Quemada (2012) exists a relationship between the LAI and the ground cover (GC) or also known as canopy cover (CC). This CC or Green Canopy Cover ranges from 0 % (bare soil) to 100 % (full canopy cover) (Steduto et al., 2012).

The fraction intercepted of photosynthetically active radiation (FIPAR), or Ground Cover (GC), was calculated according to the formula of Monsi and Saeki (1953), depicting the relationship between light transmission and leaf area of Equation 10. The radiation extinction coefficient (k) is based on experience values and was determined according to the respective crop within the time frame.

Equation 10: Relationship between light transmission and leaf area

$$FIPAR = 1 - e^{-K \times LAI}$$

760

The LAI data used was generated with the Google Earth Engine (GEE) as a time series, using the MODIS LAI/FPAR 4-Day Global 500 m dataset. The data is available as a time series from January 2018 to September 2020, and it is masked with a filter to cancel out high cloud cover. The overall number of satellite images usable is reduced as only 10 % cloud cover is accepted.

770 On-site indirect LAI measurements were conducted using the PAR inversion technique for leaf area index calculation on May 6th, May 20th, July 1st, and July 8th, 2020. The mean LAI values of the respective days were used to calibrate and compare the extracted LAI-MODIS dataset. The results for the different vegetation periods of the AquaCrop simulation are validated with LAI observations of the MODIS LAI/FPAR 4-Day Global 500 m dataset. Eventually, the LAI values are transformed to CC according to Equation 10 to allow calibration and validation of the AquaCrop simulation results for the respective vegetation period and the three soil types.

3.3.3 ASCAT for SM detection (Active Remote Sensing)

The ASCAT sensor is a real-aperture radar mounted on the Meteorological Operational (METOP) series satellites of the EUMETSAT Polar System (EPS). It is an active microwave remote sensing instrument initially designed for ocean monitoring. On land, its services are used to monitor and acquire SM patterns driven by precipitation and evaporation (Wagner *et al.*, 2013).

780 Several meteorological institutions like the Met Office use the ASCAT SM data for monitoring or research applications (George, 2013).

A total of three METOP satellites (A, B, and C, launched in 2006, 2012, and 2018) orbit at an altitude of 817 km around Earth, providing detailed meteorological observations of the oceans, continents, and global atmosphere on a daily all-weather operation. Revisit time of the METOP satellites is generally once or twice a day for Central Europe (EUMETSAT, 2020).

The spatial resolution of the ASCAT sensor is available at a 25 km grid. However, it is limited in application for local regions or agricultural purposes. Measurements with scatterometers like the ASCAT sensor depend on the dielectric properties of the soil surface layer, the roughness, and its vegetation (EUMETSAT, 2020).

790 More water or moisture availability in the soil surface layer results in a significant alternation and absorption behavior of the microwave (<10 GHz) frequencies emitted, which leads to SM estimation (Lalic, Eitzinger, *et al.*, 2018; EUMETSAT, 2020).

If the SM content increases, the dielectric constant at the air-soil boundary increases and backscatters the microwaves (Wagner *et al.*, 2013). The ASCAT sensor operates at a 5.3 GHz microwave frequency at C-band using vertically arranged polarized antennas, typically used to detect bare or vegetated soil surface moisture content (Lalic, Eitzinger, *et al.*, 2018; EUMETSAT, 2020). The electromagnetic waves echo from the ground and are received by the instrument, while the backscatter signal is analyzed and detected spectrally (Thaler *et al.*, 2018).

800 The backscattering intensity positively correlates with the SM content and implies a direct comparative measurement of bare soil's SM. One to two cm of the topsoil layer is measured with the ASCAT sensor, which is strongly dependent on the C-band backscatter of the electromagnetic waves. Nevertheless, surface roughness and vegetation have a significant impact on the efficiency of measurements and thus need correction (Wagner *et al.*, 2013).

S1ASCAT for SM detection

810 The S1ASCAT satellite data used is based on the 'BMon' project led by the TU Vienna. S1ASCAT is developing the initial ASCAT satellite images and has resolutions of up to 100 m (Kristelly, 2020). The technique combines the ASCAT and Sentinel 1 backscatter, interface and process the data in model simulations, and subsequently provides several SM products for different soil depths. Thus, the underlying concept in that matter is the temporal stability of SM over time (Wagner *et al.*, 2008). SM measured on a local scale (Sentinel 1) with 500 m resolution is correlated to the mean SM content over an area (ASCAT) of 25 km (Wagner *et al.*, 2008). For example, neighboring local pixels with similar physical properties, for example, texture or land cover, show higher coherence in SM, respectively (Wagner *et al.*, 2008).

The rather local Sentinel 1 backscatter, combined with the regional scale ASCAT backscatter, is used to downscale towards a pixel size of 500 m, based on directional-weighted average calculations (Panic, 2020). The data is validated based on meteorological data, outflow, groundwater, and yield (Kristelly, 2020). Moreover, Wagner *et al.* (2013) describe several advisory flags implemented to process the ASCAT data to increase precise SM estimation retrieval. Such advisory flags regard frozen soil conditions, snow cover, surface water fraction, or topographic complexity (Wagner *et al.*, 2013).

820 The SM products are available daily. However, only the years from 2018 through 2020 are featured in the analysis. The soil water index (SWI) represents soil moisture profile in several soil depths as relative soil saturation, ranging from 0 % SM at a PWP to 100 % SM at FC (Brocca *et al.*, 2010; Wagner *et al.*, 2013; Kristelly, 2020).

For comparability reasons, the relative soil saturation [%] of the S1ASCAT-SWI products was transformed towards absolute soil moisture in % vol. With knowledge about the soil porosity, the volumetric SM content was calculated according to Wagner *et al.* (2013) and is provided in chapter 3.6.4 Transformation of satellite and simulation data based on soil porosity.

The resolution is 500 m, with used soil profile depths of 0-1, 0-5, and 0-10 cm for the analysis.

3.3.4 SMAP for SM detection (Active Remote Sensing)

830 The SM Active Passive (SMAP) mission was developed by NASA and launched in April 2015 (Brocca, Ciabatta, *et al.*, 2017). It uses an L-band radiometer and an L-band high-resolution radar. With the radiometer spatial resolution of the SM product of roughly 36 km, the temporal resolution has a two-day revisit time (Brocca, Ciabatta, *et al.*, 2017).

The L-band radiometer uses a 1.4 GHz frequency, has a spatial resolution for hydroclimatology at 40 km, and penetrates the bare soil up to 5 cm below ground (Entekhabi *et al.*, 2010). Its L-band radar uses a frequency of 1.26 GHz and has a spatial resolution for hydrometeorology at 10 km. The overall mission's approach is to integrate radar and

radiometer to combine active and passive remote sensing for SM estimation (Entekhabi *et al.*, 2010). According to Entekhabi *et al.* (2010), the SMAP mission is designed to observe and collect measurements of the surface SM and the freeze and thaw state. The radar backscatter is highly influenced by surface roughness and the overall vegetation structure, performing more adequately in low-vegetation conditions (Entekhabi *et al.*, 2010). Amongst its application of space-based SM, observations are drought monitoring for plant water stress and information on water availability for SM status to provide data for model predictions (Entekhabi *et al.*, 2010).

The SMAP SM product was extracted with the help of the GEE as a time series from January 2018 to September 2020. The data is available on a three-day basis and features the root zone soil depth of 0-100 cm. The given unit is relative soil saturation ranging from 0% SM at a PWP to 100% SM at FC. The resolution of the analyzed data has a pixel size of 10 km. According to Entekhabi *et al.* (2010), the medium resolution SM product of 10 km combines the coarse resolution radiometer and the fine resolution radar observations. Like the S1ASCAT-SWI products, the SMAP product of RSS [%] was transformed towards absolute soil moisture in % vol. and is described in more detail in chapter 3.6.4 Transformation of satellite and simulation data based on soil porosity.

3.4 Simulation Programs and SM

Modeling and simulations require data inputs. Therefore lack of data, methods, or information impacts future climate assessments, influencing the environment (Eitzinger *et al.*, 2008). According to Eitzinger *et al.* (2008), an increasing simplification of simulation features a higher uncertainty in simulated results. Increasing process parameters in a rather complex model fosters higher uncertainty accordingly. The human factor with the parameters management, climate scenarios, spatio-temporal variability, and soil parameters are another driver of uncertainty in models (Eitzinger *et al.*, 2008). Meteorological inputs represent an essential link between accurately modeled SM data and the performance of quality and quantity standards (Brocca, Ciabatta, *et al.*, 2017). These standards, in turn, depend on the spatio-temporal resolution of soil information, management of land use, and the meteorological data itself (Brocca, Ciabatta, *et al.*, 2017). Thus, for a robust model calibration over a range of environmental conditions, it is crucial to include field observations regarding soils or climate in particular (Eitzinger *et al.*, 2013).

3.4.1 ARIS

The ARIS data originates from a web and GIS-based operational monitoring system, the 'Agro Drought Information System' – ADIS (Eitzinger *et al.*, 2016). However, its abbreviation stands for 'Agricultural Risk Information System'. It was developed during the research project 'AgroDroughtAustria' (ADA) and is applied to important crops to cover diseases, abiotic (drought, frost, heat, strong wind) and biotic (pests) stresses (Eitzinger *et al.*, 2016; Eitzinger, 2018).

ARIS was developed as a monitoring and prediction tool for climate change adaptation. It is closely related to the Austrian climate conditions to provide valuable parameters for decision support. The main focus lies in identifying extreme weather and high-risk weather conditions with significance to crop cultivation and yield (Eitzinger *et al.*, 2016; Ikwandienst, 2020).

ARIS's resolution is displayed on a 0.5 km grid (Eitzinger *et al.*, 2016), based on spatial data of several parameters like weather data of the INCA product from ZAMG, the available soil data of BFW (2020) with its online platform eBod and land use classes from CORINE (Eitzinger, 2018). The simulated model considers the soil and site with the phenological development of specific crops as well as the relevant water demand, respectively. Two soil depths are featured in the soil water balance, with 0-40 cm and 40-100 cm for selected field

890 crops (Eitzinger *et al.*, 2016). There are three indicators in the ARIS data, first the current soil water deficit. Second is the site-specific degree of drought (in relatively existing plant-available soil water). Third, drought (reference depth 0-20 cm) and heat estimate the crop-specific stress level. The simulations are executed daily for the Austrian grid points for several crops like winter Wheat and spring Barley, grassland, and other crops (Eitzinger, 2018).

The limitation of the ARIS simulation is the spatial resolution of the 0.5 km grid. Therefore, small-scale parameters deviate from the initial resolution, with a constraint of simulation results. Considerations of several parameters like soil cultivation, crop variation, and fertilization are also unaccounted for. Outdated land-use classes from 2012, like cropland conversion or vice versa, are an additional limiting factor for the ARIS monitoring implementation (Ikwarndienst, 2020).

900 The data analyzed starts at the beginning of 2018 until 2020, featuring the three different crop types cultivated within its respective season. The resolution is 500 m, featuring the two individual soil depths as relative soil saturation. It ranges from 0 % being SM at PWP to 100 % being SM at FC.

Like the S1ASCAT-SWI and SMAP products of RSS [%], the ARIS estimations were transformed towards absolute soil moisture in % vol., which is described in more detail in chapter 3.6.4 Transformation of satellite and simulation data based on soil porosity.

Figure 13 features a simulation for winter Wheat from July to September 2015 with its RSS [%]. According to the color scheme, there is a shift from a dry to an elevated SM condition in the Marchfeld region.

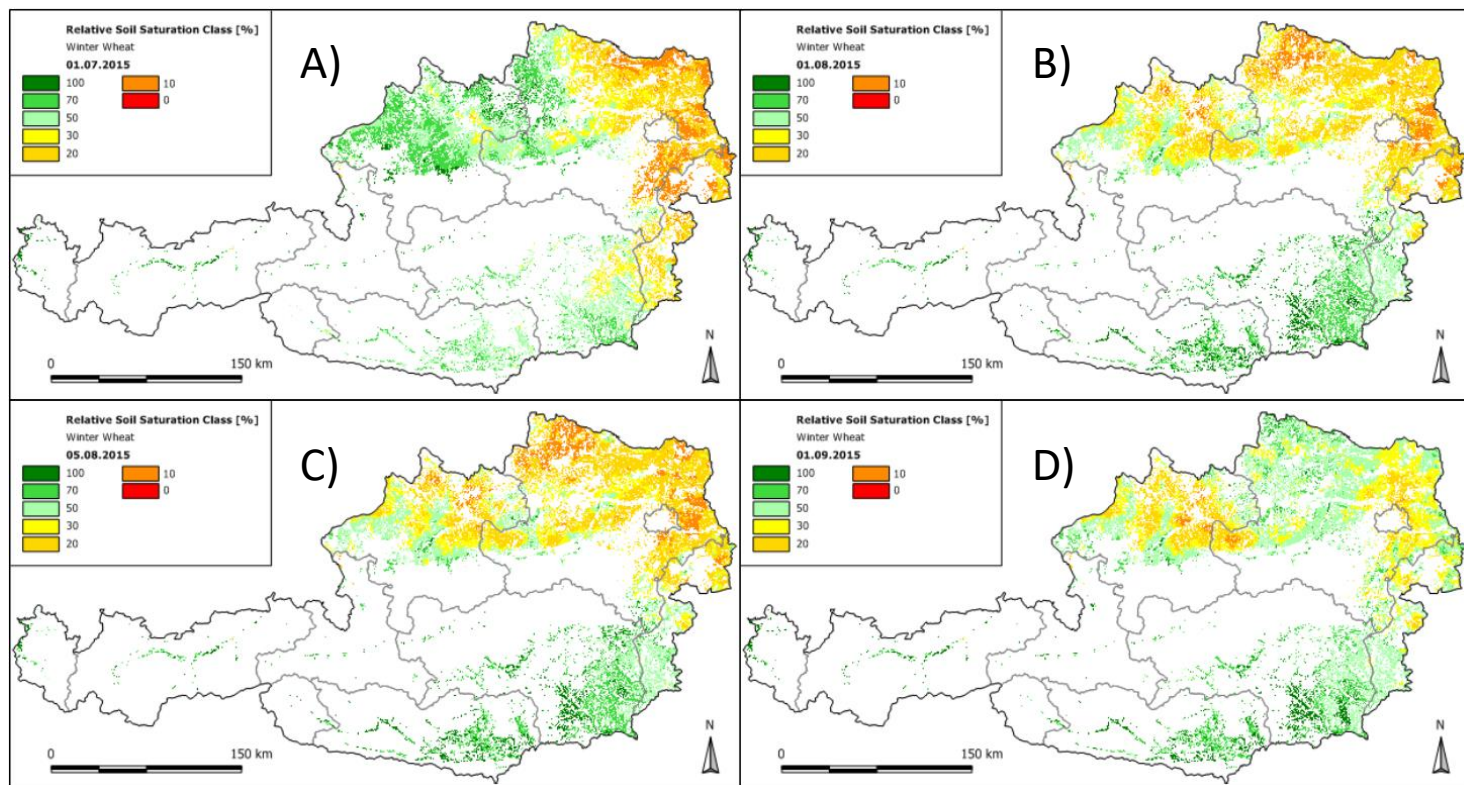


Figure 13: ARIS simulation of winter Wheat with a classified RSS [%] for A) July 1st 2015, B) August 1st 2015, C) August 5th 2015, D) September 1st 2015 (Source: Eitzinger et al. 2016)

3.4.2 AquaCrop

910 AquaCrop, a growth model for crops developed by the Land and Water Division of FAO, is a software to address food security and an assessment tool for crop production to represent the effects of environment and management on crop production (Steduto *et al.*, 2012). This model is designed to optimally balance accuracy, simplicity, and robustness (Steduto *et al.*, 2009). Small but necessary parameters and intuitive input variables determine the widely applicable modeling software (Steduto *et al.*, 2012; FAO, 2020). Nevertheless, its calculation procedures and complex biophysical processes accurately simulate the crop's feedback to the soil-plant system (FAO, 2020).

For instance, AquaCrop simulates several parameters as probable output with input parameters like water as the key limiting factor of the planned crop production (FAO, 2020).

920 The idea behind the software is to increase agricultural production with the help of efficient water practices (Araya, Keesstra, and Stroosnijder, 2010).

The output utilized for the analysis comprises the CC [%] for model validation and the soil water content [vol. %] in five and 15 cm soil depths as data acquisition.

Foundation of the AquaCrop simulation program

Most of the food production is dependent on plant available water throughout the world. Its use is crucial to develop a high standard nutrition supply for civilization, with special regard to arid and semi-arid regions. In these territories, precipitation lacks the crop's demand (Steduto *et al.*, 2012).

930 However, Doorenbos and Kassam (1979) introduced, under the patronage of the FAO, a transparent and straightforward tool to calculate the interdependencies of consumed water and crop yield (Y), with the eventual description of Y response to Evapotranspiration (ET). This simple equation is used for numerous types of crops and vegetables, or by extension, biomass

production (herbaceous or woody species) in a general sense (Equation 11) (Steduto *et al.*, 2012).

Equation 11, introduced by Doorenbos and Kassam (1979), was innovative and game-changing at the time. Thus it is seen as standard and foundation of crop yield response to water and modern interpretations with simulation models like AquaCrop (Steduto *et al.*, 2012):

Equation 11: Standard of crop yield response to water

$$\left(1 - \frac{Y_a}{Y_x}\right) = K_y \left(1 - \frac{ET_a}{ET_x}\right)$$

Equation 11 features the relative yield reduction related to the corresponding relative reduction of evapotranspiration; Y_a = actual yield and Y_x = maximum yield (in tons per hectare), ET_x = maximum crop evapotranspiration and ET_a = actual evapotranspiration (in mm per growing season), K = yield response factor. Equation 11 applies to all herbaceous plants (Source: Doorenbos and Kassam, 1979).

Another vital component of the initial Equation 11 is determining the maximum crop evapotranspiration ET_x also known as ET_c , visualized in Equation 12. The reference evapotranspiration (ET_o), featured in Equation 12, is based on the FAO Penman-Monteith equation, which represents the modern benchmark of ET_o , according to Allen *et al.* (1998).

Equation 12: Determination of maximum crop evapotranspiration

$$ET_x = K_c \times ET_o$$

*Equation 12 features ET_x = maximum crop evapotranspiration and ET_o = reference crop evapotranspiration (in mm per growing season), K_c = crop coefficient (Source: Steduto *et al.* 2012).*

The simulation software AquaCrop is founded on Equation 12. However, world-renowned specialists in their respective fields collaborated to develop AquaCrop further to provide a tool for strategic planning and management of water in agriculture. Especially with climate change on the rise, heavy rainfall events or droughts occur on a more frequent pattern. A valuable tool like AquaCrop helps improve future agricultural applications of herbaceous crops to increase efficiency and productivity (Steduto *et al.*, 2012).

Based on the scientific foundation of Equation 11 and Penman-Monteith's equation to calculate ET_o , further developments composing of biomass calculation concerning transpired water are implemented in AquaCrop, considering the concept linking Y and crop water use (Steduto *et al.*, 2009). Nevertheless, AquaCrop separates crucial parameters and estimates biomass production directly through productive crop transpiration (Tr), disregarding non-productive soil evaporation (E) (Steduto *et al.*, 2012). These advancements are depicted in

Equation 13, featuring B , WP , and Tr (B = biomass $\left[\frac{kg}{m^2}\right]$, Tr = crop transpiration [mm], WP = water productivity parameter $\left[\frac{kg}{m^2/mm}\right]$).

Equation 13: Calculation of biomass in AquaCrop

$$B = WP \times \sum Tr$$

980 This separation of Y from harvestable biomass (HI or harvest index) is another critical aspect that was improved with the advancement of the AquaCrop modeling software, eventually introducing crucial information about stress and environmental parameters on Y (Steduto *et al.*, 2012). In modern agriculture, crops are frequently harvested abundantly for fractions of the plants or their fruits. The remaining biomass is deemed unprofitable or useless. Equation 14 thus highlights the importance of segregating Y into HI and B (Steduto *et al.*, 2012).

Equation 14: Calculation of yield in AquaCrop

$$Y = HI \times B$$

990 The overall advancements of the AquaCrop software, starting with Equation 11 as foundation and Equation 12 and Equation 13 as major improvements, form the heart of the simulation program. However, further innovation is the downscaling of time from seasonal growth stages towards daily crop response to water dynamics. The previously mentioned HI is quantified daily throughout the Y formation period. An accurate determination of daily soil water information enhances the AquaCrop software to simulate highly dynamic growth models rather than static approaches (Steduto *et al.*, 2012).

With B production being highly dependent on solar radiation as the driving force of the soil-plant-atmosphere continuum, Figure 14 emphasizes on herbaceous crops as a function of their water consumption with respect to solar radiation. The interconnection of distinct parameters shows the advanced approach of AquaCrop in comparison with its predecessor from Doorenbos and Kassam (1979) (Figure 14) (Steduto *et al.*, 2012).

1000 Steduto *et al.* (2012) show the relationship (upper triangle a,) that links B to Tr, expressed in Equation 12 and Equation 13. Hereby, water productivity (WP) as a parameter is presented to illustrate daily time steps (Figure 14) (Steduto *et al.*, 2012).

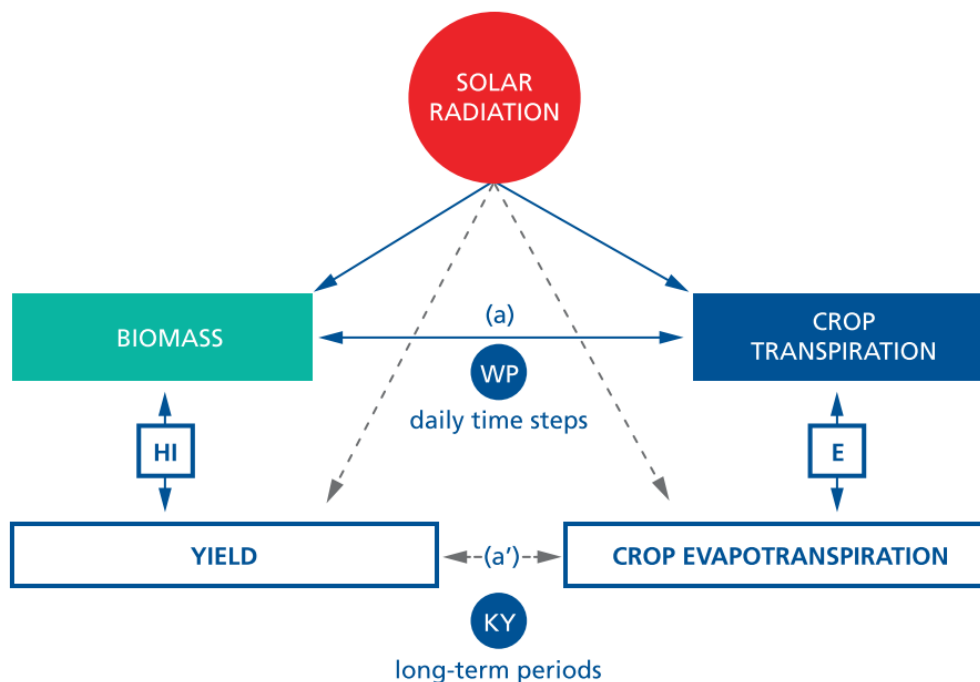


Figure 14: Interdependencies of parameters influencing B , Tr , Y , ET_c (Source: Steduto et al., 2012)

The former modeling but a rather linear approach concerning Equation 11 from Doorenbos and Kassam (1979) features long-term periodical modeling of crop production (K_y) as an input parameter. This relationship (lower triangle a') ties Y to ET with respect to Penman-Monteith's ET_o calculation and Equation 12 (Steduto et al., 2012).

Above the set of advanced Equations, additional relevant model components are incorporated into the AquaCrop software (Steduto et al., 2012), following in the next chapter.

Supplementary model components of AquaCrop

1010 The final output of AquaCrop simulations is growth, productivity, and water use with respect to altered water availability. Nevertheless, the AquaCrop simulation includes shifting water availability and varying environmental conditions like climate change scenarios. Yet, unpredictable parameters like pests and diseases are not featured in AquaCrop (Steduto et al., 2012).

Nevertheless, the following model components significantly impact the final outcomes of the simulation results of the AquaCrop software.

Crop parameters

1020 One of AquaCrop's software components is the crop feature, which has several subcomponents comprising phenology, canopy cover, rooting depth, soil evaporation, biomass production, and harvestable yield (Steduto et al., 2012).

However, calibrated default values are implemented in the FAO AquaCrop model to exploit for simulation. These default values are subdivided into conservative, cultivar-specific, and less conservative parameters (Raes et al., 2018).

The conservative crop parameters feature non-limiting and favorable conditions as calibration input. They remain applicable to stress conditions, yet no changes in management practices or geographical location applies. An adjustment to local conditions of the relevant cultivar location is not needed for simulation success (Raes et al., 2018).

In contrast, the cultivar-specific crop parameters involve modifications if environmental conditions or crop type deviate from initial FAO crop calibration within the AquaCrop database.

1030 These parameters are affected by several components like the soil profile, management practices, sowing date, or weather parameters to account for local variability and environmental conditions (Raes *et al.*, 2018).

Subcomponents like phenology are based on growing degree days (GDD), which provide valuable information and represent damaging or inhibitory effects of cold temperatures on crop phenology (Steduto *et al.*, 2012).

Another crucial component is canopy development, an essential supplementary component of AquaCrop, determining water transpiration and biomass production. It is expressed as a CC and can be obtained with the help of remote sensing expertise. Based on leaf senescence, declining green canopy covers result in dropping transpiration plus photosynthetic activity and, in turn, slows down biomass production (Steduto *et al.*, 2012).

The soil evaporation is calculated with respect to CC, which on the other hand, determines the shading of the wetted soil. Canopy senescence now affects soil evaporation in a positive correlation (Steduto *et al.*, 2012).

In general, crop root growth is co-dependent, pending on the photosynthetic activity of the crop. As a result, AquaCrop incorporates the simulation of an effective rooting depth with regard to the water extraction pattern of the cultivar (Steduto *et al.*, 2012).

Another subcomponent is biomass water productivity (WP). It is paramount and sits at the core of AquaCrop operation modeling software. As the last subcomponent, harvestable yield is simulated in AquaCrop based on the harvest index (HI) (Steduto *et al.*, 2012).

1050 Soil parameters

The soil parameters are typically specified by the user of AquaCrop, featuring up to five different horizons and their textural layers. AquaCrop can estimate soil hydraulic characteristics according to its texture classes, derived through pedo-transfer functions (Steduto *et al.*, 2009), determining water retention in the fine soil fraction at saturation (θ_{sat}). FC constitutes the upper limit of volumetric water holding capacity, the PWP representing the lower limit of the volumetric water holding capacity. Additional parameters are the drainage coefficient and hydraulic conductivity at saturation (K_{sat}) (Steduto *et al.*, 2009).

Water movement parameters, including percolation, runoff, capillary rise, and groundwater movements (e.g., saline groundwater table entering the soil profile), are considered and derived in AquaCrop from the determined hydraulic characteristics with a variable simulation period (Steduto *et al.*, 2012).

Climate parameters

Several daily values are associated with climate, including minimum and maximum air temperature (T_x and T_n), precipitation, or reference evapotranspiration (ET_o). ET_o is defined according to the FAO Penman-Monteith equation (Allen *et al.*, 1998; Steduto *et al.*, 2012).

The given temperatures, in general, affect phenology (crop development) and may limit growth or biomass accumulation. Furthermore, crop development relies on water stress or, to be more precise, on the water balance of the soil root zone, which is driven by precipitation and evapotranspiration, which is directly influenced by climate (Steduto *et al.*, 2009).

1070 Water productivity is affected by atmospheric CO₂ concentrations, regulating stomatal conductance and canopy expansion. Even though annual CO₂ cycles fluctuate with respect to time and location (Steduto *et al.*, 2009, 2012). Thus, annual mean carbon dioxide concentrations of the atmosphere, precipitation, and temperature are relevant parameters to incorporate in the AquaCrop model simulation (Steduto *et al.*, 2012).

Management parameters

Management practices in AquaCrop are split up into two categories. It can be chosen between specific water management options, like irrigation and non-irrigation (green water or

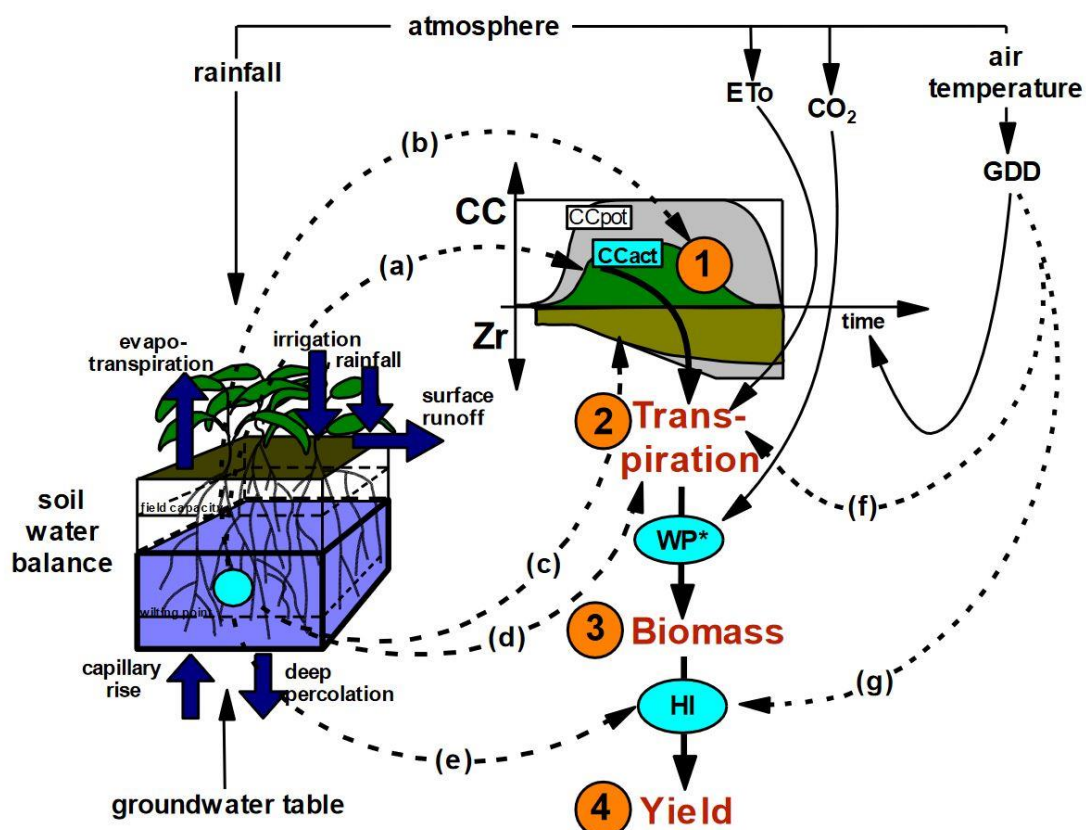
precipitation), and field management practices. The application methods of water management are selected amongst sprinkler-, drip- or surface irrigation options, defining the schedules or intervals, depth, and quality of the irrigation scheme, or an allowable water depletion with fixed percentages. Nevertheless, AquaCrop can automatically generate time schedules and schemes (Steduto *et al.*, 2009, 2012).

Day-by-day irrigation simulations can be applied and observed with effects on crop canopy and transpiration or eventually yield responses to deficit irrigation (Steduto *et al.*, 2009).

The second management category refers to field management practices such as mulching the soil for soil evaporation reduction, the control of surface runoff with small ponds and dykes, and the definition of soil fertility levels to grow crops during its life cycle (Steduto *et al.*, 2012). With the AquaCrop model, no nutrient balances are computed. Yet, fertility regimes concerning yield response and biomass accumulation are assessed with several fertility category parameters, ranging from near-optimal to poor (Steduto *et al.*, 2009).

Calculation scheme of AquaCrop

The AquaCrop simulation features four calculation steps based on few input parameters comprising of soil and groundwater data, crop parameters, meteorological parameters, and field management practices. These four main steps are composed of the estimation of green CC, Tr, B, and the eventual Y as a simulation output. Weed infestation and Tr and other stresses like temperature, salt, or water deficiencies directly impact the calculation of the AquaCrop simulation (Figure 15) (Vanuytrecht *et al.*, 2014; FAO, 2017).



1100 Figure 15: Calculation scheme of AquaCrop implying different pathways impacted by temperature and water stress (a-g) (Source: Vanuytrecht *et al.*, 2014)

Figure 15 shows the calculation scheme and implies how different pathways are impacted by temperature or water stresses (a-g). The dotted lines indicate stress processes, respectively. Water productivity is (WP), (Zr) is the rooting depth (Vanuytrecht et al., 2014).

Input parameters for AquaCrop simulations

1110 The required input parameters for an AquaCrop simulation are small. However, the simulated crop environment is dependent on valid and sound data for a successful crop development simulation. Input parameters comprise meteorological data such as precipitation and temperature, crop and soil characteristics, and management practices. The relevant information is stored in files to easily access the AquaCrop software (Steduto *et al.*, 2012). Amongst the input parameters utilized are also default parameters from the existing AquaCrop database. For example, the CO₂ observations for the climate data origin from the Mauna Loa Observatory in Hawaii.

The remaining climate input parameters utilized for the AquaCrop simulation originate from the meteorological stations in Rutzendorf and Groß-Enzersdorf, from 2018 through 2020. The meteorological data is uploaded into AquaCrop as a text file (Figure 16).

1120 For the crop input parameter calibration, field observation data from the BVW is used. It comprises the crop rotation, featuring the three crop types. The overall actual yield in $\left[\frac{kg}{ha}\right]$ dry matter. The compilation of the harvest index for the years 2019 and 2020. The overall sowing rate in $\left[\frac{kg}{ha}\right]$, as well as the sowing date and harvest date for the respective periods.

The remaining crop parameters were either default values or iteratively estimated and adjusted based on the actual yield as a reference parameter.

The soil and groundwater characteristics are based on the digital soil map eBod featuring three different soil types with their respective soil profile horizons and textures. The data was, wherever possible, validated through the MUBIL project reports. Three individual soil types are generated and featured in the simulations. The parameters included are default values and feature the volumetric water content of FC, PWP, as well as saturation and hydraulic conductivity (Ksat) (Steduto *et al.*, 2012).

1130 The management data utilized for the AquaCrop simulation comprises the irrigation and field management practices.

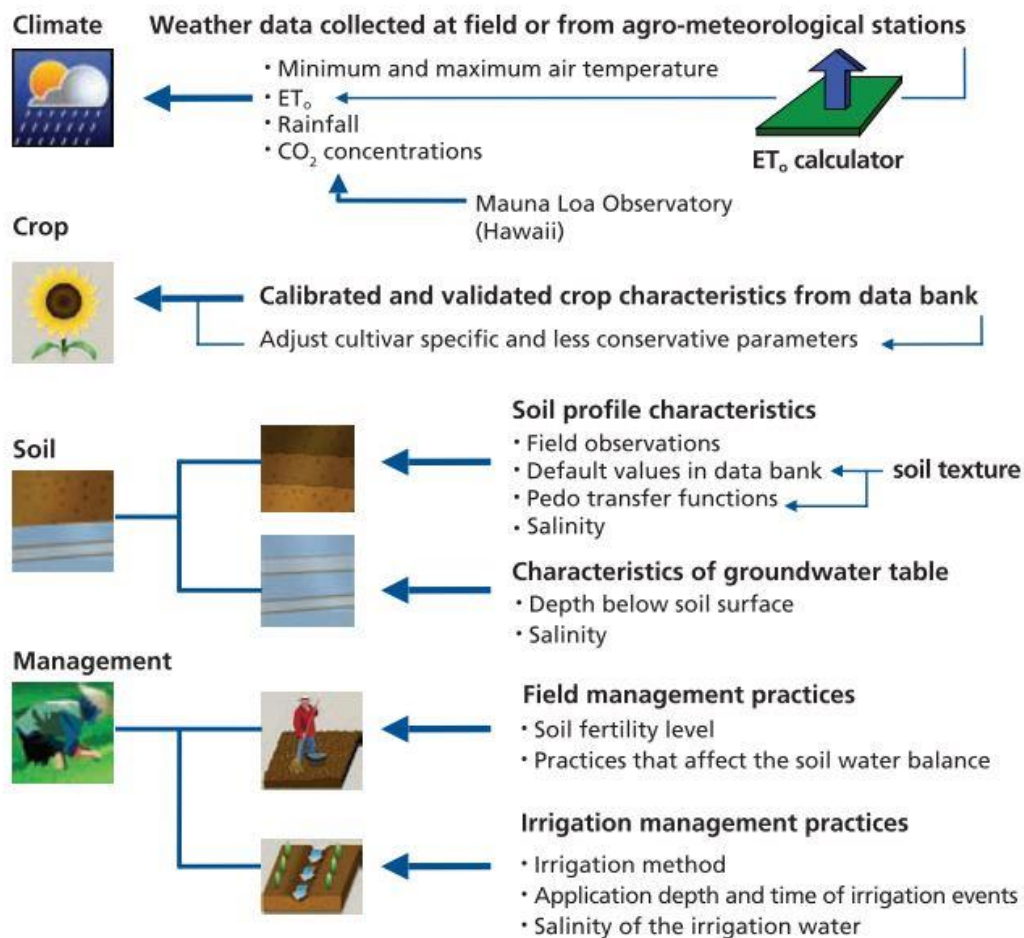


Figure 16: Required input parameters for the AquaCrop simulation (Source: Steduto et al. 2012)

As the last step, AquaCrop provides an additional option to include parameters of the initial conditions of the simulation period. CC, as well as soil water conditions, are amongst the specifications possible. This specification provides the user with a tool to compare the simulated data.

For the simulation performed, the initial conditions of the soil water content during 2019 and 2020 are based on the SM FDR probe from the meteorological station. The initial SM content for the growing period 2018 is estimated by climate data and established on behalf of precipitation before sowing—the CC for validation origins from the LAI-MODIS remote sensing data.

1140

The soil water content of the model output is divided into 12 individual soil profile compartments covering the entire root zone. The default size of the compartments has ten cm steps, starting at five cm (Raes et al., 2018).

For the analysis, only the depth in five and 15 cm were considered.

3.5 Statistical Analysis

Statistical analysis was performed using Microsoft Excel and the software R (Version 4.0.2). The Pearson Correlation Coefficient was used to characterize and validate the relationship between the simulated dataset of the AquaCrop CC and the LAI-MODIS dataset. A strong positive relationship was assumed by values from 0.7 to 1, whereas values below 0.5 to negative values were assumed to have a strong negative relationship (Mittag, 2014).

1150

The correlation analysis between in-situ, simulation, and remote sensing measurements was a linear regression used to characterize and validate the correlation analysis, respectively.

An R^2 ranging from 0.5 to 1 was assumed to be a good fit. In comparison, moderate correlation was assumed with R^2 values from 0.3 to 0.49. A poor correlation was assumed with R^2 values less than 0.3. The independent variables were either measurements with Parrot or the Met-station, whereas the dependent variables were the simulation and remote sensing datasets (Frost, 2018).

1160 The data was validated with a residual plot and a residual density curve to check for normal distribution. The p-value of the analyses was checked for significant relationships ($p < 0.05$ and $p < 0.001$) between the explanatory and dependent variable or null hypothesis dismissal.

The root mean square error (RMSE) was used to measure the error of the model. It is an indicator of how close the observed data points are compared to the predicted values. RMSE is an absolute measure of fit, compared to R^2 , which is deemed a relative measure of fit. The lower the RMSE values, the better the fit (Mittag, 2014; Frost, 2018).

Nevertheless, it is vital to check the perspective and statistical application of the RMSE conducted. A higher RMSE does not necessarily determine a poor fit, as it depends on the results to be compared with each other.

1170 The mean bias error (MBE) was used to explain and further quantify the bias of the predictions compared to the observations (Kato, 2016).

For example, if the model simulation- and satellite product estimations (predictions) were overestimated ($MBE > 0$) or underestimated ($MBE < 0$) compared to the reference measurement observations (e.g., TDR, Parrot, and the weather station) (AgriMetSoft, 2019). The mean bias error is a standard metric to evaluate forecast accuracy and represent a systematic error of over-or underestimations (Pal, 2016).

3.6 Scaling of the datasets

3.6.1 Preparation of in-situ, satellite, and simulation data for comparison

1180 The available satellite datasets are given in different units, opposed to the underlying in-situ datasets. Hence, the TDR, Parrot, AquaCrop, and the FDR sensor of the meteorological station are given in vol. % as a unit. However, the ARIS, S1ASCAT-SWI, and SMAP product units are given in relative SM [%].

To compare the satellite and simulation datasets, the reference sensors, e.g., Parrot and FDR, are converted into relative SM [%], respectively. Hence the transformed Parrot data is indicated as follows in the results section: **Parrot_rel**

Similarly, the FDR Met-Station is indicated as follows: **Weatherstation_20cm_rel**

Likewise, remaining data given in relative soil saturation is indicated as follows: **SWI_001_rel; SWI_005_rel; SWI_010_rel; ARIS_rel; SMAP_rel**

1190 This practice is deemed a profound procedure to compare in-situ measurements with satellite data (Albergel *et al.*, 2010; Brocca *et al.*, 2010).

For example, the lowest measured value within the measurement periods of the sensors defines 0 % relative SM. The highest measured value within the period defines 100 % relative SM, such as the research of Albergel *et al.* (2012) suggests.

This principle was applied for the datasets of Parrot (2019) and the meteorological station (2019-2020). During the operation of the sensors, the lowest and highest measured values set the upper and lower boundary range.

The datasets given in consistent units, e.g., SM [vol. %], are compared without unit adaption. Such variables with consistent units of the results section are indicated as follows:

1200 **Weatherstation_10cm; WS_20cm** for the weather station; **TDR** for the time domain reflectometry; **AquaCrop_B1_5cm** or **AquaCrop_B1_15cm** for the AquaCrop simulation variables.

3.6.2 Definition of FC and PWP for the experimental field

The PWP was determined based on TDR measurements on July 5th, 2019. The same applies to the FC, which was determined based on TDR measurements on July 24th, 2020.

The mean FC was characterized as 19 vol. % and the PWP was characterized as 9 % vol. Thus, the FC and PWP were part of the correlation analysis of the SM in vol. % for indication purposes. The relative SM [%] correlation comparison includes the FC and PWP, as defined by the minimum and maximum range of the Parrot and FDR sensors.

3.6.3 Calibration of in-situ sensors

1210 Unfortunately, the base reference measurements with TDR were time-consuming and tedious. As a result, only little data was available. In comparison, the available Parrot data covers a large portion of the vegetation period of Wheat in 2019. Furthermore, it ranges from April 4th, 2019, until July 6th, 2019. Thus, the Parrots were used as the new independent variable for the analysis of 2019. The Parrot time series data was therefore calibrated for the subsequent usage. Moreover, the Parrot measurement values were given in an uncalibrated digital value. Thus, based on a comparison of linear and polynomial regression results, the Parrot sensors were calibrated with the help of polynomial regression.

In the following step, the TDR sensor values were defined as the independent variable, and the Parrot sensor values were defined as the dependent variable (Equation 15).

1220

Equation 15: Polynomial regression of TDR vs. Parrot

$$y = 0.021x^2 - 0.021x + 14.258$$

For further calculations, all Parrot measurements were inserted in Equation 15. After the transformation, all Parrot measurements were assumed to equal volumetric soil moisture. The calibrated Parrot sensors are highlighted as follows in the results section: **Parrots_cal** or **Parrot_B1** for the Parrot sensors overlain by soil type B1.

1230

The weather station sensor in ten cm soil depth provided insufficient data. Thus, the weather station's 20 cm soil depth sensor was used as the independent variable for the following correlation analyses to dismiss lacking SM time-series data for 2020.

3.6.4 Transformation of satellite and simulation data based on soil porosity

The soil porosity at the experimental field was established with the HYDROBOD2 raster dataset. The dataset is used to characterize hydrologic soil parameters and helped, therefore, to determine the soil porosity in the upper soil layer.

According to the HYDROBOD2 dataset, the soil porosity in the upper soil layer marks at $41.5 \left[\frac{m^3}{m^3} \right]$. It is established on the statistical mean over the experimental field.

Of course, there is spatial variability. However, the underlying dataset provides not enough resources to feature such high heterogeneity. In contrast, soil porosity can also be established

1240

The RSS [%] satellite and simulation data was initially given in the degree of relative soil saturation and subsequently transformed into volumetric SM content [%] based on Equation 16. It was used to convert the satellite and simulation data into volumetric SM content, as Wagner *et al.* (2013) suggest. The S1ASCAT-SWI, SMAP, and ARIS, given in RSS [%], were

transformed into volumetric soil moisture [% vol.], accordingly. Eventually, the transformed data were compared with the remaining datasets in trendline charts.

Equation 16: Calculation of volumetric soil moisture content (θ), based on the degree of saturation (m_s), and soil porosity (ϕ), (Source: Wagner et al., 2013)

1250

$$\theta = m_s \times \phi$$

The ARIS data was first adapted to the simulation parameters. The RSS of the ARIS simulation was pre-defined with a PWP of 16 % and a FC of 38 %. Thus, the range of the RSS min of the ARIS simulation starts at 0 %, which is defined as 16 % PWP. Likewise, 100 % RSS establishes the FC at 38 %. Afterward, it was transformed according to Equation 16.

3.7 Overview of the analysis scheme

1260

The following Figure 17 demonstrates a brief overview of the analysis conducted. Each column represents the respective vegetation period with the reference sensors of ARIS in 2018, Parrot in 2019, and the FDR Met-Station in 2020 in blue. The different SM estimation methods investigated in our research are indicated in the white boxes of each column – the statistical analysis is based on the reference sensors (highlighted in blue) of each vegetation period and calculated with linear regression, respectively. The soil profile depth or soil layer depth of each satellite product, simulation result, or in-situ sensor is indicated.

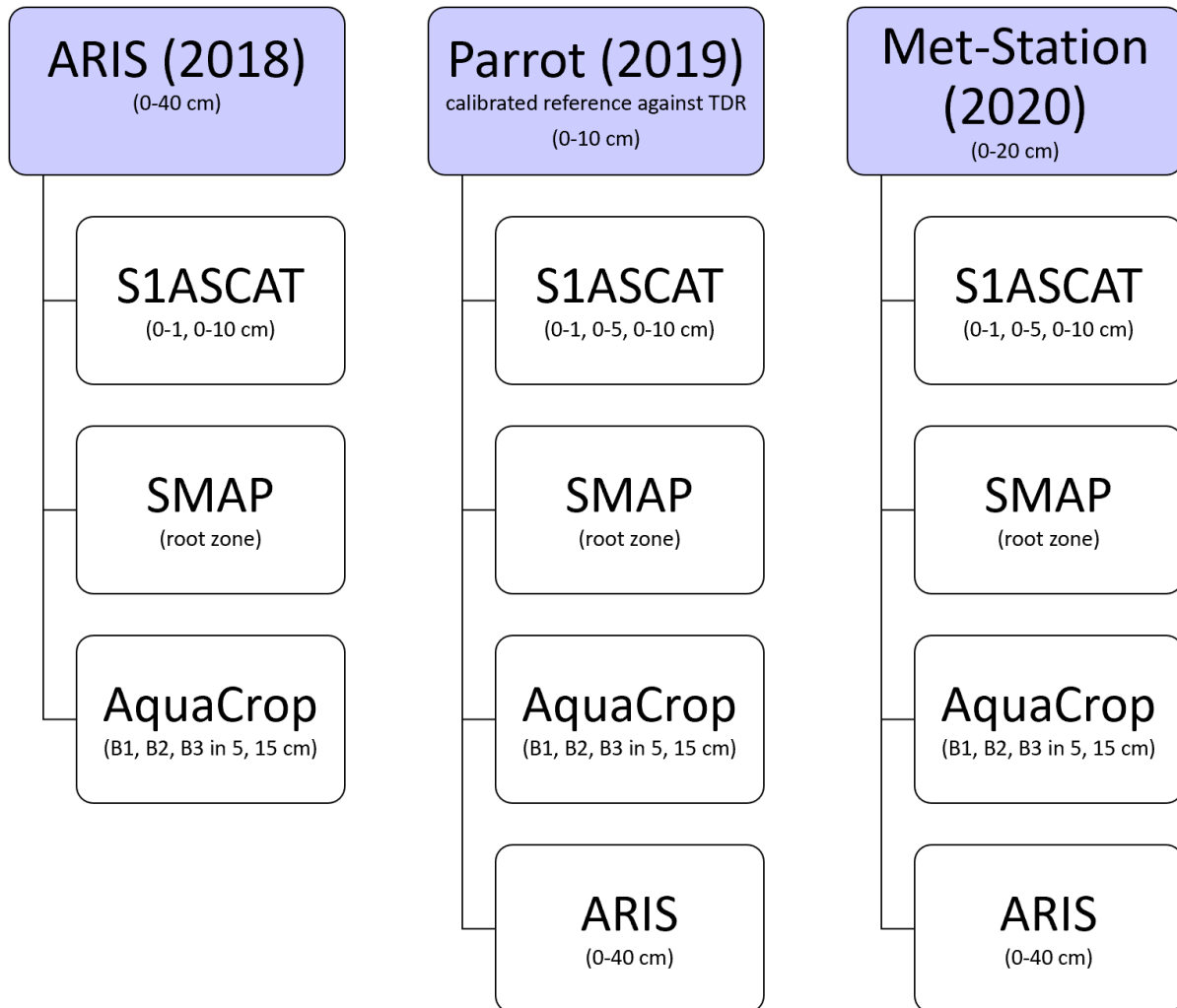


Figure 17: Overview of the statistical analysis conducted for all three vegetation periods; The reference sensors are highlighted (in blue) and were compared based on linear regression with the SM estimates (white boxes) accordingly

4. Results

4.1 AquaCrop simulation analysis based on LAI-MODIS observations

1270 The first analysis conducted was based on the LAI-MODIS dataset and the AquaCrop simulation output. Three simulations per vegetation period (respective growing periods of the three crops for the three dominant soil types B1, B2, and B3) were conducted. The AquaCrop output in Figure 18 is given as a blue area and determines the green canopy cover [%]. The LAI-MODIS observations feature one observation per day, depending on the cloud coverage and data availability, indicated by the red dots given in CC [%]. The analysis is based on the Pearson Correlation Coefficient and ranges from 70 % to 94 % during 2019 and 2020, demonstrated in Figure 18 D-I. The p-value for the dismissal of the null hypothesis was determined at values <0.001 .

For the vegetation period in 2018 (Figure 18A-C), insufficient data validity resulted in a negative correlation.

1280 Figure 18A-C shows the vegetation period of Barley from April to July 2018. The AquaCrop simulation deviates from the observed LAI-MODIS CC.

In contrast, Figure 18D-F provides correlations of about 90 % for the AquaCrop simulation compared with the LAI-MODIS dataset of 2019. The observations fit with the course of vegetation simulated. Figure 18G-I comprises Rye and starts in October 2019, reaching into July 2020. Between 70 to 90 % correlation was achieved in Wheat and Rye's statistical analysis.

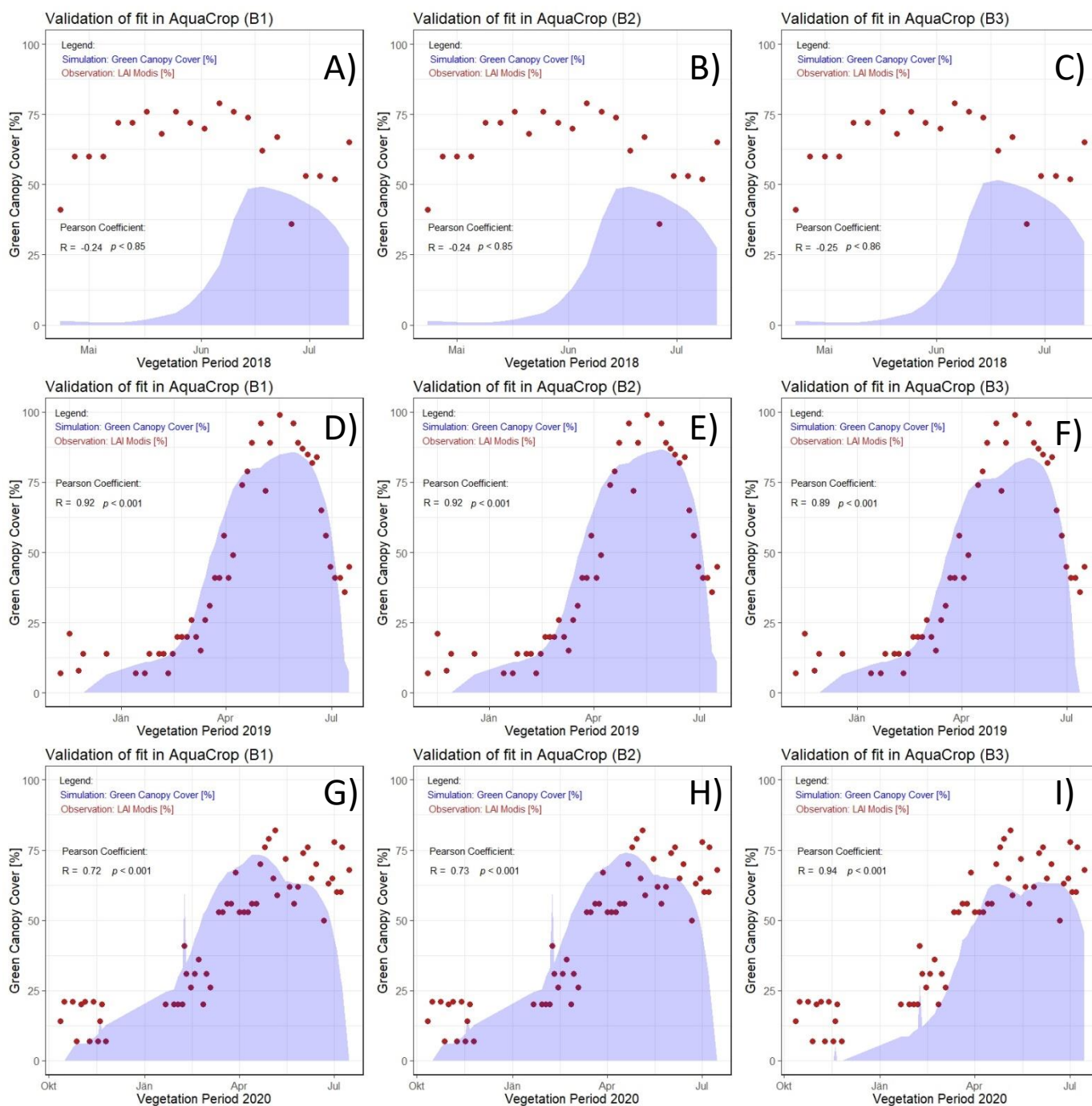


Figure 18: Validation of fit of the AquaCrop simulation output A) Barley B1, B) Barley B2, C) Barley B3, D) Wheat B1, E) Wheat B2, F) Wheat B3, G) Rye B1, H) Rye B2, I) Rye B3; the statistical analysis is based on the Pearson Correlation Coefficient; statistical differences were accepted at $p > 0.05$ (B1 – B3 refers to the three applied soil types as defined in chapter: 3.1.3 Soil Conditions)

1290 4.2 Spatial Variability of soil moisture (SM)

The spatial variability of SM on the experimental field is visually demonstrated for two days in April 2019 and two days in May and June 2019, based on the kriging interpolation method. The sensor used for in-situ measurement named Parrot (see methods) was placed in the upper soil layer (approximately 0-5 cm soil depth). The sensor output unit is volumetric SM [%]. Figure 19A-B shows the spatial soil moisture for April 4th and April 15th, 2019, respectively. The experimental field perimeter is highlighted in yellow. The locations of the Parrot in-situ sensors are marked as black dots. The measured SM range during both days is shown in the colored scale in the legend. Dark red indicates low values, whereas dark blue values indicate higher SM values.

1300 The color range, nevertheless, is determined by the daily min. and max. values measured all over the field. To better interpret the spatial variation in Figure 19, the overall precipitation occurrence two weeks before and during the measurements is featured shown in Figure 20. During March 18th and April 15th, there were only three precipitation events with low amounts of rain (approximately 12 mm), affecting near-surface soil water content only temporarily. Figure 19A on April 4th shows, therefore, slightly higher SM observations compared to April 15th (Figure 19B), due to the negative soil water balance in between despite some minor precipitation of about 5 mm

1310 Within the experimental field were individual 'islands' providing different ranges in SM, depending on the site location. Especially in the south and western part of the experimental field was less SM measured, indicated in red to dark red. The northwest and eastern part of the experimental field fostered higher SM in comparison. Thus, there, the soil water holding capacity appeared higher, indicated by the blue areas.

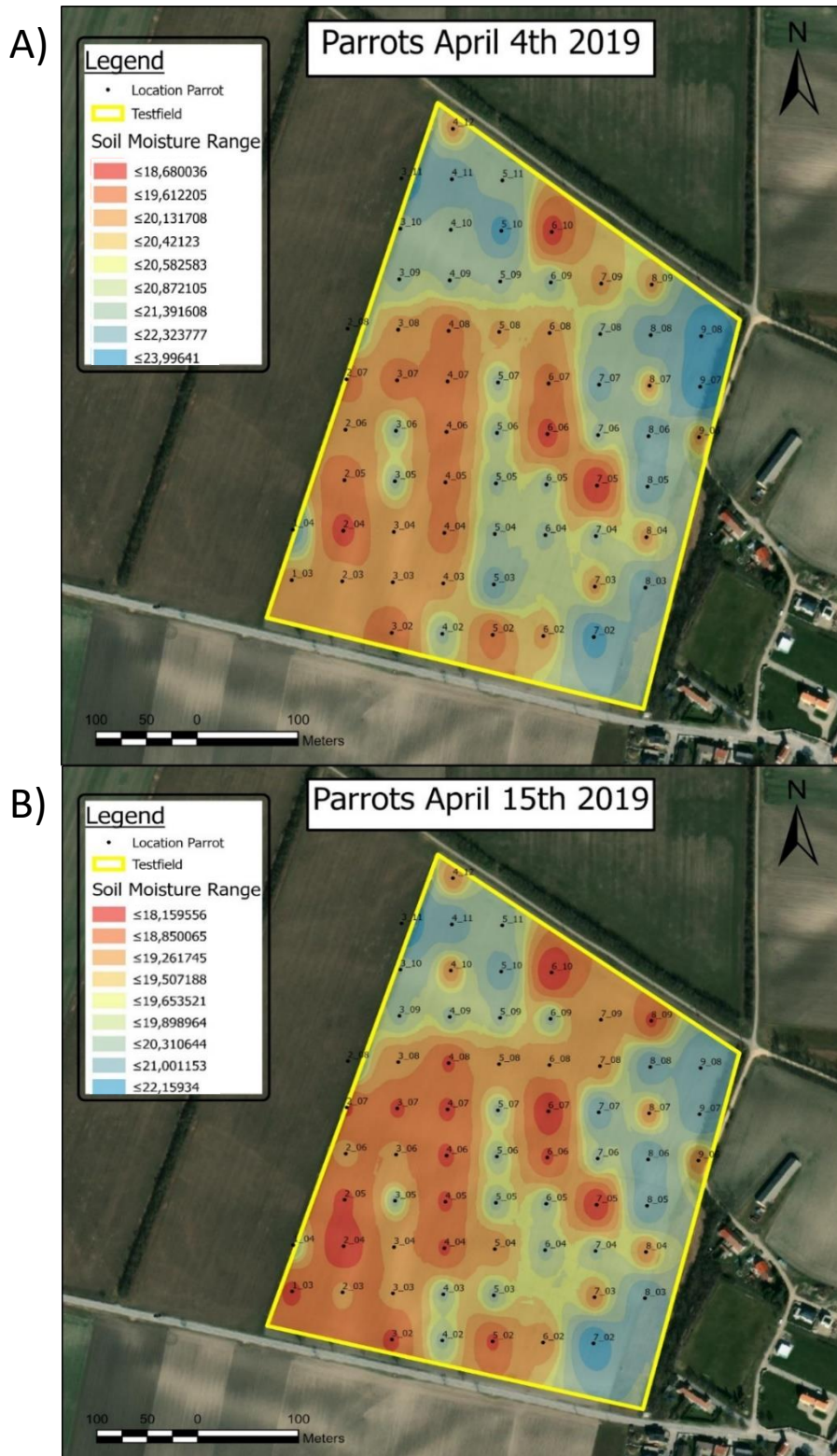


Figure 19: Spatial variability of soil moisture for A) April 4th, and B) April 15th 2019 across the experimental field in Rutzendorf, based on kriging

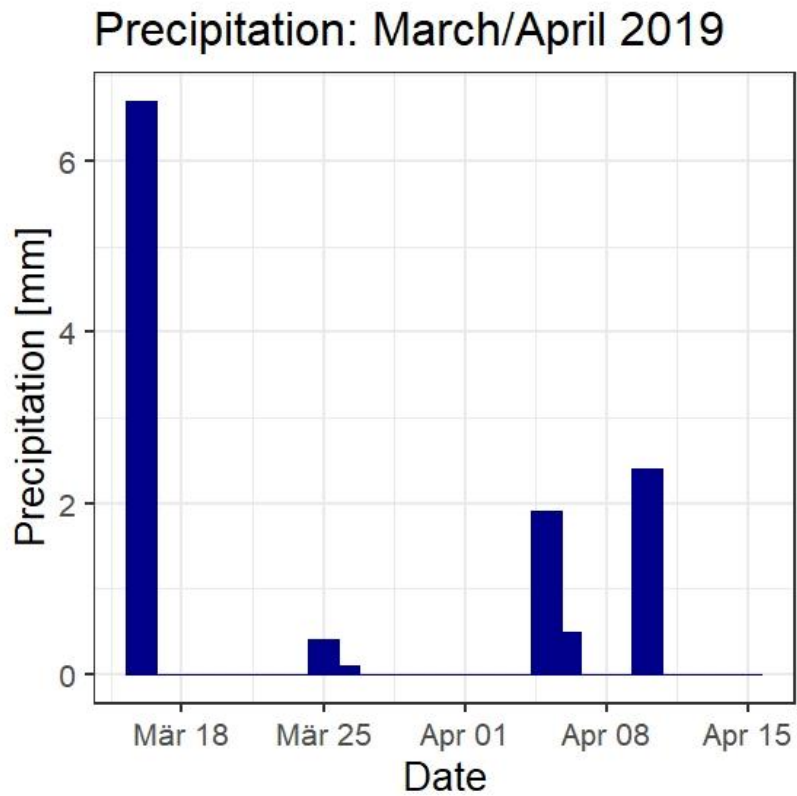


Figure 20: Precipitation graph for March and April 2019, prior to Parrot measurements

During the time frame from mid-May to the beginning of June in 2019, the weather was increasingly wet, with much higher precipitation events than in April 2019. Figure 21 shows the precipitation pattern starting on the first of May until the beginning of June 2019. There were more precipitation events during a similar time span compared to the precipitation graph of April 2019.

1320

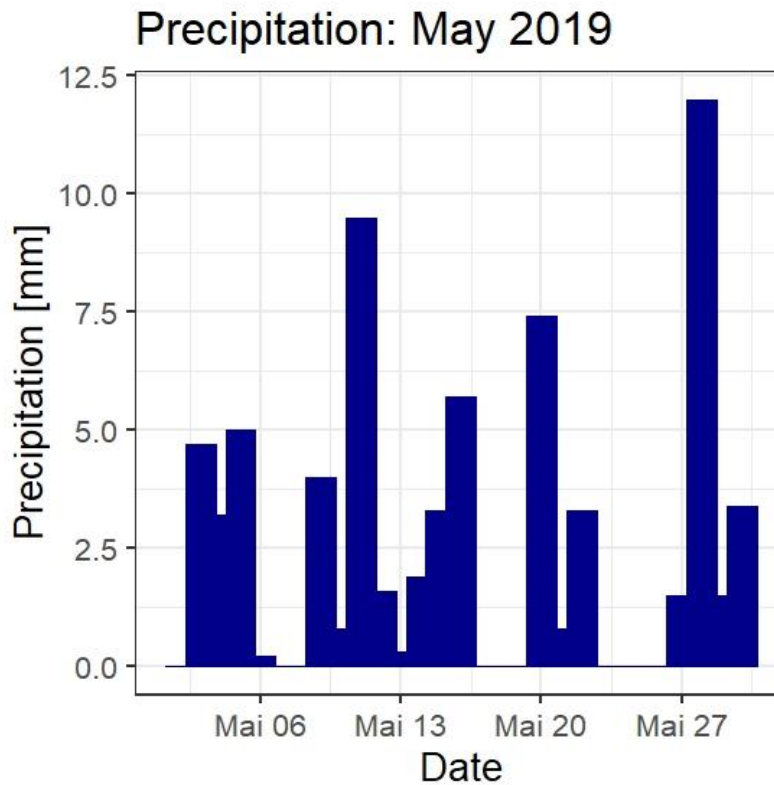


Figure 21: Precipitation graph for May 2019, prior to Parrot measurements

1330 The spatial variability of SM during the more wet period (Figure 22) is shown for May 15th (Figure 22A) and June 1st (Figure 22B). Again, the color range for SM is determined by the min. and max. measurements of the respective day. The SM regime, especially regarding the soil water holding capacity, corresponds with the higher and lower SM occurrences (see also Figure 19). Accordingly, especially in the experimental field's northern part, the soil showed the highest measured soil water contents.

The areas of higher SM during May and June also correspond to the overall SM measured during the more dry conditions in April. The middle and south-western parts generally appeared to foster a different texture with less water holding capacity than the eastern and northern parts of the experimental field. In both days of the investigation in May and June, the soil appeared almost at FC or exceeding it as precipitation was high before and during measurements.

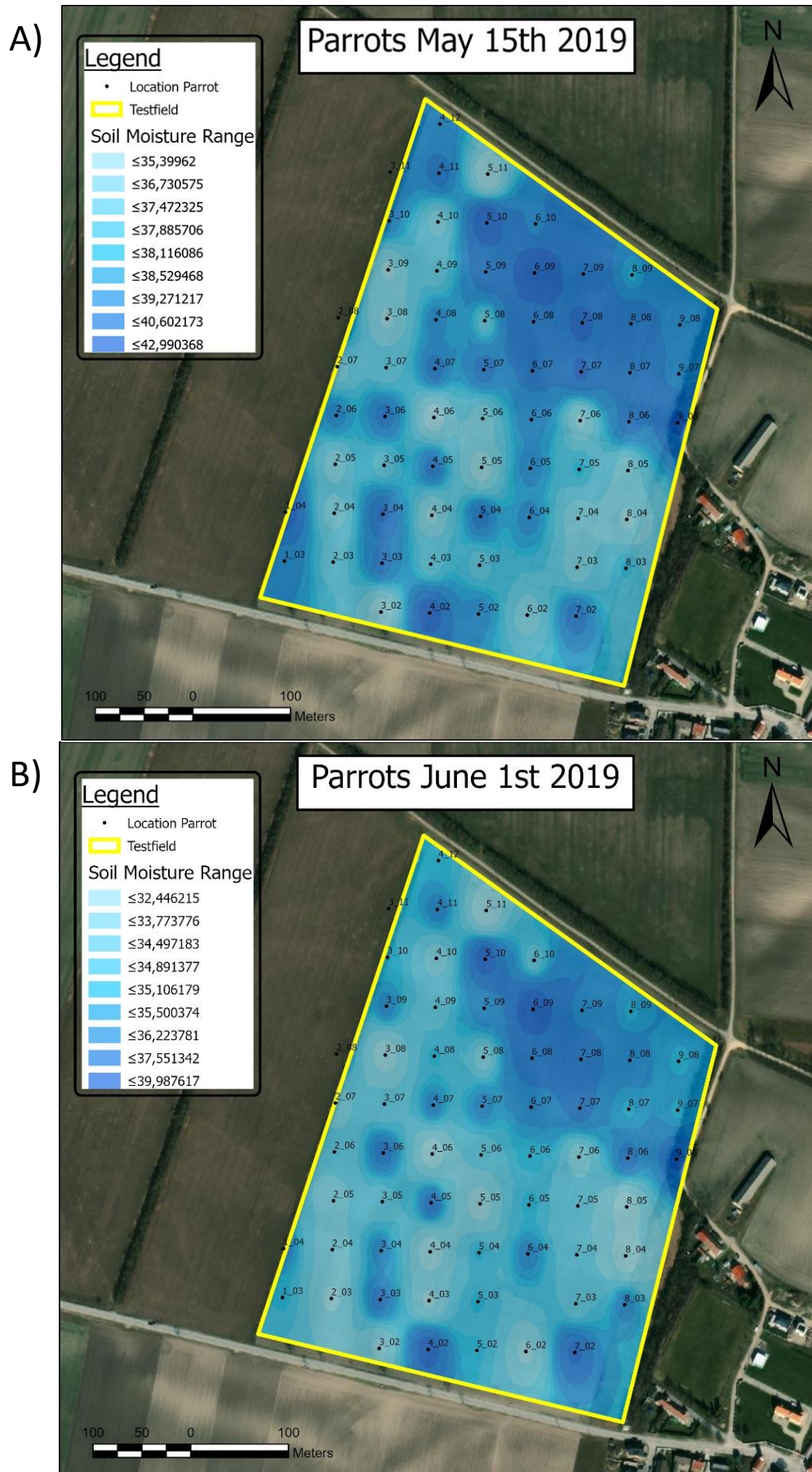


Figure 22: Spatial variability of soil moisture for A) May 15th, and B) June 1st 2019 across the experimental field in Rutzendorf, based on kriging

1340 Figure 23 presents the precipitation course before TDR measurements on July 24th, 2020, indicating moderate soil water contents, as shown in Figure 24. Figure 24 features a zoom effect with a set of three different resolutions comprising 250x250 m, 125x125 m, and 50x50 m, fostering the TDR measurement points from July 24th, 2020. Figure 24A shows the 250 m grid with an SM range between 29 and 15 % vol. Figure 24B shows the 125 m grid with a SM range between 32 and 15 % vol., indicated by higher SM in blue and lower SM in red. Finally, Figure 24C shows the 50 m grid, where the SM lies between 29 and 14 % vol. However, only a few measurement points were taken on the 50x50 m grid due to a sensor failure.

1350 The respective SM range is based on kriging calculations and depends on the gridded measurement points with their min. and max values of the TDR measurements for that day. For example, Figure 24A is based on the 250 m grid and Figure 24B on the 125 m grid. In Figure 24C, in the 50 m grid with measurement points, only the upper two rows of measurement points are subject to interpretation due to missing data.

Between some of the measurement points, SM varies up to 10 % in volume.

1360 Two weeks prior to the TDR measurements, the precipitation pattern shows continuous but medium precipitation events (Figure 23). However, even though constant precipitation occurred during the summer and July, e.g., relatively high temperatures were monitored, leading to high evapotranspiration rates of the canopy. The measured SM was, therefore, lower compared to May and June. Nevertheless, some parts of the experimental test field foster higher amounts of SM, probably due to higher soil water holding capacity at the measurement point.

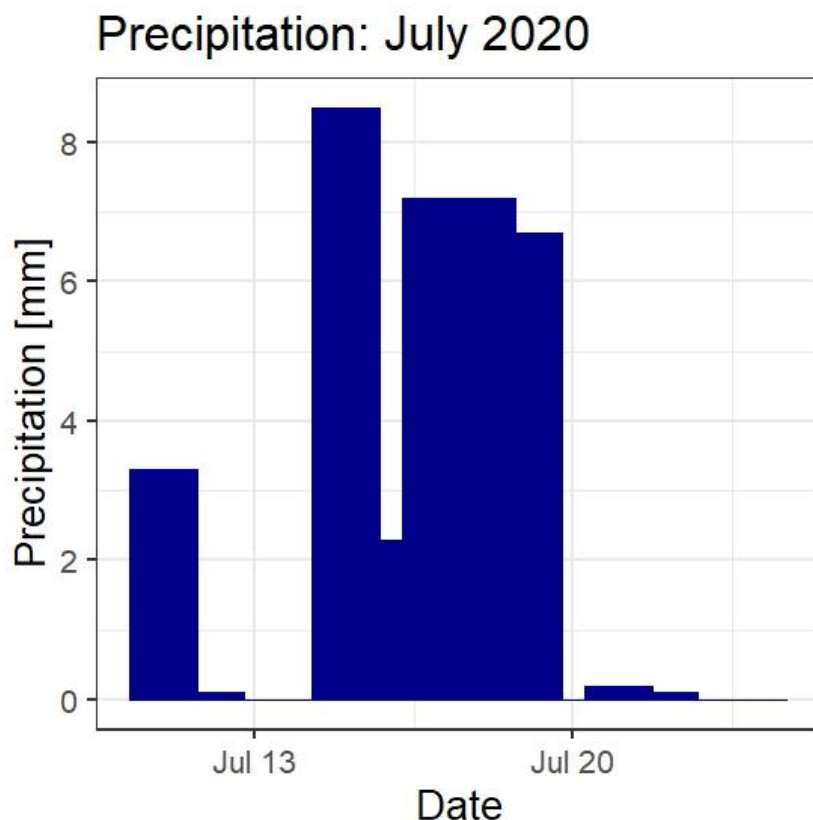


Figure 23: Precipitation graph for July 2020, prior TDR measurements

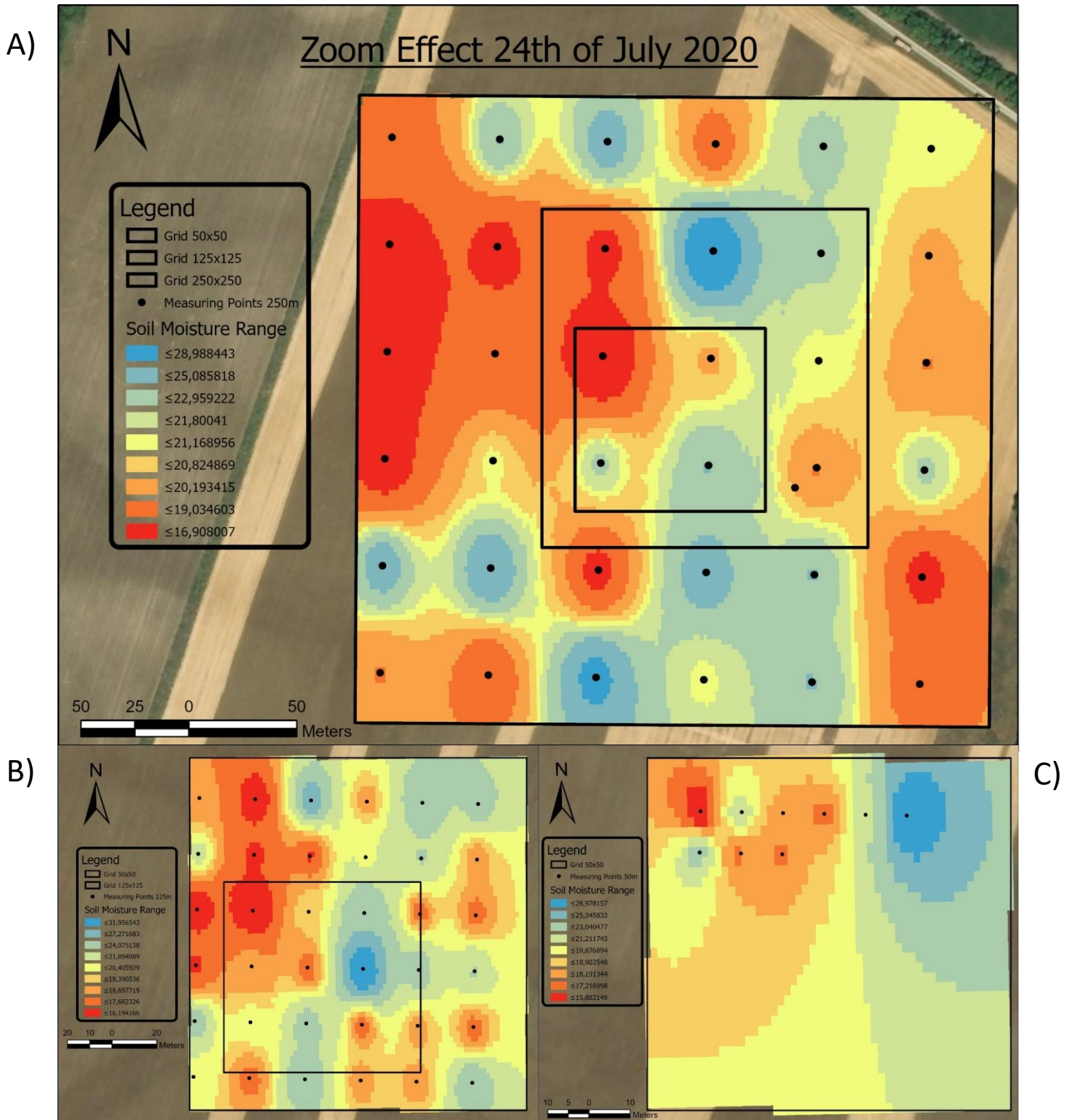


Figure 24: Zoom effect of TDR measurement based spatial interpolated SM on July 24th 2020, for A) measurements in the 250 m grid, B) measurements in the 125 m grid, C) measurements in the 50 m grid

4.3 Validation of in-situ Parrot sensors

In the following section, three baseline analyses are featured. Linear regressions were used for the analysis of different methodological SM measurements. The RMSE is determined as the following step.

4.3.1 Analysis of Parrot and TDR in-situ measurements in 2019

1370 The gridded TDR SM output from April 4th, 2019, June 1st, 2019, and July 5th, 2019 was linearly regressed with the equivalent SM output of the corresponding Parrot devices at the same measurement points (Figure 25A-C).

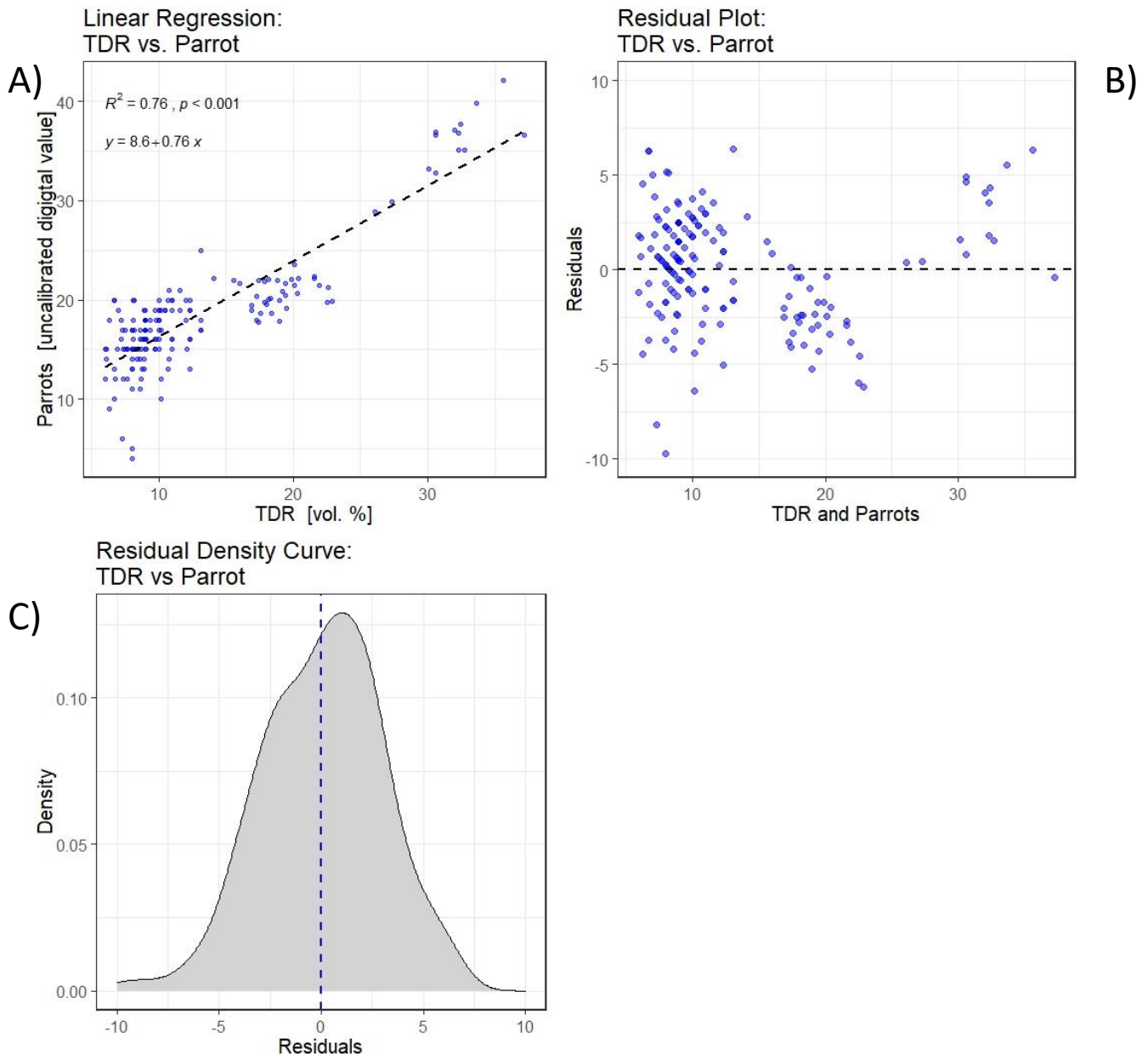


Figure 25: Statistical analysis of TDR vs. Parrot for A) linear regression, B) residual plot, and C) residual density curve

Overall, the TDR measurements exhibit the base reference and were thus set as the independent variable for the statistical analysis. An R^2 of 0.76 was observed between the TDR measurements and the 'Parrot' sensors (Figure 25A). The residual distribution was random, as shown in Figure 25B-C. Therefore, the null hypothesis was dismissed ($p < 0.001$). In general, a correlation of TDR and Parrot measurements was proved.

1380 4.3.2 Analysis of Parrot and FDR met-station in-situ measurements in 2019

The following analysis describes the calibrated SM mean of all Parrots (Parrot_cal) over the experimental field compared with one meteorological station within the field for 10 cm soil depth. It was measured by three FDR-sensors of the Z-weather station (Met-station_10cm) from April to July 2019 (Figure 26A-C).

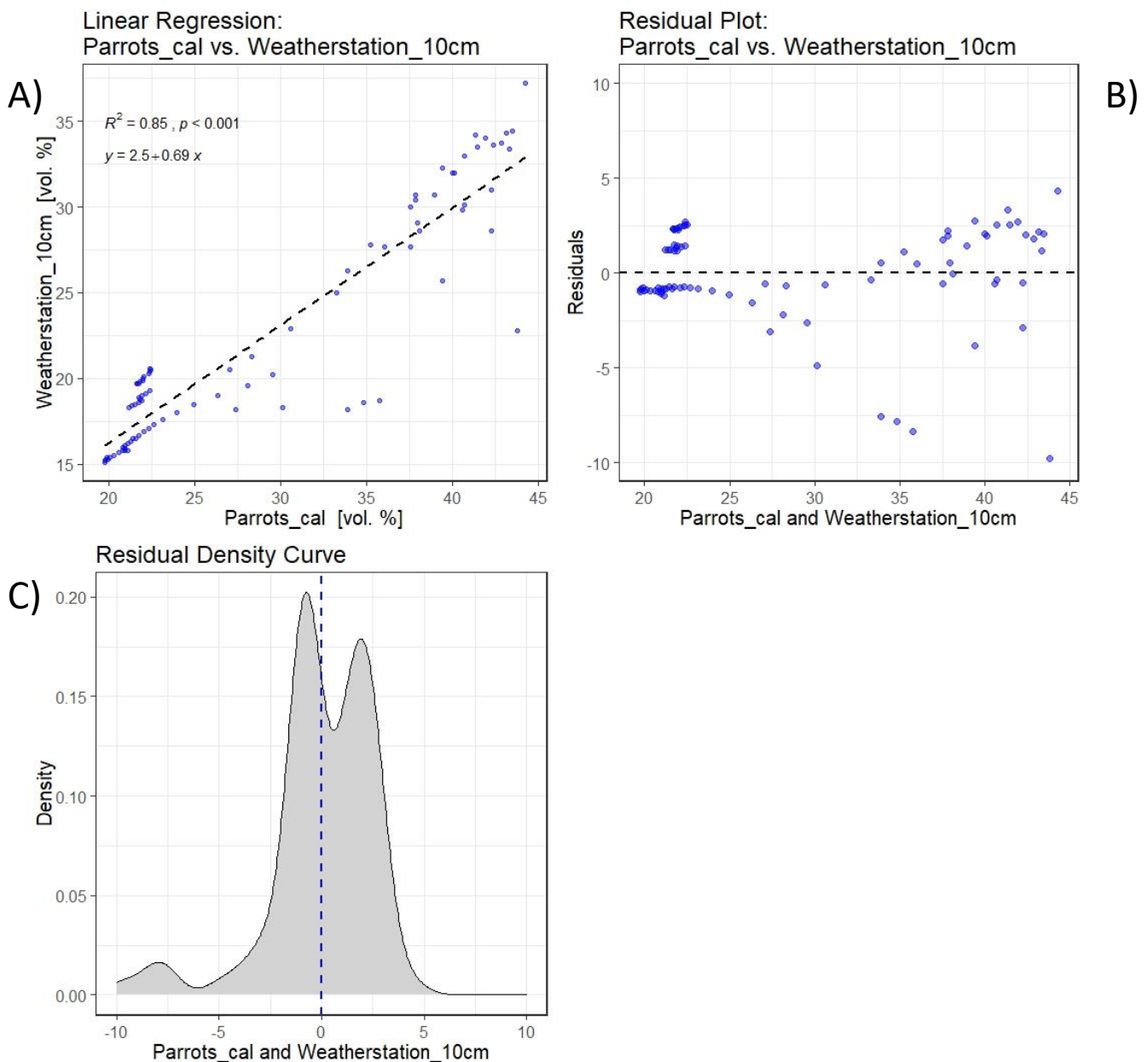


Figure 26: Statistical analysis of Parrot_cal vs. Met-station_10cm for A) linear regression, B) residual plot, and C), residual density curve

Since the new independent variable for the vegetation period in 2019 is the Parrot_cal, an overall correlation analysis is conducted to check if the weather station's sensors can be used as a proxy for the vegetation period in 2020.

The linear regression between the Parrot sensors and the FDR Met-station with R^2 of 0.85 is similar but higher than the baseline reference comprising TDR and Parrot.

1390 Further, just one single Parrot (Parrot_cal_42) was compared for redundancy purposes (Annex 1). The location of this Parrot device was in closest proximity to the weather station’s sensor. It shows a similar correlation with an R^2 of 0.79 as the mean Parrot measurements of the experimental field do. To check for the normal distribution of the two analyses, density plots with a confidence interval of 0.95 are shown in Figure 26C and Annex 1C. The density plots and residual plots are used to validate the corresponding linear regressions.

4.3.3 Overview of R^2 and RMSE

1400 The RMSE, R^2 , p-value, MBE, and the normal distribution were calculated for the baseline sensor analysis. According to the statistical analysis, all data were valid and achieved correlation. The R^2 is good, and the RMSE is relatively low compared to the entire measurement range. The RMSE is determined by the errors of the predicted values of the linear regression and, thus, is low in the baseline sensor analysis (Table 1). The mean bias error calculations indicate an overestimation of the Parrot measurements compared to the TDR measurements. The FDR Met-station, on the other hand, underestimates SM according to the MBE calculated. Nevertheless, the results are in line and following the behavior of SM for the respective soil depths and measurements conducted.

As a result of the analysis, the Parrot and weather station sensor were used as a proxy baseline reference for the following satellite- and AquaCrop simulation data comparisons.

Table 1: Summary of the baseline sensor analysis 2019

Absolute Soil Water Content [m^3/m^3]	RMSE	R^2	MBE	p-value < 0.001	normal distribution
TDR vs. Parrot	3.04	0.76	5.53	YES	YES
Parrot_cal vs. Weatherstation_10cm	2.53	0.85	-6.59	YES	YES
Parrot_cal_42 vs. Weatherstation_10cm	2.96	0.79	1.30	YES	YES

4.4 Temporal correlation analysis 2019 with satellite products and models

1410 The various remote sensing-based SM estimation methodologies are assessed and analyzed for correlation throughout the following chapter. It was executed according to the proxy reference of the calibrated Parrot measurements independent variable that continuously measured time-series.

A few key figures are presented as bold examples for better comprehension and a more precise overview of the results section. The relative soil water content range starts at 0 and goes up to 100 %. The satellite remote sensing SM estimations and the ARIS model can only provide one value throughout the experimental field but instead provide a temporal tool to compare changes in SM over a period of time.

1420 For the satellite products and the comparison with the ARIS model, the comparisons were made in relative soil water content and related changes (see chapter: 3.6.1 Preparation of in-situ, satellite, and simulation data for comparison).

The first satellite product compared to was the **S1ASCAT-SWI** SM. The dependent variable SWI_001_rel of the S1ASCAT SM product is regressed against the independent variable Parrots_rel in Figure 27A-D. The data are displayed in relative SM [%]. SWI_001_rel represents the SM of 0-1 cm of the top soil layer.

The overall correlation based on the linear regression between the Parrots_rel and SWI_001_rel has an R^2 of 0.6 (Figure 27A). The residual plot in Figure 27C shows a random distribution of the predicted values Figure 27B provides the SM trendline of the Parrot_rel and

1430 the S1ASCAT SWI_001_rel SM depth from the period April to July 2019. The Parrot data shows a higher fluctuation and relative SM [%] than the observed SWI_001_rel SM. In Figure 27D, the precipitation graph is plotted from April to July 2019. It corresponds well with the variations of relative SM during Mai and June, with corresponding moderate to strong precipitation events.

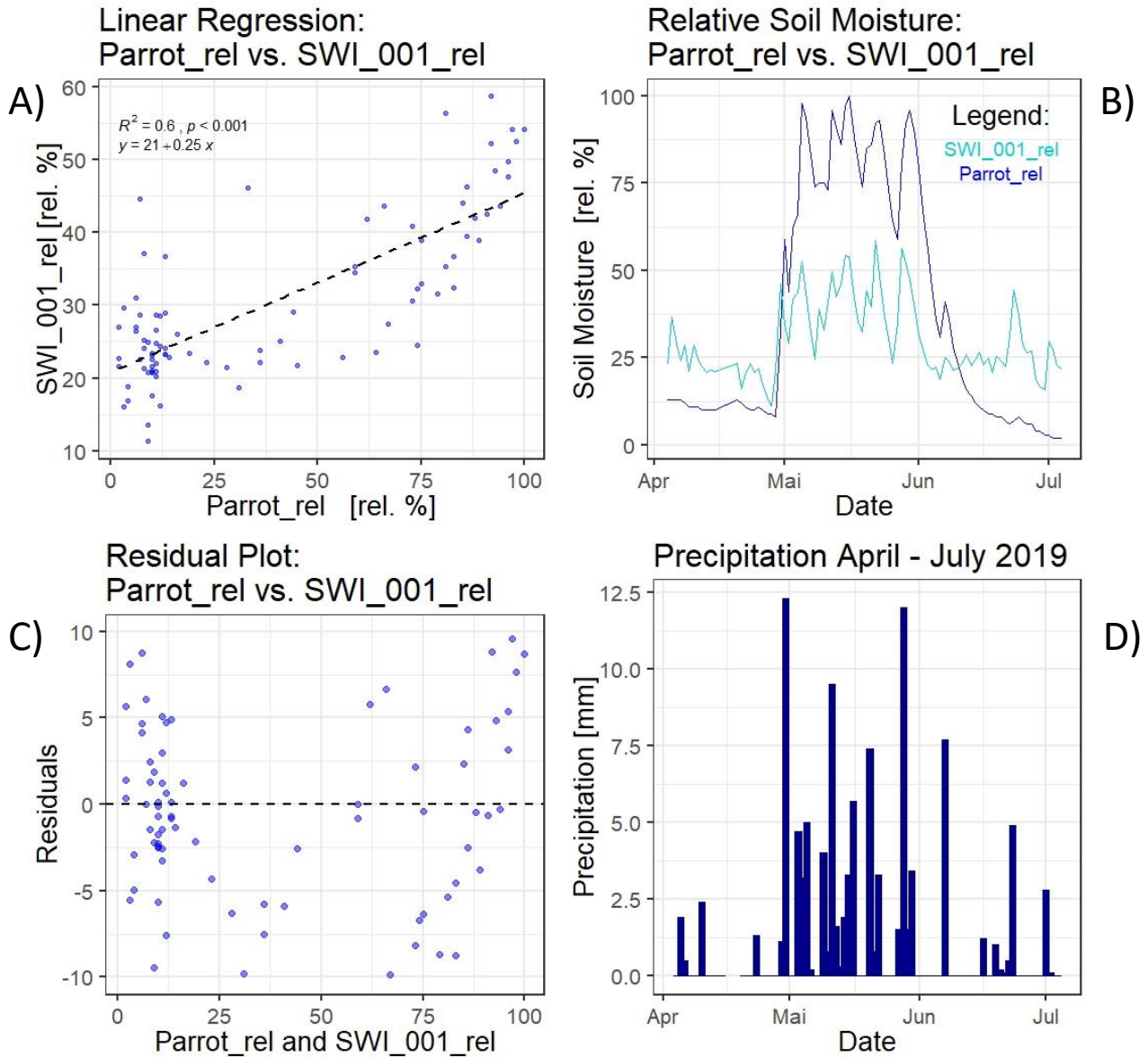


Figure 27: Statistical analysis of Parrots_rel vs. SWI_001_rel for A) linear regression, B) SM trend of Parrots and SWI_001 over time, C) residual plot and D), precipitation graph

1440 The second S1ASCAT SM product is provided for a soil depth of five cm (Annex 2). There is a correlation with an R^2 of 0.82, and the residual errors show random distribution. Compared to the S1ASCAT-SWI SM product of 0-1 cm, the SM trendline of SWI_005_rel shows a lower fluctuation, which agrees with the theory. It also shows lower values than Parrot_rel. The precipitation graph corresponds with the SM trendline of SWI_005_rel. However, the pattern is smoother compared to SWI_001. A short time delay can be detected between the actual precipitation events and the measured SWI_005_rel values according to the soil moisture storage term coming into consideration.

The third S1ASCAT SM product, taken for comparison, is SWI_010_rel, which reflects the SM up to ten cm soil depth (Annex 3). The correlation with Parrot_rel has an R^2 of 0.64, and random distribution is given. The SM trendline follows the precipitation pattern with a time lag. Nevertheless, it is smoother than the previous SWI products and has a lower response towards changes in precipitation.

1450 The second satellite data compared was the **SMAP** SM product (Annex 4). The analysis starts in April 2019 and ends in July 2019. However, it features only coverage through the SMAP SM product for every third day. Thus, the total amount of data obtained is lower compared to the previous S1ASCAT-SWI analysis. The R^2 received between Parrot_rel and SMAP_rel is 0.44, and the residuals presented are randomly distributed (Annex 4C). The SM trendline of the SMAP SM corresponds with a time lag during the peak with the SM trendline of Parrot_rel. The SMAP_rel observations trail behind the precipitation pattern and the Parrot_rel measurements.

The remaining S1ASCAT-SWI products in five and ten cm soil depths are analyzed and featured in the Appendix section (Annex 2 and Annex 3). The SMAP product is visualized in Annex 4 in the Appendix section.

1460

4.4.1 Comparison with simulation models (ARIS and AquaCrop)

The highest correlation achieved the analysis of Parrot_rel with the **ARIS_rel** SM output (Figure 28A-D). Figure 28A shows a correlation with an R^2 of 0.92. Some elevated errors are presented in Figure 28C. These relative errors accumulate predominantly in the lower and higher range of the measurements demonstrated in the residual plot.

The course of Parrot_rel and ARIS_rel is well matched, with peaks during intense precipitation events (Figure 28B and D). During drier periods, the ARIS data shows slightly lower SM values. However, during moderate to high precipitation events, its SM corresponds well to the SM trendline of Parrots_rel. ARIS's SM relates well to the overall precipitation events according to Figure 28D too.

1470

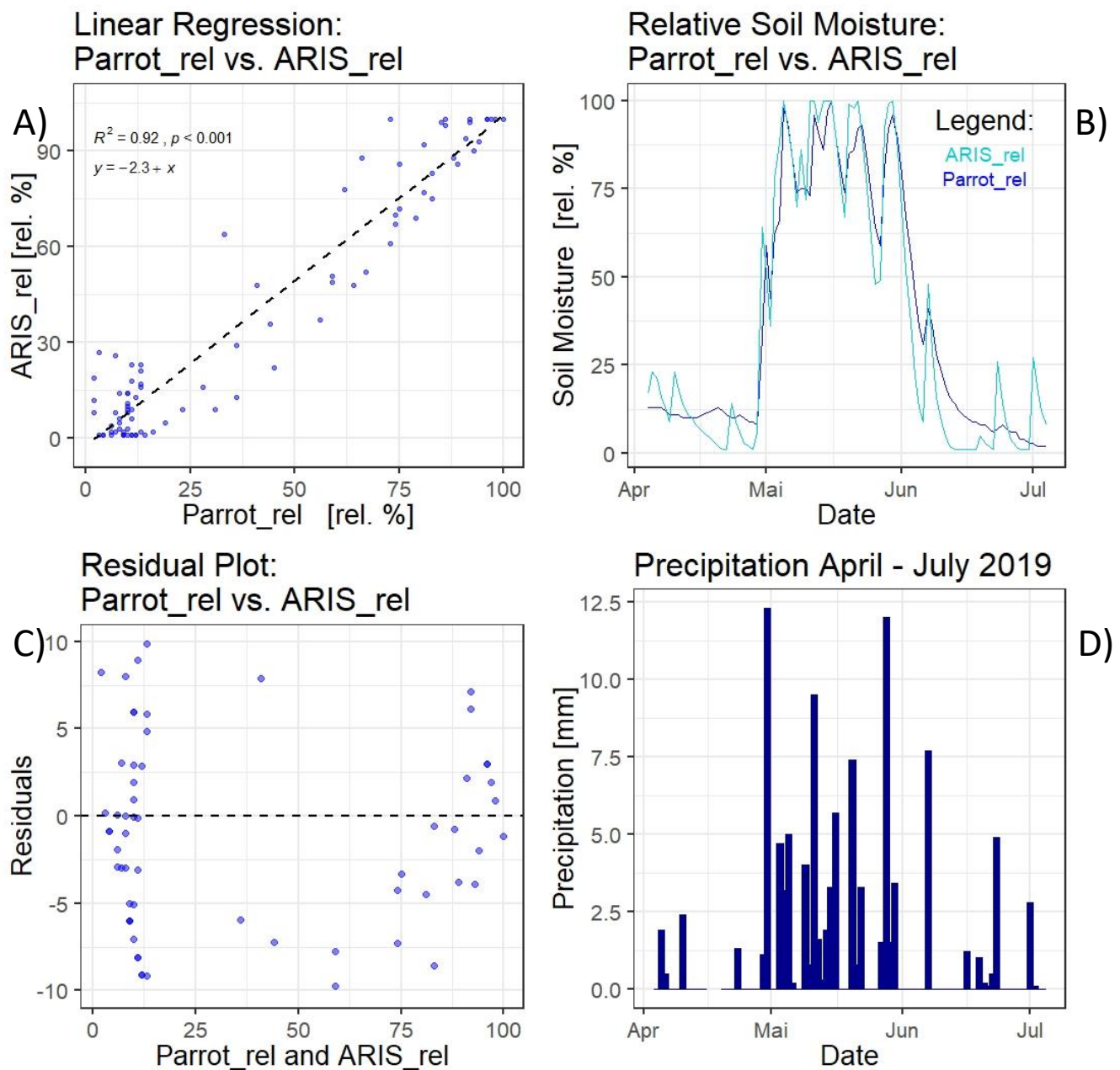


Figure 28: Statistical analysis of Parrots_rel vs. ARIS_rel_rel for A) linear regression, B) SM trend of Parrots and ARIS_rel over time, C) residual plot, and D), precipitation graph

Another central part of the results section constitutes simulated **AquaCrop** time series, compared with the Parrot in-situ SM measurements, regarding the different soil types. All three soil types (B1, B2, B3) in two different soil depths (five and 15 cm) were compared with the Parrot measurements. In this case, the comparison was based on the absolute soil moisture content in % vol.

Figure 29A-D presents the comparison between the ‘Parrot’ sensors located on soil type B1 and the AquaCrop model of soil type B1 for a soil depth of five cm. According to the linear regression shown in Figure 29A, the R^2 is 0.63. The residuals are visualized in Figure 29C. The observed SM response concerning the precipitation pattern is shown in Figure 29D. Especially during moderate to strong precipitation events, vital feedback in the SM trend can be detected.

The FC and PWP applied in AquaCrop are presented in the SM trendline of Figure 29B.

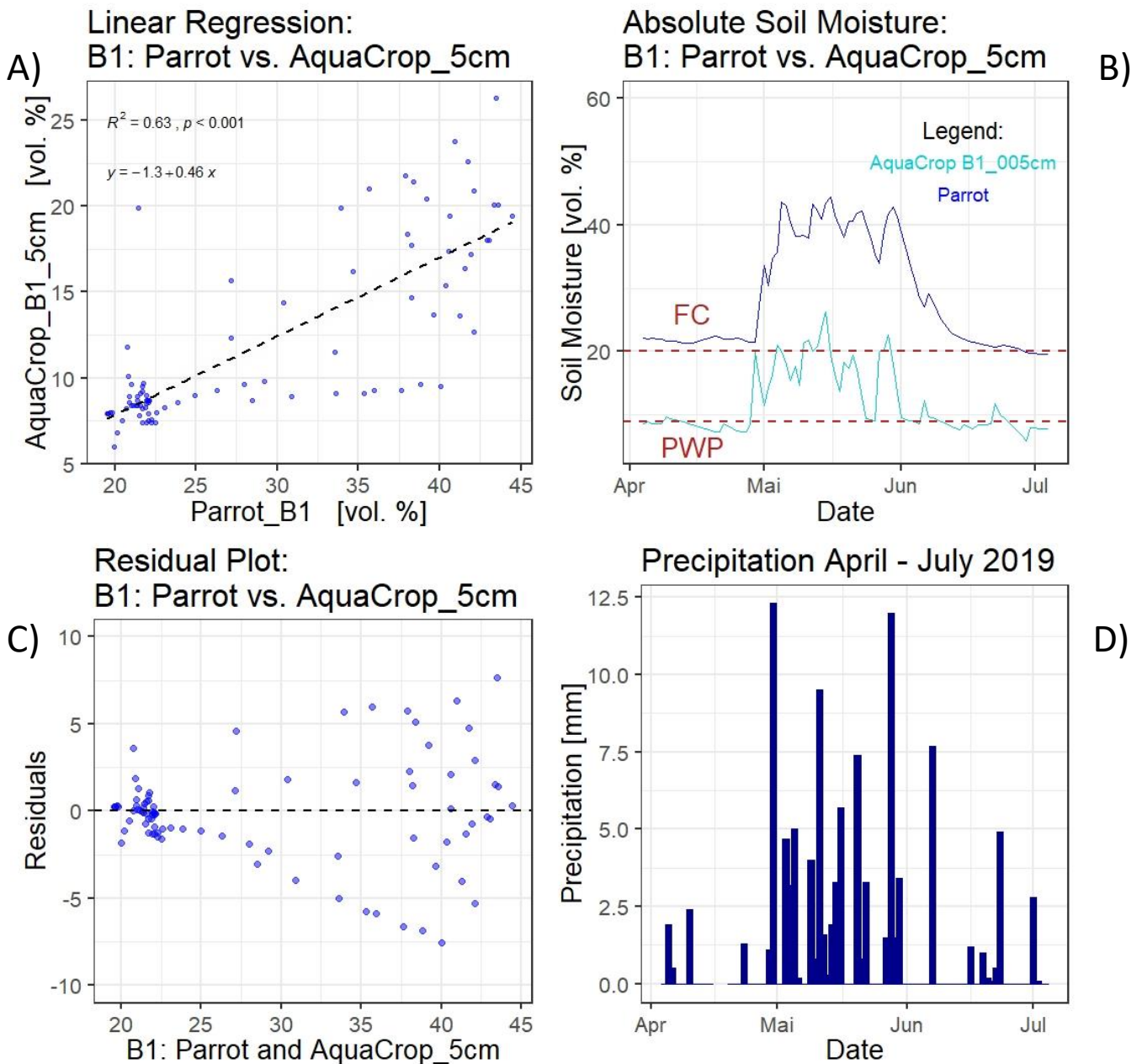


Figure 29: Statistical analysis of Parrots vs. AquaCrop_B1_5cm for A) linear regression, B) SM trend of Parrots and AquaCrop_B1_5cm over time, C) residual plot, and D), precipitation graph

The R^2 of the AquaCrop simulation for the soil depth of 15 cm is 0.43 (Annex 5). The SM trendline of the simulation reacts slow, compared to the precipitation graph. Thus, the precipitation feedback of the AquaCrop simulation in 15 cm soil depth is smaller than measured, indicating that the FC and PWP in the model setting do not match the reality (in contrast to ARIS).

1490

Soil type B2 and type B3, with respective soil depths of five to 15 cm, are statistically analyzed with linear regression (Annex 6 through Annex 9)

Soil type B3 with the soil depth of 15 cm was dismissed for further analysis because of perfect fitting data and a lack of random distribution (Annex 9).

4.4.2 Summary of the year 2019 analysis

An overview of the independent variable of calibrated Parrot and all dependent variable trendlines with its absolute SM in % vol. is presented in Figure 30A-L (see chapter: 3.6.1 Preparation of in-situ, satellite, and simulation data for comparison; and 3.6.4 Transformation of satellite and simulation data based on soil porosity). Figure 30A-C present the S1ASCAT SM products and show an effect of decreased dependency on precipitation (Figure 30L) concerning volumetric SM [%].

1500

The second row provides the absolute SM featuring ARIS (Figure 30D), SMAP (Figure 30E), and the AquaCrop simulation of soil type B1 in five cm depth (Figure 30F). The last two rows visualize the AquaCrop simulation of soil type B1 in 15 cm and B2 in five- and 15 cm soil depths (Figure 30H-I).

Finally, the AquaCrop simulation of soil type B3 is presented in Figure 30J-K with five and 15 cm respective soil depths. For individual interpretation, Figure 30L provides the precipitation course from April to July 2019. Based on the mean TDR measurements, all SM trendlines have the FC and PWP incorporated to assess the trendlines visually. It is visible that shallow soil depth seems to foster higher fluctuation and levels in SM regarding precipitation occurrence. In Figure 30A-C, it is demonstrated that the S1ASCAT-SWI SM levels decrease with increasing soil depth and trail little behind the precipitation emergence. It can be assumed that the deeper the soil layer, the better and constant the SM regime is, with less fluctuation and a smoother trendline. However, the S1ASCAT-SWI products show a similar offset in SM estimation like the AquaCrop simulations compared with the calibrated Parrot reference measurements. This circumstance is also indicated in the statistical variable of the MBE calculation. Both the S1ASCAT-SWI products and the AquaCrop simulations underestimate SM compared with the calibrated Parrot measurements.

1510

1520

In contrast, the ARIS trendline in Figure 30D aligns nicely with the Parrot SM measurements, also for absolute SM. Both methods, ARIS and S1ASCAT-SWI, are prone to high fluctuations in precipitation patterns and thus fit well.

It can be seen that the PWP and FC levels applied for a sandy soil type in AquaCrop do not match the reality, which is approximately represented by the lowest and highest absolute SM values of the calibrated Parrot sensor.

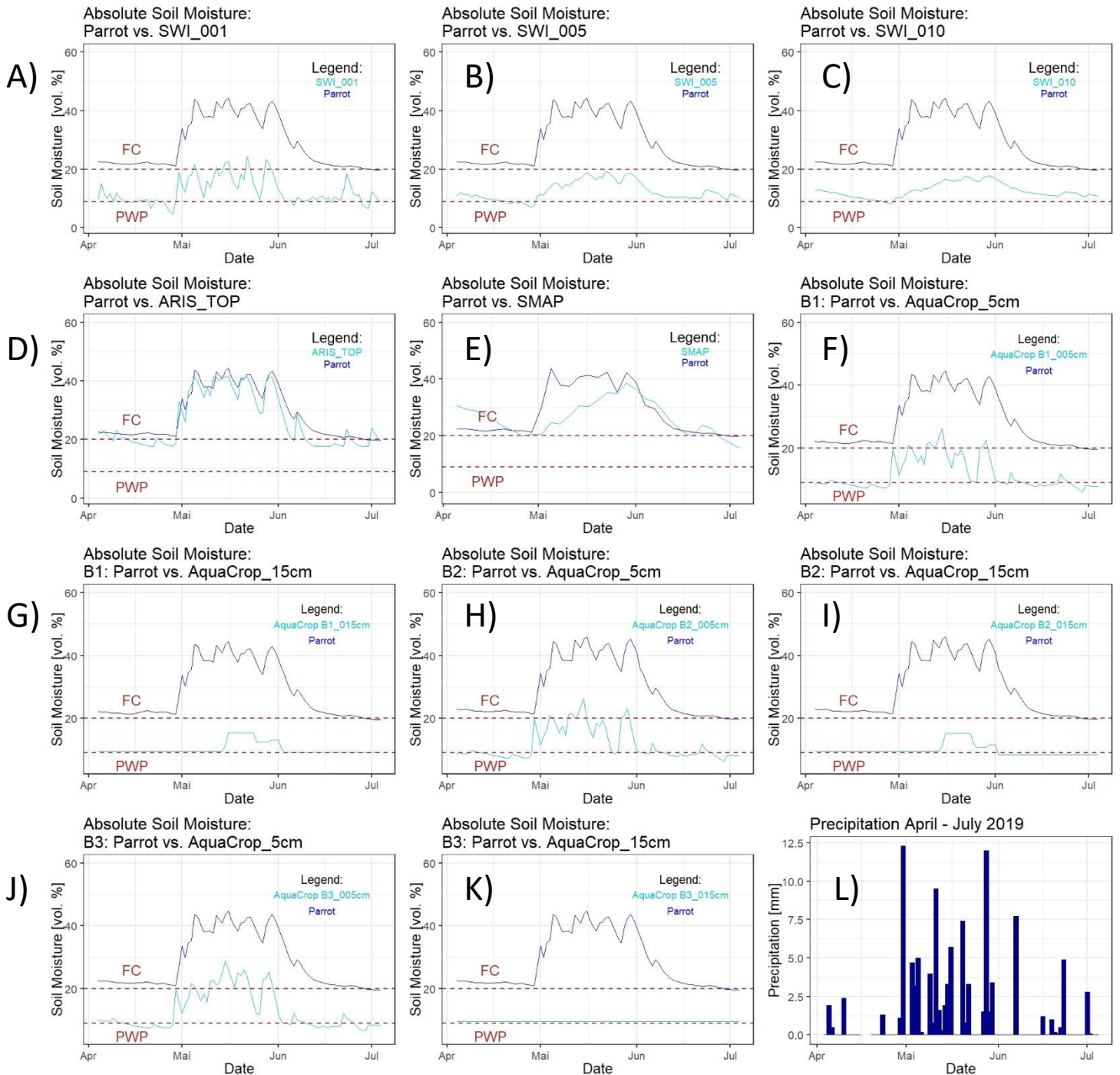
In Figure 30E, the SMAP product demonstrates a discrepancy or time lag of the SM estimation. However, the overall estimation seems accurate according to the Parrot measurements in the respective time frame.

1530

Figure 30F-K demonstrates the remaining AquaCrop simulations for the respective soil depths and soil types B1, B2, and B3. The upper soil layer provides a good response regarding the precipitation pattern. However, there is a bias on the SM level due to the inadequate setting of FC and PWP (which were default values in the AquaCrop software for the respective soil types). Nevertheless, with an increasing soil depth of the AquaCrop simulation, a lower

Evaluation of multi-level methodical soil moisture measurements

response after precipitation events occurs, which agrees with the other methods. SM remains longer within the deeper layers of soil, respectively.



1540 Figure 30: Trendline comparison of Parrot and A) SWI_001, B) SWI_005, C) SWI_010, D) ARIS, E) SMAP, F) AquaCrop_B1_5cm, G) AquaCrop_B1_15cm, H) AquaCrop_B2_5cm, I) AquaCrop_B2_15cm, J) AquaCrop_B3_5cm, K) AquaCrop_B4_15cm, and L) Precipitation graph

4.4.3 Overview of R² and RMSE

In the following Table 2, statistical analyses for the compared methods are presented. They are presented for the relative soil moisture changes (indicated as Relative Soil Saturation) and absolute soil moisture changes (indicated as Absolute Soil Water Content), with the RMSE, R², MBE, p-value, and the normal distribution. The lower the RMSE value, the less residual variance was observed in the linear regression analysis. However, it is essential to mention that the ARIS or SWI_001 data has higher SM fluctuation after precipitation events. Thus, the RMSE is higher compared to some sensors less prone to precipitation. Nonetheless, for final decision-making, the RMSE, of course, is a starting point as a good indicator to assess further management strategies.

Overall the MBE shows that SM of the S1ASCAT-SWI estimations and the AquaCrop simulation estimations are underestimated compared with the Parrot measurements. However, AquaCrop deviates more than the S1ASCAT-SWI products. ARIS shows the best estimation outcome with an MBE of 0.95 compared with the reference of Parrot. Based on the MBE, SMAP estimations are highly overestimated compared with the reference measurement.

The normal distribution's lower or upper boundary observations result in a flattened out peak (100 %) and bottom (0 %) of relative SM range observations.

Nevertheless, the ARIS data was deemed normally distributed. The same applies to the SMAP data. However, only a low volume of observations for the SMAP data was available for the respective period. One variable was dismissed due to a perfect fit and missing normal distribution (Annex 9C). Thus, the output of Parrot_B3 vs. AquaCrop_B3_15cm could not be calculated with the underlying software of R.

Table 2: Summary of the sensor comparison analysis 2019

Relative Soil Saturation [%]	RMSE	R ²	MBE	p-value < 0.001	normal distribution
Parrot vs. SWI_001	6.96	0.60	-8.38	YES	YES
Parrot vs. SWI_005	3.30	0.82	-8.17	YES	YES
Parrot vs. SWI_010	3.59	0.64	-7.84	YES	YES
Parrot vs. ARIS	10.72	0.92	-0.95	YES	YES, upper and lower boundary
Parrot vs. SMAP	10.77	0.44	26.26	YES	little observations, upper and lower boundary
Absolute Soil Water Content [m ³ /m ³]					
Parrot B1 vs. B1_5cm	3.08	0.63	-16.89	YES	YES
Parrot B1 vs. B1_15cm	1.45	0.43	-18.38	YES	YES
Parrot_B2 vs. B2_5cm	3.13	0.61	-17.43	YES	YES
Parrot_B2 vs. B2_15cm	1.49	0.44	-19.45	YES	YES
Parrot_B3 vs. B3_5cm	3.25	0.73	-15.81	YES	YES
Parrot_B3 vs. B3_15cm	-	-	-19.35	Perfect Fit	NO

1570 4.5 Temporal correlation analysis 2020 with satellite products and models

The timeframe for observations lasted from October 2019 to July 2020. The **S1ASCAT-SWI** SM product in 0-1 cm soil depth was regressed against the independent variable of the weather station FDR sensor in 20 cm soil depth (Figure 31). According to the linear regression statistics conducted, Figure 31A shows an R^2 of 0.52. The residual errors of the following Figures were checked for normal distribution. A residual-plot summary is presented in Annex 19G in the Appendix section.

1580 Figure 31C visualizes the correlation of the independent variable WS_020cm_rel compared with the dependent variable of SWI_001_rel. The SM trendline response matches the precipitation pattern (Figure 31B), which shows a similar sequence of peaks and troughs. A lower increase in SM can be observed during the summer months, starting in April towards July, even though precipitation events are more potent and enduring due to much higher evaporation rates of the canopy.

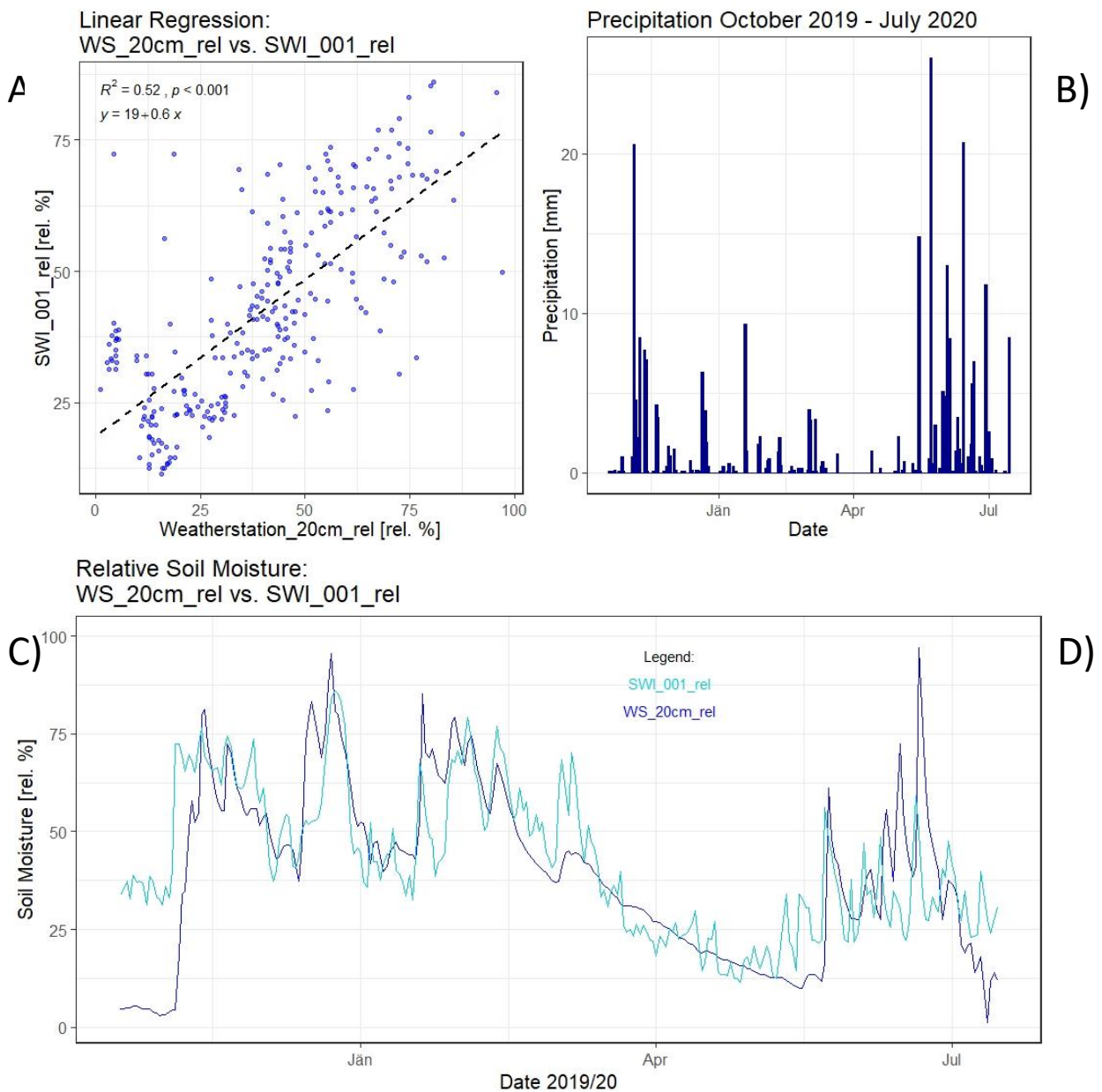


Figure 31: Statistical analysis of WS_20cm_rel and SWI_001_rel for A) linear regression, B) precipitation graph, and C) trend of WS_20cm_rel and SWI_001_rel

A lower fluctuation in SM response is shown in the data of the weather station WS_20cm_rel and thus, aligns well with the satellite data of S1ASCAT-SWI.

1590 In Annex 10, the correlation analysis for the S1ASCAT SWI_005 variable is demonstrated and features a soil depth of 0-5 cm. The observed R^2 is 0.61, and the SM response matches the precipitation pattern. Starting in October 2019, the SM trendline of SWI_005_rel compared with the variable WS_20cm_rel shows a similar correlation. Fewer peaks and troughs in the SM values can be observed compared to Figure 31, with the SWI_001_rel as a variable.

The final S1ASCAT-SWI product is presented in Annex 11, and, according to the correlation analysis, it presents an R^2 of 0.57. Both the trendline and the precipitation graphs align, and the S1ASCAT-SWI products in lower soil depths are smoother in SM estimation and lag little in their visualization after precipitation events.

1600 The second satellite remote sensing SM data is the **SMAP_rel** SM product which was regressed with the independent variable of **WS_020_rel** (Annex 12). The observed R^2 is 0.32. Compared to the SMAP_rel observations for 2019, the time series during the vegetation period of 2020 provides significantly more observations. The two primary peaks in the SMAP_rel data trail behind the in-situ sensor data during winter. Its peaks and troughs are correlating better in the summer period. However, during winter, an overestimation of SM with a significant lag was observed. Especially during February and March, a significant peak of the SMAP_rel product was observed (unknown reason).

4.5.1 Comparison of simulation models (ARIS and AquaCrop)

Figure 32 presents the ARIS simulation for relative SM (see Figure 33 for absolute SM comparison), where an R^2 of 0.55 was estimated. The random distribution is presented in Annex 19J, featuring the trendlines. The ARIS data responds to the precipitation pattern well (Figure 32B), especially during the growing season.

1610 There is a high fluctuation of SM during the summer month for the ARIS data, correlating with the weather station's sensor. However, with a bit higher variability range. This circumstance is probably caused by local deviation of soil water holding capacity from the ARIS setting. During the early vegetation period starting in October 2019, the SM product of ARIS is mostly at FC overestimating SM compared to the in-situ sensor. A biased crop factor probably causes this behavior for evapotranspiration for the winter dormancy period in ARIS.

According to precipitation pattern and season, the ARIS data strongly reacts to rain fluctuations with peaks and troughs, reflecting depletion of SM close to wilting point or vice versa an increase towards FC. Especially in April 2020, the ARIS dataset visualizes a low volume in precipitation. After this dry phase, intense precipitation events from May onward increase the highly fluctuating response of the ARIS data.

1620

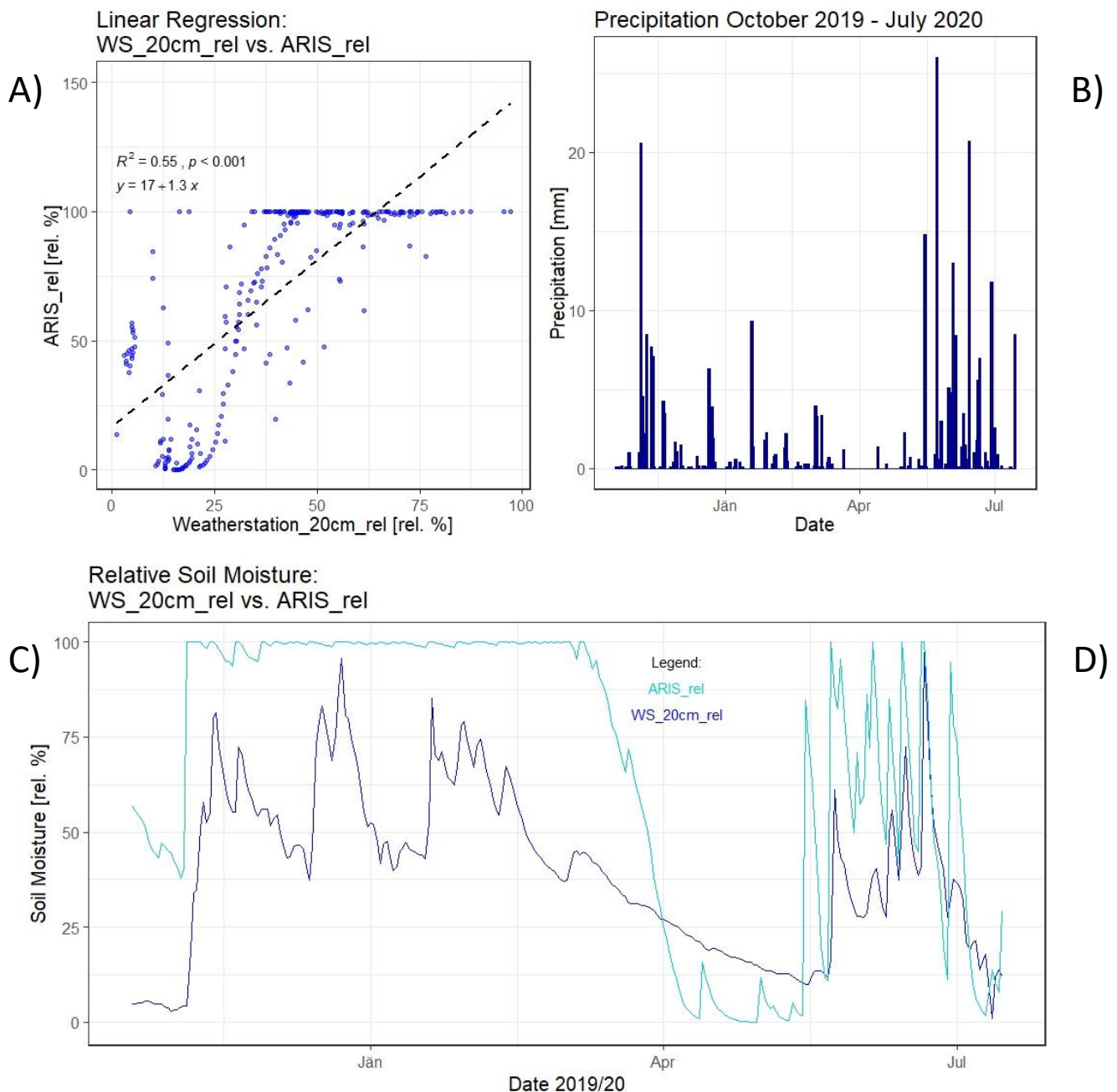


Figure 32: Statistical analysis of WS_20cm_rel and ARIS_rel for A) linear regression, B) precipitation graph, and C) trend of WS_20cm_rel and ARIS_rel

The **AquaCrop B1_5cm** simulation result of absolute SM was likewise regressed with the variable WS_20cm (Annex 13). In that case, an R^2 of 0.49 is estimated. According to the SM trendlines of the sensors, there is a slight offset. The independent variable WS_020 achieves higher SM observations compared to the AquaCrop B1_5cm observations. The peaks and troughs are respectably ordered according to the precipitation pattern and similar intensity. The absolute SM trendline of WS_020 and B1_005 has a high response concerning precipitation events if looked closely.

1630

The variable of AquaCrop B1_15cm correlates with an R^2 of 0.57 to the WS_20cm variable (Annex 14). According to the precipitation pattern, the SM trendline is smoother with no peaks. Instead, a leveling of SM at FC or PWP is observed. The 15 cm soil depth in the AquaCrop simulation has very low fluctuation in SM response. The soil types B2 and B3, with their respective soil depths of five to 15 cm, were likewise statistically analyzed with linear

regression with the independent variable WS_20cm, respectively. Due to similar results, Annex 15 and Annex 16 feature soil type B2 in five and 15 cm soil depth with R^2 of 0.49 and 0.57. Annex 17 and Annex 18 likewise show the two soil depths in five and 15 cm of soil type B3 with values of R^2 of 0.60 and 0.54.

1640 All residual plots are presented in Annex 19. The best random distribution is achieved by the satellite estimations of S1ASCAT_SWI and SMAP. The ARIS residual distribution plateaus during the winter period and biases the random distribution. The same applies to the AquaCrop simulation estimations. Especially the AquaCrop data for 15cm soil has a plateau in maximum SM and minimum SM estimations resulting in a biased residual plot, respectively.

4.5.2 Summary of year 2020 analysis

An overview of the relationship between the independent variable of WS_20cm and all dependent variable trendlines with its absolute SM % vol is presented in Figure 33. As calibrated Parrot values were not available for 2020, the WS_20cm sensor was used as the reference, which proved to be a good proxy for the Parrots in 2019 (see chapter: 4.3 Validation of in-situ 'Parrot' sensors).

1650 Figure 33A-C present the S1ASCAT-SWI SM products and show an effect of reduced response to precipitation (Figure 33L) with increasing soil depths concerning volumetric SM [%].

The second row provides the absolute SM featuring ARIS in Figure 33D, SMAP in Figure 33E, and the AquaCrop simulation of soil type B1 in five cm depth in Figure 33F. The last two rows visualize the AquaCrop simulation of soil type B1 in 15 cm in Figure 33G, and B2 in five and 15 cm in Figure 33H-I.

1660 Finally, the AquaCrop simulation of soil type B3 in five and 15 cm is presented in Figure 33J-K. For individual interpretation, Figure 33L provides the precipitation graph of the vegetation period. The FC and PWP for the site based on the TDR measurements are indicated in the dotted lines. The S1ASCAT-SWI products in Figure 33A-C show a similar response of SM with increasing depths as in the previous chapter for the Parrot sensors in 2019. Overall, the SM feedback correlates nicely but smoothens with depth. ARIS overestimates the SM more than in 2019, as demonstrated in Figure 33D. The potential reasons were mentioned there, but further, we have to consider that for 2020, in contrast to 2019, just a single measurement point from the field is used as the reference, rather than an average on measurement points which adds uncertainty.

1670 Similar results were obtained for the SMAP product (Figure 33D). It seems that SMAP overestimates the SM regime in general during winter, too (as the ARIS model). However, during the summer period, SM estimations are underestimated if compared with the weather station sensor. The AquaCrop simulations fit best for the top soil layer in five cm soil depth to the WS_20cm and to the level of FC and PWP for that single point. The five cm soil depth has much higher fluctuations, responds differently, and is more prone to precipitation events than the 15 cm simulation data. Soil type B3 behaves differently during winter regarding SM estimation, related to the texture and structure, probably because the B3 soil characteristics do not meet the measurement point soil characteristics.

The MBE of the vegetation period 2020 shows a lower over- and underestimation of the S1ASCAT-SWI products and the AquaCrop simulations. This circumstance is also visible in Figure 33A-C and F-K with its closer correlating trendline plots.

The same applies to the SMAP product with overestimations of SM and a higher deviation in measurements.

1680

Evaluation of multi-level methodical soil moisture measurements

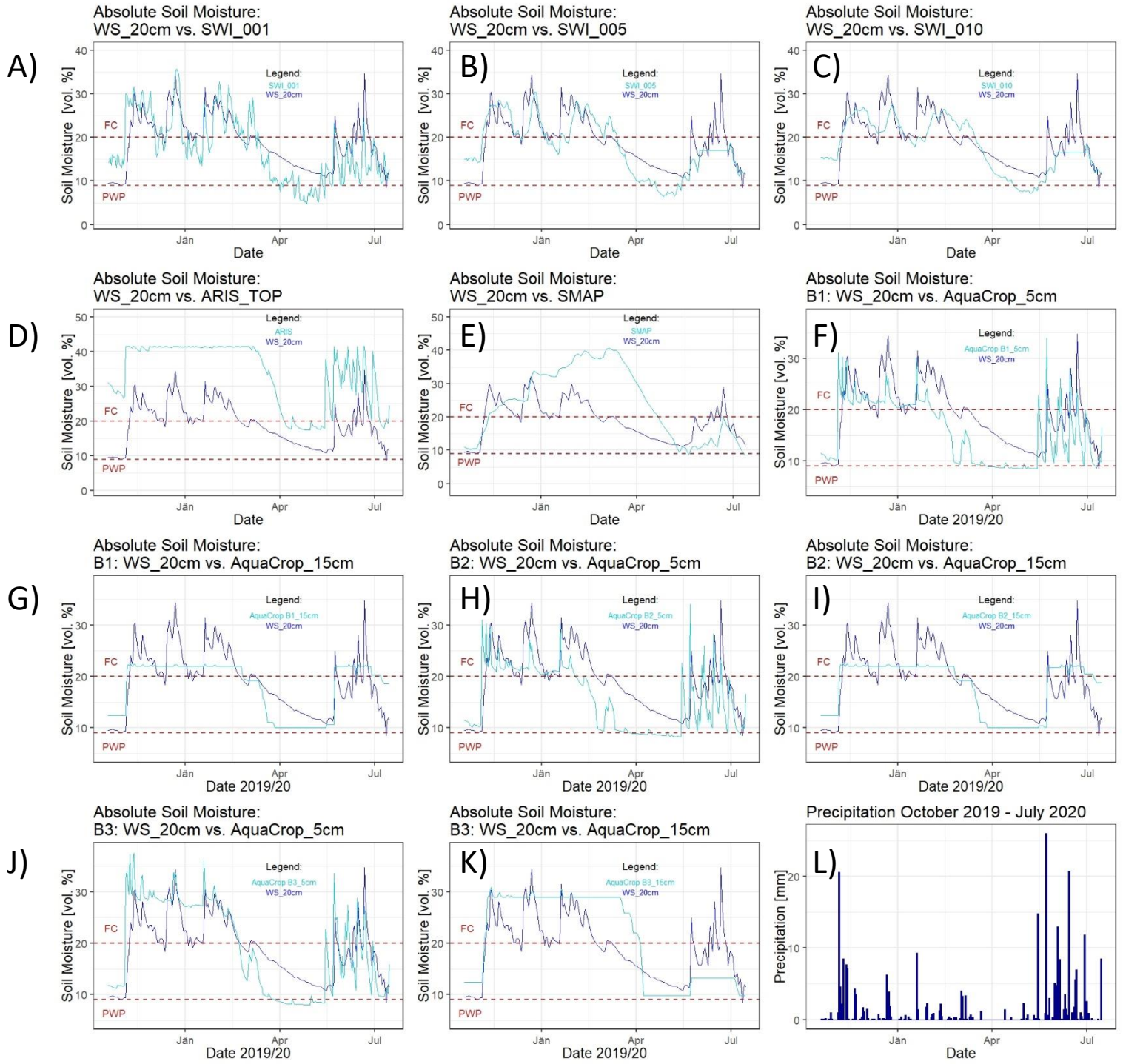


Figure 33: Trendline comparison of Parrot and A) SWI_001, B) SWI_005, C) SWI_010, D) ARIS, E) SMAP, F) AquaCrop_B1_5cm, G) AquaCrop_B1_15cm, H) AquaCrop_B2_5cm, I) AquaCrop_B2_15cm, J) AquaCrop_B3_5cm, K) AquaCrop_B4_15cm, and L) Precipitation graph

4.5.3 Overview of R² and RMSE

In Table 3, the sensor's statistical analysis of the compared methods for the relative soil moisture changes (indicated as Relative Soil Saturation) and absolute soil moisture changes (indicated as Absolute Soil Water Content) is presented. It comprises all R² values, the p-values defined as <0.001, MBE, and the RMSE are presented. The normal distribution is presented in the Appendix section Annex 19.

1690

The lack of normal distribution in the AquaCrop data is related to the low sensitivity of the SM in the soil depth of 15 cm and a stepwise change of SM, which could be based on a software algorithm characteristic. The low volume of variation and persistent SM in the respective soil depth of 15 cm was the reason for such plateaus of mainly maximum SM estimations and minimum SM observations. Thus, they set an upper and lower boundary in the data.

ARIS shows somehow similar behavior, with less sensitivity and positive bias of SM, especially during winter when it comes near the cutting effect of FC. However, below FC and during the growing period, the response improved compared to the in-situ sensor. The reason for this behavior of ARIS lies in an inadequate KC factor for evapotranspiration during winter. It resulted in a high volume of simulated values for the RSS, causing a clustering in the scattering of the variance in residuals (Annex 19). If looking at the ARIS and SMAP relative SM (RSS) results, the RMSE analysis based on the variable WS_20cm is unsatisfactory. However, this is related to the high scattering of the residuals. In the case of ARIS, it is mainly based on the deviation during the winter period. Vice versa, the low volume of residual scattering for the AquaCrop simulations causes better RMSE values than the S1ASCAT-SWI and the ARIS data (Annex 19). However, based on absolute SM values, the span is reduced to a range of about 0-60%. In contrast, the RSS span ranges between 0-100%.

1700

In Table 3, the MBE presented shows an overestimation of the S1ASCAT-SWI products. However, especially the SMAP product features an overestimation. The overrepresentation of the MBE in the ARIS SM data originates in the deviation during the winter period, respectively. Likewise, the AquaCrop simulation estimations are over- and underestimating the SM data, dependent on the soil type, compared with the FDR Met-station, indicated in the MBE value. In general, the lower over- and underestimations in MBE compared to 2019 are related to fewer deviations in the mean of the observations (FDR Met-station) vs. predictions (S1ASCAT-SWI and AquaCrop).

1710

Like for the year 2019, in 2020, the normal distribution's lower or upper boundary observations result in a flattened out peak (100 %) and bottom (0 %) of relative SM range observations.

Table 3: Summary of the comparison analysis 2020

Relative Soil Saturation [%]	RMSE	R ²	MBE	p-value < 0.001	normal distribution
WS_20cm vs. SWI_001	12.48	0.52	2.63	YES	YES
WS_20cm vs. SWI_005	9.57	0.61	3.57	YES	YES
WS_20cm vs. SWI_010	9.15	0.57	3.64	YES	YES
WS_20cm vs. ARIS	25.07	0.55	28.24	YES	high scattering with min/max restrictions
WS_20m vs. SMAP	21.14	0.32	18.67	YES	YES, but high scattering
Absolute Soil Water Content [m ³ /m ³]					
WS_20cm vs. B1_005	4.35	0.49	-3.29	YES	YES, but lower boundary min
WS_20cm vs. B1_015	3.32	0.57	-0.96	YES	upper/lower boundary
WS_20cm vs. B2_005	4.36	0.49	-3.32	YES	YES, but lower boundary min
WS_20cm vs. B2_015	3.33	0.57	-0.98	YES	upper/lower boundary
WS_20cm vs. B3_005	5.54	0.60	0.26	YES	YES, but lower boundary min
WS_20cm vs. B3_015	5.77	0.54	1.93	YES	upper/lower boundary

1720

4.6 Temporal correlation analysis 2018 with satellite products and models

For the vegetation period in 2018, there was no reference in-situ sensor data available. Thus, the ARIS SM product was used as the independent variable, as it was proved to fit reasonably well in compared to the spatial mean Parrot in-situ measurements in 2019. For better comprehension and a more precise overview, only selected Figures are presented.

The dependent variables for the analysis in 2018 are the two **S1ASCAT-SWI** SM products, the SMAP product, and the simulation results from AquaCrop. Higher peak fluctuation of the ARIS product is connected to a strong response towards precipitation and a potential bias of water-holding capacity and FC and PWP setting in the ARIS simulation. This fluctuation effect is visually boosted by the short observation interval from April to July.

1730

Figure 34 presents the analysis of ARIS_rel with the dependent variable of SWI_001_rel. Figure 34A reveals an R^2 of 0.69. Next, the residuals are presented in Figure 34C and the trendline is visualized in Figure 34B. Figure 34D presents the precipitation graph. Both SM trendlines show a dependency on precipitation. However, ARIS is fluctuating higher than the S1ASCAT SWI_001_rel estimation, as it was characteristic behavior in the other investigation years.

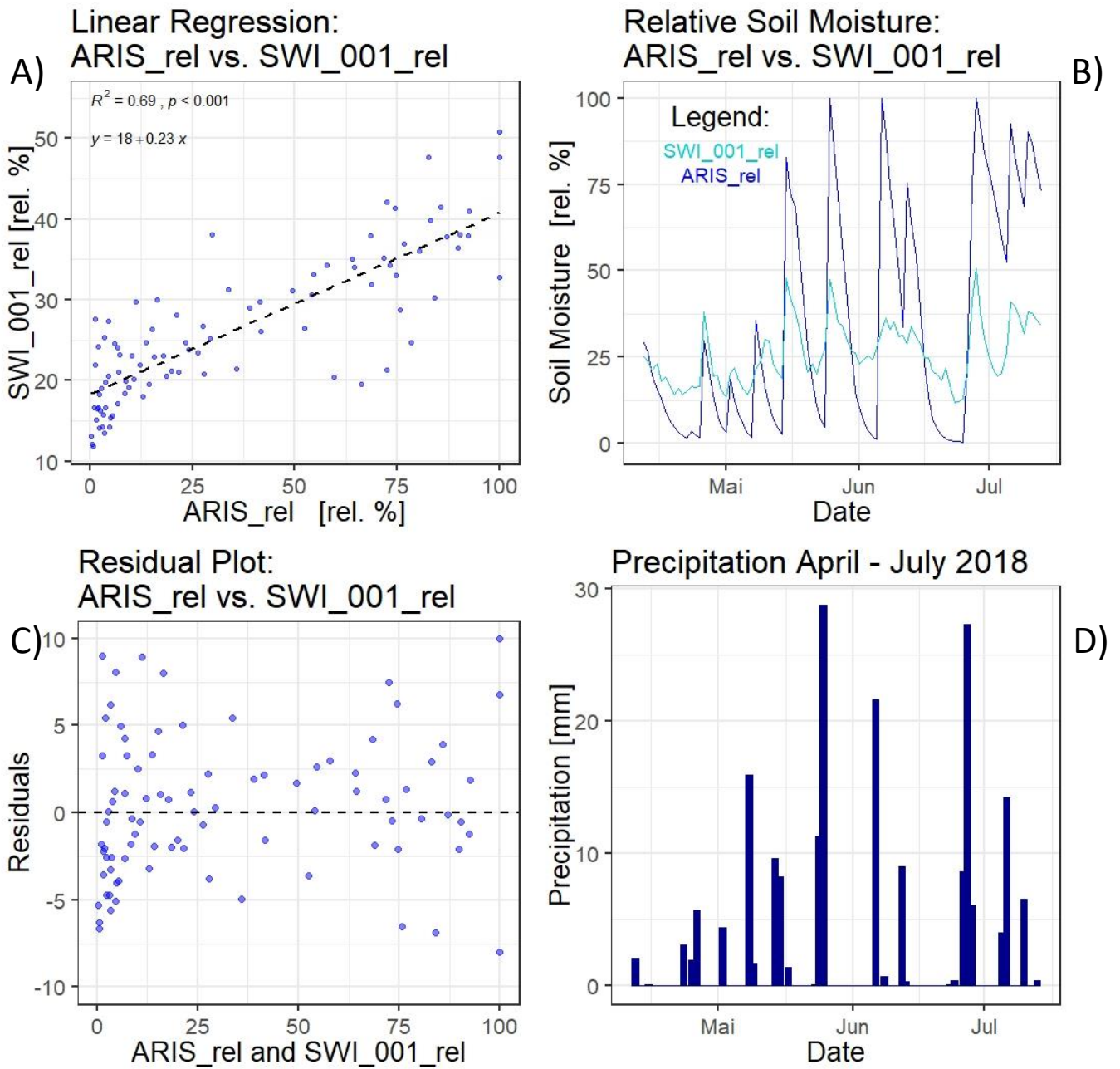


Figure 34: Statistical analysis of ARIS_rel vs. SWI_001_rel for A) linear regression, B) SM trend of ARIS_rel and SWI_001_rel over time, C) residual plot, and D), precipitation graph

1740

The second S1ASCAT-SWI product reflects SM for a 0-10 cm depth with an R^2 value of 0.33 and a normal distribution (Annex 20). Similar behavior is observed when checking the trendline of SM. A relatively smooth trend of the SWI_010_rel product faces the high fluctuating ARIS data, also in that soil depth.

1750 The second satellite sensor product compared was the **SMAP** product with an R^2 of 0.15 and a normal distribution (Annex 21). There is an exceedingly low correlation due to the time lag of the SMAP SM product, which was also evident in the other two years. The SMAP trendline over the short period from April to July has a negative movement compared to the ARIS data's high fluctuating positive SM response.

1760 The **AquaCrop** simulation data correlate little with the ARIS simulation results, too. Especially for the level of SM rather than the variation of SM (see below). This circumstance could lie in differences, as already mentioned in the analysis of the two other years. Soil types B1 and B2 in five and 15 cm soil depth have R^2 values of 0.16 and lower (Annex 22, Annex 23, Annex 24, and Annex 25). The residuals are normally distributed. The soil type B3, compared with the ARIS model, achieves an R^2 of 0.15 (Annex 26). In comparison, soil type B3 has a better correlation in the soil depth of 15 cm and an R^2 of 0.36 (Annex 27). However, the normal distribution has flaws with clustering in low and high SM ranges, probably based on a software-specific characteristic of SM output at the deeper soil depth. The analysis's SM trendline courses of the AquaCrop simulations show a similar trend (fluctuation) of precipitation in five cm soil depths. There is an offset of the ARIS trendline compared to the AquaCrop simulation trendlines.

1770

As a final and competitive correlation analysis, Figure 35 shows the independent variable **SWI_001** versus the **AquaCrop simulation B2 in five cm** soil depth. In Figure 35A, the linear regression with an R^2 of 0.45 is shown. Figure 35B visualizes the SM trendline in % vol. The S1ASCAT-SWI was recalculated to absolute SM for better comparison, respectively (see chapter: 3.6.4 Transformation of satellite and simulation data based on soil porosity). Figure 35C-D shows the residual plot and the precipitation graph.

The independent variable SWI_001 was used in particular for the correlation analysis in Figure 35. It shows how the satellite data of S1ASCAT-SWI performs compared to the simulation data of ARIS in the previous examples. As there is lower fluctuation in the S1ASCAT-SWI data, a bias of SM holding potential of ARIS is possible. According to the SM trendline graph, the top layer of the AquaCrop simulation data and the top layer of the S1ASCAT-SWI product seem to match well.

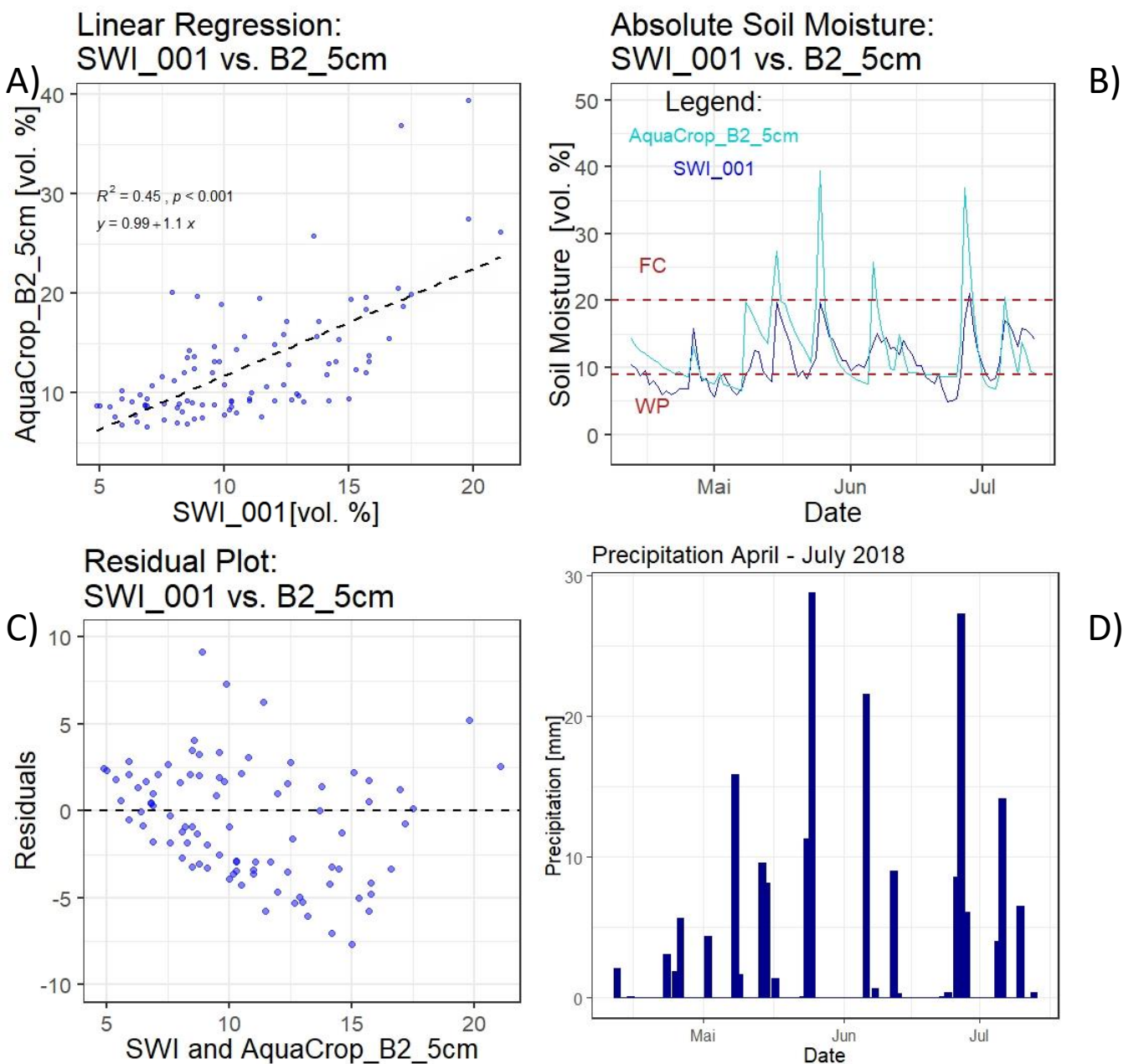


Figure 35: Statistical analysis of SWI_001 vs. AquaCrop_B2_5cm for A) linear regression, B) SM trend of SWI_001 and AquaCrop_B2_5cm over time, C) residual plot, and D), precipitation graph

4.6.1 Summary of year 2018 analysis

1780

In Figure 36, all trendline graphs are presented. Figure 36A-B comprises the S1ASCAT-SWI SM estimations. The individual sensor's SM units are presented in % vol. The increased precipitation volume causes the high fluctuation of the ARIS data during June and July 2018. The SMAP SM trendline is presented in Figure 36C. Figure 36D-I features the AquaCrop simulations of all three soil types B1, B2, and B3, with five and 15 cm respective soil depths.

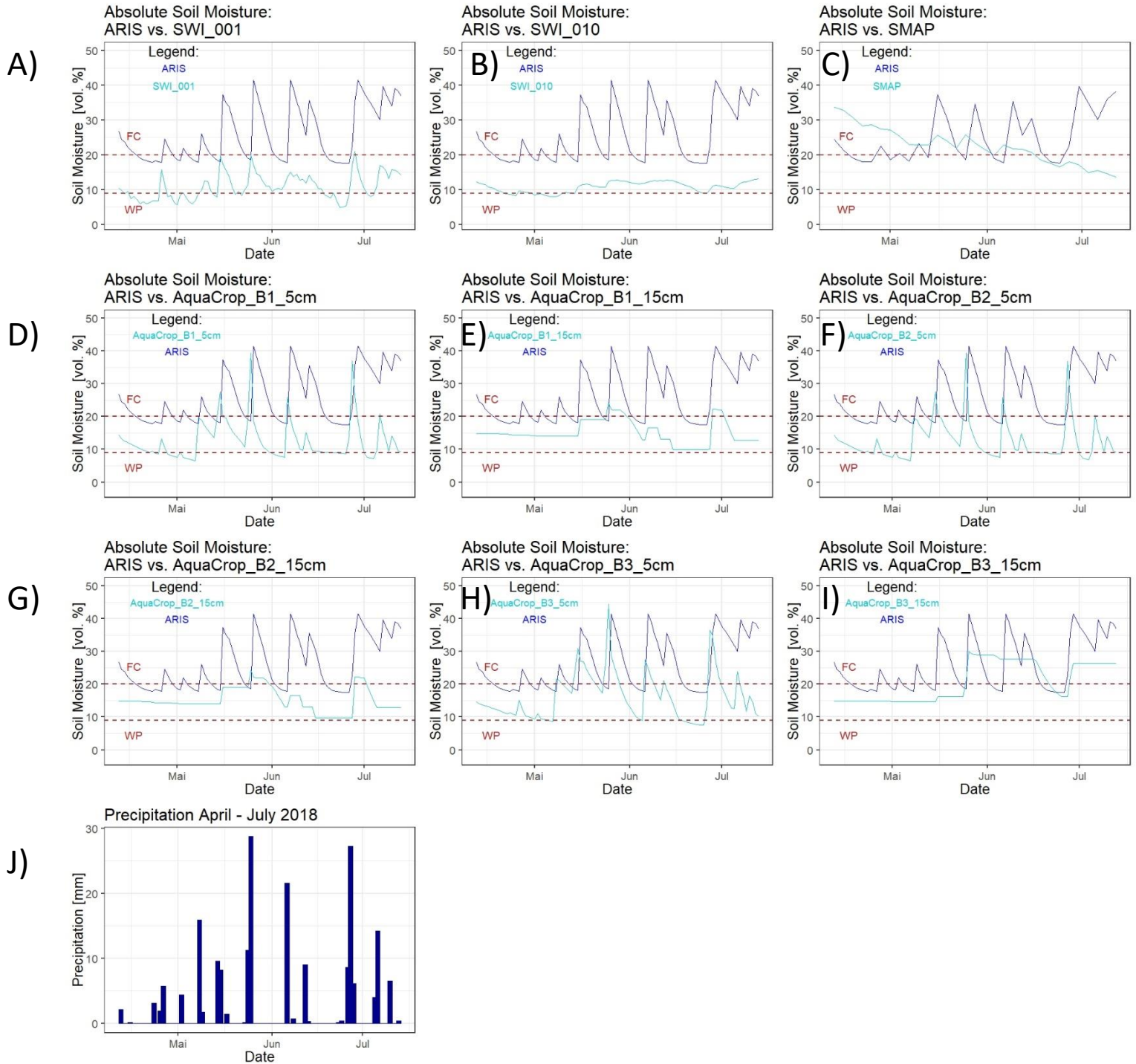


Figure 36: Trendline comparison of ARIS and A) SWI_001, B) SWI_005, C) SMAP, D) AquaCrop_B1_5cm, E) AquaCrop_B1_15cm, F) AquaCrop_B2_5cm, G) AquaCrop_B2_15cm, H) AquaCrop_B3_5cm, I) AquaCrop_B4_15cm and item J) the precipitation graph

1790

According to Figure 36, the trendlines of the upper soil layers seem to match the ARIS data better than deeper layers (e.g., AquaCrop in 15 cm soil depth and the S1ASCAT-SWI data of 0-10 cm soil depth). ARIS fluctuates higher and closely tracks and responds towards distinctive precipitation patterns. Thus, SWI_001 correlates with the ARIS data better than S1ASCAT SWI_010 or SMAP. The same applies to the AquaCrop simulations in the five cm upper soil layer compared to the 15 cm soil layer depths. The upper layers are prone to substantial variations in precipitation patterns and meteorological events resulting in a strong response in SM fluctuations. Hence they fit the course of ARIS better compared to layers less prone to fluctuations and variations.

1800

The trendline offset featured in Figure 36A-B and D-I can be explained with the statistical variable of MBE similarly. For example, the higher an over-and underestimation, indicated by the MBE variable, the higher the deviation of SM estimations in the mean of observations (ARIS) vs. predictions (S1ASCAT-SWI and AquaCrop).

4.6.2 Overview of R² and RMSE

The method comparison analysis for 2018 is presented in Table 4. According to the statistical analysis of relative SM change for ARIS_rel and SWI_010_rel, an R² of 0.33 was observed. The results for SWI_010_rel are presented in Annex 20. The SMAP_rel SM product has an R² of 0.15 (Annex 21). Likewise, the AquaCrop simulations for soil types B1, B2, and B3 with their two soil depth are featured in the Appendix section (Annex 22, Annex 23, Annex 24, Annex 25, Annex 26, and Annex 27).

1810 The simulation results of AquaCrop (absolute SM change) in the upper soil compartment do not correlate well with ARIS's independent variable. Similarly, the S1ASCAT-SWI data lacks correlation with the ARIS simulation product regarding absolute SM changes (Figure 36). However, the dependent variable SWI_001_rel has the highest correlation with ARIS_rel and thus correlates well with the ARIS simulation product regarding relative SM change (Figure 34). The higher fluctuation and exposure of SWI_001_rel than SWI_010_rel result from the difference in considered soil layer depth. The deeper the measurement, the smoother is the course of SM. The AquaCrop simulations in 15 cm soil depth have a better but still very weak correlation than the five cm soil depth.

1820 Regarding the MBE statistics, the S1ASCAT-SWI SM products are underestimating, compared with the ARIS reference estimations. SMAP is overestimating SM like in 2019 and 2020. AquaCrop underestimates the SM compared with the ARIS simulation estimations. The higher offset of the SM estimations, indicated in the trendlines of Figure 36A-K, results in a higher MBE (Table 4), as it is also presented for the data of 2019.

The S1ASCAT-SWI_001 SM and the AquaCrop B2_005 estimation correlates well with the absolute SM change.

However, the trendline shows that both methods underestimate the overall SM during precipitation events and the overall time of observation (Figure 35B and D) compared to ARIS. It appears that AquaCrop is more sensitive towards precipitation events than S1ASCAT-SWI_001. However, compared to the ARIS simulation, AquaCrop's upper soil layer simulations of five cm underestimated SM after all.

1830 The MBE of the AquaCrop simulation compared with SWI_001 shows an overestimation with a value of 1.79.

Table 4: Summary of the comparison analysis 2018

Relative Soil Saturation [%]	RMSE	R ²	MBE	p-value < 0.001	normal distribution
ARIS vs. SWI_001	4.98	0.69	-8.67	YES	YES
ARIS vs. SWI_010	2.98	0.33	-8.75	YES	YES
ARIS vs. SMAP	11.56	0.15	17.15	NO	high scattering
Absolute Soil Water Content [m ³ /m ³]					
ARIS vs. B1_005	5.86	0.02	-13.04	NO	YES
ARIS vs. B1_015	3.28	0.16	-10.59	YES	YES
ARIS vs. B2_005	5.88	0.02	-13.11	NO	YES
ARIS vs. B2_015	3.28	0.16	-10.57	YES	YES
ARIS vs. B3_005	6.60	0.15	-9.47	YES	YES
ARIS vs. B3_015	4.79	0.36	-5.00	YES	upper/lower boundary
Absolute Soil Water Content [m ³ /m ³]					
SWI_001 vs. B2_005	4.41	0.45	1.79	YES	YES

5. Discussion

High spatial variability of soil conditions requires improvements in the agricultural management of crops to overcome anthropogenic climate change impacts on yields. Thus, the accurate determination of soil water availability in a high space and time scale is crucial to estimate and mitigate drought impacts on crops, e.g., through precision farming techniques. Furthermore, seasonal water shortages increase the risk for yield failures, especially during the sensitive stages of crop growth.

1840 Consequently, the soil-climate interface regarding SM determines yield and, overall, agrarian production. To overcome high fluctuations in yield, a sound understanding of the SM regime is essential. Monitoring and estimation techniques are thus paramount to detect and optimize agricultural production.

Due to a gap of state-of-the-art in-situ SM grid networks, a sound basis of data is expensive and time-consuming. For example, spatio-temporal TDR and FDR sensor datasets are scarce and limited for operational application. Even point-in-situ measurements on a large-scale resolution are limited and are mostly part of weather station networks. Low-cost sensors such as the Parrot sensors applied in our study could fill these gaps partly. However, they are often weak in robustness and calibration. Further, they are time-consuming to read out the data if

1850 not integrated with an automatic data transfer system. Which again will raise the costs of implementation.

Precision farming techniques may help future agricultural applications to fill the gap between in-situ point measurements and the required spatio-temporal resolution for crop management. Thus, selected SM spatio-temporal data from satellite remote sensing products combined with crop-soil-water balance models were investigated at field-scale in our study.

5.1 Tools for detecting SM at high spatial resolution by satellite remote sensing and model simulations

Our study demonstrates that satellite remote sensing techniques can support crop-soil-water relation analysis. Amongst the satellite data assessed are the **LAI-MODIS**-based observations

1860 that show a good agreement in the time course of observed LAI and the simulated AquaCrop LAI. The results indicate that LAI-MODIS can validate the AquaCrop simulation from sowing to final yield. It demonstrates that remote sensing, like LAI-MODIS, is a good predictor for the AquaCrop simulation performance.

Additional satellite remote sensing applications for crop-soil-water relation analysis are the **S1ASCAT-SWI** and SMAP products for SM estimates. Based on the correlation analysis results to a trustful reference (grid TDR in-situ measurements), the data suggests that the S1ASCAT-SWI products are a valuable and objective source for SM estimation on a field scale (500x500 m). Especially the SWI data for 0-5 cm soil depth is the most robust indicator for SM

1870 near the soil surface. However, the SM estimates for soil depths of 0-1 and 0-10 cm of the S1ASCAT-SWI products likewise provide valid and valuable SM estimations at the field scale. Of course, this high spatio-temporal resolution of the S1ASCAT-SWI products is related to the overall expenditure of the calculations and the spatial resolution of the satellite sensor, which determines the final resolution of the satellite image.

The **SMAP** SM product is the second method tested, though it is less reliable to generate valid SM estimations. The correlation with the reference sensors is low, and data suggests a lower validity of the estimated results.

1880 Amongst the two crop simulation methods analyzed are the AquaCrop simulations and the ARIS simulation. In the **ARIS** simulation, the results indicate a similarly good estimator for SM

as the S1ASCAT-SWI. The strong fluctuations of peaks and troughs within the SM range of the ARIS models are related to the underlying setting of FC and PWP. This bias may be introduced through the setting of soil map, which has a higher spatial resolution. These peaks and troughs, or more precisely, this 'cutting' effect of the SM calculations, result from the cascade method used in the ARIS model at the specific soil layers, respectively. This circumstance leads to a distortion of the statistical analysis by accumulating the extreme values compared to the in-situ data from the measurements.

1890 The analyzed **AquaCrop** products suggest a sound and robust correlation for the five cm soil depth. The 15 cm soil depth outputs are likewise an adequate source for rough SM estimations, which is probably an effect of a simplified soil-water-balance calculation procedure in AquaCrop for that specific soil depth. However, dependent on the input data, higher spatial variability of soil conditions can be considered by the AquaCrop application on high spatial resolution (compared to ARIS, which is fixed to 500x500 m resolution in soil properties). For example, we implemented three individual soil types in the AquaCrop simulation calculations. Nevertheless, a good soil survey with reliable and high spatial resolution data is still required for sound spatial SM estimates.

1900 During verification of the LAI-MODIS data, the pixel location was checked for possible deviations. However, the experimental test site is perfectly overlaid by the LAI-MODIS pixel. Thus, neighboring fields do not intercept or impact the canopy cover feedback of the satellite imagery.

In conclusion, the validation of the AquaCrop simulation based on LAI-MODIS data is a promising tool and works nicely for larger cultivated fields. Smaller fields, however, might require on-site LAI measurements for calibration. This circumstance is related to the limitations of spatial resolution of this satellite imagery product. For the LAI-MODIS dataset, a spatial resolution of 500x500 m per pixel set the boundary for an application. Thus, higher resolution analysis seems impossible with the LAI-MODIS satellite data. However, much higher spatial resolution LAI data from other satellite sensors (e.g., Sentinel) are already available.

1910 Cloud coverage limits the number of observations or clusters observations during particular cloud-free meteorologic events too. Thus, in few circumstances, cloud coverage may distort observations negatively.

In contrast to the hypothesis, delineating spatial variability in SM is impossible, based on calibrated S1ASCAT-SWI, SMAP products. For the crop simulation tools, ARIS and AquaCrop, the spatial resolution is bound to the resolution on soil property inputs (especially FC and PWP), which was also not available below the field scale in our study. Of course, the temporal resolution is high with the daily time step simulation based on daily weather data in the two crop models and the S1ASCAT-SWI product.

1920 Only the SMAP product provides a lower temporal pattern of three-day observations. Nevertheless, based on our research methods, the SM spatial variability on field-scale could only be assessed with gridded in-situ measurements like the Parrot sensors. The spatial resolution of the crop simulation- and satellite estimations is too low (for the reasons mentioned above) for a possible high-resolution field-scale application. The circumstances shift in favor of these satellite products on a lower resolution or pixel size of 500x500 m.

However, a good and substituted delineation of spatial variability could only be visually presented with the help of the gridded Parrot measurements.

1930 The Parrot spatial-variability data clarifies how the SM variability expands over the experimental field. There are 'islands' of high and low SM, which have different reasons. These reasons could be 'fostered' by local extremes, even in a smaller grid. One of them is undoubtedly connected to the overall texture and structure of the upper soil compartment. Soil properties such as soil texture, soil pore volume, organic content, or soil structure determine how long and how much water the soil retains and thus, determines the overall SM regime.

The dominating differences in soil texture at our experimental site are defined by the Prater Terraces' geomorphology and the Danube River's former meandering while shaping the Marchfeld region.

During the day and night operation of the Parrot sensors were rain periods and dry periods. Very high SM observations of the Parrot devices do not depict the plant's available water, rather the short-term saturation above FC during and briefly after precipitation events. Therefore, no tendencies towards PWP were observed during some stages of observation, which suggests that the experimental field is at or above FC during wet phases. Nevertheless, the different soil textures spread out over the experimental field. They show that drainage is higher in some parts of the field than others, depending on infiltration and soil water conductivity, which is again related to soil properties such as soil texture.

1940

A refined approach applying a zoom effect provided a deeper insight into the relationship between spatial variability and spatial resolution. Dependent on the resolution, the tendencies of the SM estimations across the experimental field were correct. However, if one zooms in on a respective area, the spatial resolution increases if the range scaling steps applied are automatically adapted to the – normally decreasing – full range during zooming.

1950

Spatial variability detection based on remote sensing techniques works currently on a field level resolution (one pixel per 500x500 m). If higher spatial variability detection for SM estimation is required, gridded in-situ sensors on a smaller grid size than 500 m are viable. For example, between the in-situ measurement points of the grid, we see a variability of up to 10 % vol. It is essential to mention that there was continuous moderate precipitation during the phase of our grid in-situ measurements. However, even when constant precipitation occurred during the summer season (July in particular), significant spatial variation in SM was measured. The energy balance during this time of year strongly drives evapotranspiration of the upper rooted soil layers. Thus, some parts of the experimental field foster higher amounts of SM than others due to the variations in soil water holding capacity over the field.

1960

5.1.1 Results achieved in the context of state-of-the-art

While previous research has focused on in-situ SM measurements and weather variables to detect crop water status, the research of Ezenne *et al.* (2019) demonstrates that spatio-temporal variability of SM can be achieved with the help of unmanned aircraft systems (UAS), such as drones. Of course, the UAS's aim determines the camera application, whether thermal or hyperspectral cameras are used for the crop-water-stress indication (Ezenne *et al.*, 2019). The UAS presented in their study work with different equipment than satellite missions like ASCAT or SMAP that work with microwave detection systems. It was demonstrated that higher spatial variability in SM could be detected with UAS and thermal camera systems based on water stress detection through crop canopy temperature measurements.

1970

The research of van Opstal *et al.* (2019) likewise demonstrates that a combination of flying sensors with AquaCrop helps to assess the heterogeneity adequately and increase spatial variability. The combination of UAS and simulation programs can provide a better understanding of water productivity assessment and nutrition deficiencies on a spatial scale with higher resolution. Moreover, the research proved that strengths in crop simulation come with the possibility of applying future scenarios (van Opstal *et al.*, 2019).

1980

The work of Zappa *et al.* (2019) demonstrates a different approach to access higher spatial variability at the sub-field level with a resolution of 30 m to cover spatial heterogeneity. They used machine learning and training sets based on ASCAT and SMAP satellite data combined with model prediction. A comparable approach also was presented by Vergopolan *et al.* (2020), interfacing remotely sensed vegetation indices with meteorological conditions, soil physical properties, and a model simulation for predictions. They achieved sub-farm scale spatial variability of 30 m, respectively.

These results indicate that satellite remote sensing like S1ASCAT, SMAP, and modeling tools such as AquaCrop or ARIS provides an innovative solution for SM estimation.

1990 However, our study demonstrated that an application for high-resolution spatial variability of SM at the sub-field level is not feasible due to inadequate satellite sensor resolution. All sensor products except SMAP provide moderate to good correlation to SM's spatial mean and temporal course, according to the reference SM analysis on a field scale (500x500 m). Especially the S1ASCAT-SWI products, the AquaCrop, and ARIS simulation seem to be a significant asset in close to real-time SM estimation. Thus, considering the underlying problem of increasing climate extremes, close tracking of the SM status on a field scale is vital to counter drought conditions and poor crop growing conditions in agronomy. Nevertheless, it is vital to mention that a bias occurred for the AquaCrop and S1ASCAT-SWI estimations during our study. The bias is assumed to be based on inadequate PWP and FC settings in the soil water calculation algorithm, which underestimates the SM occurrence in the AquaCrop simulations and the S1ASCAT-SWI products. SMAP, in contrast, was less reliable in our study for field-scale usage than the three other products.

5.2 Estimation of SM to combat increasing droughts

2000 Suppose one takes a closer look at the calibrated satellite and crop simulation data used as a beneficial tool to achieve crop-soil-water relations compared with in-situ measuring devices. In that case, the study demonstrates that the hypothesis is in line with the results. The data contributes a clearer understanding of the application to estimate SM and use satellite imagery to validate, e.g., the AquaCrop model for the specific conditions.

If directly looked at the simulation and remote sensing applications, the **ARIS** simulation of SM responds to precipitation events more intensely and in good agreement with the grid-based calibrated in-situ measurements compared to the S1ASCAT-SWI data. High fluctuations of the ARIS SM estimations aggravate comparability with remote sensing data.

2010 The way the ARIS input data are set up, comprising different parameters including meteorological and soil input data at the field scale, is sound. The SM estimates correlate well with the Parrot data, especially during the growing period. Just during winter and the early vegetation period starting in October 2019, the SM estimate of ARIS is mostly at FC due to underestimated evapotranspiration during the non-growing season. The underestimation is based on a biased KC (crop coefficient) that needs adaptation.

In 2020, during the summer month, there is also high fluctuation observed in the ARIS data. Still, it correlates with the weather station's sensor with some overestimation in SM. However, the weather station sensor is just one reference point within the field and could be biased compared to the field mean level in 2020.

2020 According to precipitation pattern and season, the ARIS data strongly reacts to precipitation with peaks and troughs, reflecting depletion of SM close to PWP or vice versa an increase towards FC. Especially in April 2020, the ARIS SM estimates dataset visualize a low volume in precipitation. After this dry phase, intense precipitation events from May onward increase the highly fluctuating response of the ARIS data. However, the models fit the actual soil water storage and retention potential. Biases within a selected point in the field may result from temporal deviations, besides the soil-water-balance calculation simplifications. For example, the ARIS software applies the soil layer setting and cascade approach (see above).

2030 The results of the **S1ASCAT-SWI** fit with the theory that microwave satellite remote sensing SM estimation is a beneficial tool for crop-soil-water analysis at a larger scale. However, dependent on the soil depth of the SM product, a time delay can be observed.

2040 According to the statistical analysis, the S1ASCAT-SWI products correlate well and are robust data. Nevertheless, the S1ASCAT-SWI products show a strong negative bias in absolute calculated SM and lower SM fluctuations than the calibrated Parrot in-situ measurement. The S1ASCAT-SWI products compared with the single weather station sensor foster similar correlation and robustness while having a lower negative bias in SM, which could be a local effect, as the weather station sensor does not represent the field scale. Overall, the trendline of the SM estimation matches the precipitation pattern well. However, it is smoother than the ARIS data for both years of surveillance. In general, there is a lower fluctuation and response to the precipitation pattern in the S1ASCAT-SWI data than in the crop simulation programs. The primary asset of the S1ASCAT-SWI data, SMAP, and ARIS is the interpolation of the data. This results, for example, in the higher resolution of the S1ASCAT-SWI products and a smoothed SM pattern. However, the smoothed pattern and negative bias could reflect a bias in the S1ASCAT-SWI product instead.

2050 Considering the **SMAP** product, the results demonstrate low correlation and low validity of SM estimation. The data is inadequate to explain SM occurrence on a field scale. Overall, the SM estimation lacks accurate trends. The SMAP product temporarily over- and underestimates the SM with a strong delay to precipitation occurrences. This circumstance is probably related to the reference soil depth of root-zone up to 1 m instead of specific soil layers of defined depths. Compared to the in-situ reference sensors, the SMAP SM occurrence response consequently trails behind precipitation events and the moister winter period. This strong delay of SM trend in SMAP does not reflect rooting depths of most shallow rooting crops and is probably related to soil depths of >1m of perennial plants such as tress and representing an average of a deeper soil depth only. Nevertheless, SMAP is still an adequate source for long-term SM trend estimation, reflecting a deeper soil depth. An advantage over other data is the public accessibility and availability with the Google Earth Engine. Porosity is likewise required for better visualization or interpretation of relative soil saturation data but at lower resolution online available for Lower Austria.

2060

The **AquaCrop** results suggest that a good correlation can be achieved with model simulations for SM estimation, given that representative information about the site characteristics is available, especially the PWP and FC. Thus, accurate input data is crucial for precise simulation results, especially for modeling scenarios. According to the theory, the model simulation for five cm soil depth fosters higher fluctuation and aligns with the precipitation pattern well. Compared to the ARIS and in-situ measurements, the FC and PWP are underestimated in all three soil types. In contrast, the correlation analysis of AquaCrop in 15 cm for the year 2019 seems to have little correlation or fosters a lower SM estimation explanation. The situation changes for the year 2020 and the weather station sensor in 20 cm soil depth. Here the AquaCrop simulation in 15 cm soil depth fits better with higher correlation and validity. The FC is constantly high during the winter, even though the precipitation volume is moderate to low (see the reasons for deviations for the 15 cm soil depth simulation that were already explained before). According to the theory, in low precipitation periods, the AquaCrop simulation approaches the PWP (which is given as an input soil property) but never drops lower. The peaks and troughs are respectably ordered according to the precipitation pattern. If looked closely at 2020, the absolute SM trendline of WS_020 and B1_005 show a high response concerning precipitation events. This incident is most likely associated with AquaCrop, and its software design as the simulation program incorporates daily meteorological data and creates its output based on this data. Hence, peaks and troughs correlate nicely with the precipitation pattern accordingly.

2070

2080

Furthermore, the AquaCrop simulation process incorporates crop growth and crop water demand and accordingly generates the CC [%]. This circumstance, in turn, can be validated through the **LAI-MODIS** dataset as presented.

2090 However, due to the way AquaCrop is set up, the LAI-MODIS dataset helps just as a guide to validate the simulation. It cannot incorporate the acquired LAI-MODIS observations directly in the software. One has to return to the data input interface of AquaCrop and adjust all data entries manually to increase model validation (e.g., adapting the plant and plant-canopy specific characteristics).

It is important to mention that the simulated CC of Barley in 2018 in AquaCrop shows no correlation with the LAI-MODIS dataset's observations. In reality, Buckwheat and Grainpea were grown in the experimental field. However, AquaCrop has no pre-defined crop growth parameters for Buckwheat nor Grainpea. Thus, Barley was used for the initial simulation in 2018 due to its similar growing season.

2100 Compared to the original LAI-MODIS response of Grainpea and Buckwheat, the in AquaCrop executed simulation of Barley as crop type could falsify the simulation process. Another probable explanation of the misfit of LAI-MODIS and the Barley-based simulated CC is that there is a lower volume of LAI-MODIS observations for comparison. Hence, outliers intensify the deviation.

An additional probable factor is that a test with two different crops was conducted in the experimental field. Buckwheat and Grainpea were sown simultaneously with a lower sowing rate in kg/ha, resulting in a lower plant density on site. Thus, a more possible explanation of the deviating feedback of the LAI-MODIS dataset is that fallow land or/and the grown crops have a significantly different reflection characteristic than Barley. For example, higher chlorophyll content with its reflection in the NIR spectrum of the wavelength is picked up by the LAI-MODIS mission, which results in higher reflection feedback.

2110 Eitzinger *et al.* (2003) showed that simulation of future crop management scenarios and the modeling of different climatic scenarios improve the understanding of effects on crop-soil-water balance effects. With the help of simulations, counter measurements to mitigate drought impact and low water availability are valuable assets to understand climatic pressures on agricultural production more in-depth. Lalić *et al.* (2018) likewise demonstrated model simulations and their ability to help improve forecasts in mitigating crop damage risks and water management or policy measures. Such simulations provide thus, valuable insight into further planning and mitigation of drought events.

2120 However, agro-climatic models can only predict well, as long as the data input is sound, representative for the respective sites, and complete. Nevertheless, uncertainty remains, especially for unpredictable biotic and abiotic diseases caused by, for example, increased leaf-wetness (Thaler *et al.*, 2012).

One of the benefits of simulations like in the ARIS-based drought monitoring is to access the SM estimation via the internet on maps for specific crop types and dates (Eitzinger *et al.*, 2016). Such simulations foster high interest for insurance companies or stakeholders in general, that are involved in the agricultural sector (Eitzinger *et al.*, 2016). However, for many practical applications at the field level and below, a higher spatial resolution than 1 km is necessary.

2130 In case of drought, or crop stress in general, the decision-making process can thus profit from simulation programs available to the public. AquaCrop, on the other hand, needs individual input on field-scale about the conditions prevalent. Nevertheless, as FAO (2017) mentions, AquaCrop can be used as a planning tool or support management decisions, e.g., irrigation scheduling and water demand assessments of irrigation projects.

Complimentary satellite remote sensing data such as the ASCAT-SWI soil moisture product is highly beneficial in providing reliable SM monitoring, even though it was initially not designed for that specific purpose (Brocca, Crow, *et al.*, 2017). Nevertheless, the technology and multi-

angle measurement capabilities allow reliable SM estimations (Brocca, Crow, *et al.*, 2017) for practical applications with already useable spatial scales of 1 km. Amongst the benefits of remote sensing applications, as the S1ASCAT-SWI product is, are the high spatio-temporal coverage compared to the relatively low costs for large-scale applications (Brocca, Ciabatta, *et al.*, 2017). Nevertheless, L. Brocca *et al.* (2017) debate three critical limitations related to satellite SM products. For once the shallow penetration (1-2 cm) of the topsoil layer, second a coarser spatial resolution as in-situ measurements, and third, low quality of SM estimations under specific surface conditions (Brocca, Ciabatta, *et al.*, 2017). Of course, spatial downscaling techniques and root-zone SM estimation by coupled soil water balance algorithms seem to overcome some of the critical limitations presented. The work of Zappa *et al.* (2019) demonstrates that such downscaling procedures from coarse remote sensing data can help to receive higher resolution SM estimations. However, for high spatial resolution, a local calibration, and validation, considering specific soil conditions, is highly recommended, especially for detecting absolute soil moisture and crop available soil water content.

2140

Compared to the S1ASCAT-SWI products, the SMAP product has lower spatio-temporal resolution and falls shorter in representing the SM conditions on the agricultural field scale (Vergopolan *et al.*, 2020). Nevertheless, on a larger scale, the SMAP product shows promising results in SM estimation (Suman *et al.*, 2020). Suman *et al.* (2020) also mentioned an overestimation of SM and high RMSE. They relate it towards vegetation effects on the sensor-based SM product. Likewise, as in this research, Suman *et al.* (2020) experienced a lower SMAP SM estimate during the winter months. They related them to higher complexities of snow cover or frozen soil. Among the benefits of the SMAP data are the dataset's better availability and cloud computing capability, for example, with the Google Earth Engine.

2150

Nevertheless, as Luca Brocca *et al.* (2017) point out, missing cloud computing facilities, web mapping services, and tools need to be developed to provide nonexperts access to the ASCAT SM data. These beneficial SM products could provide end-users with valuable information about the on-site SM regime. However, large datasets and formatting foster technical constraints (Brocca, Crow, *et al.*, 2017).

2160

This study suggests that close to real-time SM estimations are available or possible with the satellite sensors and the modeling programs researched. Thus, temporal irrigation during the most sensitive growth stages can likely be an option to apply, built on close monitoring of the SM regime. Based on the analysis, it supports the theory that considering long-term observations, all products closely track the SM and provide crucial information about the trend of SM over time. This valuable information suggests that management practices can be adjusted to mitigate high-stress periods, respectively. In theory, if the SM status on field-scale is known, a shift in management strategies like crop type changes or an increase in hedgerows can preserve SM better to overcome droughts. Of course, short-term management practices like no-tillage approaches or a change of crop-rotation schemes towards a more persistent water stress level may have adequate results in maintaining crop yields stable.

2170

The study results align with the hypothesis that SM estimation based on different methodologies channel further developments in management practices or irrigation scheduling. Especially if the stress on field-scale is high and yields declined in the past years, there will be an incentive to find explanations of yield losses. Thus, tools such as S1ASCAT-SWI, SMAP, ARIS, or AquaCrop will be crucial assets to estimate SM and make decisions to mitigate drought losses, given that they are well-calibrated for the relevant site conditions. The results suggest that close to real-time SM estimation can provide crucial information for irrigation scheduling. Of course, given that meteorological data is accessible in real-time or close to real-time to apply in simulation programs.

2180

2190 The results of continuous SM estimation tracking should be taken into account when considering how the warming of 2°C in the air temperature impacts yield of crops. A shortened growing period of up to 20 days due to the warmer climate towards 2100 maybe even worsened by light-textured soils, respectively. Thus, changes in management strategies from plowing towards minimum tillage could increase the mean yield of winter Wheat by up to 8 %. This effect can be associated with higher soil water storage and the improved supply of crop soil water (Thaler *et al.*, 2012).

Thaler *et al.* (2012) also demonstrate that alternative adaptation options like hedgerows are predicted to reduce wind speeds and positively affect soils like Chernozems or Fluvisols with medium and moderately fine-textured soils. The regional mean-yield level thus can be positively impacted with management strategies for future elevated water stress scenarios. Amongst the benefits are that unproductive evaporative losses from the crop are reduced with hedges (Thaler *et al.*, 2012).

2200 Hence, farm practice adaptations to reduce crop growth-limiting factors like water stress or heat aim to beneficially use production resources (Thaler *et al.*, 2012). Nevertheless, such long-term adaptations require significant structural changes in the farming system and need careful agro-economic planning (Eitzinger *et al.*, 2010). Additionally, several stakeholders, such as policymakers and water and land planning organizations, have stakes in structural transformations (Eitzinger *et al.*, 2010).

2210 Another focus comes toward the management strategy of mulching. It has a high potential to reduce the soil evaporation from the soil surface and subsequently reduces the green water footprint in crop growth (Hoekstra *et al.*, 2011; van Opstal *et al.*, 2019). The research of van Opstal *et al.* (2019) addresses the benefit of an AquaCrop simulation to adjust management strategies for soil water retention. Thus, they demonstrate that mulching practices impact seasonal water consumption and, subsequently the water productivity. These results build on existing evidence, also mentioned in the research of Eitzinger *et al.* (2008), that soils with low soil water storage capacity benefit from water-saving production techniques and constitute an essential requirement for climate adaptation. Lalic *et al.*'s (2018) research also promotes new management strategies for long-term adaptation strategies to improve water use efficiency. Among these innovative strategies, such as tillage improvements and crop rotation schemes, mulching constitutes a good source for increasing water use efficiency.

2220 While this present research has focused on satellite and simulation data to estimate SM and to monitor spatial variability, the results of Ezenne *et al.* (2019) show that unmanned aerial systems (UAS) like drones with thermal sensors can monitor and quantify spatial- and temporal SM variability for irrigation scheduling. UAS thermal imaging can be directly linked towards automated real-time irrigation scheduling, respectively (Ezenne *et al.*, 2019).

The primary finding comprises a sound understanding of the SM estimation based on satellite remote sensing and simulation products. The study demonstrated how such SM estimation could assist further management decisions as an agricultural application. However, the research supports the claim that only sound metadata combined with simulations and satellite remote sensing can assist high spatial resolution SM estimations.

5.3 The combination of methods for SM estimation

2230 Combining the AquaCrop simulation with the LAI-MODIS remote sensing data provides a better understanding of the validity of simulations. Nevertheless, as demonstrated beforehand, missing plug-in adjustments in AquaCrop aggravate end-user applications.

For example, a combination of methods such as remote sensing with modeling can improve or increase calibration significantly for delineation of spatio-temporal SM and improve yield estimation (Wagner *et al.*, 2020). Methods, for example, simulations interfaced with remote

2240 sensing, can likewise help assess soil heterogeneity at the field scale. In van Opstal *et al.*'s (2019) research, it is demonstrated that such a combination helps to assess the spatial variability of soil properties and crop conditions. For example, water productivity assessment and nutrition deficiencies can visually be demonstrated with higher resolution. The work of Zappa *et al.* (2019) and Vergopolan *et al.* (2020) demonstrates a different approach to access higher spatial variability at the sub-field level with resolutions of 30 m to cover spatial heterogeneity. They used machine learning and training sets based on satellite data and combined it with model prediction.

5.4 Limitations of simulation and remote sensing techniques

2250 The generalizability of the results is limited by the underlying soil type of a site. At our experimental site, Rutzendorf, the prevalent soil type is Chernozem, and thus, the upper soil layers behave regarding the SM accordingly. Amongst the limitations is the inter-comparability of different soil depths. The research suggests that different soil depths and depth ranges of measurements determine the outcome of the statistical analysis. Due to the lack of data (e.g., PWP and FC) on some soil layers, the results show deviations and cannot provide the best statistical outcome. For high SM estimation results, good accurate input data is required. Thus, a limitation comprises the actuality in time and the accuracy of the simulation, the remote sensing data, and the in-situ sensors.

2260 The SM TDR reference measurements, on the other hand, were constrained by time and costs, and thus, only a low volume of measurements could be provided. These reference SM measurements were used for the FC and PWP trendline charts to compare the data visually. Likewise, a higher volume of observations would have enhanced the credibility of the measurements. The same applies to the regression analysis of the TDR reference measurements and the Parrot devices. In general, more and more frequent measurements would have increased credibility. Nevertheless, the underlying data for comparing Parrot and TDR measurements was enough to deviate correlations for further analysis using calibrated Parrot values for absolute spatial soil moisture estimates.

Due to the lack of in-situ sensor data for the Rye vegetation period from October 2019 till June 2020, the methodological choice was constrained by an already existing sensor setup. Thus, during the evaluation process, the meteorological station was the only existing reference in the experimental field during the time frame in question.

2270 Regarding the met-station observations, the one-point measurement of a satellite-based pixel (representing the field average), compared to the one-point soil sensor measurement of the meteorological station at the edge of the experimental field, inadequately compares an exceedingly complex soil heterogeneity. In that matter, a measurement grid like the Parrot setup in spring and summer 2019 would be a more adequate approach to compare one remote sensing pixel with a size of 500x500 m. However, long-term in-situ monitoring on-site was beyond the scope of this study. Such long-term monitoring would be more beneficial to understand better the overall SM regime of the experimental field based on simulated and satellite-based remote sensing techniques. Nevertheless, only a grid network would most likely accurately determine the SM estimations and be feasible for further comparisons with satellite remote sensing data.

2280 Similar circumstances apply to the existing Parrot in-situ measurements compared to the meteorological station. The Parrot setup was pre-defined, and the sensors were thus used for comparability reasons. Luckily, three consecutive months were monitored with about 70 Parrot sensors scattered across the experimental field. Nevertheless, it would have been interesting to see the performance of the Parrot devices during the winter and spring period as well. For once, whether performance is good, for others to have an extended time frame of correlation analysis.

If we take a closer look at the analysis in 2018, data reliability was affected by a lack of in-situ reference sensor observations or measurements in general. It can be assumed that, however, based on the good performance of ARIS in 2019, that the ARIS simulations for 2018 meet the SM fluctuations well.

2290 Overall, the reliability of the generated data might be impacted by a consistent transformation of units from relative SM (of the satellite products) into volumetric SM, which reduces accuracy in the long run. Thus, a limiting factor is missing information about soil properties such as porosity compared with volumetric in-situ SM observations or crop simulations.

The porosity used in our study originates from the HYDROBOD2 data and can be seen as an asset to achieve visual comparability of the trendline diagrams regarding the various measurement methods. However, limitations are indeed the accuracy of the raster data of HYDROBOD2. The porosity in our study has a coarse scale of 500x500 m. The low resolution does not depict the high spatial variability in porosity at the experimental field and thus, bears a bias in the data.

2300 Nevertheless, suppose porosity information is unavailable for a site, according to state-of-the-art research, it is common practice to transform volumetric in-situ measurements into relative SM values for comparability reasons. This principle, however, is merely executed if no further knowledge about the porosity on site is available, and a transformation of relative soil saturation towards volumetric soil saturation is thus not entirely accurate.

2310 Such transformation procedures are increasingly relevant if the SM information is needed for irrigation scheduling or water demand assessments. Especially where information on absolute moisture and site-specific soil properties (in specific soil water holding capacity information) is necessary. However, this unit-juggling is also necessary if volumetric and relative SM observations need to be compared. Nevertheless, it is vital to acknowledge how well the in-situ reference measurements determine SM. Substantially, the accuracy of sensors is paramount to adequately relate the in-situ measurements to satellite remote sensing measurements given in relative SM.

The SM heatmaps in chapter 4.2 (Spatial Variability of soil moisture (SM)) lack an identical SM range for comparison. This circumstance is visible in very dry periods compared to moist periods. Especially if April 2019 is compared to May and June 2019. The SM range deviates from one Figure to another.

Similarly, the three zoom images lack the same SM range, respectively. Misinterpretation or confusion of the presented results may be the consequence.

However, the software was the limiting factor in that matter. Thus it is vital to indicate all SM ranges for all individual images to minimize errors.

2320

6. Conclusion and prospects for future

The research aimed to identify effective methodologies to estimate spatio-temporal SM of crop fields and test methods to identify spatial variability. After climate change-related extreme weather events increase steadily, the estimation and prediction of SM in the presence of drought and heavy rainfall events require sound knowledge to strengthen future crop production.

2330 Based on the field measurements and statistical analysis conducted, it can be concluded that S1ASCAT-SWI, AquaCrop, and ARIS are suitable tools based on successful calibration and validation in estimating SM at field scale for application in crop production. For an above-field scales trend application and a deeper integrated soil depth, SMAP constitutes a valid product to estimate SM. However, SMAP is less feasible for field-scale, short-term assessments, or higher spatial variability detection.

2340 The research has shown that direct high-resolution (below field scale, in the range of few meters) spatial variability detection of SM is currently impossible with the methods researched comprising S1ASCAT-SWI, SMAP, AquaCrop, and ARIS. The crop simulation applications of ARIS and AquaCrop are limited mainly through unavailable high spatial resolution soil properties, needed as inputs and the satellite products by technical constraints of sensor resolution for validation. Nevertheless, the results indicate that these applications are currently beneficial at field scale and daily time-steps to estimate SM and provide decision support for crop management options to mitigate crop drought stress situations. The data assessment has shown that climate-mitigating efforts can be derived from existing knowledge about SM regimes. Moreover, current research showed various strategies to combat SM limitations in the agricultural sector.

2350 While missing in-situ SM measuring networks in high spatial resolution grid scales limit a broader above-field assessment of satellite and simulation products, our result provides new insight into a better understanding of SM estimation for agricultural applications. Several studies, including the underlying analysis, show that combining remote sensing techniques interfaced with simulation tools fosters accurate SM estimation. The research clearly illustrates that SM estimation techniques without in-situ measurements are generally applicable but need to be tested and validated for biases or deviations before using specific applications. However, it raised the question of end-user-friendly accessibility for satellite remote sensing data too.

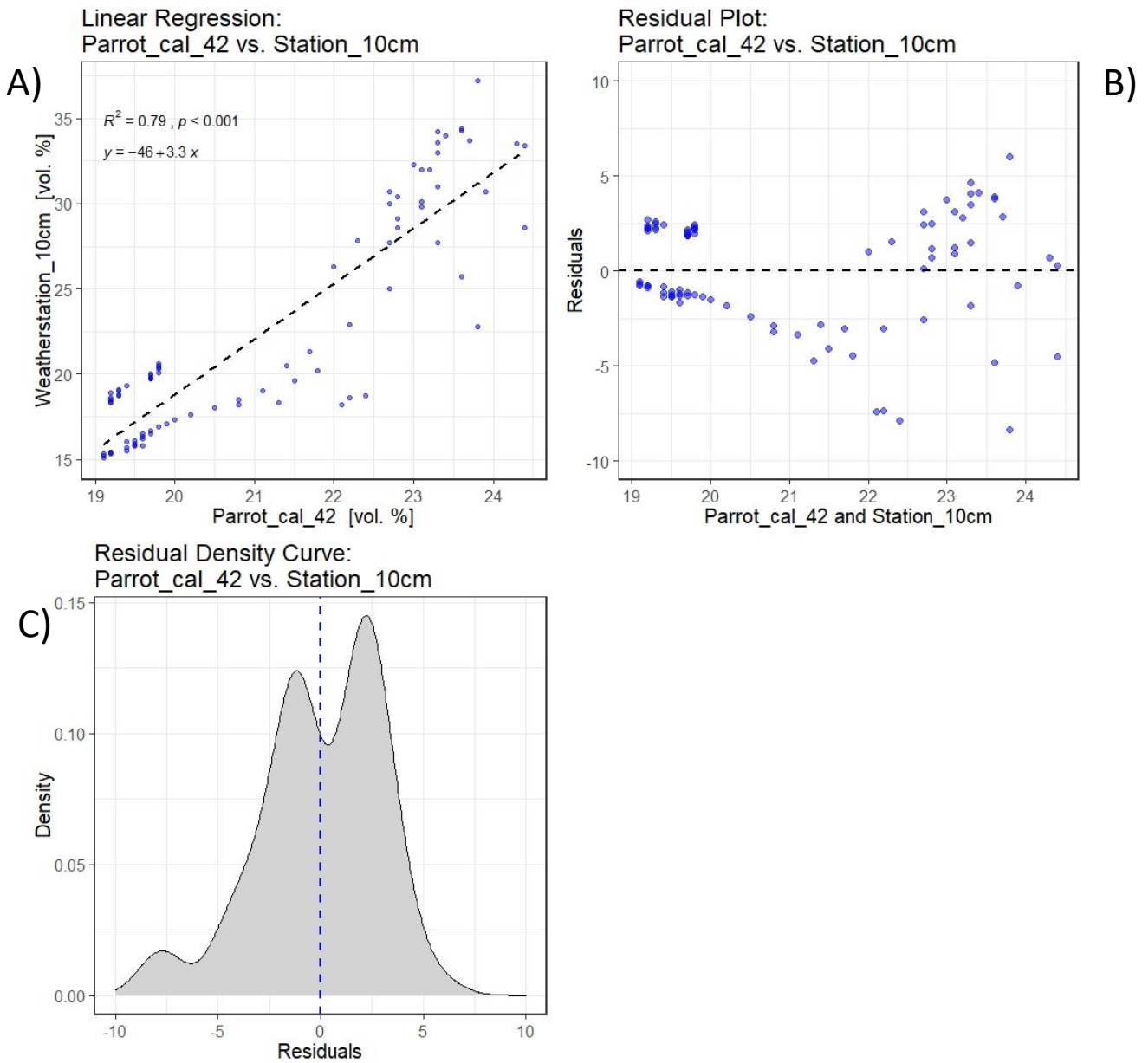
Based on these conclusions, data availability should be improved with consideration to expand access for end-users and non-GIS experts. Especially, the SM unit-juggling needs development to achieve better comparability of different SM estimations in relative and volumetric units. It would also support validation efforts on in-situ measured data sets by stakeholders themselves. In general, the data availability with cloud computing or publicly available data access should be improved.

2360 Future studies should consider that sub-field level spatial variability in soil heterogeneity is challenging to monitor based on remote sensing applications as the S1ASCAT-SWI or SMAP products are. The more background knowledge about the agricultural field exists in terms of meteorological data, soil physical properties, e.g., the clearer a distinction of spatial variability can be made with simulation models. However, the limiting factor is missing knowledge about such background information as soil surveys are expensive, labor-intensive, and often unavailable at suitable spatial scales. A transition towards an extensive in-situ measurement grid like in the United States would help to generate profound background parameters to calibrate and aim for spatial variability detection based on simulations.

To better understand the implications of these results, further research could address the spatial variability detection of SM based on UAS and drones in particular.

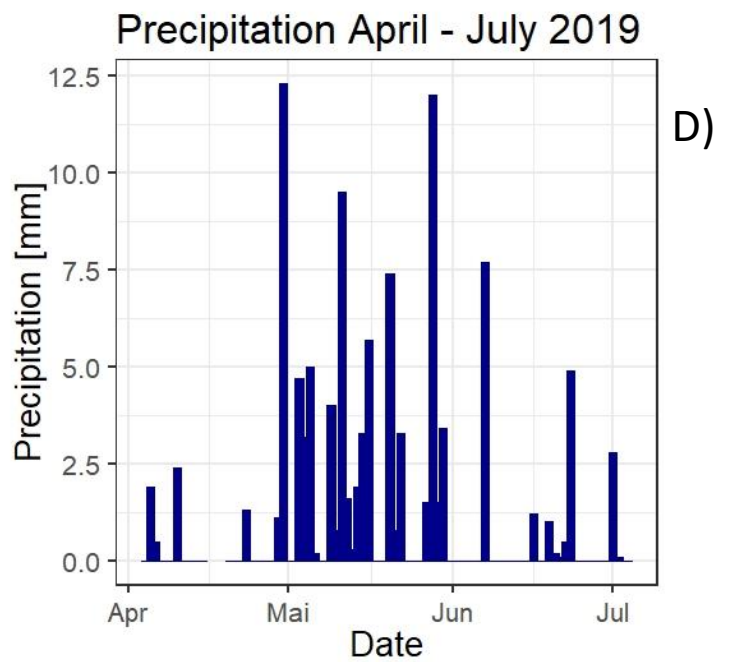
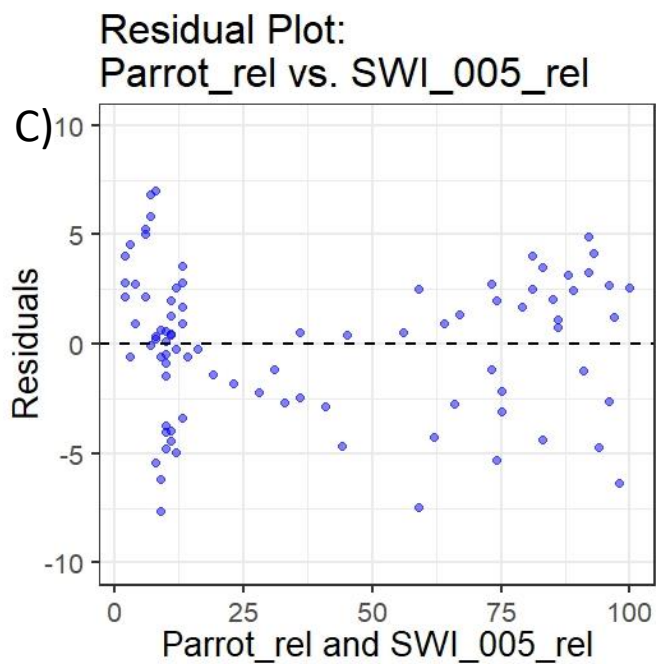
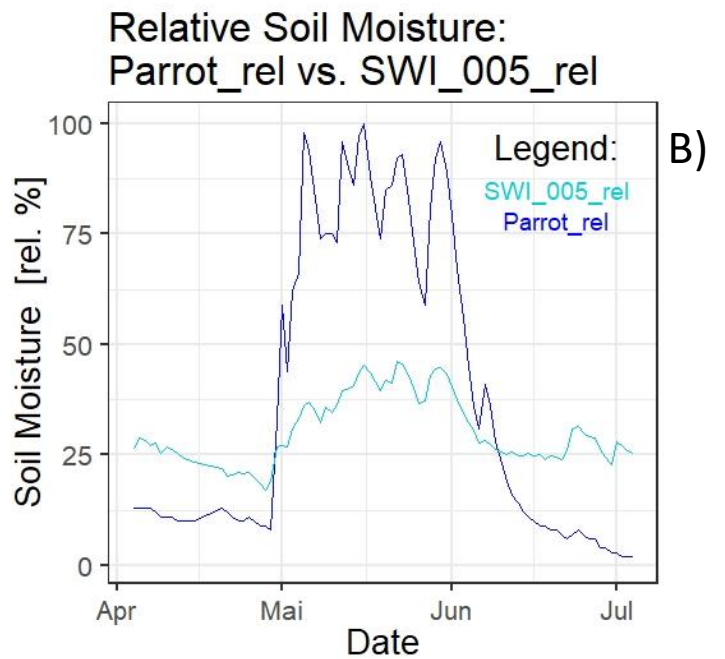
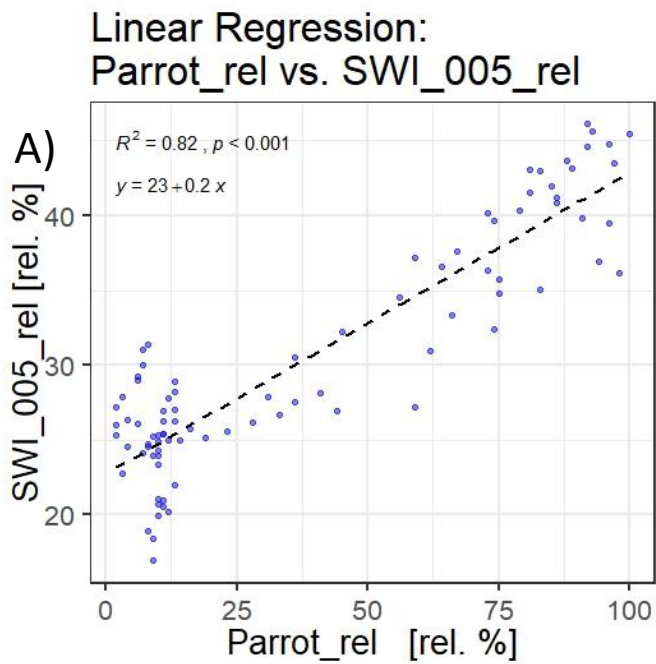
Appendix

Complimentary Baseline Analysis

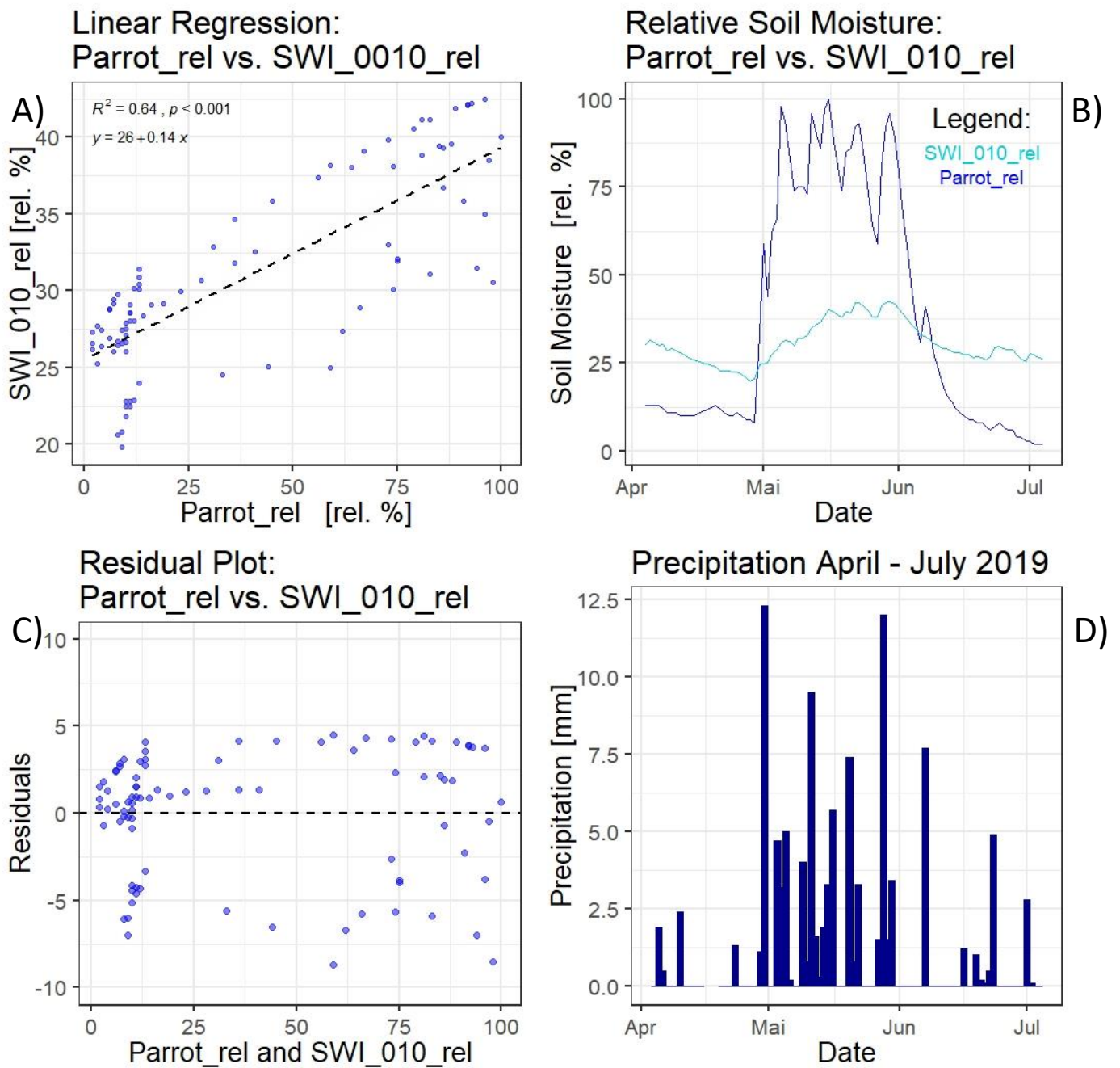


Annex 1: Statistical analysis of Parrot_cal_42 vs. Met-station_10cm for A) linear regression, B) residual plot, and C), residual density curve

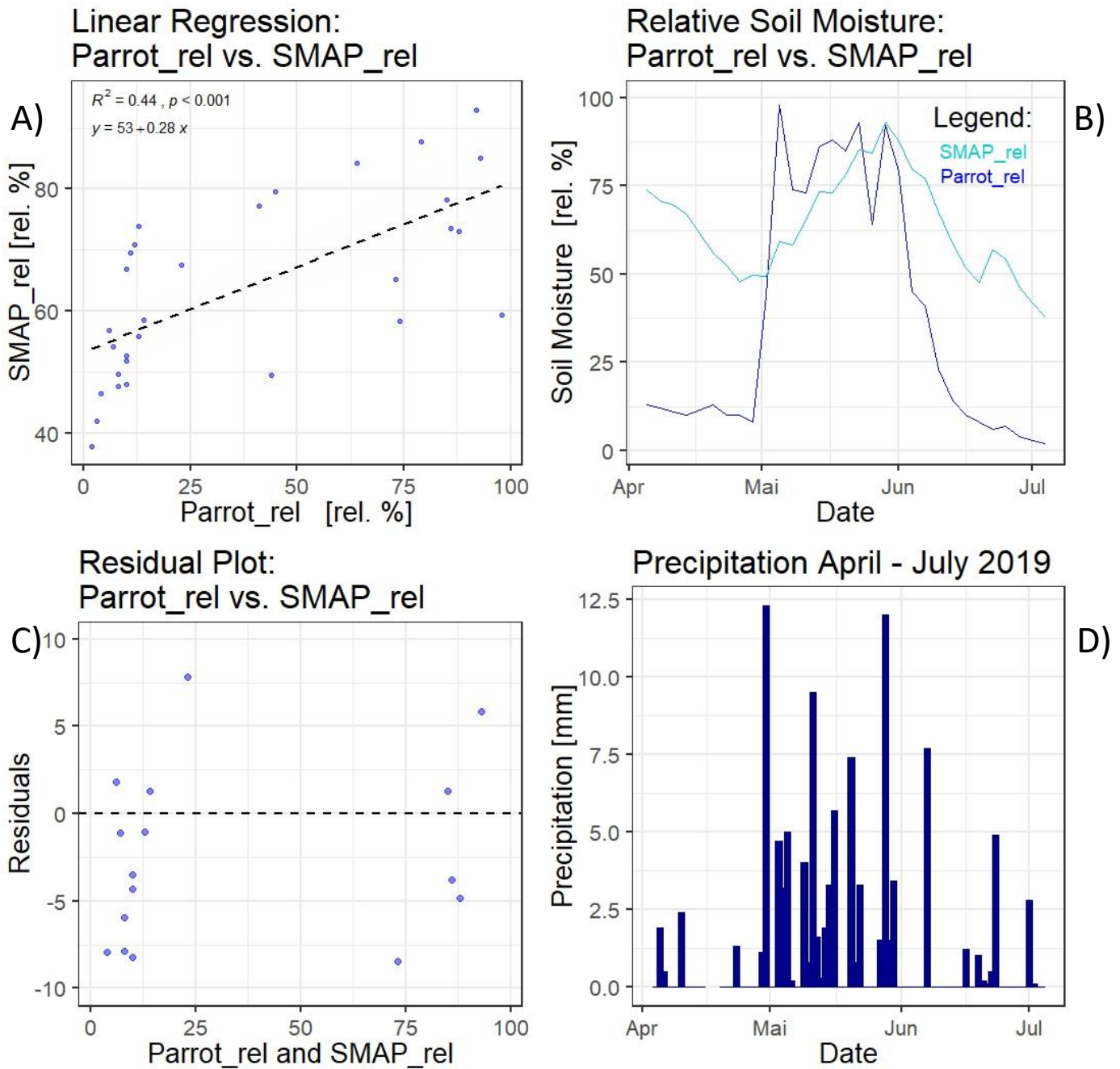
Vegetation Period 2019



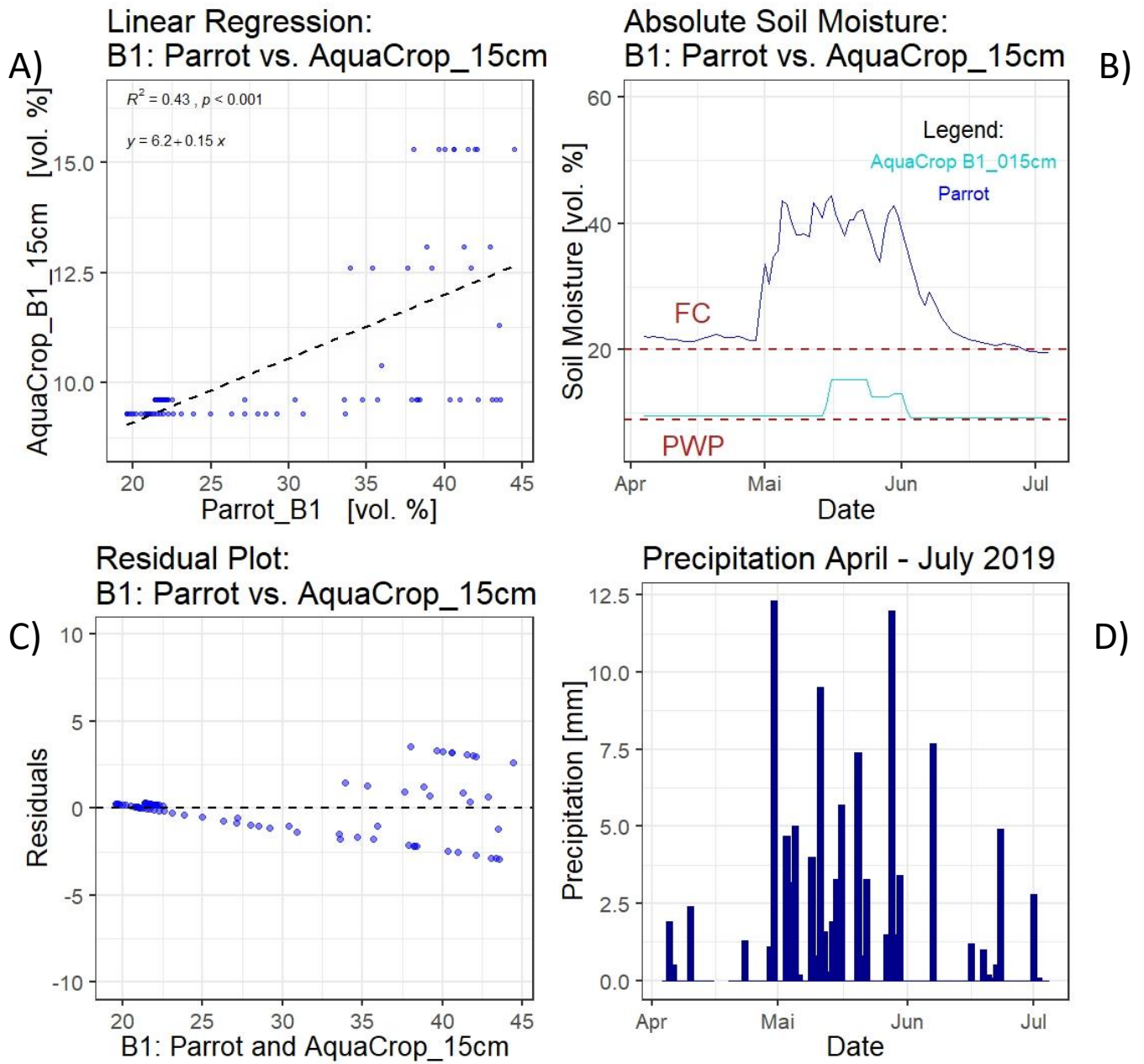
Annex 2: Statistical analysis of Parrots_rel vs. SWI_005_rel for A) linear regression, B) SM trend of Parrots and SWI_005_rel over time, C) residual plot, and D), precipitation graph



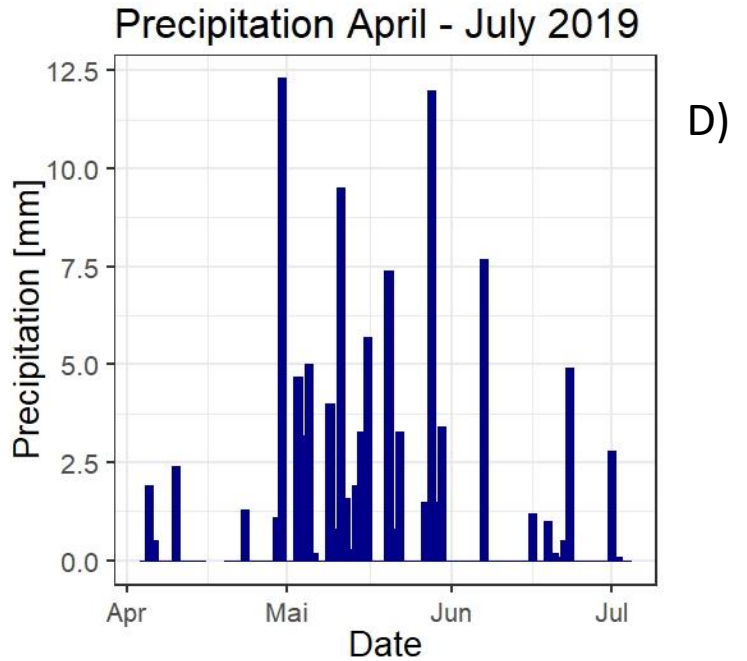
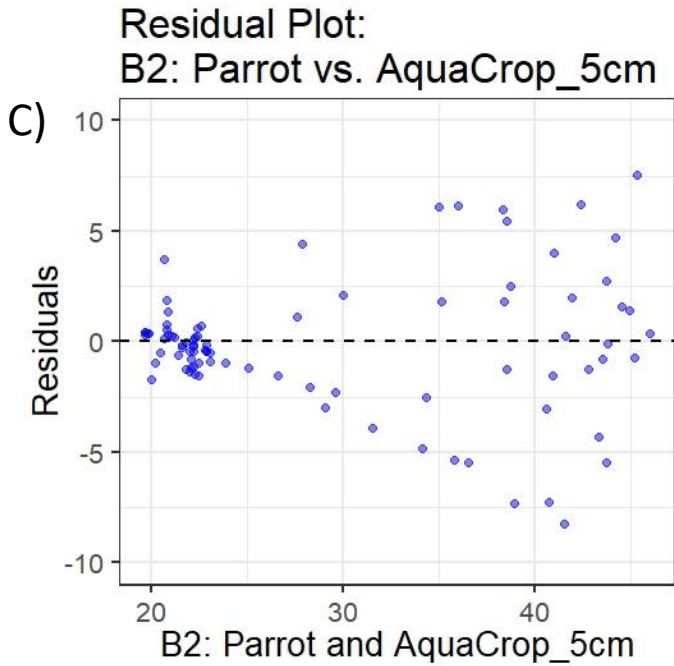
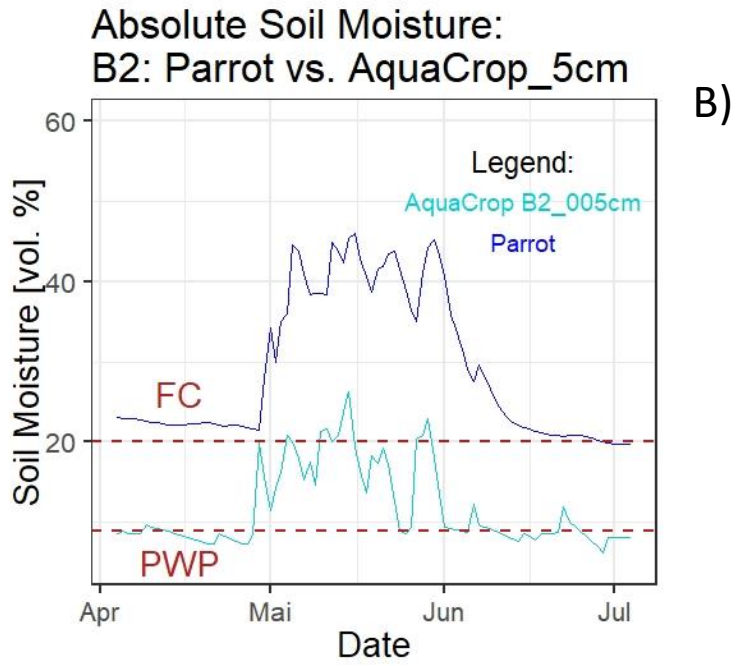
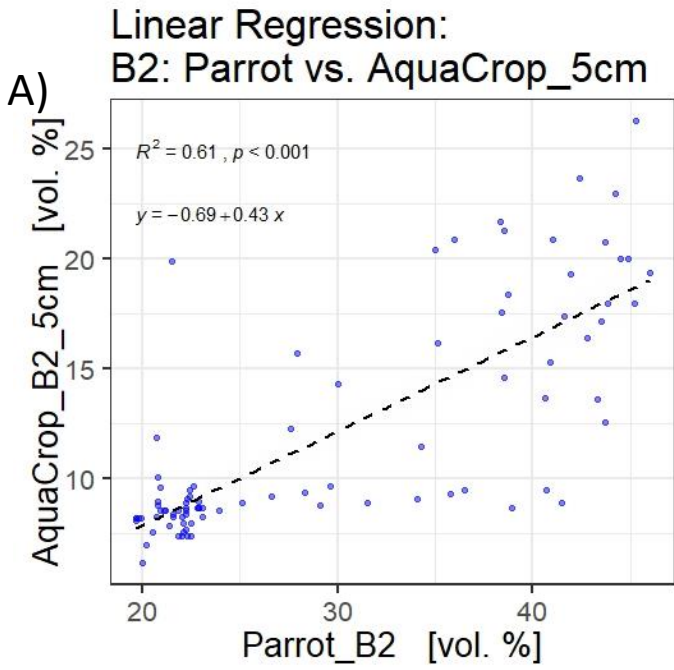
Annex 3: Statistical analysis of Parrots_rel vs. SWI_010_rel for A) linear regression, B) SM trend of Parrots and SWI_010_rel over time, C) residual plot, and D), precipitation graph



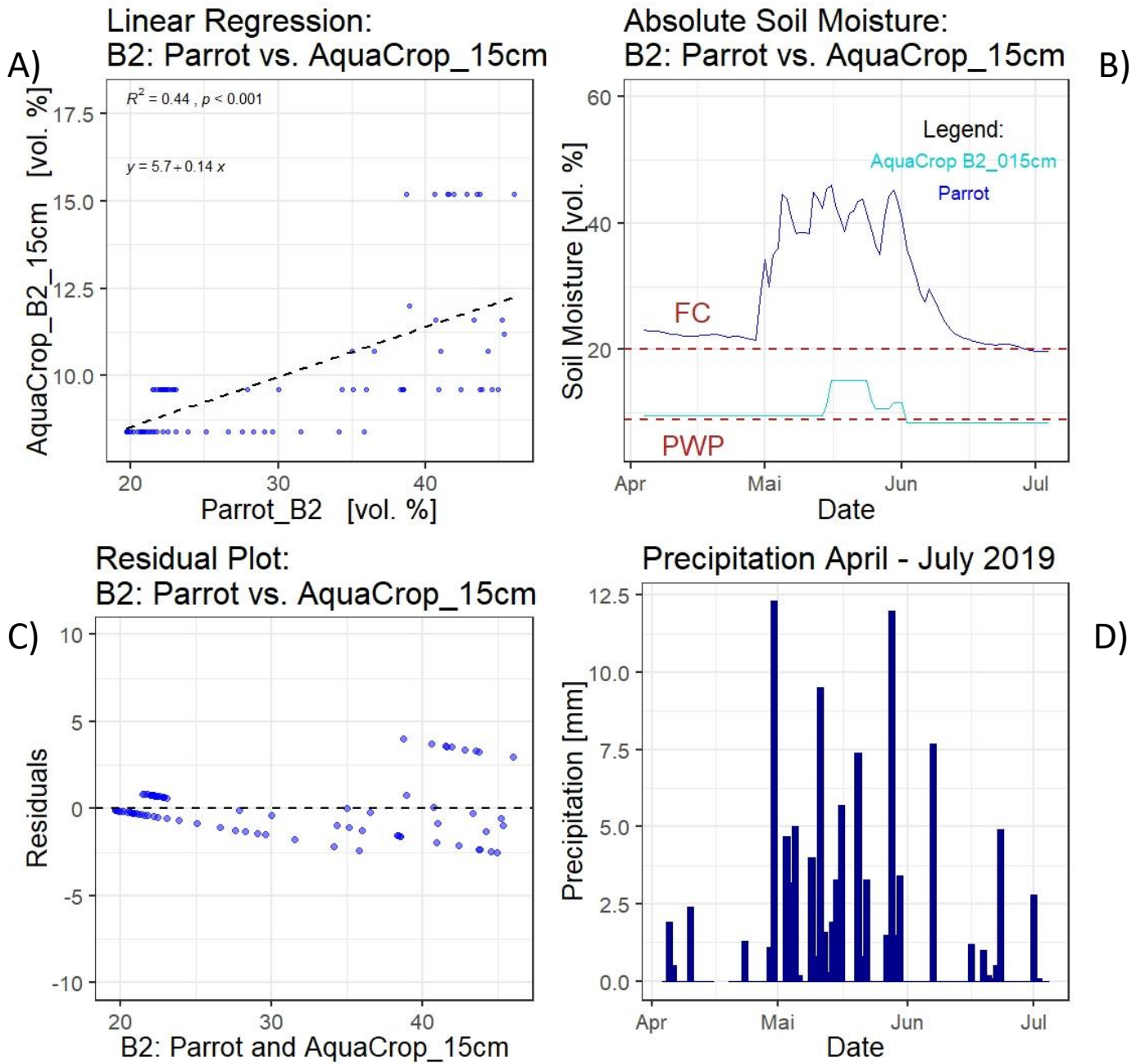
Annex 4: Statistical analysis of Parrots_rel vs. SMAP_rel_rel for A) linear regression, B) SM trend of Parrots and SMAP_rel over time, C) residual plot, and D), precipitation graph



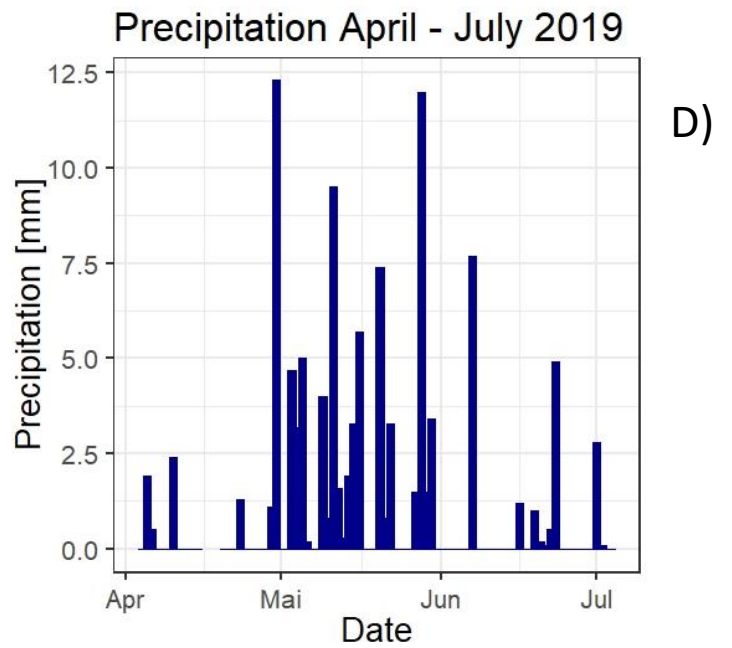
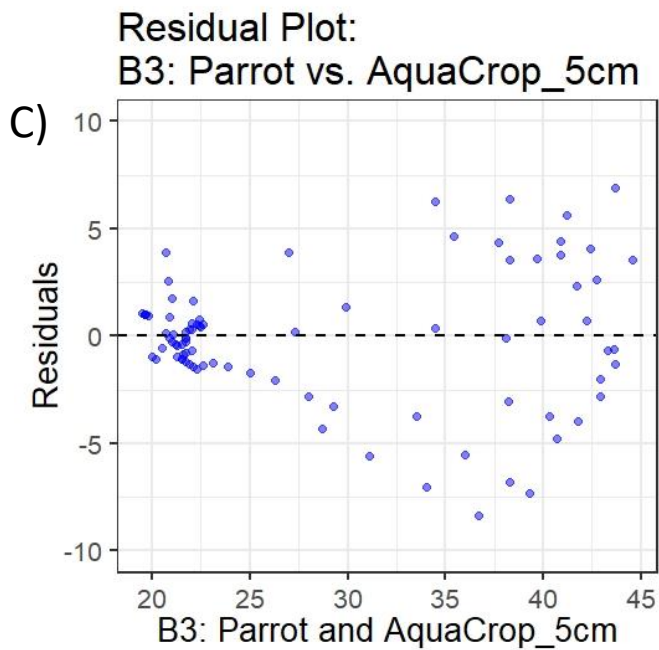
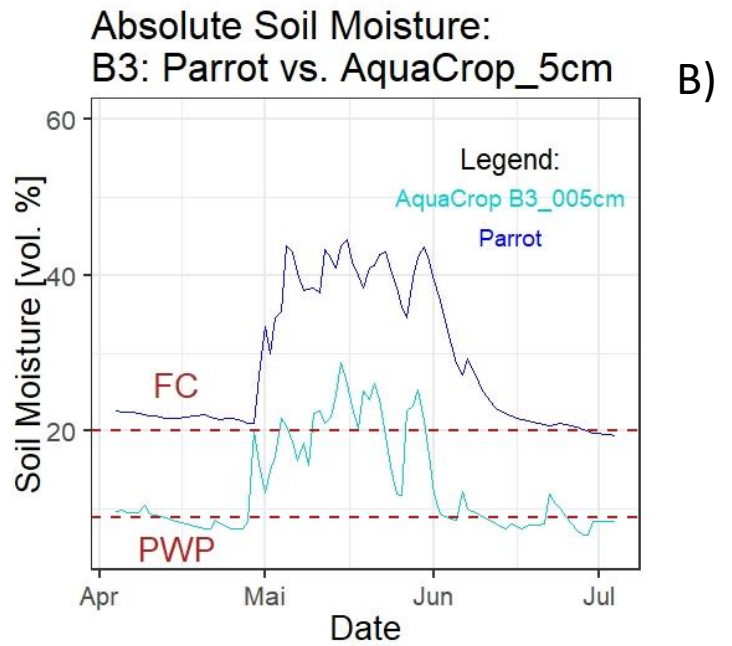
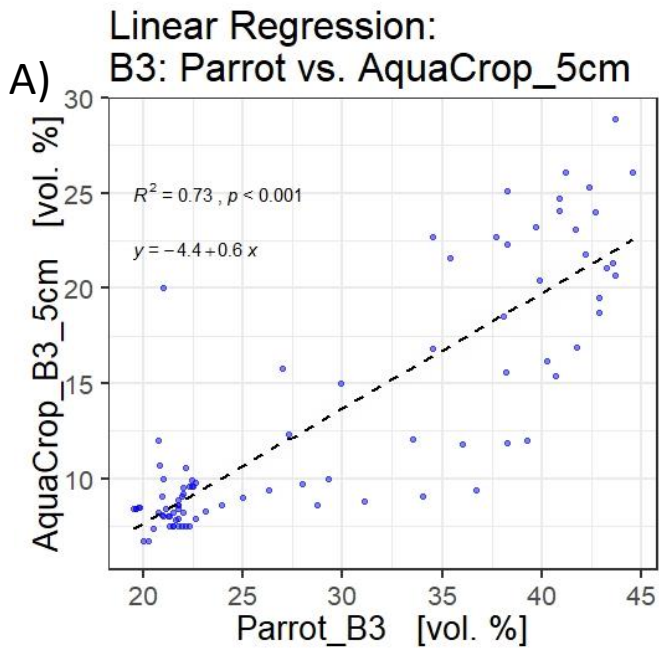
Annex 5: Statistical analysis of Parrots vs. AquaCrop_B1_15cm for A) linear regression, B) SM trend of Parrots and AquaCrop_B1_15cm over time, C) residual plot, and D), precipitation graph



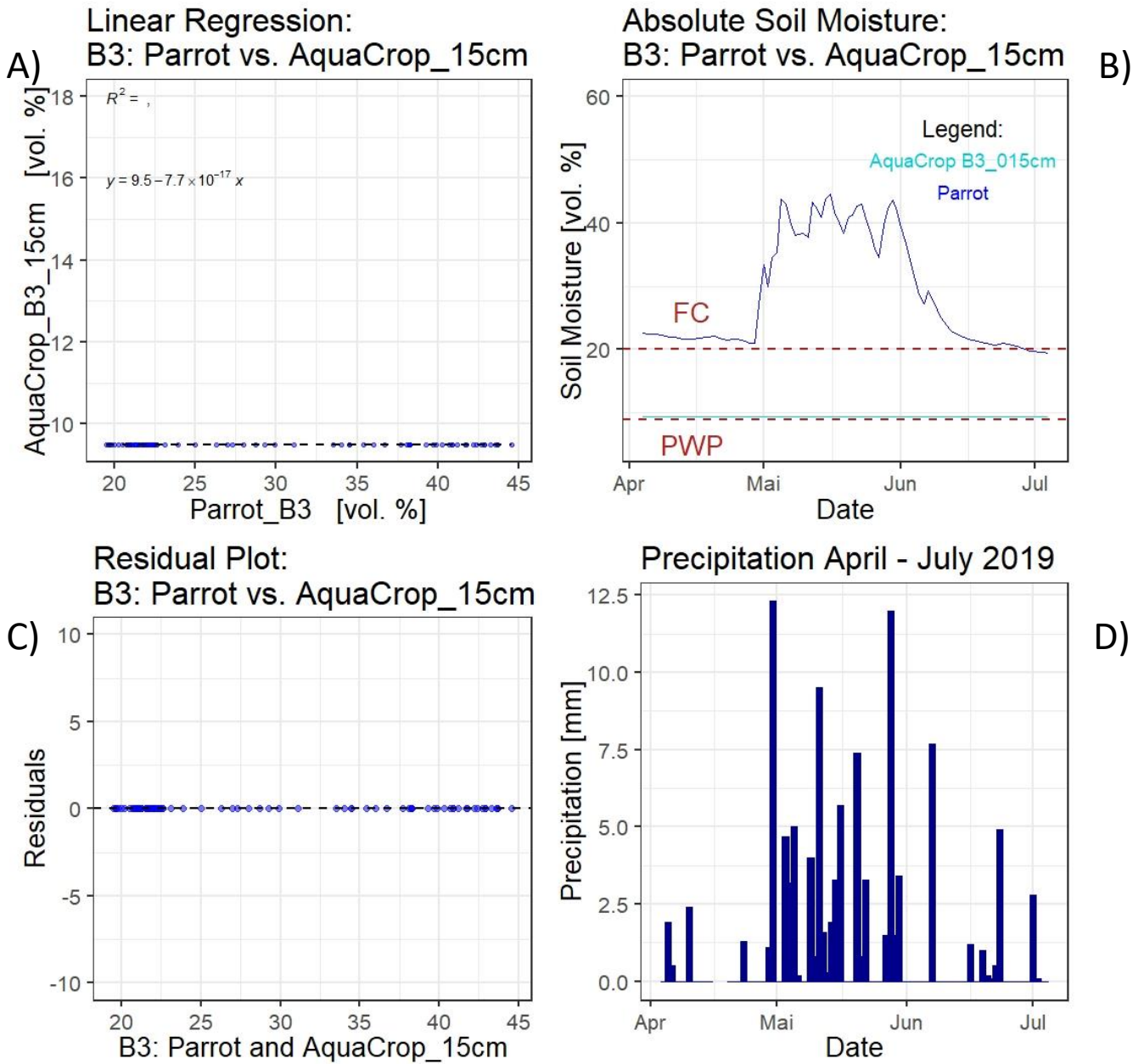
Annex 6: Statistical analysis of Parrots vs. AquaCrop_B2_5cm for A) linear regression, B) SM trend of Parrots and AquaCrop_B2_5cm over time, C) residual plot, and D), precipitation graph



Annex 7: Statistical analysis of Parrots vs. AquaCrop_B2_15cm for A) linear regression, B) SM trend of Parrots and AquaCrop_B2_15cm over time, C) residual plot, and D), precipitation graph

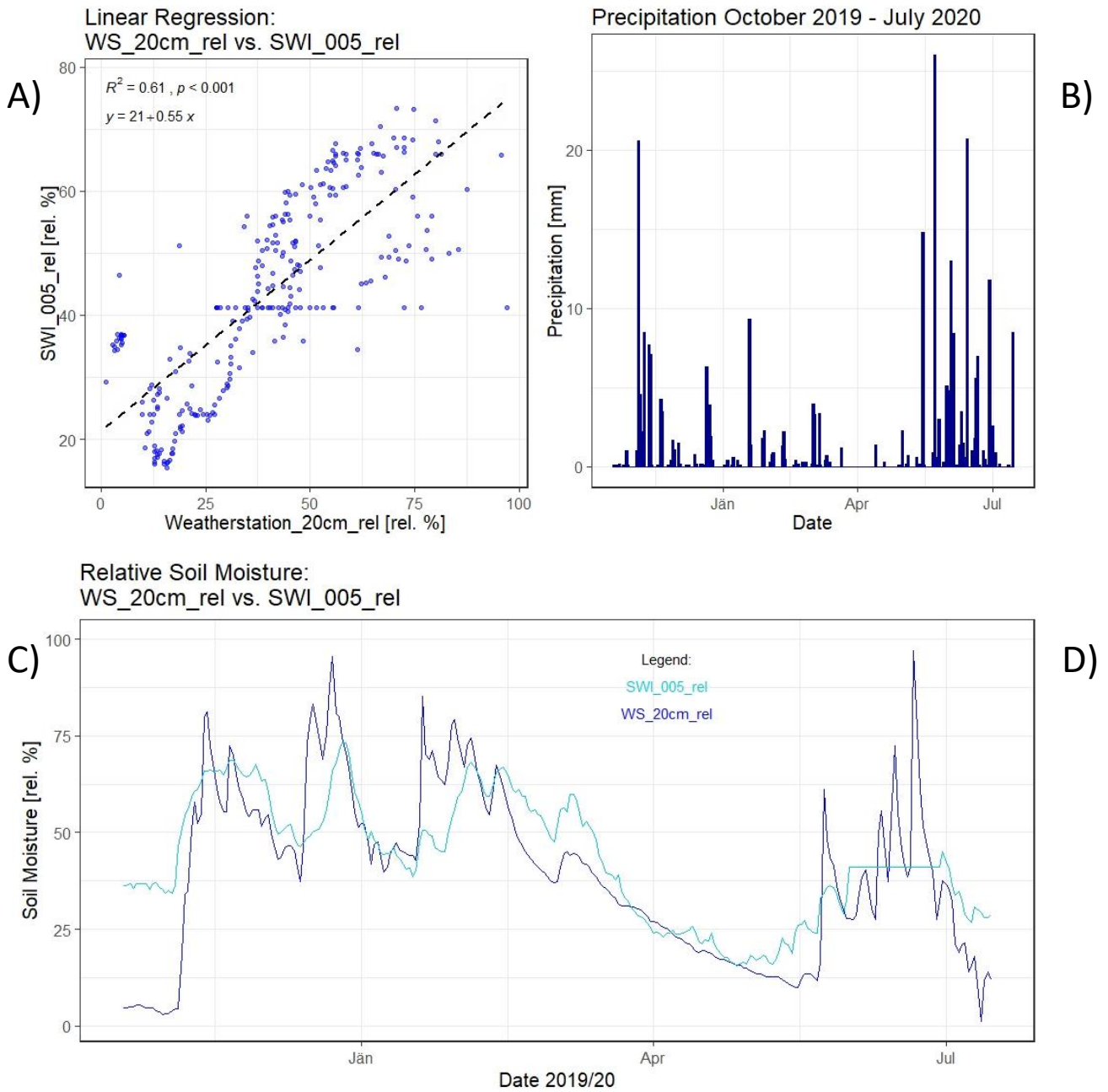


Annex 8: Statistical analysis of Parrots vs. AquaCrop_B3_5cm for A) linear regression, B) SM trend of Parrots and AquaCrop_B3_5cm over time, C) residual plot, and D), precipitation graph

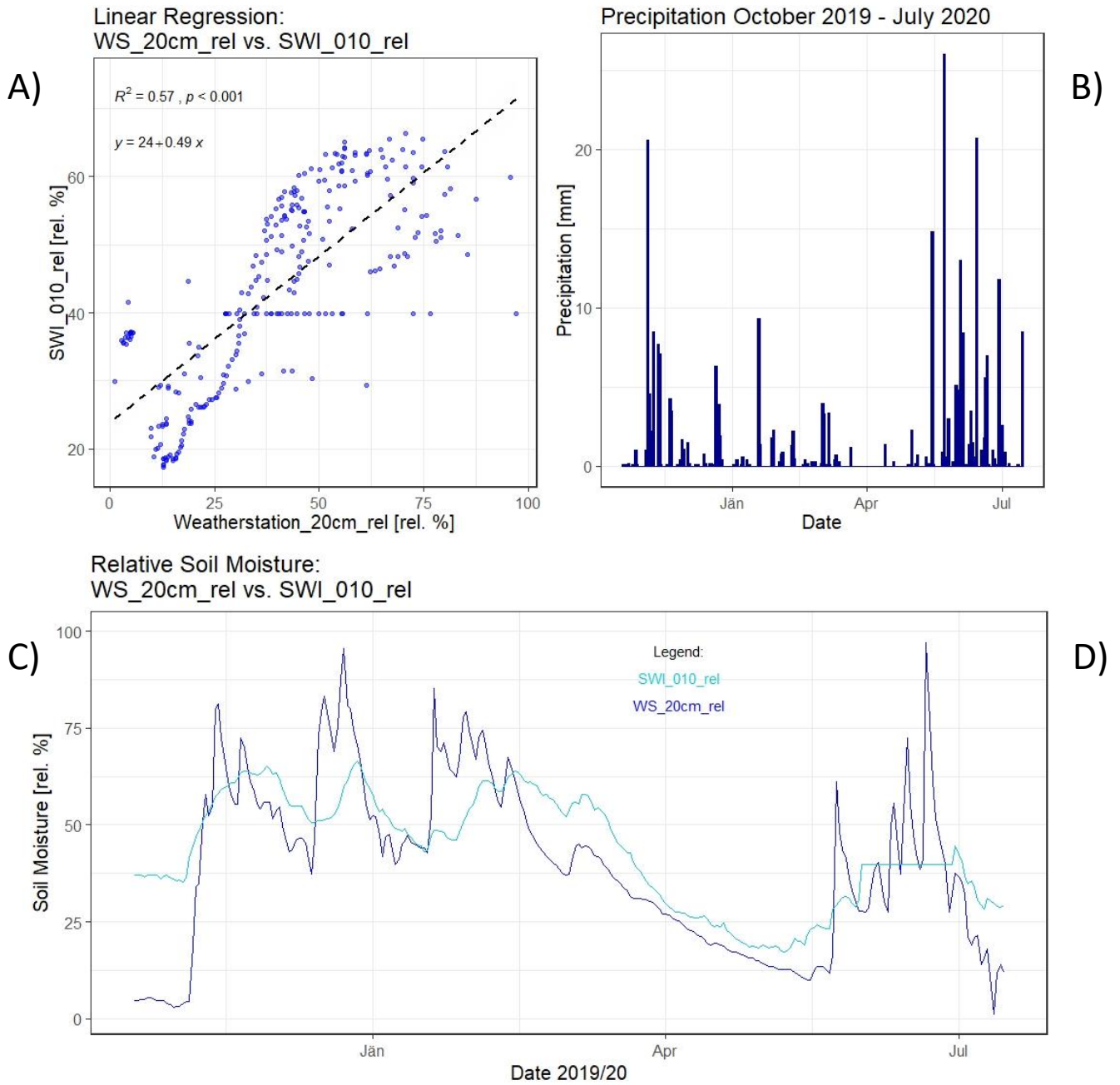


Annex 9: Statistical analysis of Parrots vs. AquaCrop_B3_15cm for A) linear regression, B) SM trend of Parrots and AquaCrop_B3_15cm over time, C) residual plot, and D), precipitation graph

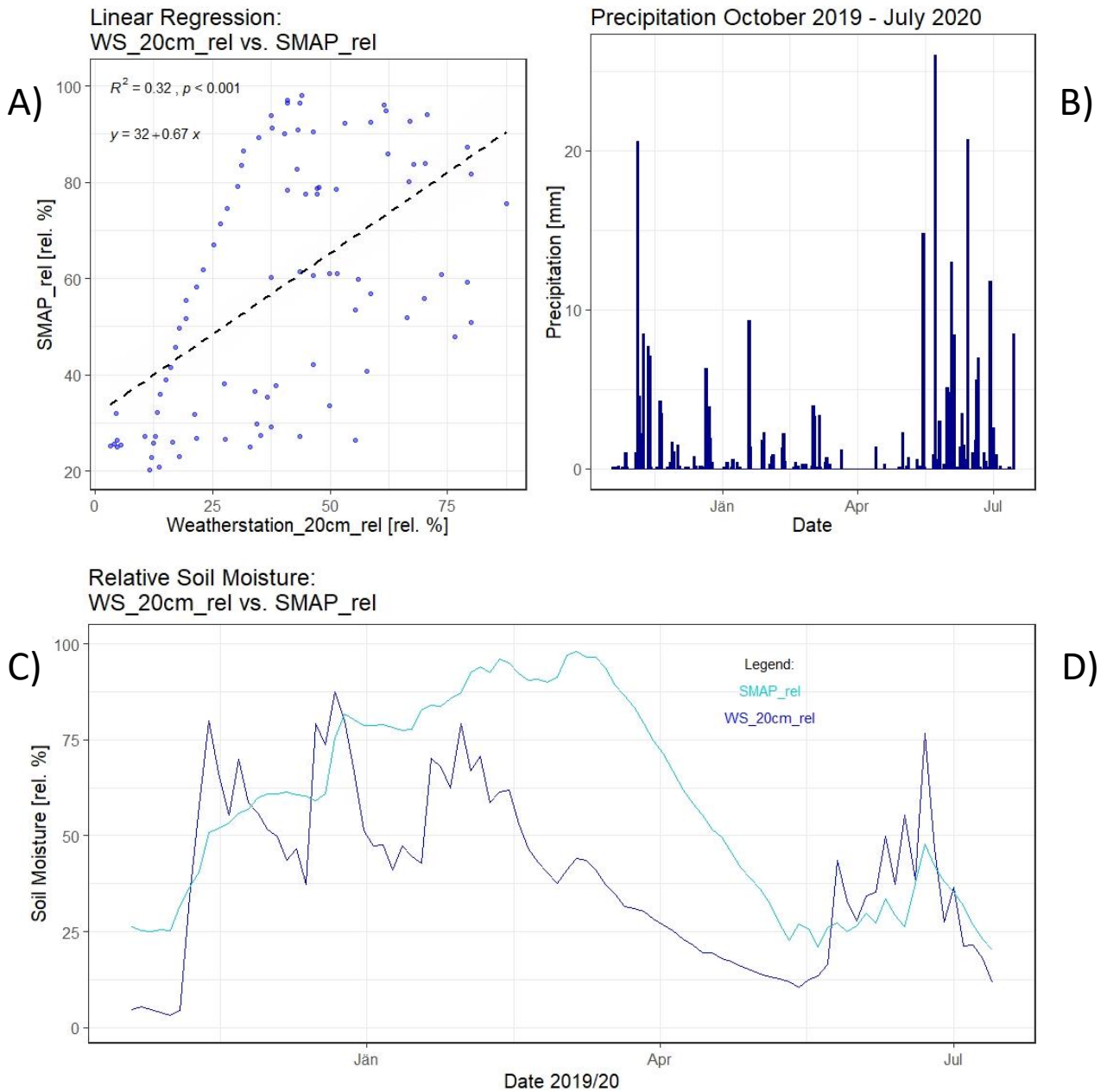
Vegetation Period 2020



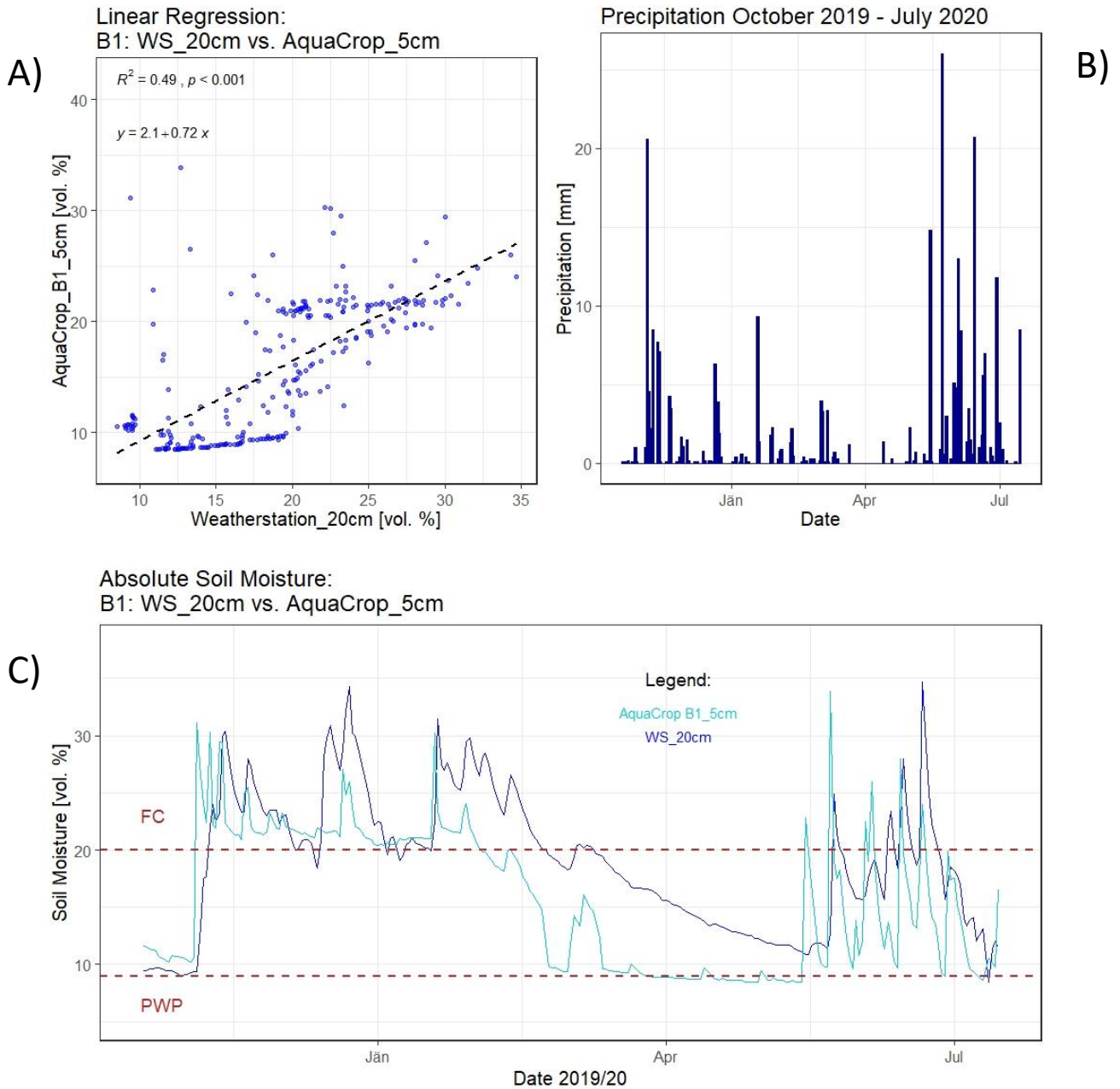
Annex 10: Statistical analysis of WS_20cm_rel vs. SWI_005_rel for A) linear regression, B) precipitation graph, and C) trend of WS_20cm_rel and SWI_005_rel



2380
 Annex 11: Statistical analysis of WS_20cm_rel vs. SWI_010_rel for A) linear regression, B) precipitation graph, and C) trend of WS_20cm_rel and SWI_010_rel

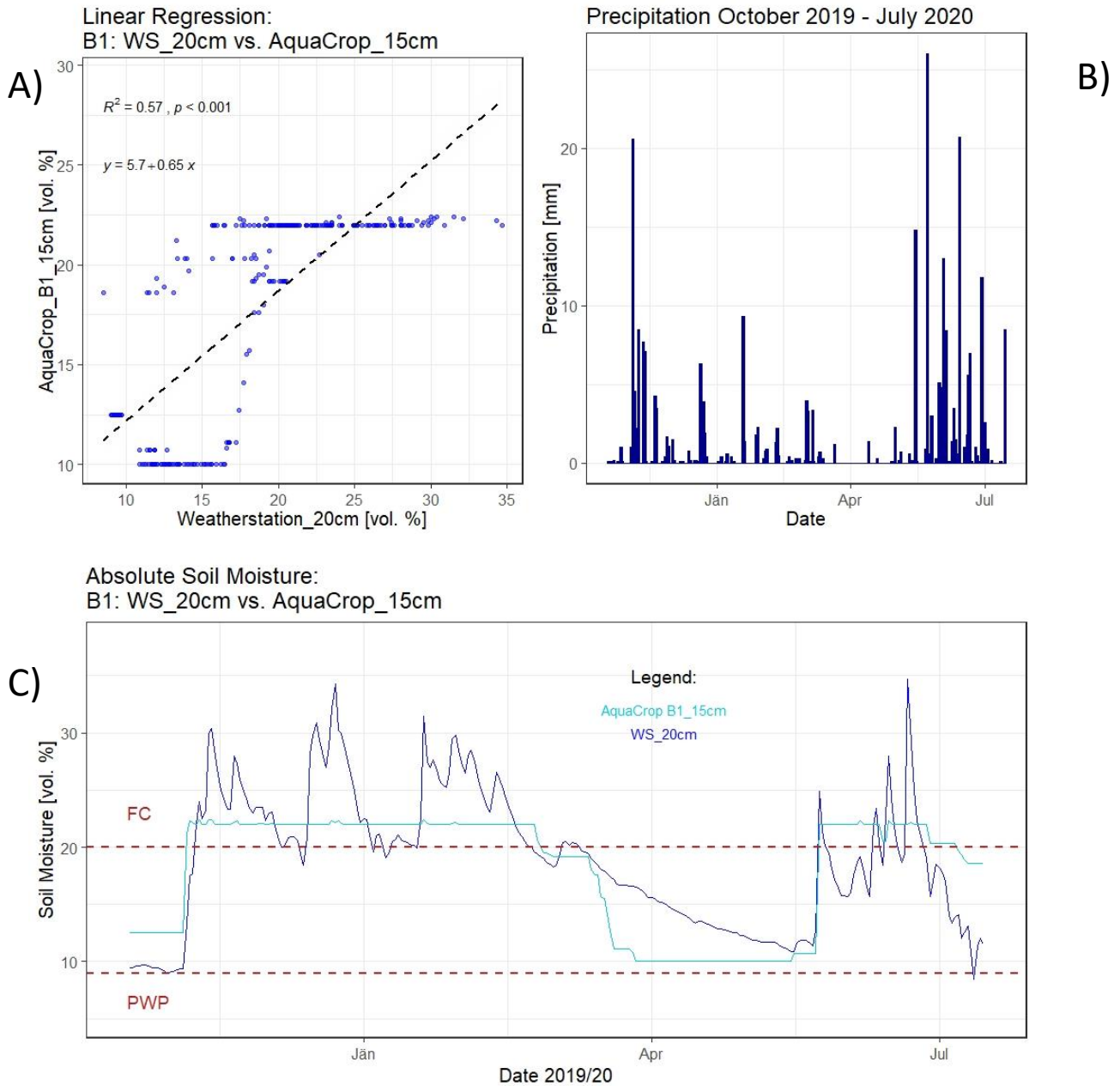


Annex 12: Statistical analysis of WS_20cm_rel and SMAP_rel for A) linear regression, B) precipitation graph, and C) trend of WS_20cm_rel and SMAP_rel

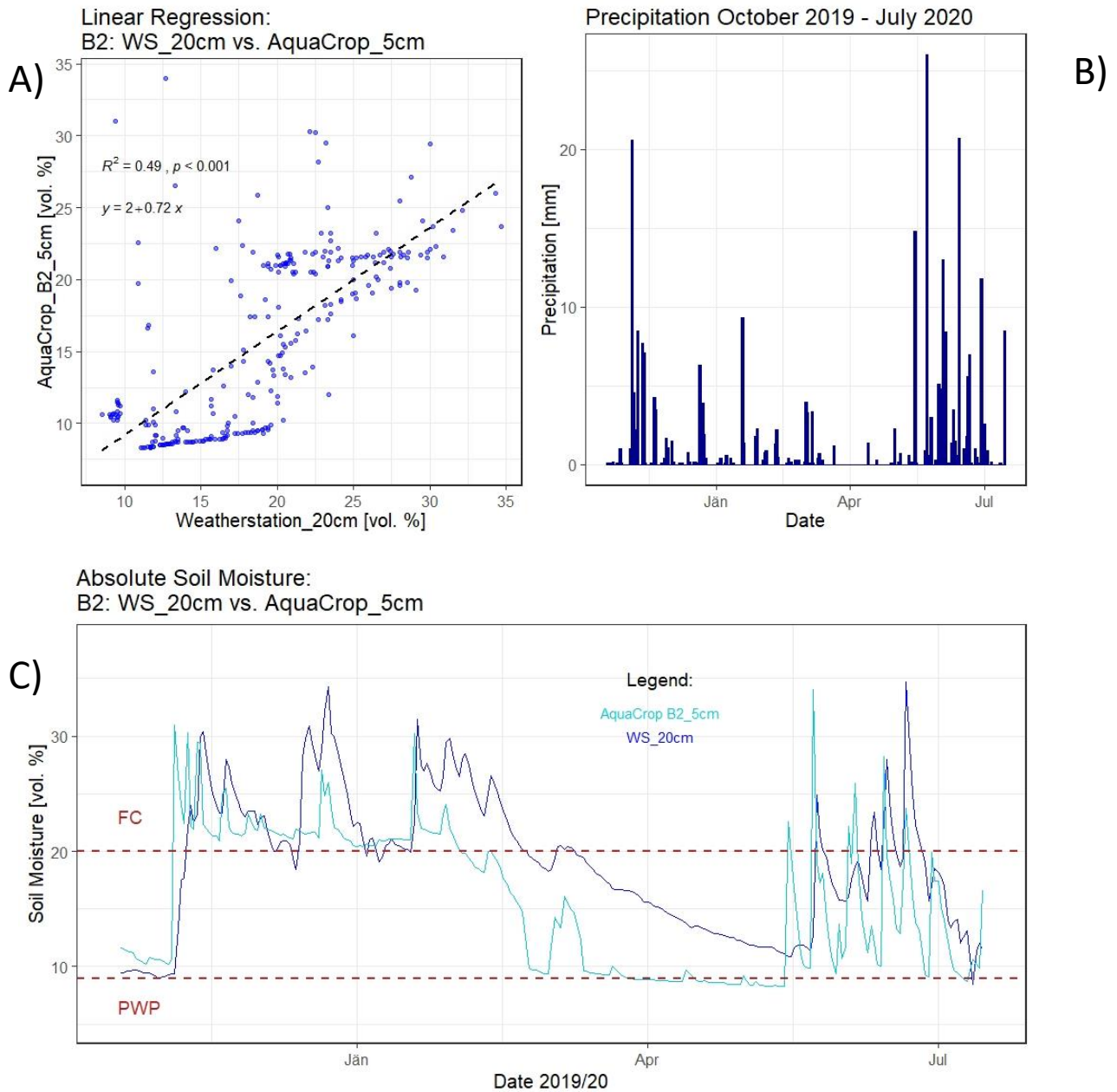


2390

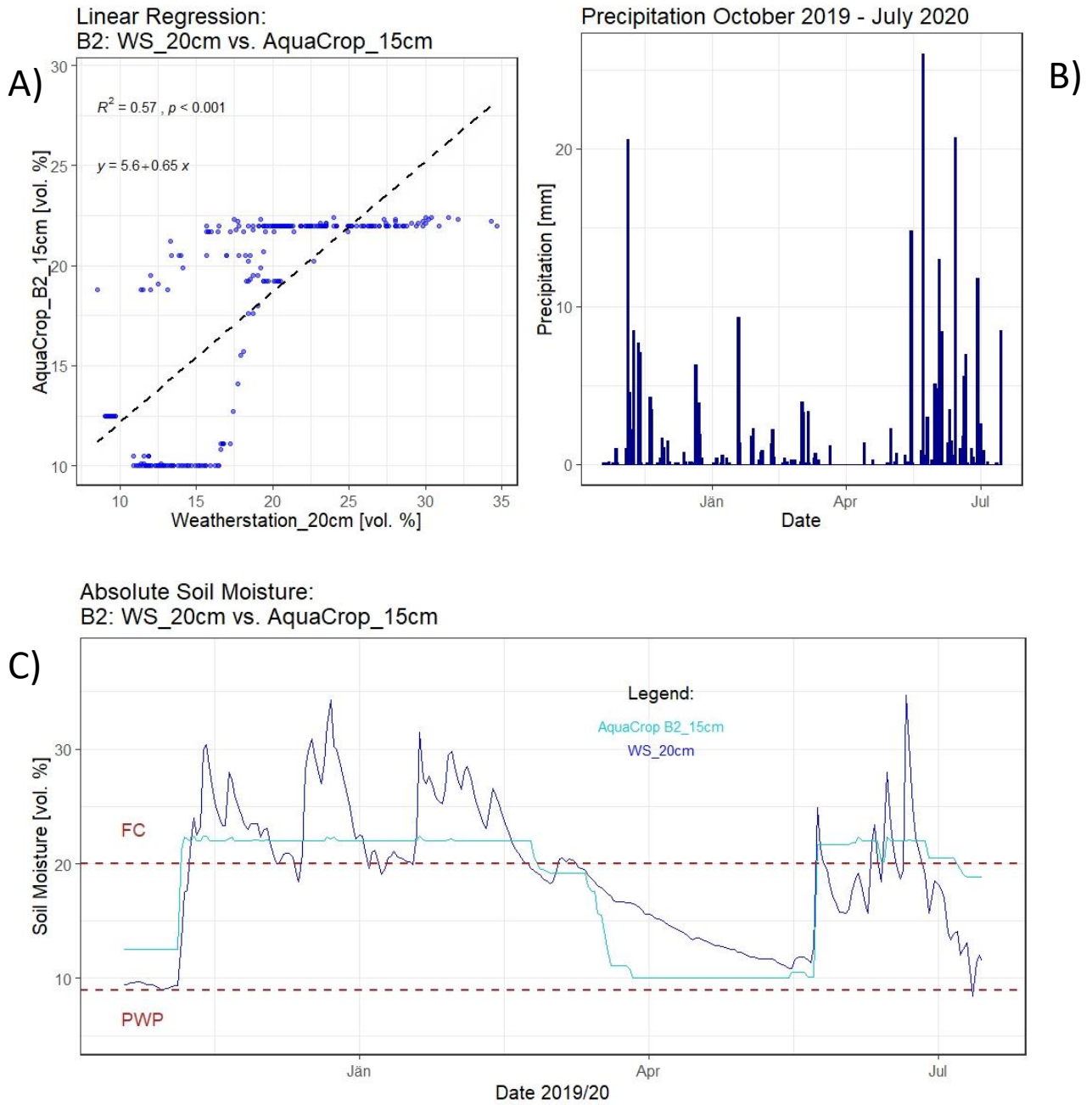
Annex 13: Statistical analysis of WS_20cm and AquaCrop_B1_5cm for A) linear regression, B) precipitation graph, and C) trend of WS_20cm and AquaCrop_B1_5cm



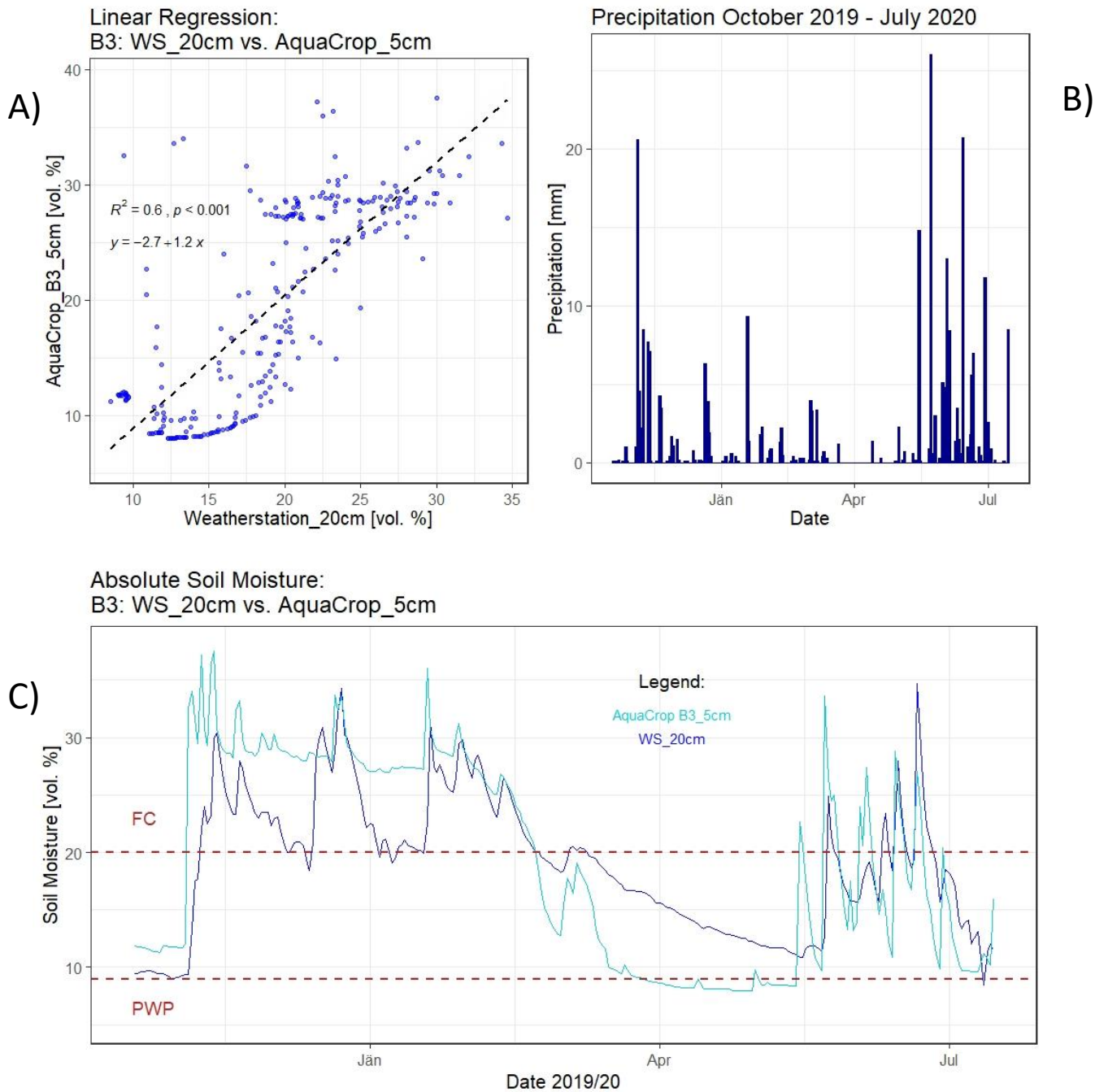
Annex 14: Statistical analysis of WS_20cm and AquaCrop_B1_15cm for A) linear regression, B) precipitation graph, and C) trend of WS_20cm and AquaCrop_B1_15cm



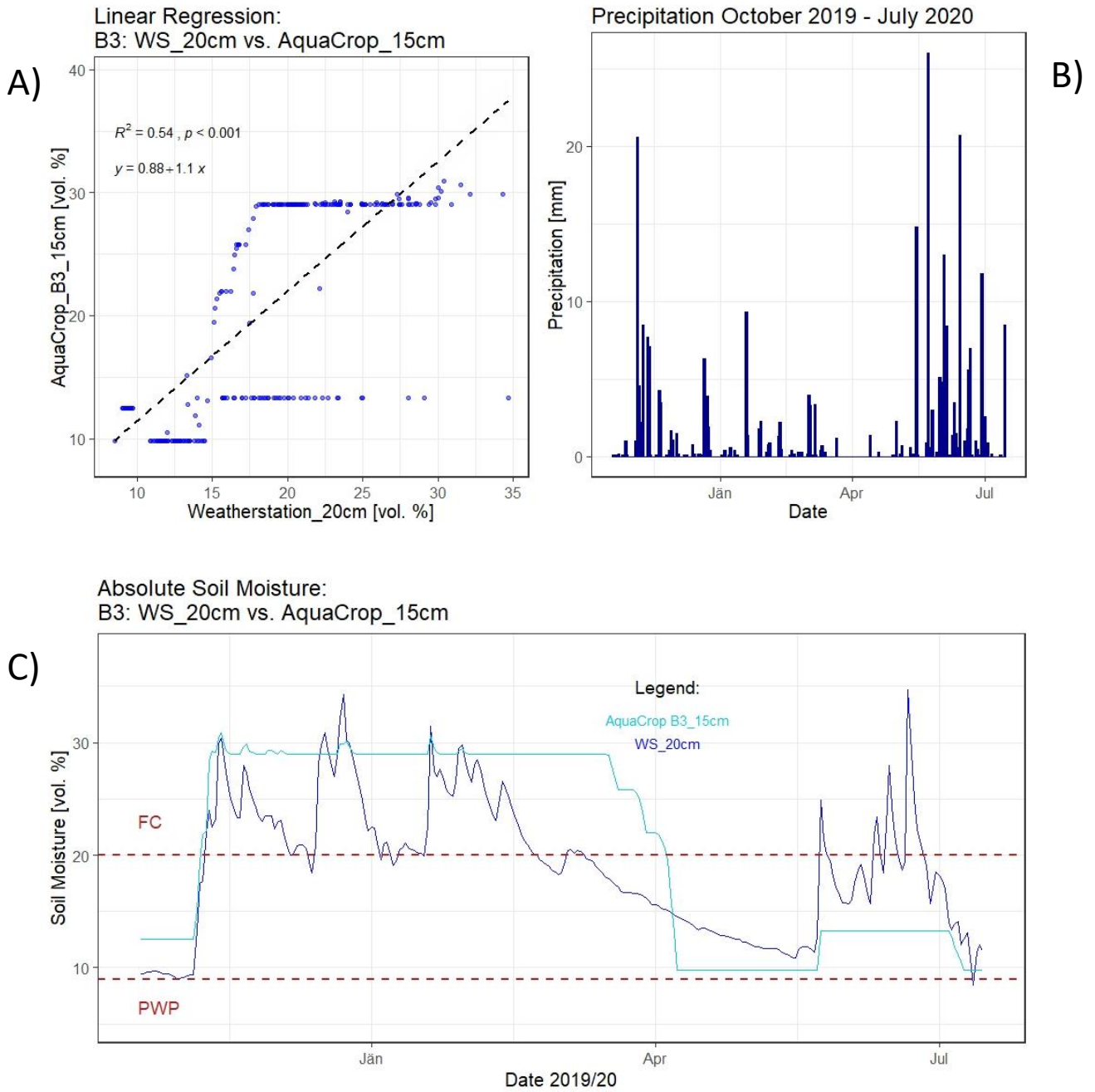
Annex 15: Statistical analysis of WS_20cm and AquaCrop_B2_5cm for A) linear regression, B) precipitation graph, and C) trend of WS_20cm and AquaCrop_B2_5cm



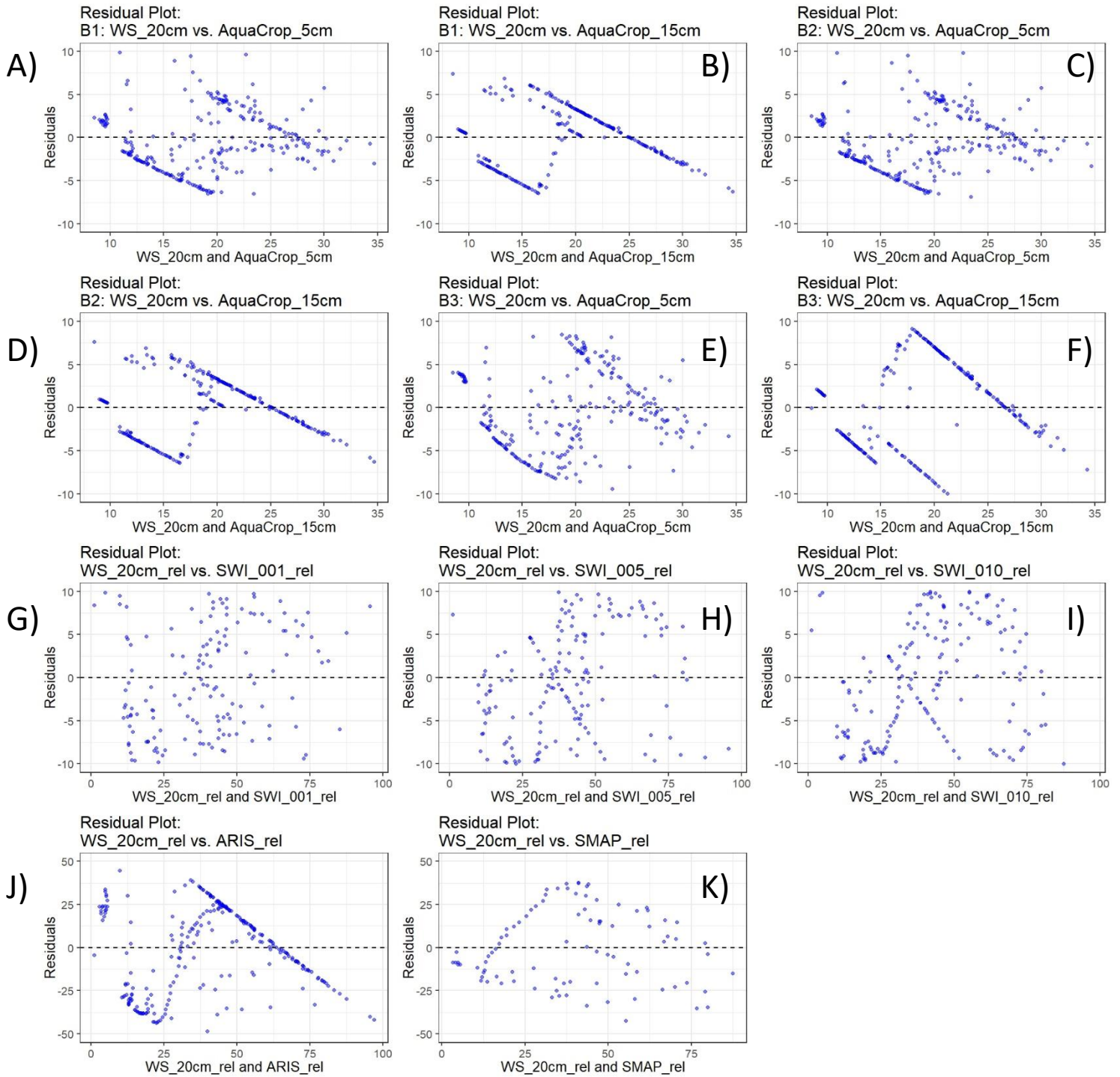
Annex 16: Statistical analysis of WS_20cm and AquaCrop_B2_15cm for A) linear regression, B) precipitation graph, and C) trend of WS_20cm and AquaCrop_B2_15cm



Annex 17: Statistical analysis of WS_20cm and AquaCrop_B3_5cm for A) linear regression, B) precipitation graph, and C) trend of WS_20cm and AquaCrop_B3_5cm

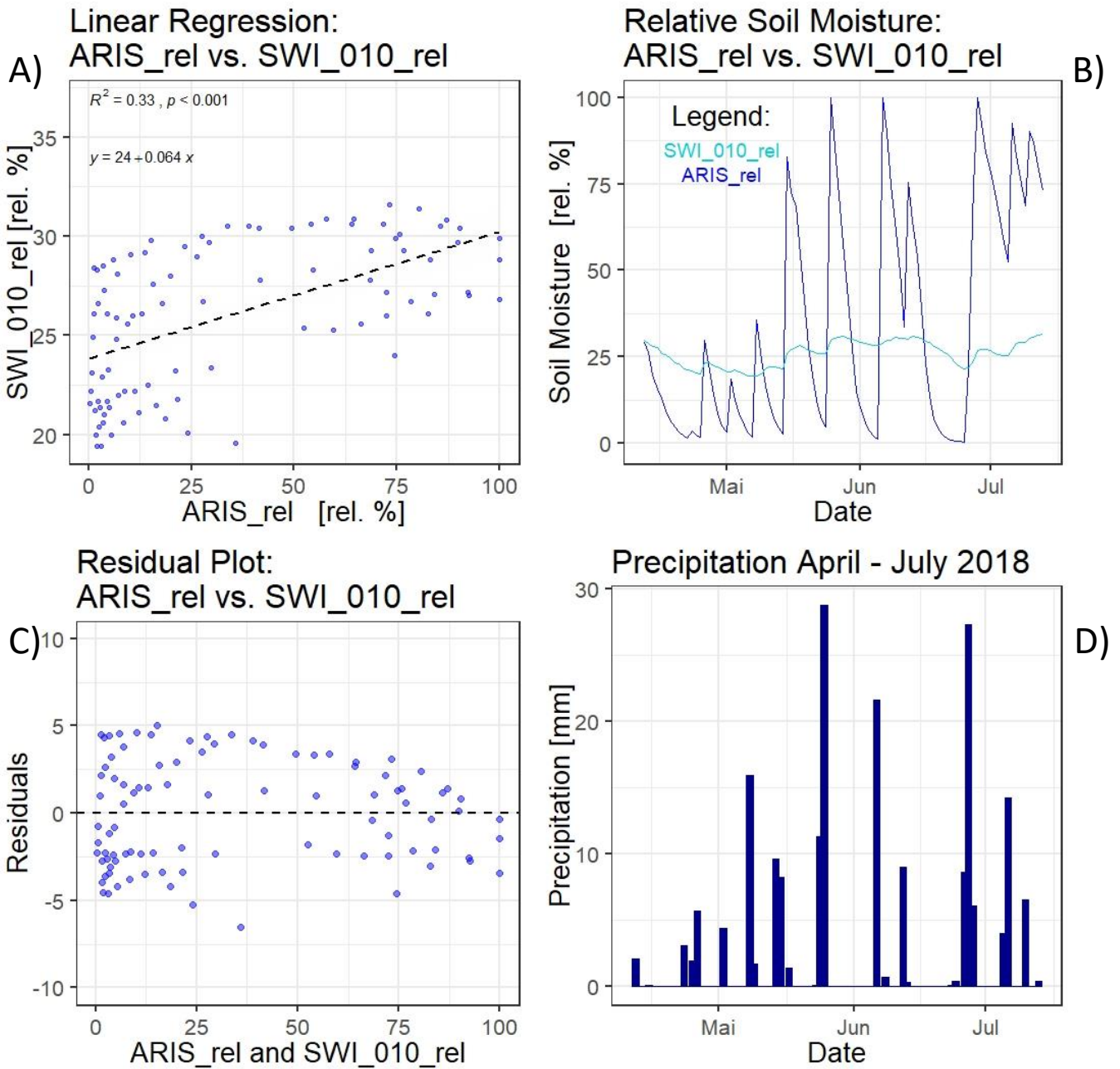


Annex 18: Statistical analysis of WS_20cm and AquaCrop_B3_15cm for A) linear regression, B) precipitation graph, and C) trend of WS_20cm and AquaCrop_B3_5cm

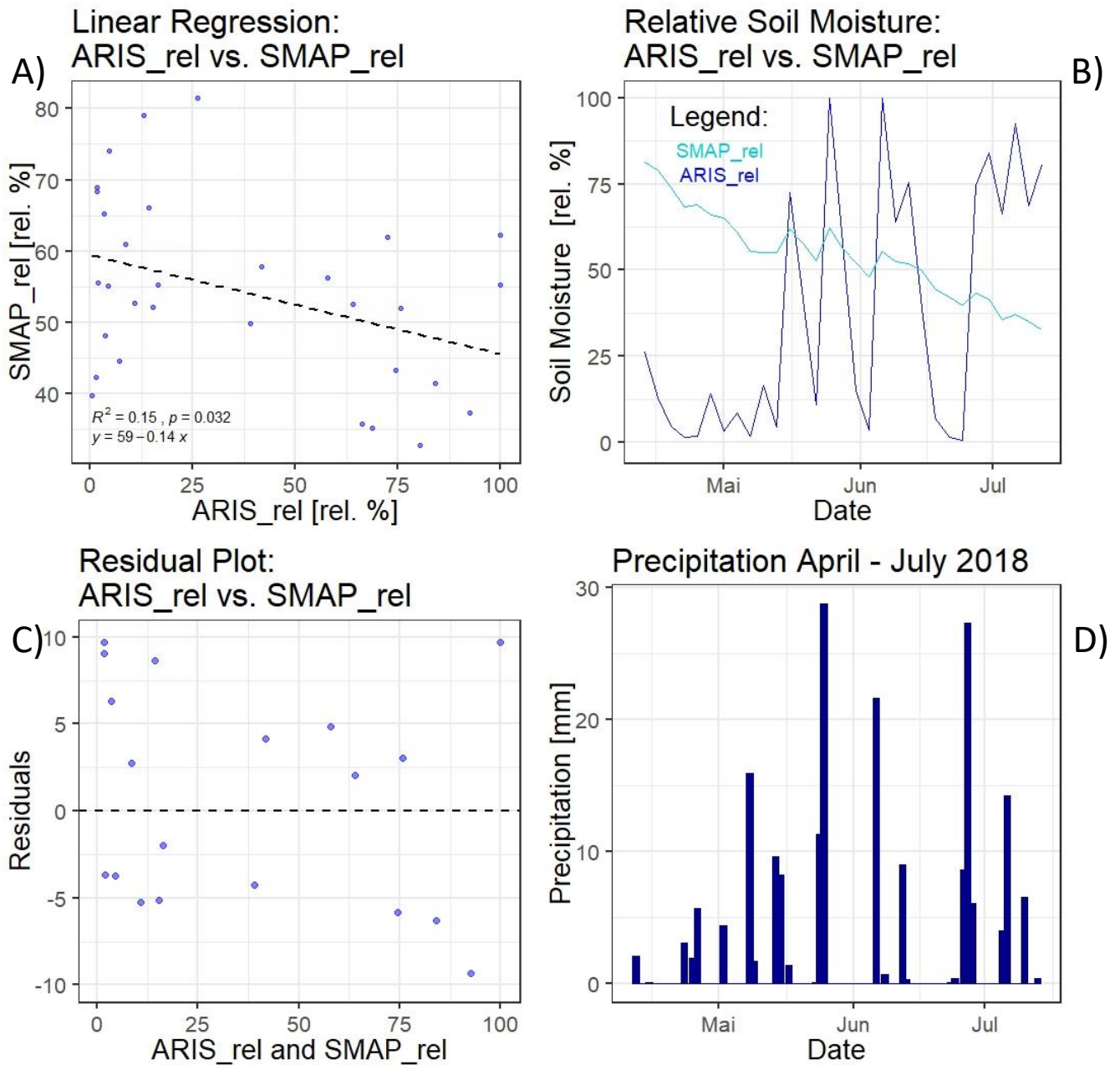


Annex 19: Statistical analysis of random distribution for WS_20cm and A) AquaCrop_B1_5cm, B) AquaCrop_B1_15cm, C) AquaCrop_B2_5cm, D) AquaCrop_B2_15cm, E) AquaCrop_B3_5cm, F) AquaCrop_B4_15cm, G) SWI_001_rel, H) SWI_005_rel, I) SWI_010_rel, J) ARIS_rel, and K) SMAP_rel

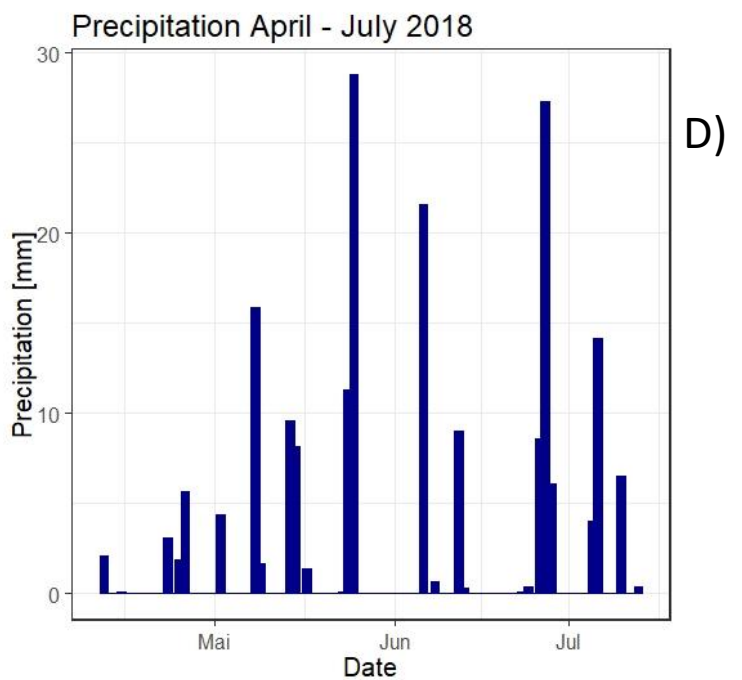
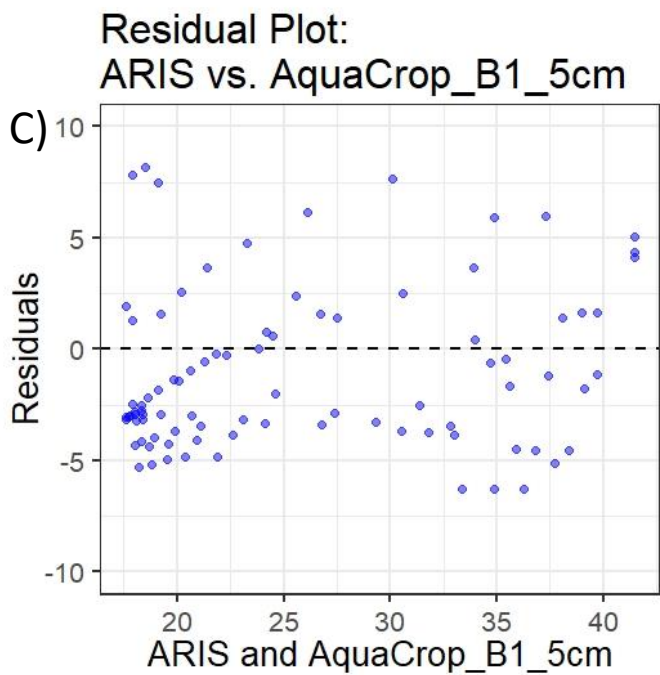
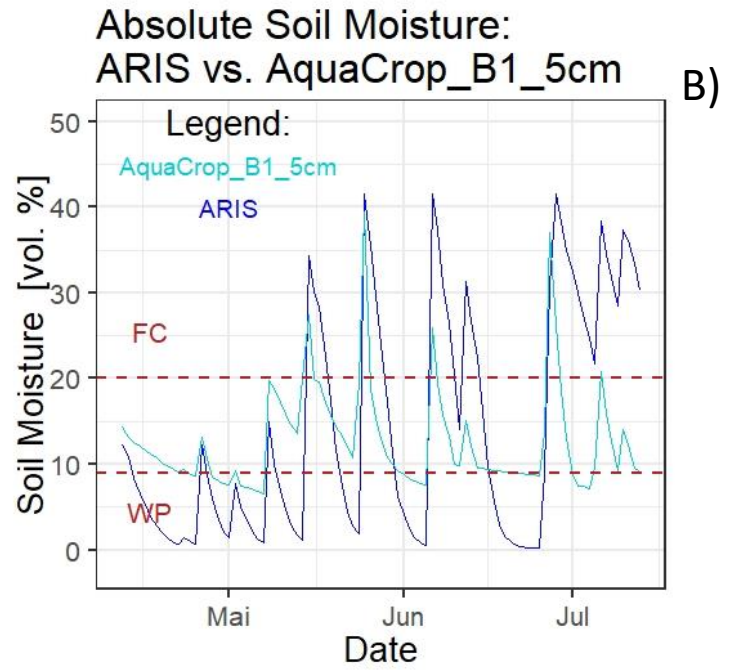
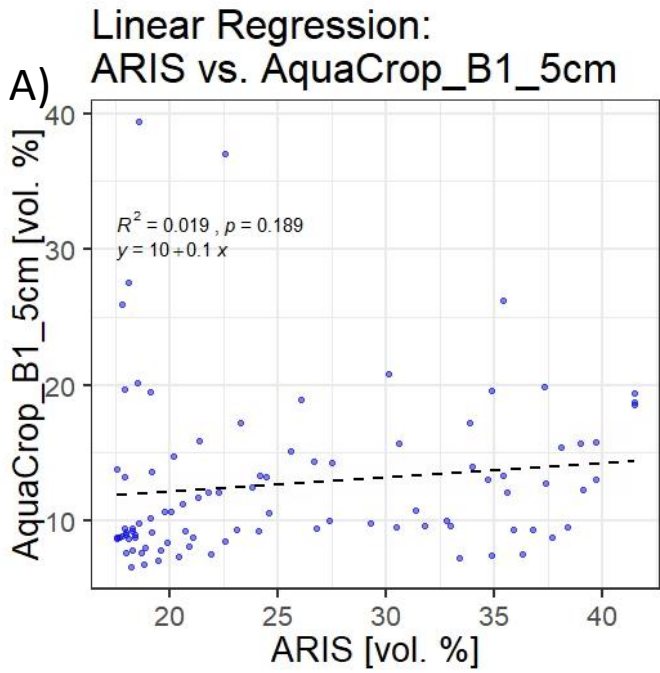
Vegetation Period 2018



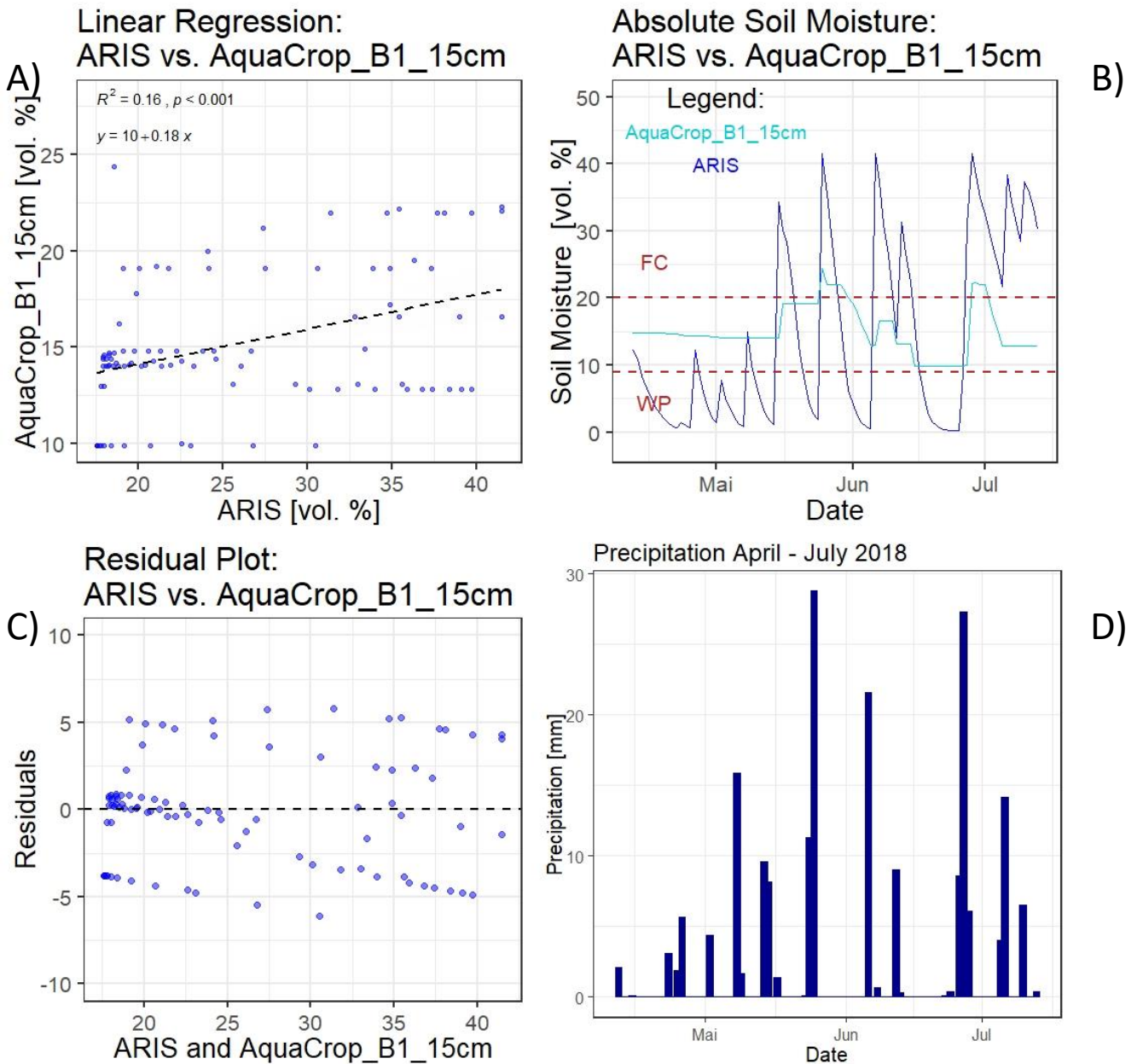
Annex 20: Statistical analysis of ARIS_rel vs. SWI_010_rel for A) linear regression, B) SM trend of ARIS_rel and SWI_010_rel over time, C) residual plot, and D), precipitation graph



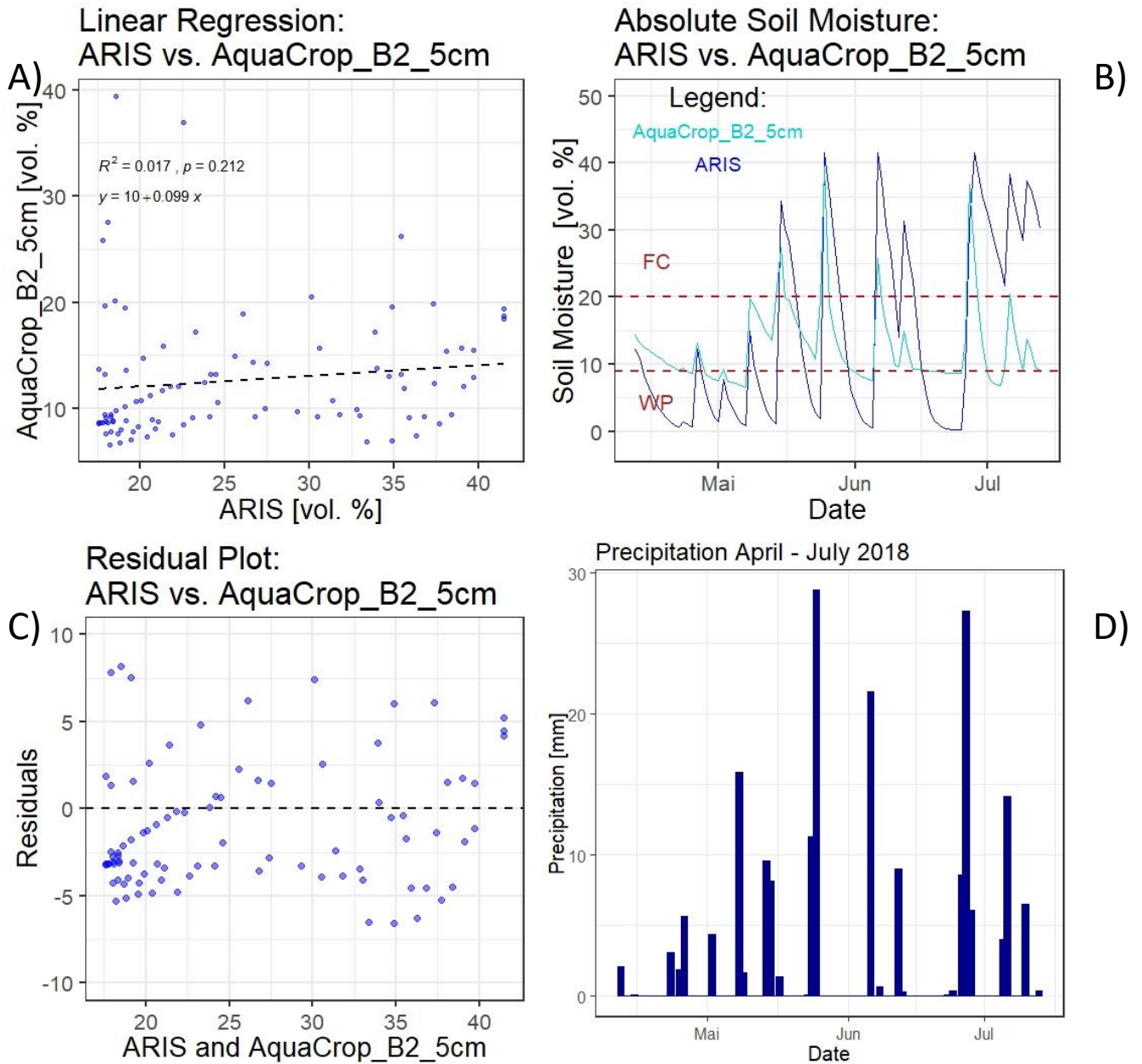
Annex 21: Statistical analysis of ARIS_rel vs. SMAP_rel for A) linear regression, B) SM trend of ARIS_rel and SMAP_rel over time, C) residual plot, and D), precipitation graph



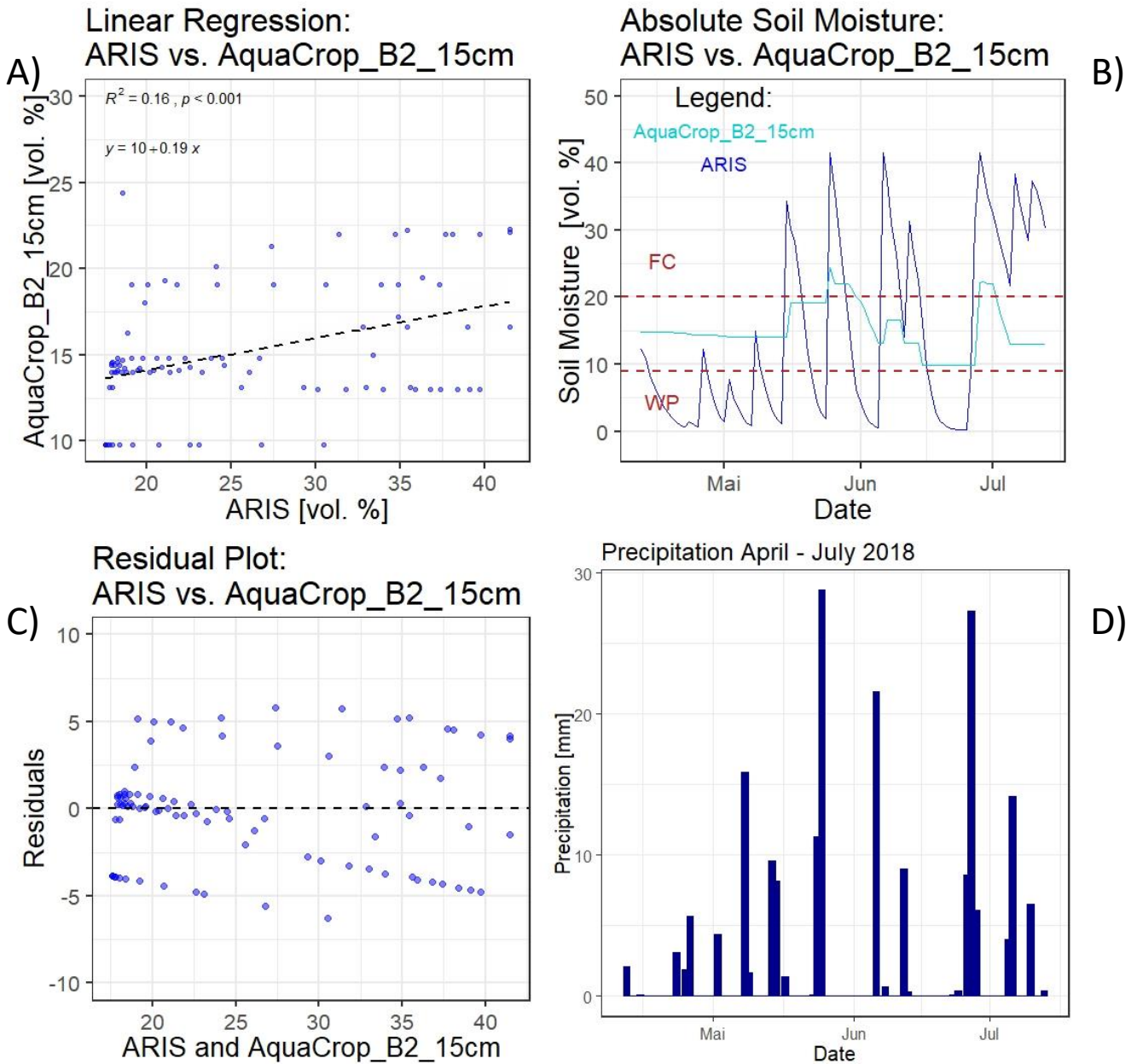
Annex 22: Statistical analysis of ARIS vs. AquaCrop_B1_5cm for A) linear regression, B) SM trend of ARIS and AquaCrop_B1_5cm over time, C) residual plot, and D), precipitation graph



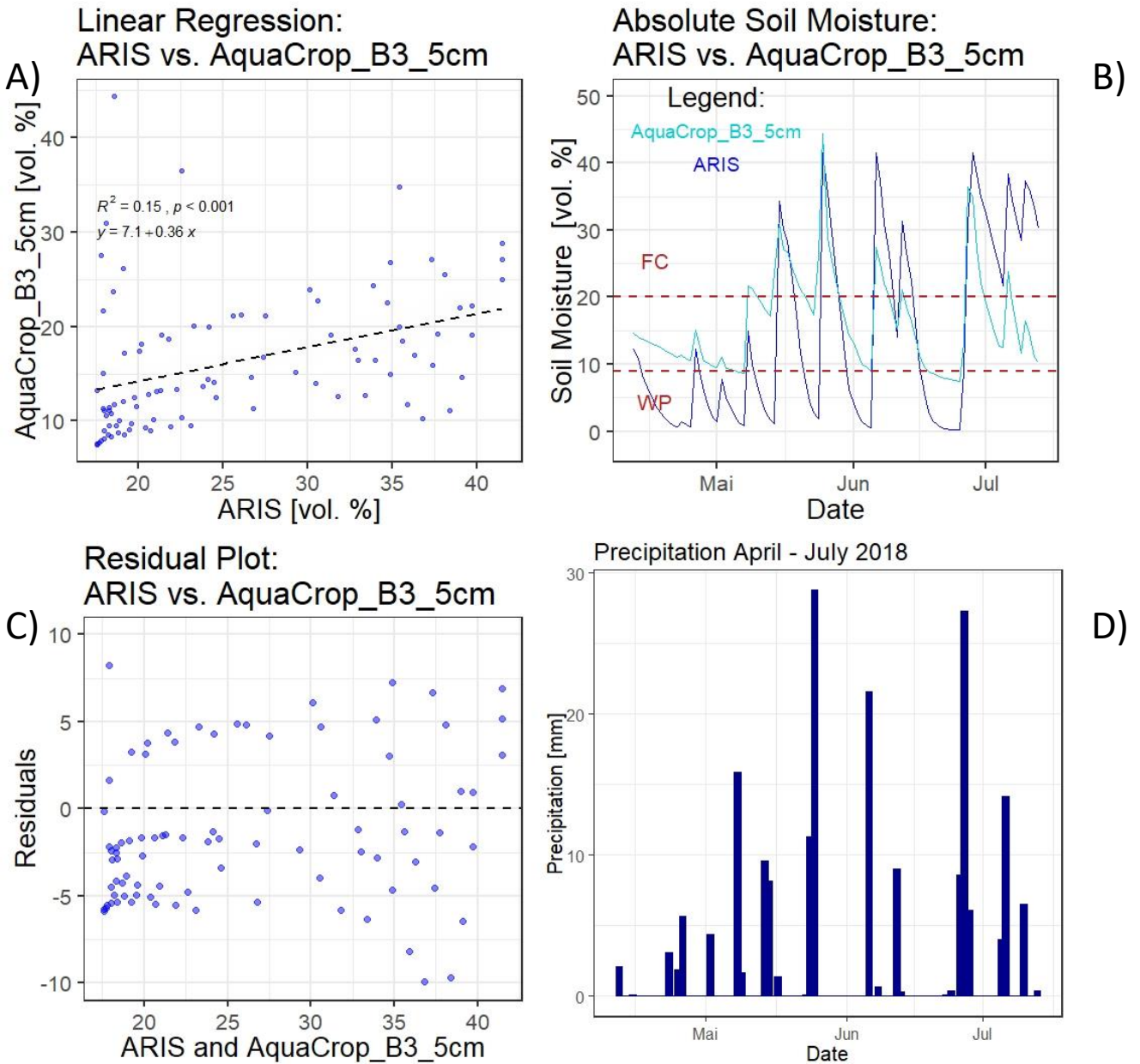
Annex 23: Statistical analysis of ARIS vs. AquaCrop_B1_15cm for A) linear regression, B) SM trend of ARIS and AquaCrop_B1_15cm over time, C) residual plot, and D), precipitation graph



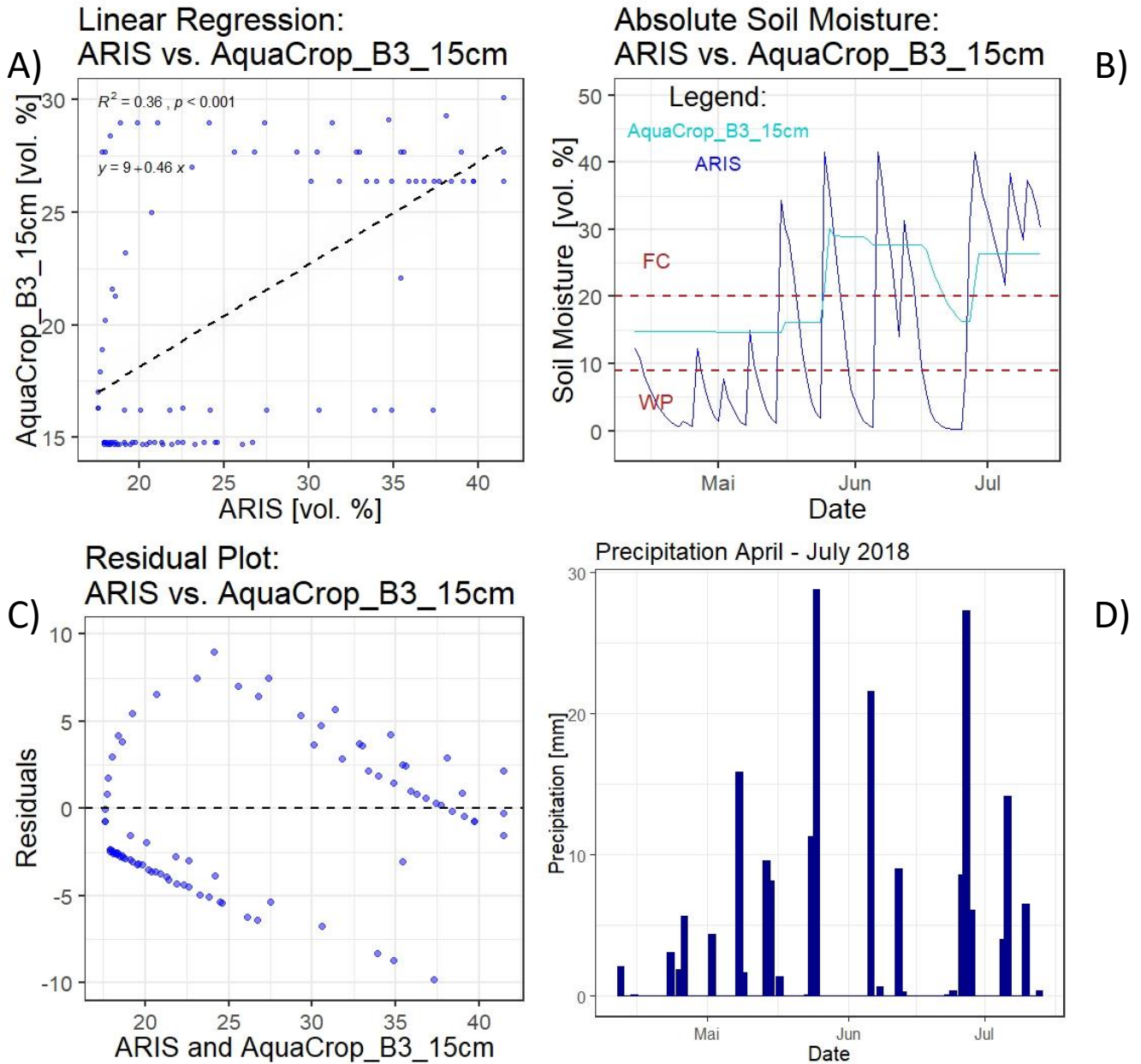
Annex 24: Statistical analysis of ARIS vs. AquaCrop_B2_5cm for A) linear regression, B) SM trend of ARIS and AquaCrop_B2_5cm over time, C) residual plot, and D), precipitation graph



Annex 25: Statistical analysis of ARIS vs. AquaCrop_B2_15cm for A) linear regression, B) SM trend of ARIS and AquaCrop_B2_15cm over time, C) residual plot, and D), precipitation graph



Annex 26: Statistical analysis of ARIS vs. AquaCrop_B3_5cm for A) linear regression, B) SM trend of ARIS and AquaCrop_B3_5cm over time, C) residual plot, and D), precipitation graph



Annex 27: Statistical analysis of ARIS vs. AquaCrop_B3_15cm for A) linear regression, B) SM trend of ARIS and AquaCrop_B3_15cm over time, C) residual plot, and D), precipitation graph

List of Acronyms

B

B *Above Ground Biomass*
BVW *Landwirtschaftliche Bundesversuchswirtschaften GmbH*

C

CC *Canopy Cover*

E

E *Soil Evaporation*
ETa *Actual Evaporation*
ETc *Maximum Crop Evapotranspiration*
ETo *Reference Evapotranspiration*
ETx *Maximum Evapotranspiration*

F

FC *Field Capacity*
FDR *Frequency Domain Reflectometry*
FIPAR *Fraction Intercepted of Photosynthetically Active Radiation*

G

GC *Ground Cover*
GDD *Growing Degree Days*
GEE *Google Earth Engine*
GIS *Geo-Information Systems*

H

HI
..... *Harvest Index*

K

kPa *Kilo Pascal*

L

LAI *Leaf Area Index*

M

Met-station *Meteorologic Station*

N

NDVI.....*Normalized Digital Vegetation Index*
NIR.....*Near-Infrared*

P

Parrot.....*Parrot Flower Power Sensor*
PWP.....*Permanent Wilting Point*

R

RSS.....*Relative Soil Saturation*

S

SM.....*Soil Moisture*
SWI.....*Soil Water Index*

T

TDR.....*Time Domain Reflectometry*
TIR.....*Thermal-Infrared*
Tn.....
.....*Maximum Air Temperature*
Tr.....
.....*Transpiration*
Tx.....
.....*Minimum Air Temperature*

W

WP.....*Water Productivity*

Y

Y.....*Crop Yield*
Ya.....*Actual Yield*
Yx.....
.....*Maximum Yield*

Z

ZAMG.....*Zentralanstalt für Meteorologie und Geodynamik*

Table of Contents

Equations

EQUATION 1: GRAVIMETRIC WATER CONTENT (θ_g OR W)	12
EQUATION 2: DEFINITION OF VOLUMETRIC WATER CONTENT (θ_v)	12
EQUATION 3: CALCULATION OF VOLUMETRIC WATER CONTENT (θ_v)	13
EQUATION 4: TRANSIT TIME THROUGH MATTER	22
EQUATION 5: CAPACITANCE CALCULATION.....	23
EQUATION 6: CALCULATION OF CHARGE TIME T OF THE CAPACITOR.....	23
EQUATION 7: PARALLEL PLATE CAPACITOR AND ITS CAPACITANCE.....	24
EQUATION 8: LINEAR FUNCTION OF THE DIELECTRIC PERMITTIVITY	24
EQUATION 9: TDR DETERMINES K BASED ON T ALONG THE TRANSMISSION LINE	24
EQUATION 10: RELATIONSHIP BETWEEN LIGHT TRANSMISSION AND LEAF AREA.....	32
EQUATION 11: STANDARD OF CROP YIELD RESPONSE TO WATER.....	37
EQUATION 12: DETERMINATION OF MAXIMUM CROP EVAPOTRANSPIRATION.....	37
EQUATION 13: CALCULATION OF BIOMASS IN AQUACROP	38
EQUATION 14: CALCULATION OF YIELD IN AQUACROP	38
EQUATION 15: POLYNOMIAL REGRESSION OF TDR VS. PARROT.....	45
EQUATION 16: CALCULATION OF VOLUMETRIC SOIL MOISTURE CONTENT (θ), BASED ON THE DEGREE OF SATURATION (ms), AND SOIL POROSITY (ϕ), (SOURCE: WAGNER ET AL., 2013).	46

Figures

FIGURE 1: COMPONENTS OF A KNOWN VOLUME OF SOIL (SOURCE: METER, 2020).....	13
FIGURE 2: MAP OF THE STUDY AREA LOCATED IN THE DISTRICT OF GROß-ENZERSDORF, MARCHFELD, INCLUDING AN ORTHOPHOTO OF THE STUDY SITE WITH GPS LANDMARKS IN YELLOW.....	17
FIGURE 3: CLIMATE DIAGRAM OF THE TOWN GROß-ENZERSDORF.....	18
FIGURE 4: VISUALIZATION OF SOIL TYPE A) ONE (B1), B) TWO (B2), AND C) THREE (B3) (SOURCE: BFW, 2020)	19
FIGURE 5: ORTHOPHOTO OF THE EXPERIMENTAL FIELD IN RUTZENDORF, DEPICTING THE THREE PREVALENT SOIL TYPES (B1, B2, B3) ON-SITE WITH COLORED DOTS INDICATING THE IN-SITU SENSORS (SOURCE: MODIFIED AFTER BFW, 2020)	20

FIGURE 6: SETUP OF THE TDR MEASURING INSTRUMENT, COMPRISING OF A VOLTMETER, A CAR BATTERY, THE SENSOR, AND A PORTABLE BACKPACK.....	22
FIGURE 7: CHARGING PROCESS OF A CAPACITOR WITH RESPECT TO TIME (SOURCE: METER, 2020).....	23
FIGURE 8: ORTHOPHOTO OF THE EXPERIMENTAL FIELD IN RUTZENDORF WITH DIFFERENT GRIDS AND DIFFERENT GPS POINTS ON JULY 24TH, 2020	26
FIGURE 9: COMPOSITION OF THE PARROT FLOWER POWER SENSOR (SOURCE: PARROT, 2016) .	27
FIGURE 10: ORTHOPHOTO OF THE EXPERIMENTAL FIELD WITH LOCATIONS OF THE METEOROLOGIC MEASURING INSTRUMENTS.....	28
FIGURE 11: TRANSMITTANCE AND REFLECTANCE OF AN INDIVIDUAL LEAF FROM 400 TO 2000 NM (SOURCE: KNYAZIKHIN, MARSHAK AND MYNENI, 2005)	31
FIGURE 12: RELATIONSHIP BETWEEN NDVI AND LAI (SOURCE: CAMPBELL, 2020).....	31
FIGURE 13: ARIS SIMULATION OF WINTER WHEAT WITH A CLASSIFIED RSS [%] FOR A) JULY 1ST 2015, B) AUGUST 1ST 2015, C) AUGUST 5TH 2015, D) SEPTEMBER 1ST 2015 (SOURCE: EITZINGER ET AL. 2016)	36
FIGURE 14: INTERDEPENDENCIES OF PARAMETERS INFLUENCING B, TR, Y, ETC (SOURCE: STEDUTO ET AL., 2012).....	39
FIGURE 15: CALCULATION SCHEME OF AQUACROP IMPLYING DIFFERENT PATHWAYS IMPACTED BY TEMPERATURE AND WATER STRESS (A-G) (SOURCE: VANUYTRECHT ET AL., 2014).....	41
FIGURE 16: REQUIRED INPUT PARAMETERS FOR THE AQUACROP SIMULATION (SOURCE: STEDUTO ET AL. 2012).....	43
FIGURE 17: OVERVIEW OF THE STATISTICAL ANALYSIS CONDUCTED FOR ALL THREE VEGETATION PERIODS; THE REFERENCE SENSORS ARE HIGHLIGHTED (IN BLUE) AND WERE COMPARED BASED ON LINEAR REGRESSION WITH THE SM ESTIMATES (WHITE BOXES) ACCORDINGLY	47
FIGURE 18: VALIDATION OF FIT OF THE AQUACROP SIMULATION OUTPUT A) BARLEY B1, B) BARLEY B2, C) BARLEY B3, D) WHEAT B1, E) WHEAT B2, F) WHEAT B3, G) RYE B1, H) RYE B2, I) RYE B3; THE STATISTICAL ANALYSIS IS BASED ON THE PEARSON CORRELATION COEFFICIENT; STATISTICAL DIFFERENCES WERE ACCEPTED AT $P > 0.05$ (B1 – B3 REFERS TO THE THREE APPLIED SOIL TYPES AS DEFINED IN CHAPTER: 3.1.3 SOIL CONDITIONS)	49
FIGURE 19: SPATIAL VARIABILITY OF SOIL MOISTURE FOR A) APRIL 4TH, AND B) APRIL 15TH 2019 ACROSS THE EXPERIMENTAL FIELD IN RUTZENDORF, BASED ON KRIGING	51
FIGURE 20: PRECIPITATION GRAPH FOR MARCH AND APRIL 2019, PRIOR TO PARROT MEASUREMENTS	52
FIGURE 21: PRECIPITATION GRAPH FOR MAY 2019, PRIOR TO PARROT MEASUREMENTS	53
FIGURE 22: SPATIAL VARIABILITY OF SOIL MOISTURE FOR A) MAY 15TH, AND B) JUNE 1ST 2019 ACROSS THE EXPERIMENTAL FIELD IN RUTZENDORF, BASED ON KRIGING	54
FIGURE 23: PRECIPITATION GRAPH FOR JULY 2020, PRIOR TDR MEASUREMENTS.....	55
FIGURE 24: ZOOM EFFECT OF TDR MEASUREMENT BASED SPATIAL INTERPOLATED SM ON JULY 24TH 2020, FOR A) MEASUREMENTS IN THE 250 M GRID, B) MEASUREMENTS IN THE 125 M GRID, C) MEASUREMENTS IN THE 50 M GRID.....	56
FIGURE 25: STATISTICAL ANALYSIS OF TDR VS. PARROT FOR A) LINEAR REGRESSION, B) RESIDUAL PLOT, AND C) RESIDUAL DENSITY CURVE	57

FIGURE 26: STATISTICAL ANALYSIS OF PARROT_CAL VS. MET-STATION_10CM FOR A) LINEAR REGRESSION, B) RESIDUAL PLOT, AND C), RESIDUAL DENSITY CURVE.....58

FIGURE 27: STATISTICAL ANALYSIS OF PARROTS_REL VS. SWI_001_REL FOR A) LINEAR REGRESSION, B) SM TREND OF PARROTS AND SWI_001 OVER TIME, C) RESIDUAL PLOT AND D), PRECIPITATION GRAPH60

FIGURE 28: STATISTICAL ANALYSIS OF PARROTS_REL VS. ARIS_REL_REL FOR A) LINEAR REGRESSION, B) SM TREND OF PARROTS AND ARIS_REL OVER TIME, C) RESIDUAL PLOT, AND D), PRECIPITATION GRAPH62

FIGURE 29: STATISTICAL ANALYSIS OF PARROTS VS. AQUACROP_B1_5CM FOR A) LINEAR REGRESSION, B) SM TREND OF PARROTS AND AQUACROP_B1_5CM OVER TIME, C) RESIDUAL PLOT, AND D), PRECIPITATION GRAPH.....63

FIGURE 30: TRENDLINE COMPARISON OF PARROT AND A) SWI_001, B) SWI_005, C) SWI_010, D) ARIS, E) SMAP, F) AQUACROP_B1_5CM, G) AQUACROP_B1_15CM, H) AQUACROP_B2_5CM, I) AQUACROP_B2_15CM, J) AQUACROP_B3_5CM, K) AQUACROP_B4_15CM, AND L) PRECIPITATION GRAPH.....65

FIGURE 31: STATISTICAL ANALYSIS OF WS_20CM_REL AND SWI_001_REL FOR A) LINEAR REGRESSION, B) PRECIPITATION GRAPH, AND C) TREND OF WS_20CM_REL AND SWI_001_REL.....67

FIGURE 32: STATISTICAL ANALYSIS OF WS_20CM_REL AND ARIS_REL FOR A) LINEAR REGRESSION, B) PRECIPITATION GRAPH, AND C) TREND OF WS_20CM_REL AND ARIS_REL69

FIGURE 33: TRENDLINE COMPARISON OF PARROT AND A) SWI_001, B) SWI_005, C) SWI_010, D) ARIS, E) SMAP, F) AQUACROP_B1_5CM, G) AQUACROP_B1_15CM, H) AQUACROP_B2_5CM, I) AQUACROP_B2_15CM, J) AQUACROP_B3_5CM, K) AQUACROP_B4_15CM, AND L) PRECIPITATION GRAPH.....71

FIGURE 34: STATISTICAL ANALYSIS OF ARIS_REL VS. SWI_001_REL FOR A) LINEAR REGRESSION, B) SM TREND OF ARIS_REL AND SWI_001_REL OVER TIME, C) RESIDUAL PLOT, AND D), PRECIPITATION GRAPH.....74

FIGURE 35: STATISTICAL ANALYSIS OF SWI_001 VS. AQUACROP_B2_5CM FOR A) LINEAR REGRESSION, B) SM TREND OF SWI_001 AND AQUACROP_B2_5CM OVER TIME, C) RESIDUAL PLOT, AND D), PRECIPITATION GRAPH.....76

FIGURE 36: TRENDLINE COMPARISON OF ARIS AND A) SWI_001, B) SWI_005, C) SMAP, D) AQUACROP_B1_5CM, E) AQUACROP_B1_15CM, F) AQUACROP_B2_5CM, G) AQUACROP_B2_15CM, H) AQUACROP_B3_5CM, I) AQUACROP_B4_15CM AND ITEM J) THE PRECIPITATION GRAPH.....77

Tables

TABLE 1: SUMMARY OF THE BASELINE SENSOR ANALYSIS 2019.....59

TABLE 2: SUMMARY OF THE SENSOR COMPARISON ANALYSIS 201966

TABLE 3: SUMMARY OF THE COMPARISON ANALYSIS 202072

TABLE 4: SUMMARY OF THE COMPARISON ANALYSIS 201879

Annex

ANNEX 1: STATISTICAL ANALYSIS OF PARROT_CAL_42 VS. MET-STATION_10CM FOR A) LINEAR REGRESSION, B) RESIDUAL PLOT, AND C), RESIDUAL DENSITY CURVE	91
ANNEX 2: STATISTICAL ANALYSIS OF PARROTS_REL VS. SWI_005_REL FOR A) LINEAR REGRESSION, B) SM TREND OF PARROTS AND SWI_005_REL OVER TIME, C) RESIDUAL PLOT, AND D), PRECIPITATION GRAPH	92
ANNEX 3: STATISTICAL ANALYSIS OF PARROTS_REL VS. SWI_010_REL FOR A) LINEAR REGRESSION, B) SM TREND OF PARROTS AND SWI_010_REL OVER TIME, C) RESIDUAL PLOT, AND D), PRECIPITATION GRAPH	93
ANNEX 4: STATISTICAL ANALYSIS OF PARROTS_REL VS. SMAP_REL_REL FOR A) LINEAR REGRESSION, B) SM TREND OF PARROTS AND SMAP_REL OVER TIME, C) RESIDUAL PLOT, AND D), PRECIPITATION GRAPH	94
ANNEX 5: STATISTICAL ANALYSIS OF PARROTS VS. AQUACROP_B1_15CM FOR A) LINEAR REGRESSION, B) SM TREND OF PARROTS AND AQUACROP_B1_15CM OVER TIME, C) RESIDUAL PLOT, AND D), PRECIPITATION GRAPH.....	95
ANNEX 6: STATISTICAL ANALYSIS OF PARROTS VS. AQUACROP_B2_5CM FOR A) LINEAR REGRESSION, B) SM TREND OF PARROTS AND AQUACROP_B2_5CM OVER TIME, C) RESIDUAL PLOT, AND D), PRECIPITATION GRAPH.....	96
ANNEX 7: STATISTICAL ANALYSIS OF PARROTS VS. AQUACROP_B2_15CM FOR A) LINEAR REGRESSION, B) SM TREND OF PARROTS AND AQUACROP_B2_15CM OVER TIME, C) RESIDUAL PLOT, AND D), PRECIPITATION GRAPH.....	97
ANNEX 8: STATISTICAL ANALYSIS OF PARROTS VS. AQUACROP_B3_5CM FOR A) LINEAR REGRESSION, B) SM TREND OF PARROTS AND AQUACROP_B3_5CM OVER TIME, C) RESIDUAL PLOT, AND D), PRECIPITATION GRAPH.....	98
ANNEX 9: STATISTICAL ANALYSIS OF PARROTS VS. AQUACROP_B3_15CM FOR A) LINEAR REGRESSION, B) SM TREND OF PARROTS AND AQUACROP_B3_15CM OVER TIME, C) RESIDUAL PLOT, AND D), PRECIPITATION GRAPH.....	99
ANNEX 10: STATISTICAL ANALYSIS OF WS_20CM_REL VS. SWI_005_REL FOR A) LINEAR REGRESSION, B) PRECIPITATION GRAPH, AND C) TREND OF WS_20CM_REL AND SWI_005_REL.....	100
ANNEX 11: STATISTICAL ANALYSIS OF WS_20CM_REL VS. SWI_010_REL FOR A) LINEAR REGRESSION, B) PRECIPITATION GRAPH, AND C) TREND OF WS_20CM_REL AND SWI_010_REL.....	101
ANNEX 12: STATISTICAL ANALYSIS OF WS_20CM_REL AND SMAP_REL FOR A) LINEAR REGRESSION, B) PRECIPITATION GRAPH, AND C) TREND OF WS_20CM_REL AND SMAP_REL	102
ANNEX 13: STATISTICAL ANALYSIS OF WS_20CM AND AQUACROP_B1_5CM FOR A) LINEAR REGRESSION, B) PRECIPITATION GRAPH, AND C) TREND OF WS_20CM AND AQUACROP_B1_5CM.....	103
ANNEX 14: STATISTICAL ANALYSIS OF WS_20CM AND AQUACROP_B1_15CM FOR A) LINEAR REGRESSION, B) PRECIPITATION GRAPH, AND C) TREND OF WS_20CM AND AQUACROP_B1_15CM.....	104

ANNEX 15: STATISTICAL ANALYSIS OF WS_20CM AND AQUACROP_B2_5CM FOR A) LINEAR REGRESSION, B) PRECIPITATION GRAPH, AND C) TREND OF WS_20CM AND AQUACROP_B2_5CM.....	105
ANNEX 16: STATISTICAL ANALYSIS OF WS_20CM AND AQUACROP_B2_15CM FOR A) LINEAR REGRESSION, B) PRECIPITATION GRAPH, AND C) TREND OF WS_20CM AND AQUACROP_B2_15CM.....	106
ANNEX 17: STATISTICAL ANALYSIS OF WS_20CM AND AQUACROP_B3_5CM FOR A) LINEAR REGRESSION, B) PRECIPITATION GRAPH, AND C) TREND OF WS_20CM AND AQUACROP_B3_5CM.....	107
ANNEX 18: STATISTICAL ANALYSIS OF WS_20CM AND AQUACROP_B3_15CM FOR A) LINEAR REGRESSION, B) PRECIPITATION GRAPH, AND C) TREND OF WS_20CM AND AQUACROP_B3_15CM.....	108
ANNEX 19: STATISTICAL ANALYSIS OF RANDOM DISTRIBUTION FOR WS_20CM AND A) AQUACROP_B1_5CM, B) AQUACROP_B1_15CM, C) AQUACROP_B2_5CM, D) AQUACROP_B2_15CM, E) AQUACROP_B3_5CM, F) AQUACROP_B4_15CM, G) SWI_001_REL, H) SWI_005_REL, I) SWI_010_REL, J) ARIS_REL, AND K) SMAP_REL...	109
ANNEX 20: STATISTICAL ANALYSIS OF ARIS_REL VS. SWI_010_REL FOR A) LINEAR REGRESSION, B) SM TREND OF ARIS_REL AND SWI_010_REL OVER TIME, C) RESIDUAL PLOT, AND D), PRECIPITATION GRAPH.....	110
ANNEX 21: STATISTICAL ANALYSIS OF ARIS_REL VS. SMAP_REL FOR A) LINEAR REGRESSION, B) SM TREND OF ARIS_REL AND SMAP_REL OVER TIME, C) RESIDUAL PLOT, AND D), PRECIPITATION GRAPH.....	111
ANNEX 22: STATISTICAL ANALYSIS OF ARIS VS. AQUACROP_B1_5CM FOR A) LINEAR REGRESSION, B) SM TREND OF ARIS AND AQUACROP_B1_5CM OVER TIME, C) RESIDUAL PLOT, AND D), PRECIPITATION GRAPH.....	112
ANNEX 23: STATISTICAL ANALYSIS OF ARIS VS. AQUACROP_B1_15CM FOR A) LINEAR REGRESSION, B) SM TREND OF ARIS AND AQUACROP_B1_15CM OVER TIME, C) RESIDUAL PLOT, AND D), PRECIPITATION GRAPH.....	113
ANNEX 24: STATISTICAL ANALYSIS OF ARIS VS. AQUACROP_B2_5CM FOR A) LINEAR REGRESSION, B) SM TREND OF ARIS AND AQUACROP_B2_5CM OVER TIME, C) RESIDUAL PLOT, AND D), PRECIPITATION GRAPH.....	114
ANNEX 25: STATISTICAL ANALYSIS OF ARIS VS. AQUACROP_B2_15CM FOR A) LINEAR REGRESSION, B) SM TREND OF ARIS AND AQUACROP_B2_15CM OVER TIME, C) RESIDUAL PLOT, AND D), PRECIPITATION GRAPH.....	115
ANNEX 26: STATISTICAL ANALYSIS OF ARIS VS. AQUACROP_B3_5CM FOR A) LINEAR REGRESSION, B) SM TREND OF ARIS AND AQUACROP_B3_5CM OVER TIME, C) RESIDUAL PLOT, AND D), PRECIPITATION GRAPH.....	116
ANNEX 27: STATISTICAL ANALYSIS OF ARIS VS. AQUACROP_B3_15CM FOR A) LINEAR REGRESSION, B) SM TREND OF ARIS AND AQUACROP_B3_15CM OVER TIME, C) RESIDUAL PLOT, AND D), PRECIPITATION GRAPH.....	117

References

- AgriMetSoft (2019) *Online Calculations - MBE (Mean Bias Error)*. Available at: <https://agrimetsoft.com/calculators/Mean Bias Error> (Accessed: 18 August 2021).
- Albergel, C. *et al.* (2010) 'Cross-evaluation of modelled and remotely sensed surface soil moisture with in situ data in Southwestern France', *Hydrology and Earth System Sciences*, 14(11), pp. 2177–2191. doi: 10.5194/hess-14-2177-2010.
- Albergel, C. *et al.* (2012) 'Evaluation of remotely sensed and modelled soil moisture products using global ground-based in situ observations', *Remote Sensing of Environment*, 118, pp. 215–226. doi: 10.1016/j.rse.2011.11.017.
- Allen, R. G. *et al.* (1998) 'Crop Evapotranspiration - guidelines for computing crop water requirements', *FAO Irrigation and Drainage paper 56*, 300(56), p. 300. doi: 10.1016/j.eja.2010.12.001.
- Anderson, J. A. *et al.* (2009) *Cereals*. 3. Edition. Edited by M. J. Carena. New Delhi, India: Springer-Verlag New York. doi: 10.1007/978-0-387-72297-9.
- APCC (2014) *Österreichischer Sachstandsbericht Klimawandel 2014 (AAR14), Austrian Panel on Climate Change (APCC)*. Vienna, Austria. doi: 10.1553/aar14s467.
- Araya, A., Keesstra, S. D. and Stroosnijder, L. (2010) 'Simulating yield response to water of Teff (*Eragrostis tef*) with FAO's AquaCrop model', *Field Crops Research*, 116(1–2), pp. 196–204. doi: 10.1016/j.fcr.2009.12.010.
- Aydin, M. (2008) 'A model for Evaporation and Drainage investigations at Ground of Ordinary Rainfed-areas', *Ecological Modelling*, 217(1–2), pp. 148–156. doi: 10.1016/j.ecolmodel.2008.06.015.
- BFW (2020) *eBod Digitale Bodenkarte*. Available at: <https://bodenkarte.at/> (Accessed: 20 August 2020).
- BMLRT (2020) *Getreideanbau und Getreidearten in Österreich, 14th of May 2020*. Available at: <https://www.bmlrt.gv.at/land/produktion-maerkte/pflanzliche-produktion/getreide/Getreide.html> (Accessed: 18 August 2020).
- Brandtner, F. (1954) 'Jungpleistozäner Löß und fossile Böden in Niederösterreich', *E&G Quaternary Science Journal*, 4/5, pp. 49–82. doi: 10.3285/eg.04-5.1.06.
- Brocca, L. *et al.* (2010) 'ASCAT soil wetness index validation through in situ and modeled soil moisture data in central Italy', *Remote Sensing of Environment*. Elsevier Inc., 114(11), pp. 2745–2755. doi: 10.1016/j.rse.2010.06.009.
- Brocca, L., Crow, W. T., *et al.* (2017) 'A Review of the Applications of ASCAT Soil Moisture Products', *IEEE Journal of Selected Topics in Applied Earth Observations and Remote Sensing*, 10(5), pp. 2285–2306. doi: 10.1109/JSTARS.2017.2651140.
- Brocca, L., Ciabatta, L., *et al.* (2017) 'Soil moisture for hydrological applications: Open questions and new opportunities', *Water*, 9(2), p. 20. doi: 10.3390/w9020140.
- Campbell, G. S. (2020) *The researcher's complete guide to Leaf Area Index (LAI)*. Pullman, WA. USA. Available at: <https://www.metergroup.com/environment/articles/lp80-pain-free-leaf-area-index-lai/>.

Cepuder, P. and Schlederer, W. (2002) *Untersuchung der Grundwasserbelastung mit Nitrat unter Feldgemüsebau im pannonischen Klimaraum, Endbericht*. Vienna, Austria.

Doorenbos, J. and Kassam, A. H. (1979) 'Yield response to water', *FAO Irrigation and Drainage*, 33, p. 193. doi: 10.1016/B978-0-08-025675-7.50021-2.

Dubrovsky, M. *et al.* (2009) 'Application of relative drought indices in assessing climate-change impacts on drought conditions in Czechia', *Theoretical and Applied Climatology*, 96(1–2), pp. 155–171. doi: 10.1007/s00704-008-0020-x.

Eitzinger, J. *et al.* (2003) 'A simulation study of the effect of soil water balance and water stress on winter wheat production under different climate change scenarios', *Agricultural Water Management*, 61(3), pp. 195–217. doi: 10.1016/S0378-3774(03)00024-6.

Eitzinger, J. *et al.* (2008) 'Aspects on results and uncertainties of climate change impact simulation studies for agricultural crop production in Europe', *Die Bodenkultur*, 59(1–4), pp. 131–147.

Eitzinger, J. *et al.* (2010) 'Climate change and agriculture: Introductory editorial', *Journal of Agricultural Science*, 148(5), pp. 499–500. doi: 10.1017/S0021859610000481.

Eitzinger, J. *et al.* (2013) 'Sensitivities of crop models to extreme weather conditions during flowering period demonstrated for maize and winter wheat in Austria', *The Journal of Agricultural Science*, 151(6), pp. 813–835. doi: 10.1017/S0021859612000779.

Eitzinger, J. *et al.* (2016) *Drought monitoring system for Austrian agriculture - AgroDroughtAustria (Final Scientific Report of project 'AgroDroughtAustria' of the Austrian Climate Change Program)*. Vienna, Austria. Available at: https://meteo.boku.ac.at/report/BOKU-Met_Report_25_online.pdf.

Eitzinger, J. (2018) *Agricultural Risk Information System, ARIS-BOKU-MET*. Available at: <https://aris.boku.ac.at/about.html> (Accessed: 20 August 2020).

Entekhabi, D. *et al.* (2010) 'The soil moisture active passive (SMAP) mission', *Proceedings of the IEEE*, 98(5), pp. 704–716. doi: 10.1109/JPROC.2010.2043918.

EUMETSAT (2020) *The prime objective of Advanced SCATterometer (ASCAT) is to measure wind speed and direction over the ocean*. Available at: <https://www.eumetsat.int/website/home/Satellites/CurrentSatellites/Metop/MetopDesign/ASCAT/index.html> (Accessed: 20 August 2020).

Ezenne, G. I. *et al.* (2019) 'Current and potential capabilities of UAS for crop water productivity in precision agriculture', *Agricultural Water Management*. Elsevier, 218(2019), pp. 158–164. doi: 10.1016/j.agwat.2019.03.034.

FAO (2017) *AquaCrop training handbooks Book I. Understanding AquaCrop*. Edited by D. Raes. Rome, Italy: Food and Agricultural Organization of the United Nations.

FAO (2020) *What is AquaCrop*. Available at: <http://www.fao.org/aquacrop/overview/whatisaquacrop/en/> (Accessed: 27 August 2020).

Freyer, B. *et al.* (2003) *MUBIL Zwischenbericht 2003 - Monitoring der Umstellung auf*

den biologischen Landbau. Vienna, Austria.

Freyer, B. *et al.* (2013) *MUBIL IV - Langzeit-Monitoring der Auswirkungen einer Umstellung auf den biologischen Landbau*. Vienna, Austria.

Frost, I. (2018) *Einfache lineare Regression - Die Grundlage für komplexe Regressionsmodelle verstehen*. München, Germany: Springer VS. doi: 10.1007/978-3-658-19732-2.

George, P. P. (2013) *Remote Sensing of Energy Fluxes and Soil Moisture Content*. 1. Edition, *Remote Sensing of Energy Fluxes and Soil Moisture Content*. 1. Edition. Boca Raton, Florida: CRC Press, Taylor & Francis Group. doi: 10.1201/b15610.

Hall, A. E. (2001) *Crop responses to environment, Crop Responses to Environment*. Boca Raton, USA: CRC Press LLC. doi: 10.1201/9781420041088.

Hoekstra, A. Y. *et al.* (2011) *The Water Footprint Assessment Manual - Setting the Global Standard*, *Social and Environmental Accountability Journal*. London, UK. doi: 10.1080/0969160x.2011.593864.

Jones, S. B., Wraith, J. M. and Or, D. (2002) 'Time domain reflectometry measurement principles and applications', *Hydrological Processes*, 16, pp. 141–153. doi: 10.1002/hyp.513.

Kato, T. (2016) 'Prediction of photovoltaic power generation output and network operation', in Fuabashi, T. (ed.) *Integration of Distributed Energy Resources in Power Systems*. Nagoya, Japan, pp. 77–108. doi: 10.1016/c2014-0-03911-1.

Kim, S. *et al.* (2015) 'A global comparison of alternate AMSR2 soil moisture products: Why do they differ?', *Remote Sensing of Environment*, 161, pp. 43–62. doi: 10.1016/j.rse.2015.02.002.

Kizito, F. *et al.* (2008) 'Frequency, electrical conductivity and temperature analysis of a low-cost capacitance soil moisture sensor', *Journal of Hydrology*, 352(3–4), pp. 367–378. doi: 10.1016/j.jhydrol.2008.01.021.

Knyazikhin, Y., Marshak, A. and Myneni, B. (2005) 'Three-Dimensional Radiative Transfer in Vegetation Canopies', in *3D Radiative Transfer in Cloudy Atmospheres*. Berlin, Heidelberg, Germany: Springer, p. 649. doi: 10.1007/3-540-28519-9.

Kristelly, C. (2020) 'Regionalisierung des Wassergehaltes/SWI', in Fuchs, G., Kristelly, C., and Neuwirth, B. (eds) *Wasser im Boden*. Vienna, Austria.: Bundesministerium für Landwirtschaft, Regionen und Tourismus, Sektion I - Wasserwirtschaft, Abteilung I/3 - Wasserhaushalt, Marxergasse 2, 1030 Wien, p. 225.

Krzic, M. *et al.* (2010) *Virtual Soil Lab Modules, 2010*. Available at: <https://labmodules.soilweb.ca/time-domain-reflectometry/> (Accessed: 15 July 2020).

Lalic, B., Eitzinger, J., *et al.* (2018) *Agricultural Meteorology and Climatology*. Firenze, Italy: Firenze University Press. doi: 10.36253/978-88-6453-795-5.

Lalic, B., Firanj Sremac, A., *et al.* (2018) 'Seasonal forecasting of green water components and crop yield of summer crops in Serbia and Austria', *The Journal of Agricultural Science*, 156, pp. 658–672. doi: 10.1017/S0021859618000047.

Ikwardienst (2020) *Trockenheitsmonitoring- und Verhersagesystem ARIS*. Available at: <https://warndienst.lko.at/trockenheitsmonitoring-und-vorhersagesystem->

aris+2500+1073326 (Accessed: 26 August 2020).

METER (2020) *The researcher's complete guide to soil moisture*. Pullman, WA. USA.

Micheli, E., Schad, P. and Spaargaren, O. (2006) 'World Reference Base for Soil Resources 2006', *Encyclopedia of Soil Science*. 3. Edition. Rome, Italy: FAO. doi: 10.1081/e-ess3-120053850.

Mittag, H.-J. (2014) *Statistik: Eine Einführung mit interaktiven Elementen*. 3. Auflage. Heidelberg, Germany: Springer Spektrum.

Monsi, M. and Saeki, T. (1953) 'On the factor light in plant communities and its importance for matter production', *Japanese Journal of Botany*, (14), pp. 22–52.

Moran, M. S. *et al.* (2004) 'Estimating soil moisture at the watershed scale with satellite-based radar and land surface models', *Canadian Journal of Remote Sensing*, 30(5), pp. 805–826. doi: 10.5589/m04-043.

Mozny, M. *et al.* (2012) 'Use of a soil moisture network for drought monitoring in the Czech Republic', *Theoretical and Applied Climatology*, 107, pp. 99–111. doi: 10.1007/s00704-011-0460-6.

Mueller, W. (1993) *Agroklimatische Kennzeichnung des zentralen Marchfeldes. Beihefte zu den Jahrbüchern der ZAMG*, 348. Vienna, Austria.

Novelli, F. *et al.* (2019) 'Assimilation of Sentinel-2 Leaf Area Index Data into a Physically-Based Crop Growth Model for Yield Estimation', *Agronomy*, 9. doi: 10.3390/agronomy9050255.

van Opstal, J. D. *et al.* (2019) *FLYING SENSORS FOR SMALLHOLDER FARMING: AN INNOVATIVE TECHNOLOGY FOR WATER PRODUCTIVITY ASSESSMENT*, 3rd World Irrigation Forum (WIF3). Bali, Indonesia.

Otterson, D. W. (2015) 'Tech Talk: (10) Electrolytic Conductivity Measurement Basics', *Measurement and Control (United Kingdom)*, 48(8), pp. 239–241. doi: 10.1177/0020294015600473.

Pal, R. (2016) 'Validation methodologies', in *Predictive Modeling of Drug Sensitivity*. Lubbock, USA, pp. 83–108. doi: 10.1016/c2015-0-04656-1.

Panic, D. (2020) *Validation of high resolution soil moisture products over Austria*. University of Technology, Vienna.

Parrot (2016) 'Parrot Flower Power', *User Guide*, pp. 1–14. Available at: https://support.parrot.com/files/s3fs-public/firmware/flower-power_user-guide_de.pdf (Accessed: 28 August 2020).

Poutanen, K., Katina, K. and Heiniö, R. L. (2014) 'Rye', in Zhou, W. *et al.* (eds) *Bakery Products Science and Technology*. 2. Edition. John Wiley & Sons, Ltd., pp. 75–87. doi: 10.1002/9781118792001.ch4.

Raes, D. *et al.* (2018) 'Chapter 1: FAO crop-water productivity model to simulate yield response to water', in *Reference Manual, AquaCrop Version 6.0-6.1*. Rome, Italy: Food and Agricultural Organization of the United Nations, pp. 1–25. Available at: www.fao.org/publications.

Rahimzadeh-Bajgiran, P. and Berg, A. (2016) 'Soil Moisture Retrievals Using Optical/TIR Methods', in Srivastava, P., Petropoulos, G., and Kerr, Y. H. (eds)

- Satellite Soil Moisture Retrieval: Techniques and Applications*. 1. Edition. Amsterdam, Netherlands: Elsevier Inc., pp. 47–72. doi: 10.1016/B978-0-12-803388-3.00003-6.
- Ramirez-Garcia, J., Almendros, P. and Quemada, M. (2012) 'Ground cover and leaf area index relationship in a grass, legume and crucifer crop', *Plant, Soil and Environment*, 58(8), pp. 385–390. doi: 10.17221/195/2012-pse.
- Roth, C. H., Malicki, M. A. and Plagge, R. (1992) 'Empirical evaluation of the relationship between soil dielectric constant and volumetric water content as the basis for calibrating soil moisture measurements by TDR', *Journal of Soil Science*, 43(1), pp. 1–13. doi: 10.1111/j.1365-2389.1992.tb00115.x.
- Saseendran, S. A. *et al.* (2015) 'Quantifying crop water stress factors from soil water measurements in a limited irrigation experiment', *Agricultural Systems*, 137, pp. 191–205. doi: 10.1016/j.agsy.2014.11.005.
- Saue, T. and Kadaja, J. (2014) 'Water limitations on potato yield in Estonia assessed by crop modelling', *Agricultural and Forest Meteorology*, 194, pp. 20–28. doi: 10.1016/j.agrformet.2014.03.012.
- Sperl, I. (2013) '110 Jahre Grossenzersdorf', *BOKU: Das Magazin der Universität des Lebens*, pp. 4–6.
- Stadt Wien (2020) *Das Marchfeld - Die großen Landschaftsräume Wiens*. Available at: <https://www.wien.gv.at/stadtentwicklung/projekte/landschaft-freiraum/landschaft/gruenraum/landschaftsraeume/marchfeld.html> (Accessed: 18 August 2020).
- Steduto, P. *et al.* (2009) 'Aquacrop-the FAO Crop Model to Simulate Yield Response to Water: I. Concepts and Underlying Principles', *Agronomy Journal*, 101(3), pp. 426–437. doi: 10.2134/agronj2008.0139s.
- Steduto, P. *et al.* (2012) *Crop yield response to water*. Rome, Italy: Food and Agricultural Organization of the United Nations.
- Suman, S. *et al.* (2020) 'Appraisal of SMAP operational soil moisture product from a global perspective', *Remote Sensing*, 12, pp. 1–24. doi: 10.3390/rs12121977.
- Thaler, S. *et al.* (2012) 'Impacts of climate change and alternative adaptation options on winter wheat yield and water productivity in a dry climate in Central Europe', *Journal of Agricultural Science*, 150, pp. 537–555. doi: 10.1017/S0021859612000093.
- Thaler, S. *et al.* (2018) 'The performance of Metop Advanced SCATterometer soil moisture data as a complementary source for the estimation of crop-soil water balance in Central Europe', *The Journal of Agricultural Science*, pp. 1–22. doi: 10.1017/S0021859618000011.
- Todoroff, P., De Robillard, F. and Laurent, J. B. (2010) 'Interconnection of a crop growth model with remote sensing data to estimate the total available water capacity of soils', *International Geoscience and Remote Sensing Symposium (IGARSS 2010)*, pp. 1641–1644. doi: 10.1109/IGARSS.2010.5653790.
- Topp, G. C., Davis, J. L. and Annan, A. P. (1980) 'Electromagnetic Determination of Soil Water Content: Measurements in Coaxial Transmission Lines', *Water Resources Research*, 16(3), pp. 574–582. doi: 10.1029/WR016i003p00574.

Trnka, M. *et al.* (2010) 'Is rainfed crop production in central Europe at risk? Using a regional climate model to produce high resolution agroclimatic information for decision makers', *The Journal of Agricultural Science*, 148, pp. 639–656. doi: 10.1017/S0021859610000638.

Vanuytrecht, E. *et al.* (2014) 'AquaCrop: FAO's crop water productivity and yield response model', *Environmental Modelling and Software*, 62, pp. 351–360. doi: 10.1016/j.envsoft.2014.08.005.

Vergopolan, N. *et al.* (2020) 'Field-scale soil moisture bridges the spatial-scale gap between drought monitoring and agricultural yields', *Hydrology and Earth System Sciences - EGU*, pp. 1–31. doi: 10.5194/hess-25-1827-2021.

Wagner, M. P. *et al.* (2020) 'Remote Sensing Data Assimilation in Dynamic Crop Models Using Particle Swarm Optimization', *ISPRS - International Journal of Geo-Information*, 9, pp. 1–24. doi: 10.3390/ijgi9020105.

Wagner, W. *et al.* (2008) 'Temporal Stability of Soil Moisture and Radar Backscatter Observed by the Advanced Synthetic Aperture Radar (ASAR)', *Sensors*, 8, pp. 1174–1197. doi: 10.3390/s80201174.

Wagner, W. *et al.* (2013) 'The ASCAT Soil Moisture Product: A Review of its Specifications, Validation Results, and Emerging Applications', *Meteorologische Zeitschrift*, 22(1), pp. 5–33. doi: 10.1127/0941-2948/2013/0399.

WWAP (United Nations World Water Assessment Programme) (2015) *The United Nations World Water Development Report 2015: Water for a Sustainable World*. Paris, France. Available at: <http://unesdoc.unesco.org/images/0023/002318/231823E.pdf>.

Xaver, A. *et al.* (2019) 'Evaluating the suitability of the consumer low-cost Parrot Flower Power soil moisture sensor for scientific environmental applications', *Geoscientific Instrumentation, Methods and Data Systems - EGU*, pp. 1–36. doi: 10.5194/gi-9-117-2020.

Zappa, L. *et al.* (2019) 'Deriving Field Scale Soil Moisture from Satellite Observations and Ground Measurements in a Hilly Agricultural Region', *Remote Sensing*, 11, pp. 1–22. doi: 10.3390/rs11222596.